Integration of optically random media into optoelectronic devices

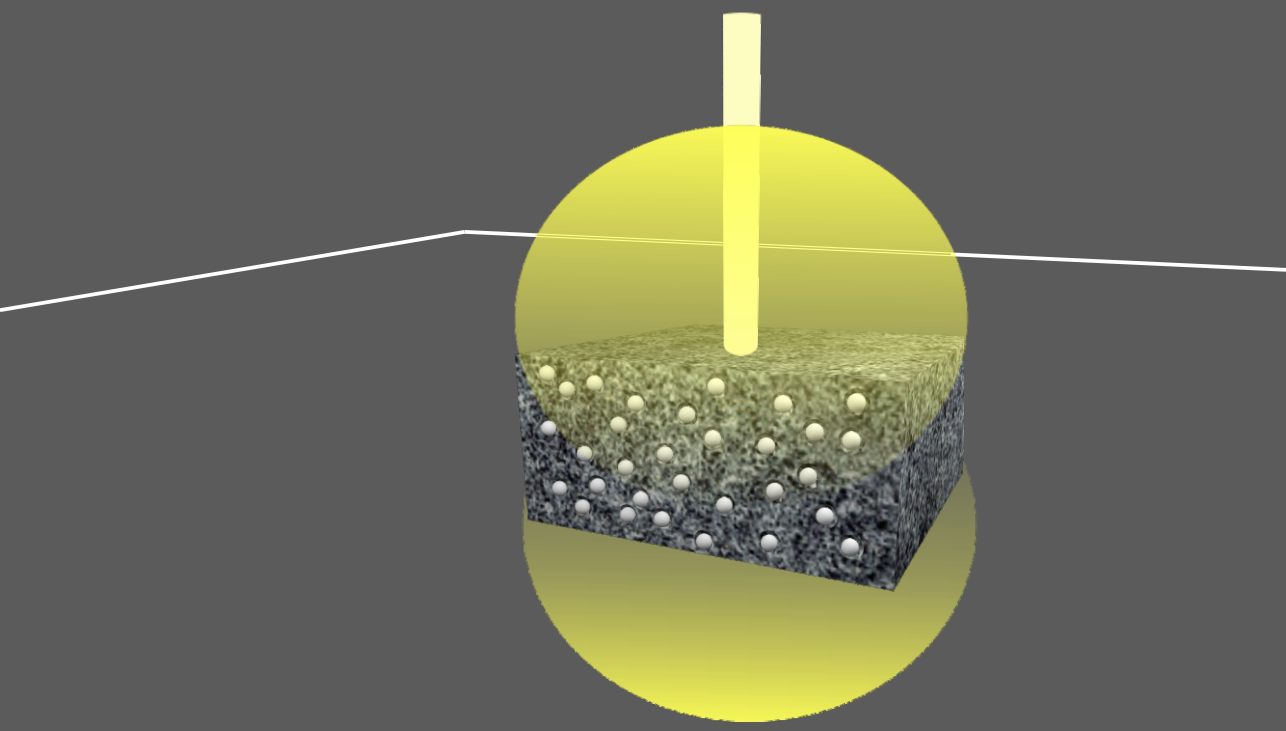

José María Miranda Muñoz

Integration of Optically Random Media into Optoelectronic Devices

Doctoral thesis presented by

José María Miranda Muñoz

Supervised by

Prof. Dr. Hernán Míguez García
Dr. Gabriel Lozano Barbero

Department of Inorganic Chemistry
Faculty of Chemistry
University of Seville

Multifunctional Optical Materials Group
Institute of Materials Science of Seville
Spanish Research Council

Seville, 2019

Contents

1 Introduction

The work described in this thesis addresses the design, fabrication and characterisation of different optically random media consisting of porous transparent matrices integrating a random distribution of monodisperse spherical high refractive index nanoparticles. In these materials, the scattering of light by each centre is assumed to be independent from that of the other particles, and therefore correlation terms can be neglected. This approximation holds for a lowly concentrated and well dispersed distribution of particles in the host matrix. In the first place, optically random media consisting in different combinations of materials exhibiting this configuration are analysed, fabricated and optically characterised. In this thesis, the scattering of light by each centre is assumed to be independent from that of the other particles, and therefore correlation terms can be neglected. This approximation holds for a lowly concentrated and well dispersed distribution of particles in the host matrix. After sensitisation with absorbing or luminescent molecules, their integration into dye-sensitized solar cells (DSSCs), as well as their use for the fabrication of colour-converting materials aimed at implementation in light-emitting devices (LEDs), is assessed. The studies detailed throughout this thesis enabled disentangling fundamental aspects of the propagation of light in random media, as well as demonstrating the possibility of taking advantage of the diffuse propagation of light for the fabrication of optoelectronic devices with enhanced properties.

This chapter provides a general overview on light scattering in optically random media. The magnitudes usually employed for the characterisation of light scattering as a function of the optical properties of the materials are defined. In order to justify the interest in the study of light propagation in these media, the regimes of weak and strong localisation are defined and some applications of optically random media are discussed. The progress in the control of the scattering properties of turbid media and the different strategies proposed for that purpose are briefly reviewed. Eventually, due to the interest of the integration of the materials proposed in this thesis as photoanodes into DSSCs and as a colour-converting element into LEDs, some

background and basic concepts on these optoelectronic devices are provided.

1.1 Light scattering in optically random media

Photonics pursues the generation and harnessing of light, and as a consequence it offers numberless applications in a vast variety of technological fields[1–3]. Specifically, controlling light propagation has been demonstrated beneficial regarding the design and fabrication of optoelectronic devices[4–6]. Light manipulation usually involves the design and synthesis of materials with specific structural properties aimed at particular applications. As a consequence, ordered architectures structured in the wavelength range presenting a certain periodicity are widely employed[7–11]. Due to the ordered nature of these nanostructures, they generally rely on diffraction and interference effects for the modification of light transport. In contrast, an interesting strategy for moulding the flow of light is also found in random structures, where strong light scattering takes place[12–19].

Light scattering is generally understood as any deviation of light from rectilinear propagation caused by any wavelength-scale inhomogeneity, such as a particle of a certain refractive index, and it is generally an elastic event. An optically random medium commonly consists in a dielectric or semiconductor material in which its building blocks, or a fraction of these, are placed in a disordered manner, thus presenting a random modulation of the refractive index. The refractive index contrast between its components and the surrounding medium triggers light scattering at each of these building blocks, which act as scattering centres. Due to successive scattering events, light propagates in a diffusive manner, exiting the material at random directions and endowing it with a characteristic whitish opacity. This is the case of media such as clouds, sugar or colloidal suspensions, which despite their microscopic transparency appear white and opaque due to multiple scattering of the light. Because of the deviation of the light rays, the object appears blurry to the eye on the other side of the random medium, Fig. 1.1(a), and, for large enough thicknesses, the wave vector of the propagating beam loses memory of its initial direction and the source becomes invisible, as illustrated

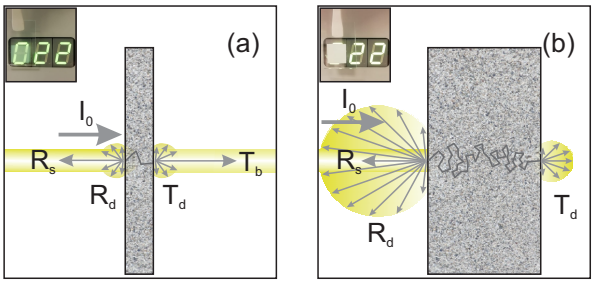

Figure 1.1: Illustration of light scattering in a slab of an optically random medium of different thicknesses. In (a) light is scattered only a few times throughout the whole thickness of the slab, causing partial blurrying of the object, as displayed in the corresponding inset. In (b) light is scattered a large number of times, causing total diffuse propagation of the light and complete opacity of the film, as displayed in the corresponding inset. I_0 refers to the intensity of the incident beam, R_s to the fraction of this intensity specularly reflected, R_d and T_d to the fraction of light reflected and transmitted, respectively, after being scattered and T_b the fraction of light transmitted unaffected by scattering.

in Fig. 1.1(b), as it happens for the sun during a cloudy day or for light going through a piece of paper. Optically random media have drawn special attention due to the interesting optical phenomena that arise when light propagates through a highly disordered medium, such as Anderson localisation for electromagnetic waves[20–22], weak localisation[12,13,23], which leads to the emergence of the so-called enhanced backscattering cone, image reconstruction[24–26] or phenomena of random lasing[27–29], among others.

In this scenario, a description of the propagation of light in turbid media requires the characterisation of their diffusion properties. A key parameter in this regard is the scattering mean free path, ℓ_{sc}, defined as the average distance covered by a photon before undergoing a scattering event. The optical response of a random material is dictated by the relationship between its thickness, L, and ℓ_{sc}. If $L < \ell_{sc}$, the probability for a scattering event to occur is low and the material displays high transparency as long as absorption is negligible. For $L > \ell_{sc}$, scattering is more likely and partial or total diffuse propa-

gation of light occurs depending on the value of L with respect to ℓ_{sc}. In this range, whereas insufficient thickness causes only a fraction of the light to propagate diffusively, thus still allowing a significant ballistic component on the other side of the medium, for a large enough value of L, multiple scattering ensures total diffuse light transport. From the definition of ℓ_{sc}, strong scattering entails short values of ℓ_{sc}. A measurement of the scattering strength of a random material at a specific wavelength is provided by the inverse of the localisation parameter, $k\ell_{sc}$, often referred to as the Ioffe-Regel parameter, being k the wave vector in the material. Therefore, $k\ell_{sc} \gg 1$ for a weakly scattering random medium. In a limit situation of extremely strong scattering where $k\ell_{sc} \simeq 1$, light transport is seriously hampered and localisation occurs as a consequence of wave interference effects[23,30].

In a first approximation, if each scattering centre is placed apart from the rest, the scattering triggered by each centre is assumed to be independent from that of the other particles and therefore correlation terms can be neglected. In this situation, which corresponds to the independent-scattering approximation, ℓ_{sc} is defined as[31]

$$\ell_{sc} = \frac{1}{\rho \cdot \sigma_{sc}}, \tag{1.1}$$

being ρ the particle number density and and σ_{sc} the scattering cross section of the particle. Equation 1.1 reveals that ℓ_{sc} is thus mainly dictated by σ_{sc}, this being therefore a crucial magnitude for the description of light tranport in random media. σ_{sc} determines the amount of radiation scattered by a particle in every direction and it is a function of geometrical and optical parameters, namely, the size and shape of the scattering centre, the complex refractive index of both the particle and the surrounding medium, specifically, the contrast between them, and the wavelength of the incident light, λ. The relation between particle size and light wavelength allows the definition of three well-defined regimes of scattering. In the limit of scattering particles much smaller than the wavelength of the incident light, Rayleigh scattering takes place. For this size, the scattering is very inefficient and σ_{sc} is proportional to λ^{-4}. If the particle size is much bigger than the wavelength of the incident light, the classical vision of a point-like photon impinging on a surface is retrieved. Here, ray tracing methods properly describe light scattering and the value of σ_{sc} corresponds

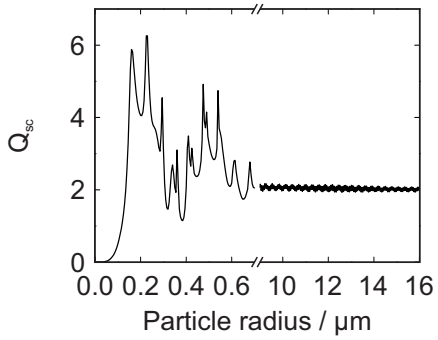

Figure 1.2: Scattering efficiency of a TiO_2 sphere in air at $\lambda = 800$ nm of a size ranging from 1 nm to 16 μm.

to twice the geometrical cross section of the scattering particle (geometrical scattering). In the intermediate region, where the size of the particles is of the order of the incident wavelength, σ_{sc} is maximal. The scattering taking place in this regime is referred to a Mie scattering and σ_{sc} becomes unpredictable and non-intuitive. In fact, the apparent size of the particle is highly dependent on the refractive index contrast between that of the scattering particle and the surrounding medium and it can be several times larger than the geometrical cross section. An analytical expression for σ_{sc} in the Mie scattering regime has only been derived for highly symmetric shapes, such as a sphere or an infinite cylinder[32,33]. These three scattering regimes can be observed in Fig. 1.2, where the scattering efficiency value of a TiO_2 sphere of different sizes in air at $\lambda = 800$ nm for is displayed. The scattering efficiency, Q_{sc}, is a normalisation of σ_{sc} to the geometrical cross section of the particle, that is, $Q_{sc} = \sigma_{sc}/\pi r^2$, where r is the radius of the sphere.

Another fundamental parameter for the characterisation of light propagation in random media is the transport mean free path, ℓ_t, defined as the average length over which the direction of propagation of light becomes fully randomised. In fact, ℓ_t is the average distance light needs to travel in a turbid medium before propagation becomes randomised. The condition of propagation in the diffuse regime is formulated as $\lambda \ll \ell_t \ll L$. As light advances, multiple scattering deviates photons from the incident beam, causing partial randomisation of the direction of propagation. In the limit of diffuse propagation,

sufficient scattering frustrates ballistic transmittance and light only propagates diffusively. ℓ_t is a function of the angular distribution of the light scattered by the particle and it is related to ℓ_{sc} according to[31]

$$\ell_t = \frac{\ell_{sc}}{1 - \langle cos\theta \rangle}, \tag{1.2}$$

where θ is the elevation angle, contained in the plane of incidence and measured with respect to the illumination direction, and the average of $cos\theta$ is evaluated by weighting the contribution at each θ angle according to the angular distribution of the light intensity provided by Mie theory. On the one hand, in the hypothetical situation of a perfectly isotropic distribution, the $cos\theta$ average cancels, resulting $\ell_t = \ell_{sc}$ and the direction of propagation of light is fully randomised after one single scattering event. On the other hand, Eq. 1.2 reveals that for a particle yielding anisotropic scattering, $\ell_t > \ell_{sc}$. One scattering event is therefore not enough to achieve full randomisation and the larger the anisotropy, the larger the discrepancy between ℓ_t and ℓ_{sc}. Whereas the angular distribution of light exiting a perfect diffuser describes a Lambertian profile, as Fig. 1.3(a) illustrates, the intensity of the light emerging from a material presenting weaker scattering displays an

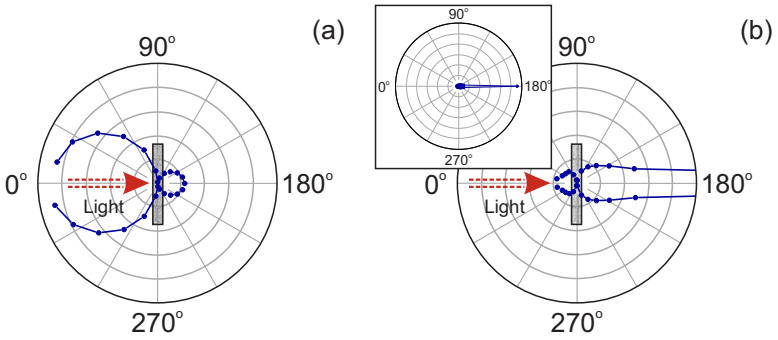

Figure 1.3: Experimental angular distribution of (a) a 100-μm thick paper sheet and (b) a weakly scattering material consisting in a 9-μm mesoporous TiO_2 film integrating nanocrystalline TiO_2 spheres of radius r = (225 $\pm$ 20) nm in a 5% concentration at λ = 600 nm. The inset in (b) displays a zoom-out of the angular distribution for a better visualisation of the ballistic component. Incoming light impinges on the left side of the slab.

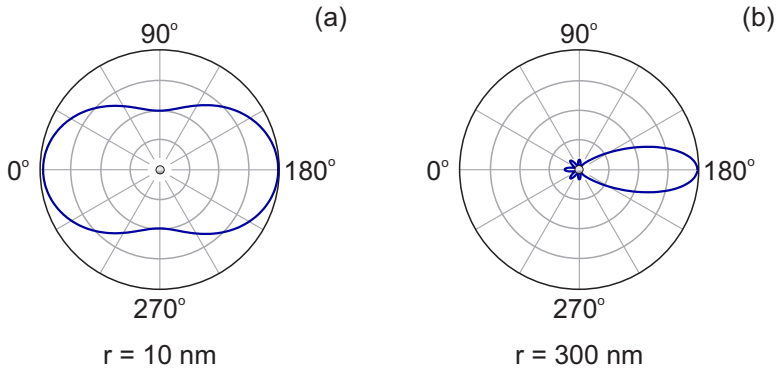

Figure 1.4: Angular distribution of the light scattered by a crystalline TiO_2 sphere of size (a) r = 10 nm and (b) r = 300 nm at $\lambda = 600$ nm.

angular-dependent distribution, whose shape is dictated by the number of scattering events, Fig. 1.3(b). In the Rayleigh scattering limit, the particles present a dipole-like distribution of the scattered light, highly isotropic, as shown in Fig. 1.4(a). In contrast, for particle sizes comparable to the wavelength of the incident light, the angular distribution is highly dependent on the shape of the scattering centre. In particular, for a spherical particle the angular distribution becomes mostly forward-oriented, as illustrated in Fig. 1.4(b).

1.2 Control of the optical response of optically random media

Turbid media in which light propagates in a diffuse manner have been a subject of interest in diverse fields. Their whiteness and opacity reveal their suitability for multiple applications, such as their use as light diffusers for integration into lamps or windows in order to generate a uniform and smooth light distribution for indoor illumination, integration into organic light-emitting diodes (OLEDs) for improvement of their luminescent and viewing properties[34–39], or for backlight units present in liquid crystal displays (LCD)[40,41]. There has also been interest in the design of structures maximising light scattering to produce highly efficient Lambertian reflectors while reducing material usage[42–46]. These systems capable of strongly scattering light in the thinnest possible thickness would be deemed valuable by indus-

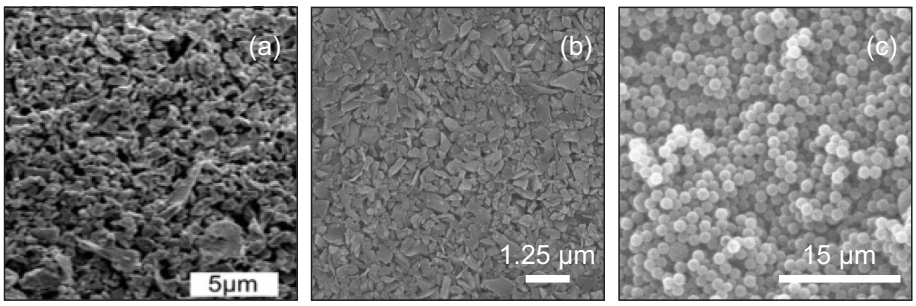

Figure 1.5: Examples of optically random media. (a) SEM image of a layer of dense GaAs particles (taken from Ref.[52]). (b) SEM image of a sample consisting of compacted Ge powder (taken from Ref.[54]). (c) SEM image of a photonic glass comprising a random distribution of polymer spheres.

tries devoted to the manufacture of commercial products exhibiting a white appearance, such as the production of paper[47].

Optically random media have also been of interest for the study of fundamental aspects of the propagation of light and multiple scattering in random media. When light propagates throughout highly scattering media and unusual optical phenomena arise as a consequence of the multiple scattering of the waves and subsequent interference. Some examples of these optically random materials are randomly packed semiconductor powder, especially relevant for their high refractive index, such as TiO_2[48–51], GaAs[52], Ge[53,54] or Si powder[55], teflon slabs[56], colloidal suspensions of particles of materials such as PS or TiO_2 generally in water[13,14,23,56–58], and random stackings of identical spherical PS building blocks, known as photonic glasses[59,60]. Figure 1.5 displays a few examples of optically random media. The main route for the characterisation of their optical properties consists in the determination of ℓ_{sc}, ℓ_t, the absorption length and the diffusion constant. Nevertheless, most of these materials present a number of problems when aiming at finely controlling the amount of disorder for a desired optical response. In most of the cases, due to the fabrication methods, their bulding blocks commonly present a relevant polydispersity in size. This, along with their usually irregular and diverse shapes, hinders an accurate prediction of light transport, excluding the possibility of performing an optical design prior to their fabrica-

tion. Besides, some of the most frequently employed materials, such as Ge, GaAs or Si, show strong absorption in the visible range of the spectrum, thus limiting the studies to be performed in the infrared region[51–55], where they remain transparent. Absorption hinders the analysis of light propagation in random media and especially the observation of localisation phenomena. As for those random materials in liquid phase, *i.e* colloidal suspensions, the refractive index contrast between the scattering particles and the liquid medium does not provide sufficiently low values of ℓ_{sc}.

Among the interesting optical phenomena derived from the propagation of light through highly scattering materials, the observation of Anderson localisation for electromagnetic waves has been long coveted and the repeatedly failed attempts at detecting it in 3-dimensional systems has made it become a holy grial in the study of optically random media. Above a certain degree of disorder, the diffusion of the light waves tends to zero and transport comes to a halt. This phenomenon is known as Anderson localisation and it derives from backscattered waves interfering constructively. In the limit of localisation, $\ell_t \rightarrow 0$, *i.e* transport is not possible, and diffusion theory fails at describing light propagation. Despite being proposed for electrons coherently scattered in semiconductor crystals presenting a certain degree of disorder[20], due to the wave nature of the electron, Anderson localisation could be expected in any wave system, such as light[21,22,61]. Anderson localisation is predicted for strongly scattering media where $k\ell_{sc} \simeq 1$, according to the Ioffe-Regel criterion. In order to approach this condition, ℓ_{sc} needs to be minimised, that is, σ_{sc} should be maximised, according to Eq. 1.1, which is achieved for a particle size in the regime of Mie scattering. In the pursuit of experimental evidence of Anderson localisation of photons, scientists came across the observation of weak localisation of light, regarded as the precursor of strong or Anderson localisation[13,23]. Weak localisation is a consequence of time-reversal symmetry of the paths of light multiply scattered in a random medium and it manifests itself as a cone of enhanced backscattered light. A light wave originated at a source entering a random material can undergo several scattering events and exit the material in the backward direction towards the source, accumulating a phase shift. Another wave can however follow the same path in the opposite direction due to time-reversal symmetry, developing the same phase

shift. The interference between these waves is constructive, resulting in an increase of intensity in the backward direction. Determination of the enhanced backscattering cone has been proved useful to understand the propagation of light in strongly scattering materials, since its width enables extraction of ℓ_t[57].

Due to the interest in tuning and controlling optical disorder, efforts have particularly been focused on the fabrication processes of these materials and the subsequent analysis of the evolution of their optical response. In the first place, liquid suspensions employing PS spheres as scattering centres offered an easy manner to tune the amount of disorder through the size and concentration of PS spheres. Besides, the spherical shape of the centres ensured identical light scattering by all the inclusions, regardless of the incidence direction of the light. Indeed, the change of the features of the backscattering cone in the range of weak localisation, which are directly related to ℓ_t, when varying the parameters dictating the conditions of the optical disorder, that is, either the size[12,58,62] or the concentration[12,13] of scattering particles, has been analysed in several ocassions. Wolf *et al.*[62] also considered the effect of different degrees of absorption in the medium by adding a luminescent dye (Rhodamine 6G) in various concentrations. Later on, porous gallium phosphide (GaP) attracted interest as an optically random medium. It is a semiconductor material presenting a high bulk refractive index ($n = 3.45$ at $\lambda = 550$ nm), transparent in part of the visible spectrum ($\lambda > 550$ nm) and, as a semiconductor, it offers the possibility to be manipulated in order to controllably introduce porosity by means of electrochemical etching of a single crystal. This allowed the fabrication of GaP chunks enabling control over the photonic strength through the amount of introduced porosity[16,63,64]. Further advances in the fabrication of turbid media with tunable scattering properties were made with the synthesis of semiconductor nanowires. Systems consisting in arrays of GaP, Si and InP nanowires have demonstrated exceptional photonic strength[65], while providing control over their scattering through their diameter, volume filling fraction and alignment[66]. Apart from the study of the characteristics of light propagation in random media, these materials also attract interest owing to the possibility of their use in numberless applications, such as optical imaging in biological systems[67], wavefront

shaping for sharp light focusing[68,69], diffusing wave spectroscopy[70] or implementation in optoelectronic devices[40,65].

1.3 Applications of optically random media

The characteristics of light propagation in optically disordered materials can find a variety of situations in which to be exploited with a specific purpose. In this section, some of the most common applications of these materials are briefly reviewed.

1.3.1 Random lasing

Since the proposals of R. V. Ambartsumyan *et al.*[71] and V. S. Letokhov *et al.*[27], optically disordered materials for the generation of laser-like emission have been intensively studied. In traditional laser action, light scattering in the resonant cavity has always been considered a nuisance, since it removes photons from the lasing mode. However, under the right conditions, strong light scattering in a disordered medium can actually be fundamental to trigger laser action. In a random medium with optical gain, recurrent scattering can serve as a feedback mechanism for the amplification of light, analogous to the

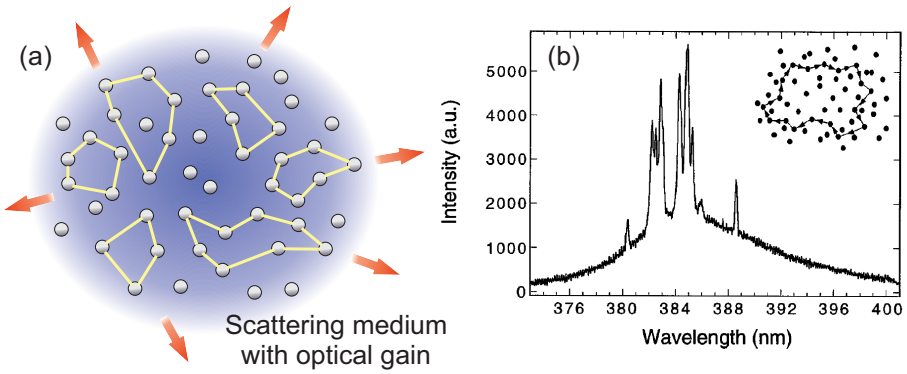

Figure 1.6: (a) Illustration of the generation of closed loops due to strong light scattering in an amplifying medium giving rise to laser action. (b) Emission spectrum of ZnO powder displaying laser action at an excitation intensity of 875 kW cm^{-2} by a pulsed Nd:YAG laser at $\lambda = 355$ nm (taken from Ref.[29]).

optical cavity in a conventional laser, as illustrated in Fig. 1.6(a). Laser action in a regular system is achieved above a threshold, where the total gain in the cavity surpasses the losses. In a strongly scattering medium, if ℓ_{sc} becomes equal to or shorter than the wavelength, light can form closed loop paths through successive scattering, undergoing amplification. In the limit where such amplification exceeds losses, laser action occurs. In a diffusion process with amplification the total gain is defined by the volume, whereas losses are proportional to the total surface[27]. It is therefore possible to achieve a situation where the intensity diverges and laser action is triggered in a random medium. The emission spectrum of a random laser is typically broader in frequency than in a conventional laser, and narrow spikes are usually present. Furthermore, the statistics of photons emitted by a random laser resembles to a great extent that of regular laser emission. The frequencies and the direction of emission are dictated by the modes formed in the random structure. A random system for lasing action can be in principle easily fabricated by grinding laser crystals[72,73], suspending high refractive index particles as individual scattering centres[28,74] or forming scattering clusters[75–77] in a dye solution, in semiconductor powder[29], photonic glasses[78] or in organic molecules employed as a gain medium[79].

1.3.2 Imaging through optically random media

When light coming from a source impinges on an optically disordered material, it is successively scattered and a fraction of it can reach the opposite interface of the material and exit as transmitted light. As previously mentioned, for a weakly scattering medium, a significant fraction of the light undergoes no scattering and it is ballistically transmitted. In this situation, the shape of the source can be retrieved. The image, however, appears somewhat blurry due to the light scattered and diffusively propagated. Here, image formation can be restricted to discerning between scattered and unscattered light and collect those photons corresponding to the latter. If the scattering in the material is too large, ballistic propagation is seriously hindered and information about the source becomes scrambled. As a result of this, the light transmitted by the material forms an apparently random speckle pattern. Full characterisation of the scattering system, which entails know-

ing the complete scattering matrix describing the disorder, would enable undoing the scattering and retrieving an image of the source[24]. Unfortunately this is not always feasible, since the usually countless elements forming the scattering matrix make it impracticable. An alternative method for unscrambling this information relies on the wave nature of light, which enables interference between the scattered waves. Such interference carries phase information, which in principle enables compensating for the disorder regardless of the complexity and decode the information[80].

Biological tissue, such as the skin, generally behaves as a highly scattering medium. Unravelling the information hidden in the propagated light waves would enable imaging of objects underneath in a non-invasive manner. As a consequence, studies focused on the reconstruction of a source placed on the other side of a strongly scattering layer have been performed[25,26,82]. In particular, the procedure proposed by O. Katz *et. al*[25] enables the reconstruction of an object between two scattering screens, as illustrated in Fig. 1.7. Light emitted by a source passes through a scattering screen and illuminates an object, which consists in a shape carved in a black screen. The object acts as an extended source and light becomes scrambled when passing through the second diffuser, which is afterwards detected by a

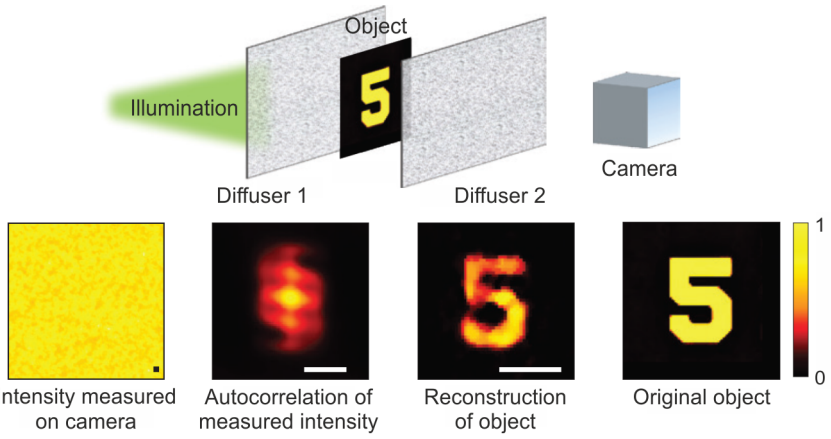

Figure 1.7: Principle of reconstruction of an object placed between two scattering screens proposed by O. Katz *et. al* (taken from Ref.[81] and Ref.[25]).

camera. The recorded image consists in a virtually constant intensity distribution displaying some random fluctuations. Autocorrelation of such intensity distribution allows retrieving information on the shape of the object for its reconstruction.

1.3.3 Light in- and out-coupling

In any application involving light harnessing, there are certain common issues, such as optical losses or parasitic absorptions, that are virtually inherent to any optical device and whose minimisation is generally desired when seeking for optimal performance. Since light management is performed through specific structures designed for a particular function, the incoming light must be in the first place coupled into the system. The presence of interfaces inevitably produces undesirable reflections reducing the fraction of light available for use. This is a well-known issue in the field of PV, where the high refractive index of the active materials hampers an efficient in-coupling of the incoming light, thus preventing maximal utilisation of the incident photons for photocurrent generation. In thin film technology, conceived to minimise material usage, insufficient optical thickness represents an additional drawback against maximal performance. On one hand, losses due to inefficient in-coupling are minimised through the implementation of anti-reflective coatings. On the other hand, texturised structures of a size in the wavelength range are integrated in order to cause a light-trapping effect due to successive light scattering and total internal reflection events and boost light absorption in the devices. Although such structures are commonly applied at the front transparent conductive oxide, they can also be found at deeper interfaces. In that sense, the integration of either inverted[83] or upright pyramids[4,83], as displayed in Fig. 1.8(a), or textures with random morphologies is regarded as the standard procedure[83–90]. Two examples of disordered textures for enhanced light in-coupling are displayed in Fig. 1.8(b) and (c). Randomly textured structures present the advantage of allowing an in-coupling of the incident light into the absorber layer in a broad spectral range. They generate a Lambertian light distribution inside the cell due to diffuse light propagation. Periodic architectures have also been proposed[91–93] and have demonstrated strong absorption enhancements[89,94,95], yet their spectral reso-

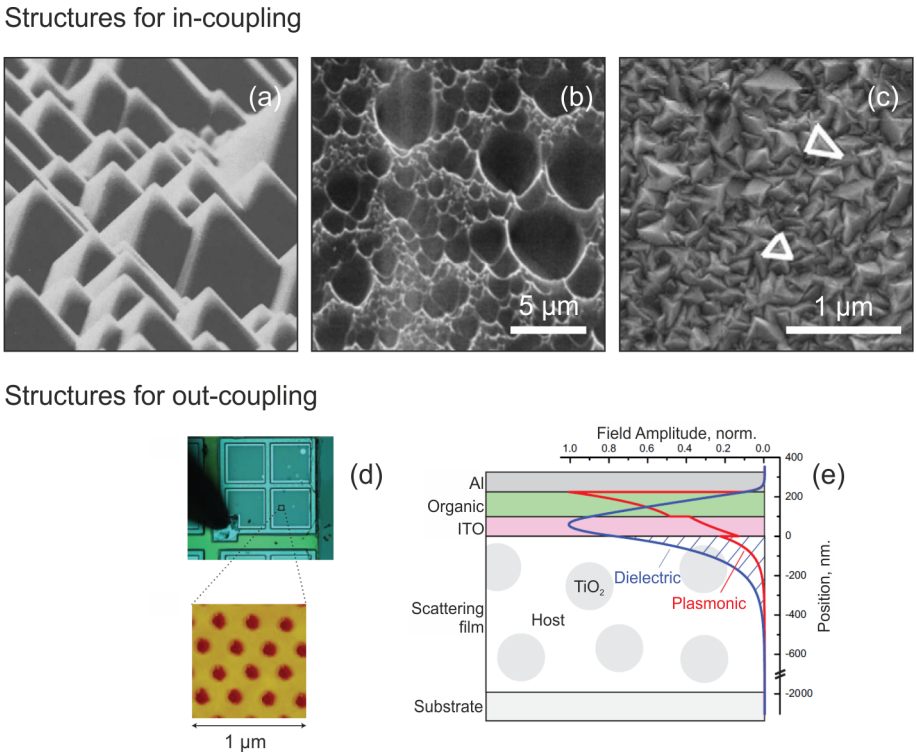

Figure 1.8: Examples of structures for in- and out-coupling applications. (a) Micrograph of a periodically textured Si surface in the shape of upright pyramids (taken from Ref.[83]). (b) SEM image of a random texture on a Si (taken from Ref.[86]). (c) SEM image of the random surface on polycrystalline boron-doped ZnO film constituted by columnar grains (taken from Ref.[87]). (d) Photonic-crystal-based LED (upper picture) and top-view atomic force microscope of the periodic structure of the photonic crystal lattice (lower picture) (taken from Ref.[6]). (e) Illustration of the structure of an OLED integrating a disordered structure (scattering layer) for enhanced light extraction (taken from Ref.[37]).

nances are typically sharper than in a disordered approach. Periodic structures provide a well-defined Fourier spectrum with strong, but scarce diffraction orders, while random architectures generate a large number of diffraction orders of weak intensity. There is, however, an optimal structure providing maximum light-trapping between these

two limit situations. With the purpose of reaching this optimum intermediate configuration, Martins *et al.*[96] proposed a design based on the supercell concept, *i.e.* gratings of larger period containing smaller unit cells, allowing to tailor the Fourier spectra created by the structure through controlled design of its aperiodicity.

The opposite situation also poses a problem. In photoluminescence (PL) applications, the inefficient out-coupling of the generated light from the emitting material results detrimental for the eventual efficiency of the device. In the situation of light generated in a film of homogeneous interfaces, due to the different refractive index value of the emitting material to that of air and taking into account that light in a luminescent material is generally emitted in all directions, a fraction of the emitted light inevitably remains trapped inside. For light emitted at angles above the critical angle defined by the escape cone, which is dictated by the refractive index contrast between the film and the surrounding medium, total internal reflection occurs and eventually results in unusable light. Inefficient out-coupling has especially been addressed in the field of light-emission for lighting applications and approaches based on either ordered[6,97] or disordered architectures, as shown in Fig. 1.8(d) and (e), respectively, have been proved to partly enhance light extraction[34,37,38,98].

Optical disorder can therefore serve as a tool to increase light incoupling in absorbing materials, while also be responsible for a more efficient light-extraction in photoluminescent materials. Scattering in a random medium is capable of enlarging the path length of the light and thus its residence time inside, which could result beneficial for boosting optical absorption and emission or to increase the PL of emitting films due to processes of improved out-coupling. The work presented in this thesis focuses specifically on the integration of materials presenting optical disorder as photoanodes into bifacial DSSCs and as conversion coatings into LEDs.

1.3.3.1 Dye-sensitized solar cells

In the current picture of global warming, progressive depletion of fossil fuel reserves and the alarming expected population growth, aggravated by a constant increase in the energy demand by the world population, the task of meeting the human energetic needs while min-

imising the harmful impact on the environment appears as an urgent challenge to overcome. The still excessive dependence on fossil fuel-based resources for the performance of human activities is leading to serious environmental issues. In this regard, alternative energy resources represent a peerless option, since they are generally based on abundant natural resources, while offering a meaningful reduction of the consequences derived from the use of fossil fuels. Among the different alternative energy sources, solar energy is proving to be a powerful contender in order to meet the world's energy demand without the environmental costs. In effect, the Earth's atmosphere receives an average power density of 1367 W m^{-2} [99], reaching the surface around 1000 W m^{-2} mostly due to absorption and scattering at the atmosphere.

Most of the available PV techonology in use is based on silicon, commonly known as first generation PV, for which devices have reached efficiencies above 25%[100]. The development of a second generation of PV devices based on thin film technology overthrew silicon as the active material for solar cells, as modest efficiencies were demonstrated while reducing material usage. In spite of the benefits of such technologies, they however present considerable drawbacks derived from the high manufacturing costs (high purity of the active material, complex fabrication processes, high processing temperatures), toxicity, pollution and opacity hindering integration in buldings[101,102]. A third generation PV emerged in an attempt to overcome these disadvantages limiting the operation of the technologies belonging to the first two generations. Third-generation devices enable low-cost PV, since they generally encompass technologies requiring easy and inexpensive fabrication procedures and low material usage. This third generation comprises four main technologies and diverse variants of these, namely, organic solar cells, quantum dot solar cells, dye-sensitized solar cells and a novel and revolutionary technology based on the use of a material comprising a perovskite structure as active material. Perovskite-based solar cells are especially relevant due to their rapid and unprecedented development, placing them at a position to potentially compete against the current commercial and mature silicon-based technologies. In fact, perovskite-based PV started as a DSSC technology, which employed organometal halide perovskite crystals as sensitisers of a TiO_2 photoanode[103,104]. The DSSC

appears as an attractive alternative to conventional PV devices due to their unique features, such as high transparency and lightweight[105]. They have been successfully developed on flexible substrates[106] and they have demonstrated remarkable performance under indoor illumination[107]. Additionally, they offer the possibility of colour choice[108], which results advantageous for architectural purposes, and they have demonstrated considerable stability[109–111]. Bifacial devices can be fabricated with them for harvesting of light impinging from all directions[112], as well as solar modules[102,113], all of the above possible through inexpensive fabrication procedures. DSSCs have seen a considerable wide number of applications due to different industrial sectors focused on their development. For instance, the Japanese company Fujikura has developed DSSCs for integration into indoor electronics, such as mobile phones. G24 Power started a nearly 5500-m^2 DSSC plant in 2007 while also achieving integration of these devices into flexible waterproof bags. Mini modules were fabricated by 3G Solar for charging electronic devices ranging from surveillance cameras to medical devices and Gunze Ltd. achieved the development of a wearable DSSC[102]. This thesis focuses on DSSCs as a target photovoltaic device for the implementation of optical disorder, mostly owing to their potential for industrialisation. Moreover, they offer the possibility to be manufactured at a large scale, since the materials are easily available, and fabrication by roll-to-roll processing is possible.

This section introduces basic concepts of a DSSCs. In particular, the working principle of a DSSC is depicted and the limitations revealing the need for approaches in order to boost their performance addressed.

Working principle of a DSSC: A DSSC is a photoelectrochemical system capable of generating a photocurrent from sunlight absorption. Ever since the first demonstration of a DSSC presenting sufficient absorption to become a competent PV technology[114,115], a wide variety of approaches have been progressively developed and implemented in the cell to reach a maximum power conversion efficiency (PCE) close to 12%[100,116]. In these devices, the active material is an absorbing dye anchored to a wide-bandgap semiconductor. The typical architecture of a DSSC consists of a film of TiO_2 nanoparticles sen-

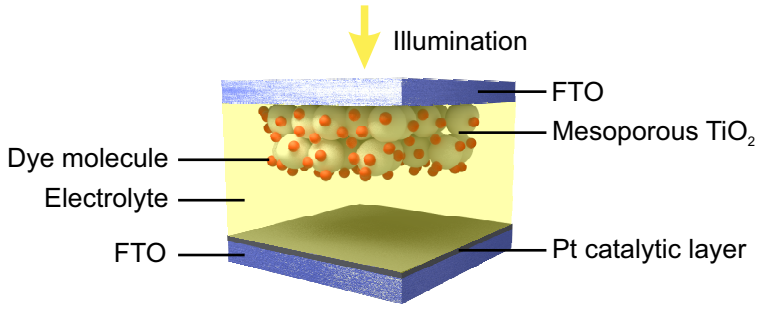

Figure 1.9: Schematic of a DSSC displaying its different constituents.

sitised with light-absorbing dye molecules, usually ruthenium (Ru) complexes, deposited on top of a transparent conductive oxide (TCO) substrate, embedded in a liquid electrolyte containing an iodide/triiodide (I^-/I_3^-) reduction-oxidation couple and a counterelectrode activated with platinum (Pt) for catalytic action, as illustrated in Fig. 1.9. The high internal surface area of the photoanode based on nanometric TiO_2 particles is advantageous for maximisation of the number of dye molecules anchored to the material, resulting in high optical absorption. The photons reaching the photoanode through the TCO substrate are absorbed by the dye molecules, exciting the electrons in the ground state, which are injected into the TiO_2-nanoparticle matrix. These electrons diffuse throughout the TiO_2 nanocrystalline network and are collected by the electrode, thus generating a photocurrent. At the same time, the oxidised dye molecules are regenerated by the iodide in the electrolyte, which diffuses to the counter-electrode as I_3^-, where it is reduced back to iodide. Recombination between electrons in the sensitised TiO_2 matrix and holes in the electrolyte can occur and is therefore a factor responsible for lowering the PCE of DSSCs.

Limitations of DSSCs: One factor limiting the performance of a DSSC derives from the short thickness required for photoanodes. Owing to the diffusion length of the generated electrons, of a few tens of microns, the thickness of the photoanode is restricted for an efficient collection of the generated electrons. While short thicknesses endow the devices with high transparency, which is regarded as an advantage of the technology, it limits the absorption capability of the inci-

dent light by the dye molecules. In that regard, the characteristics of the dye itself also limits the operation of the device, since it inevitably determines its light-harvesting capability and thus, its PCE[117]. Despite their generally broad absorption spectra, they usually present low molar extinction coefficients. Di-tetrabutylammonium *cis*-bis(isothiocyanato)bi(2,2′-bipyridil-4,4′-dicarboxylato)ruthenium(II) (N719), Fig. 1.10(a), has been extensively used as sensitiser. As with the majority of available dyes, the main drawback of N719 is its considerably weak absorption above 780 nm, critically hindering NIR light harvesting[118]. Figure 1.10(b) displays the absorption curve of an 8-μm thick mesoporous TiO_2 film sensitised with N719. Despite spanning over most of the visible range of the spectrum, the absorptance of this sensitised TiO_2 dramatically drops in the red region, hardly presenting absorption in the NIR, where the incident solar photon flux is still relevant. Therefore, experimental approaches for light-harvesting enhancement in this range of weak absorption would help boosting the performance of DSSCs presenting this issue. The most extended approach in order to counteract insufficient absorption consists in the inclusion of a backscattering layer consisting in large TiO_2 particles of a size around 200 nm on top of the photoactive electrode[119–123]. As a consequence, light not absorbed within the photoanode is diffusively reflected back into the electrode, offering a second chance for absorp-

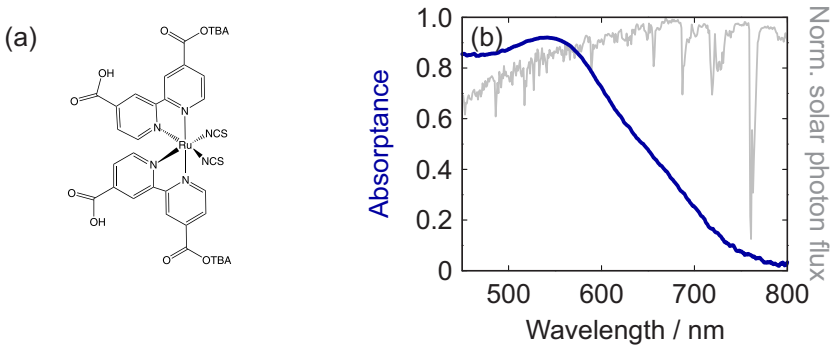

Figure 1.10: (a) Molecular structure of the dye N719. (b) Absorption curve of an 8-μm thick mesoporous TiO_2 film sensitised with N719 (blue line). The normalised incident solar photon flux has been included for comparison (gray line).

tion. In fact, the device for which the highest efficiency up to date was reported included a 5-μm-thick backscattering layer[116]. The integration of a backscattering layer inevitably leads to a loss of transparency in the cell. Therefore, a trade-off between performance of the device and transparency must be met.

Photoanodes including optical disorder have been considered as a strategy to boost light harvesting in DSSCs. This strategy profits from the diffuse light due to scattering triggered by the presence of scattering centres in order to enlarge the optical path of light, thus increasing the probability of absorption. J. Xi *et al.*[124] explored the effect on the PCE of DSSCs of including a mixture of individual TiO_2 nanocrystallites with microsized TiO_2 aggregates into their photoanode, attaining a considerable highest 7.59% PCE for an electrode including 30%-70% aggregates-nanocrystallite mixture. S. Hore *et al.*[125] considered air cavities of around 400 nm as scattering centres instead of high refractive index particles, which led to PCEs as high as 6.7%. A rather different strategy still based on light scattering was developed by Z. Tian *et al.*[126], who introduced a porosity gradient in the photoanode of a DSSC as a means to generate light scattering, demonstrating an increase of the PCE.

1.3.3.2 Colour converters for light-emitting devices

Lighting is nowadays so profoundly interwoven with daily human activities that its importance may often go unnoticed. Throughout the history of lighting, diverse technologies have been developed for outdoor and indoor illumination, from the burning of natural gas and the birth of the incandescent bulb to fluorescent tubes and compact fluorescent lamps based on the electrical excitation of a gas. Nonetheless, a relatively recent technology is revolutionising the way light is generated for human benefit, especially with the demonstration of its potential to replace conventional artificial light sources within the last two decades. Such technology relies on the PL of a semiconductor p-i-n junction through an electrical current, forming a light-emitting diode (LED). Lighting of streets, homes and workplaces accounts for an important fraction of the generated energy. More specifically, around 16% of the total electricity consumption in the U.S. in year 2015 was derived from lighting applications[127]. For this reason,

light sources presenting better performance would result in significant savings and less environmental impact. The advantages of LEDs have proved them a strong candidate to become a predominant low-cost lighting technology. In comparison to conventional incandescent light bulbs, which lose up to 95% the energy as heat[128], LEDs effectively transform a larger fraction of the input electrical current into luminous energy, yielding a current conversion efficiency around 40%. They present a compact size and operate with no need of the hazardous mercury vapour typically required for fluorescent tubes. Moreover, whereas the latter requires excitation around 254 nm, LEDs can be designed for excitation at a wavelength in the range 330-450 nm, which would also contribute to lower energy demands by reducing the quantum deficit. Eventually, LED technology allows tuning of the properties of the emission, such as directionality, spectral power distribution or colour temperature.

This section offers briefly addresses the architecture and operation of a typical light-emitting diode, as well as some downsides requiring special heed in order to take the technology to a higher maturity level.

Structure and operation of an LED: Solid-state light sources base their operation on the electroluminescence of a semiconductor material for light generation. Studies on GaN[129,130] led to the demonstration of a bright blue LED in 1994[131], followed by the rapid development of efficient and viable blue, green and yellow LEDs[132]. The birth of the first efficient blue LED opened the door to the generation of white light from a solid-state device. Additionally, since blue is located at the short-wavelength edge of the visible spectrum, downshifting through luminescent materials into other colours would be in principle possible[133].

LED chips essentially comprise a p-type semiconductor, presenting abundant holes, and an n-type semiconductor, rich in free electrons, in contact, forming a p-n junction. More specifically, the n-type material, which presents a large bandgap, is followed by successive thin layers of alternating smaller and larger bandgap materials, giving rise to the formation of quantum wells that efficiently trap holes and electrons. Topping the structure, a semiconductor layer of a hole-

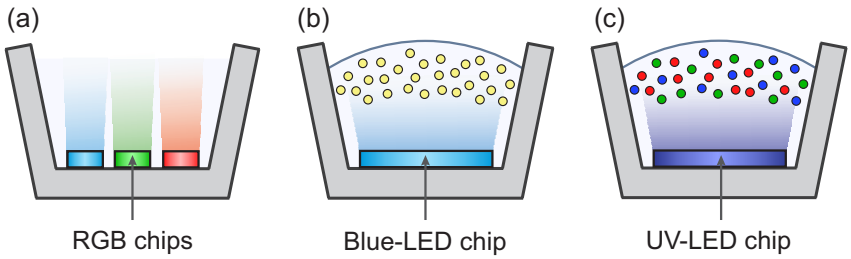

Figure 1.11: Principal strategies proposed for the generation of white-LED light. (a) Device based on three individual chips emitting blue, green and red light, (b) device based on a blue-emitting chip coated with yellow-emitting YAG:Ce phosphors and (c) device based on a UV-emitting chip coated with red, green and blue-emitting phosphors

rich material is placed. Recombination of holes from the valence band with electrons from the conduction band creates light of a colour defined by the energy gap between the bands.

Combination of different-colour light-emitting diodes would in principle enable selection of the wavelength of the emitted light, Fig. 1.11(a). However, the process of light generation presents poor efficiencies in some cases, as it is for the production of green and yellow colour, whose light-generation efficiency is currently around 20% or even below. This prevents multi-LED devices from achieving high efficiencies. Moreover, the different dependence of the lumen output on the operation temperature for different LED colours creates the necessity for additional circuitry for the control of temperature. For instance, the conversion efficiency of green and yellow LEDs have been proven to decrease significantly faster than blue LEDs with increasing temperature. As a result, reliable white light generation from a combination of red, green and blue LEDs still remains a challenge. For these reasons, this architecture has been overshadowed by a phosphor-converted LED (PC-LED) configuration, Fig. 1.11(b) and (c). Commercial white LEDs typically present a PC-LED architecture, based on an emitting chip coated with a layer of luminescent materials (phosphors) generally dispersed in a polymeric matrix. This phosphor coating is known as conversion coating and it presents the capability to absorb light emitted by the chip for re-emission at a longer wavelength

according to the Stokes shift, which is dictated by the chemical nature of the phosphor. These devices commonly combine a chip consisting in a GaN semiconductor film, presenting intense blue emission in the 420-500 nm range, with a conversion coating based on yellow-emitting cerium-doped YAG phosphors, as illustrated in Fig. 1.11(b). In some situations, PC-LEDs simply offer a more efficient process of light generation than directly from LED chips. However, the use of blue radiation as excitation imposes a limitation that appears as a drawback. There is a short number of available phosphors that can be efficiently excited with blue light and, in fact, YAG:Ce phosphors are rather an exception. Furthermore, due to the lack of red component in the emission spectrum of YAG:Ce, this device provides cold white light yielding poor colour rendering, that is, it is not able to faithfully reproduce the true colour of an object upon illumination. Other inorganic phosphors for appropriate colour-conversion have been investigated as an alternative to common YAG:Ce. For instance, a white-emitting LED yielding a colour rendering index as high as 90.5 (over 100) was built by exciting a combination of green-emitting $SrSi_2O_2N_2$:Eu^{2+} and red-emitting $CaSiN_2$:Eu^{2+} phosphors with a blue chip[134]. For conversion layers combining green- and red-emitting phosphors for the generation of white light from a blue LED chip, green-emitting Eu^{3+}-doped $LaSi_3N_5$ phosphor is especially promising due to its broadband photoluminescence peak at 549 nm[135] and as for the red component, $Ca_2ZnSi_2O_7$:Eu^{2+} can efficiently absorb 460-nm blue light[136]. In order to overcome the issues posed by the common PC-LED architecture based on a blue-emitting chip in combination with YAG:Ce phosphors, substitution of the blue by an UV-emitting chip in combination with red, green and blue-emitting phosphors has been proposed, Fig. 1.11(c). Not only supresses this configuration the dependence on blue light for excitation, but it also allows a broader wavelength coverage of the emission, offering a better colour rendering. Moreover, higher colour stability is expected, since fluctuations in the emission wavelength of the UV chip would not have an important influence on the emission colour of the device. Nonetheless, the need to combine three different phosphors poses an issue. Phosphors yielding PL at two different wavelengths simultaneously have been proposed as a possible solution and phosphors such as $Sr(PO_3)_2$:Eu^{2+},Mn^{2+}, which provide a combination of blue and or-

ange emission due to the Eu^{2+} and Mn^{2+} centres, respectively, have demonstrated white emission under UV irradiation[137]. Another disadvantage is the higher energy losses that are expected in the colour-conversion processes as the excitation energy is increased. That in combination with losses owing to absorption of phosphor-emitted light by the other phosphors, places the strategy considering a blue-emitting LED as the most commonly implemented.

The use of PC-LED architectures entails drawbacks derived from employing inorganic phosphors as converting material. In particular, the high cost of the RE cations introduced as luminescence centres in most inorganic phosphors in combination with their processing, which usually involves high temperatures, high pressure or reducing conditions, limits their use. In that regard, other promising alternatives are being explored. Quantum dots (QDs), for instance, are attractive candidates. One reason for this is their high quantum yield (QY). In fact, QY values as high as 98% (for CdSe/CdS QDs)[138] have been achieved as a consequence of the efforts focused on the maximisation of the QY of QDs[139]. Furthermore, they are susceptible to be easily dispersed in a polymeric matrix for integration into an LED device, in analogy to YAG:Ce phosphors. An intermediate approach involving inorganic phosphors and QDs was devised by H. S. Jang *et al.*[140], who proposed the combination of red-emitting CdSe QDs with broad-emission greenish-yellow-emitting Sr_3SiO_5:Ce^{3+},Li^+ co-doped with Pr^{3+} so as to enhance the colour rendering of white-emitting LEDs.

Another alternative currently under investigation consists in the use of organic phosphors for the processes of down-shifting, giving rise to the so-called white hybrid light-emitting diodes (WHLEDs). The group of organic phosphors encompasses a wide range of materials, such as organic dyes[141,142], carbon nanodots[143,144] or fluorescent proteins[145,146]. The emergence of this hybrid type of luminescent devices has attracted attention owing to their promising advantages. Whereas WHLEDs offer an easy design of the emission properties, high colour quality and a cost-effective and considerable environmentally friendly manufacture, their currently low thermal and chemical stability prevent them from becoming reliable and widely employed sources for lighting applications.

The possibility of employing nano-sized RE-doped phosphors has also been proposed as an alternative to common inorganic RE-based phosphors, which usually present a grain size of the order of the micrometer, owing to their properties, such as size tunability for improved optical quality, reduced light scattering or narrow emission band. The uncontrolled light scattering of YAG:Ce phosphor-based conversion layers hampers an optical design for a desired optical response of the material. In contrast, nano-sized phosphors offer the possibility of optical quality when employed for the fabrication of films, thus allowing control over the optical properties of the luminescent films through different strategies, such as nanostructuring or integration of particles.

Current drawbacks and limitations of LED technology: Despite the benefits of the LED technology, there are still some issues to be overcome in pursuit of efficient operation and safety. Among those issues, two of them present special relevance. One is related to the strong blue component in the emission spectrum of white PC-LEDs based on a blue diode, Fig. 1.12(a). Figure 1.12(b) displays the emission spectrum of a standard white-light LED, which reveals an important contribution of the blue light emitted by the chip to the device emission spectrum. Whereas blue light has been proven to play a crucial role in mood[147] and the correct regulation of circadian rhythms[148],

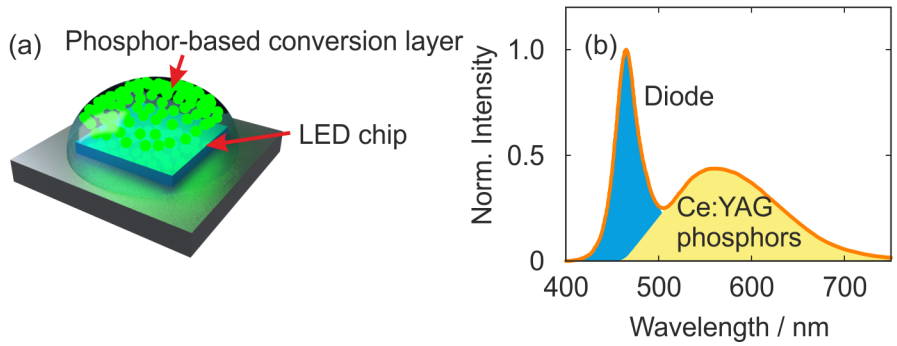

Figure 1.12: (a) Schematic of a light-emitting device in a PC-LED configuration. (b) Emission sprectrum of a typical white LED comprising a blue diode coated with yellow-emitting Ce:YAG phosphors as conversion material.

there are signs that it could in turn become a negative agent due to incessant exposure, especially for the eye, owing to the high transparency of the cornea and the lens to blue light[149]. Moreover, outdoor applications of white PC-LEDs could result in an intensification of light pollution due to the high scattering cross section of the molecules in the atmosphere at shorter wavelengths. Light pollution has been linked to a series of harms not only in humans, but especially wildlife, such as birds[150–152], insects[153] and trees[154]. Furthermore, as previously mentioned, the use of YAG:Ce as standard phosphors in combination with a blue-emitting chip yields poor colour rendering, as well as cold shades of white. The other main issue derives from the large refractive index of the materials required for the fabrication of the different components of LEDs. As a consequence, a significant fraction of the light produced in the active region can be trapped by means of total internal reflection in the different elements comprising the LED device, therefore not contributing to the usable light. In this regard, strategies for the enhancement of the extraction efficiency, such as surface roughening[155] or nanostructures integration into the diode[156], have been proposed. Hence the importance of developing approaches in order to achieve more efficient processes of light outcoupling from the different components of an LED device.

1.4 This thesis

1.4.1 Objectives

The work depicted in this thesis focuses on the study of the phenomena of light absorption and emission enhancement in optically random media, as well as their integration into light-emitting and third-generation PV devices. The project proposes the fabrication of novel optically disordered media by randomly distributing scattering centres of controlled size and shape in films of transparent matrices, which enables a design of their scattering properties.

A series of objectives are pursued from a fundamental point of view. In the first place, the project proposes the fabrication of optically disordered materials with the appropriate features to originate an enhancement of the optical absorption and emission. Gaining un-

derstanding of the effect of the phenomenon of multiple scattering in these materials on the processes of light absorption and emission by dye molecules embedded in their structure or by nanomaterials is sought for. At the same time, it is of interest to find if the features of these optically disordered materials, which display a photonic glass structure, can yield a resonant enhancement of the optical absorption and emission. Eventually, a complete characterisation of their optical response is required in order to analyse how light propagates in them, as well as to assess their suitability for integration into optoelectronic devices.

From a technological perspective, a double objective is pursued. Firstly, an enhancement of the PCE of DSSCs by integrating different amounts of optical disorder into their sensitised electrode is proposed. The mechanism responsible for such improvement is based on an increase of the residence time of light inside the photoanode as a consequence of multiple scattering phenomena. A longer residence time of light would in principle boost the absorption probability and thus give rise to an increase of the number of generated photocarriers. The other side of this technological objective aims at increasing the efficiency of light-emitting devices integrating conversion layers comprising phosphors in combination with optical disorder.

1.4.2 Overview

The research activity giving rise to the results depicted in this thesis was performed in the Institute of Materials Science of Seville under the supervision of Prof. Dr. Hernán Míguez and Dr. Gabriel Lozano. Realisation of this work was possible through funding received by the Spanish Ministry of Education and Vocational Training through an FPU programme under grant FPU14/00890.

The results obtained during the development of this thesis project are depicted in the next chapters as follows:

- Chapter 2 details the different experimental procedures employed for the fabrication of the diverse components of the *Mie glasses*, such as the synthesis of the scattering centres and nano- phosphors, as well as the preparation of transparent matrices. The fabrication of DSSCs is also depicted. A second sec-

tion is devoted to the characterisation techniques used for the analysis of different aspects of light propagation and generation in the materials of study. Here, the approaches to perform a photoelectrical characterisation of DSSCs required for assessment of their operation are also described. The last section presents the theoretical methods required for the analysis of the systems at some point of the work, ranging from theoretical formalisms to numerical approaches employed for the simulation of the fabricated materials and their optical properties, as well as electrical characteristics of DSSCs.

- Chapter 3 focuses on the analysis of light transport in the different fabricated *Mie glasses* and the characterisation of the optical disorder based on ℓ_{sc} and ℓ_t. In the first place, simulations of different combinations of materials for which strong scattering is expected are presented and the suitability of such combinations for the aims of the work evaluated in terms of σ_{sc} and ℓ_{sc}, thus justifying the combinations eventually selected. From these results, the optical properties of transparent matrices of TiO_2 and SiO_2 are analysed and the effect of the presence of disorder on their optical response is studied. The possibility of describing light propagation in these materials according to Mie formalism is investigated.

- Chapter 4 is devoted to the integration of the TiO_2-based *Mie glass* as photoanode into bifacial DSSCs. A theoretical study on the performance of the cell in relation to the features of the scattering centres is presented, which enables an optical design of the device. After that, an electrical characterisation of the fabricated cells allowing an evaluation of the cell operation with respect to the properties of the scattering centres is presented. Their performance as bifacial devices is also assessed.

- Chapter 5 presents the study of emission enhancement in those *Mie glasses* displaying luminescence. In the first place, the emission improvement in the TiO_2-based *Mie glass* when sensitised with molecules of an emitting dye as a function of the parameters of the integrated inclusions is evaluated. The last section

focuses on the analysis of the PL properties of transparent luminescent films based on nanophosphors and the *Mie glass* resulting from integrating scattering centres into their structure. The emission enhancement due to a more efficient outcoupling of light from the films triggered by the presence of optical disorder is analysed.

Bibliography

[1] B. E. A. Saleh and M. C. Teich, *Fundamentals of Photonics*. Wiley-Interscience, 1991, ISBN: 0-471-83965-5.

[2] R. S. Quimby, *Photonics and Lasers: An Introduction*. Wiley-Interscience, 2006, ISBN: 0-471-71974-9.

[3] B. Jalali and S. Fathpour, "Silicon Photonics," *Journal of Lightwave Technology*, vol. 24, pp. 4600–4615, 2006.

[4] P. Campbell and M. A. Green, "Light trapping properties of pyramidally textured surfaces," *Journal of Applied Physics*, vol. 62, pp. 243–249, 1987.

[5] B. Curtin, R. Biswas, and V. Dalal, "Photonic crystal based back reflectors for light management and enhanced absorption in amorphous silicon solar cells," *Applied Physics Letters*, vol. 95, p. 231 102, 2009.

[6] J. J. Wierer Jr, A. David, and M. M. Megens, "III-nitride photonic-crystal light-emitting diodes with high extraction efficiency," *Nature Photonics*, vol. 3, pp. 163–169, 2009.

[7] M. Maldovan and E. L. Thomas, *Periodic materials and interference lithography for Photonics, Phononics and Mechanics*. Wiley, 2009, ISBN: 978-3-527-31999-2.

[8] A. Yariv and M. Nakamura, "Periodic structures for integrated optics," *IEEE Journal of Quantum Electronics*, vol. 13, pp. 233–253, 1977.

[9] E. Yablonovich, "Inhibited spontaneous emission in solid-state physics nd electronics," *Physical Review Letters*, vol. 58, pp. 2059–2062, 1987.

[10] P. Vukusic, "Natural photonics," *Physics World*, vol. 17, pp. 35–39, 2004.

[11] K. Busch, G. von Freymann, S. Linden, S. F. Mingaleev, L. Tkeshelashvili, and M. Wegener, "Periodic nanostructures for photonics," *Physics Reports*, vol. 444, pp. 101–202, 2007.

[12] Y. Kuga and A. Ishimaru, "Retroreflectance from a dense distribution of spherical particles," *Journal of the Optical Society of America A*, vol. 1, pp. 831–835, 1984.

[13] P. Wolf and G. Maret, "Weak localization and coherent backscattering of photons in disordered media," *Physical Review Letters*, vol. 55, pp. 2696–2699, 1985.

[14] S. Fraden and G. Maret, "Multiple light scattering from concentrated, interacting suspensions," *Physical Review Letters*, vol. 65, pp. 512–515, 1990.

[15] F. Scheffold and G. Maret, "Universal conductance fluctuations of light," *Physical Review Letters*, vol. 81, pp. 5800–5803, 1998.

[16] P. M. Johnson, B. P. J. Bret, J. G. Rivas, J. J. Kelly, and A. Lagendijk, "Tunable photonic strength in porous GaP," *Applied Physics Letters*, vol. 80, pp. 4498–4500, 2002.

[17] P. Sebbah, B. Hu, A. Z. Genack, R. Pnini, and B. Shapiro, "Spatial-field correlation: The bulding block of mesoscopic fluctuations," *Physical Review Letters*, vol. 88, p. 123 901, 2002.

[18] P. Barthelemy, J. Bertolotti, and D. S. Wiersma, "A Lévy flight for light," *Nature*, vol. 453, pp. 495–498, 2008.

[19] D. S. Wiersma, "Disordered photonics," *Nature Photonics*, vol. 7, pp. 188–196, 2013.

[20] P. W. Anderson, "Absence of diffusion in certain random lattices," *Physical Review*, vol. 109, pp. 1492–1505, 1958.

[21] S. John, "Electromagnetic absorption in a disordered medium near a photon mobility edge," *Physical Review Letters*, vol. 53, pp. 2169–2172, 1984.

[22] P. W. Anderson, "The question of classical localization. A theory of white paint?" *Phylosophical Magazine B*, vol. 52, pp. 505–509, 1985.

[23] M. P. van Albada and A. Lagendijk, "Observation of weak localization of light in a random medium," *Physical Review Letters*, vol. 55, pp. 2692–2695, 1985.

[24] I. Freund, "Correlation imaging through multiply scattering media," *Physics Letters A*, vol. 149, pp. 502–506, 1990.

[25] O. Katz, P. Heidmann, M. Fink, and S. Gigan, "Non-invasive single-shot imaging through scattering layers and around corners via speckle correlations," *Nature Photonics*, vol. 8, pp. 784–790, 2014.

[26] B. Judkewitz, R. Horstmeyer, I. M. Vellekoop, I. N. Papadopoulos, and C. Yang, "Translation correlations in anisotropically scattering media," *Nature Physics*, vol. 11, pp. 684–689, 2015.

[27] V. S. Letokhov, "Generation of light by a scattering medium with negative resonance absorption," *Soviet Physics - Journal of Experimental and Theoretical Physics*, vol. 26, pp. 835–840, 1968.

[28] N. M. Lawandy, R. M. Balachandran, A. S. L. Gomes, and E. Sauvain, "Laser action in strongly scattering media," *Nature*, vol. 368, pp. 436–438, 1994.

[29] H. Cao, Y. G. Zhao, S. T. Ho, E. W. Seelig, Q. H. Wang, and R. P. H. Chang, "Random laser action in semiconductor powder," *Physical Review Letters*, vol. 82, pp. 2278–2281, 1999.

[30] M. Kaveh, "Localization of photons in disordered systems," *Philosophical Magazine Part B*, vol. 56, pp. 693–703, 1987.

[31] P. D. Kaplan, A. D. Dinsmore, and A. G. Yodh, "Diffuse-transmission spectroscopy: A structural probe of opaque colloidal mixtures," *Physical Review E*, vol. 50, pp. 4827–4835, 1994.

[32] G. Mie, "Beiträge zur Optik trüber Medien, speziell kolloidaler Metallösungen," *Annalen der Physik*, vol. 330, pp. 377–445, 1908.

[33] C. F. Bohren and D. R. Huffman, *Absorption and scattering of light by small particles*. Wiley, 1983, ISBN: 0-471-05772-X.

[34] J. J. Shiang, T. J. Faircloth, and A. R. Duggal, "Experimental demonstration of increased organic light emitting device output *via* volumetric light scattering," *Journal of Applied Physics*, vol. 95, pp. 2889–2895, 2004.

[35] C. L. Mulder, K. Celebi, K. M. Milaninia, and M. A. Baldo, "Saturated and efficient blue phosphorescent organic light emitting devices with Lambertian angular emission," *Applied Physics Letters*, vol. 90, p. 211 109, 2007.

[36] C. Liu, S. Liu, K. Tien, M. Hsu, H. Chang, C. Chang, C. Yang, and C. Wu, "Microcavity top-emitting organic light-emitting devices integrated with diffusers for simultaneous enhancement of efficiencies and viewing characteristics," *Applied Physics Letters*, vol. 94, p. 103 302, 2009.

[37] H. Chang, J. Lee, S. Hofmann, Y. H. Kim, L. Müller-Meskamp, B. Lüssem, C. Wu, K. Leo, and M. C. Gather, "Nano-particle based scattering layers for optical efficiency enhancement of organic light-emitting diodes and organic solar cells," *Journal of Applied Physics*, vol. 113, p. 204 502, 2013.

[38] A. Egel and U. Lemmer, "Dipole emission in stratified media with multiple spherical scatterers: Enhanced outcoupling from OLEDs," *Journal of Quantitative Spectroscopy & Radiative Transfer*, vol. 148, pp. 165–176, 2014.

[39] B. Pyo, C. W. Joo, H. S. Kim, B. Kwon, J. Lee, J. Lee, and M. C. Suh, "A nanoporous polymer film as a diffuser as well as a light extraction component for top emitting organic light emitting diodes with a strong microcavity structure," *Nanoscale*, vol. 8, pp. 8575–8582, 2016.

[40] W. L. Vos, T. W. Tukker, A. P. Mosk, A. Lagendijk, and W. L. IJzerman, "Broadband mean free path of diffuse light in polydisperse ensembles of scatterers for white light-emitting diode lighting," *Applied Optics*, vol. 52, pp. 2602–2609, 2013.

[41] A. Tagaya, M. Nagai, Y. Koike, and K. Yokoyama, "Thin liquid-crystal display backlight system with highly scattering optical transmission polymers," *Applied Optics*, vol. 40, pp. 6274–6280, 2001.

[42] L. E. McNeil and R. H. French, "Multiple scattering from rutile TiO_2 particles," *Acta Materalia*, vol. 48, pp. 4571–4576, 2000.

[43] S. M. Luke, B. T. Hallam, and P. Vukusic, "Structural optimization for broadband scattering in several ultra-thin white beetle scales," *Applied Optics*, vol. 49, pp. 4246–4254, 2010.

[44] M. Burresi, L. Cortese, L. Pattelli, M. Kolle, P. Vukusic, D. S. Wiersma, U. Steiner, and S. Vignolini, "Bright-white beetle scales optimise multiple scattering of light," *Scientific Reports*, vol. 4, pp. 1–8, 2014.

[45] S. Caixeiro, M. Peruzzo, O. D. Onelli, S. Vignolini, and R. Sapienza, "Disordered cellulose-based nanostructures for enhanced light scattering," *ACS Applied Materials & Interfaces*, vol. 9, pp. 7885–7890, 2017.

[46] J. Syurik, G. Jacucci, O. D. Onelli, H. Hölscher, and S. Vignolini, "Bio-inspired highly scattering networks via polymer phase separation," *Advanced Functional Materials*, vol. 28, p. 170 691, 2018.

[47] B. T. Hallam, A. G. Hiorns, and P. Vukusic, "Developing optical efficiency through optimized coating structure: Biomimetic inspiration from white beetles," *Applied Optics*, vol. 48, pp. 3243–3249, 2009.

[48] M. P. van Albada, J. F. de Boer, and A. Lagendijk, "Observation of long-range intensity correlation in the transport of coherent light through a random medium," *Physical Review Letters*, vol. 64, pp. 2787–2790, 1990.

[49] M. P. van Albada, B. A. van Tiggelen, A. Lagendijk, and A. Tip, "Speed of propagation of classical waves in strongly scattering media," *Physical Review Letters*, vol. 66, pp. 3132–3135, 1991.

[50] J. F. de Boer, M. C. W. van Rossum, M. P. van Albada, T. M. Nieuwenhuizen, and A. Lagendijk, "Probability distribution of multiple scattered light measured in total transmission," *Physical Review Letters*, vol. 73, pp. 2567–2570, 1994.

[51] M. Störzer, P. Gross, C. M. Aegerter, and G. Maret, "Observation of the critical regime near Anderson localization of light," *Physical Review Letters*, vol. 96, p. 063 904, 2006.

[52] T. van der Beek, P. Barthelemy, P. M. J. D. S. Wiersma, and A. Lagendijk, "Light transport through disordered layers of dense gallium arsenide submicron particles," *Physical Review B*, vol. 85, p. 115 401, 2012.

[53] J. G. Rivas, R. Sprik, and A. Lagendijk, "Midinfrared scattering and absorption in Ge powder close to the Anderson localization transition," *Physical Review E*, vol. 62, R4540–R4543, 2000.

[54] J. G. Rivas and R. Sprik and A. Lagendijk, "Static and dynamic transport of light close to the Anderson localization transition," *Physical Review E*, vol. 63, p. 046 613, 2001.

[55] J. G. Rivas, R. Sprik, C. M. Soukoulis, K. Busch, and A. Lagendijk, "Optical transmission through strong scattering and highly polydisperse media," *Europhysics Letters*, vol. 48, pp. 22–28, 1999.

[56] D. S. Wiersma, A. Muzzi, M. Colocci, and R. Righini, "Time-resolved experiments on light diffusion in anisotropic random media," *Physical Review E*, vol. 62, pp. 6681–6687, 2000.

[57] M. B. van der Mark, M. P. van Albada, and A. Lagendijk, "Light scattering in strongly scattering media: Multiple scattering and weak localization," *Physical Review B*, vol. 37, pp. 3575–3592, 1988.

[58] M. P. van Albada, M. B. van der Mark, and A. Lagendijk, "Observation of weak localization of light in a finite slab: Anisotropy

effects and light- path classification," *Physical Review Letters*, vol. 58, pp. 361–364, 1987.

[59] P. D. García, R. Sapienza, J. Bertolotti, M. D. Martín, Á. Blanco, A. Altube, L. Viña, D. S. Wiersma, and C. López, "Resonant light transport through Mie modes in photonic glasses," *Physical Review A*, vol. 78, p. 023 823, 2008.

[60] P. D. García, R. Sapienza, and C. López, "Photonic glasses: A step beyond white paint," *Advanced Materials*, vol. 22, pp. 12–19, 2010.

[61] S. John, "Strong localization of photons in certain disordered dielectric superlattices," *Physical Review Letters*, vol. 58, pp. 2486–2489, 1987.

[62] P. E. Wolf, G. Maret, E. Akkermans, and R. Maynard, "Optical coherent backscattering by random media : An experimental study," *Journal de Physique*, vol. 49, pp. 63–75, 1988.

[63] J. G. Rivas and A. Lagendijk, "Tunable photonic strength in porous GaP," *Applied Physics Letters*, vol. 80, pp. 4498–4500, 2002.

[64] P. M. Johnson, A. Imhof, B. P. J. Bret, J. G. Rivas, and A. Lagendijk, "Time-resolved pulse propagation in a strongly scattering material," *Physical Review E*, vol. 68, p. 016 604, 2003.

[65] O. L. Muskens, J. G. Rivas, R. E. Algra, E. P. A. M. Bakkers, and A. Lagendijk, "Design of light scattering in nanowire materials for photovoltaic applications," *Nano Letters*, vol. 8, pp. 2638–2642, 2008.

[66] O. L. Muskens, S. L. Diedenhofen, B. C. Kaas, R. E. Algra, E. P. A. Bakkers, J. G. Rivas, and A. Lagendijk, "Large photonic strength of highly tunable resonant nanowire materials," *Nano Letters*, vol. 9, pp. 930–934, 2009.

[67] A. Yodh and B. Chance, "Spectroscopy and imaging with diffuse light," *Physics Today*, vol. 48, pp. 34–40, 1995.

[68] I. M. Vellekoop, A. Lagendijk, and A. P. Mosk, "Exploiting disorder for perfect focusing," *Nature Photonics*, vol. 4, pp. 320–322, 2010.

[69] E. G. van Putten, A. Lagendijk, and A. P. Mosk, "Optimal concentration of light in turbid materials," *Journal of the Optical Society of America B*, vol. 28, pp. 1200–1203, 2011.

[70] D. J. Pine, D. A. Weitz, P. M. Chaikin, and E. Herbolzheimer, "Diffusing-wave spectroscopy," *Physical Review Letters*, vol. 60, pp. 1134–1137, 1988.

[71] R. V. Ambartsumyan, N. G. Basov, P. G. Kryukov, and V. S. Letokhov, "A laser with nonresonant feedback," *Soviet Physics - Journal of Experimental and Theoretical Physics*, vol. 24, pp. 481–485, 1967.

[72] V. M. Markushev, V. F. Zolin, and C. M. Briskina, "Luminescence and stimulated emission of neodymium in sodium lanthanum molybdate powders," *Soviet Journal of Quantum Electronics*, vol. 16, pp. 281–283, 1986.

[73] C. Gouedard, D. Husson, C. Sauteret, F. Auzel, and A. Migus, "Generation of spatially incoherent short pulses in laser-pumped neodymium stoichiometric crystals and powders," *Journal of the Optical Society of America B*, vol. 10, pp. 2358–2363, 1993.

[74] W. L. Sha, C. H. Liu, and R. R. Alfano, "Spectral and temporal measurements of laser action of Rhodamine 640 dye in strongly scattering media," *Optics Letters*, vol. 19, pp. 1922–1924, 1994.

[75] M. Leonetti, C. Conti, and C. López, "The mode-locking transition of random lasers," *Nature Photonics*, vol. 5, pp. 615–617, 2011.

[76] M. Leonetti and C. Conti and C. López, "Random laser tailored by directional stimulated emission," *Physical Review A*, vol. 85, p. 043 841, 2012.

[77] M. Leonetti, C. Conti, and C. López, "Tunable degree of localization in random lasers with controlled interaction," *Applied Physics Letters*, vol. 101, p. 051 104, 2012.

[78] S. Gottardo, R. Sapienza, P. D. García, A. Blanco, D. S. Wiersma, and C. López, "Resonance-driven random lasing," *Nature Photonics*, vol. 2, pp. 429–432, 2008.

[79] P. D. García, M. Ibisate, R. Sapienza, D. S. Wiersma, and C. López, "Mie resonances to tailor random lasers," *Physical Review A*, vol. 80, p. 0 138 033, 2009.

[80] A. P. Mosk, A. Lagendijk, G. Lerosey, and M. Fink, "Controlling waves in space and time for imaging and focusing in complex media," *Nature Photonics*, vol. 6, pp. 283–292, 2012.

[81] J. Bertolotti, "Peeking through the curtain," *Nature Photonics*, vol. 8, pp. 751–752, 2014.

[82] J. Bertolotti, E. G. van Putten, C. Blum, A. Lagendijk, W. L. Vos, and A. P. Mosk, "Non-invasive imaging through opaque scattering layers," *Nature*, vol. 491, pp. 232–234, 2012.

[83] P. Campbell, S. R. Wenham, and M. A. Green, "Light trapping and reflection control in solar cells using tilted crystallographic surface textures," *Solar Energy Materials and Solar Cells*, vol. 31, pp. 133–153, 1993.

[84] P. Campbell, "Light trapping in textured solar cells," *Solar Energy Materials*, vol. 21, pp. 165–172, 1990.

[85] J. Krč, F. Smole, and M. Topi*c*, "Potential of light trapping in microcrystalline silicon solar cells with textured substrates," *Progress in Photovoltaics: Research and Applications*, vol. 11, pp. 429–436, 2003.

[86] K. J. Weber and A. W. Blakers, "A novel silicon texturization methods based on etching through a silicon nitride mask," *Progress in Photovoltaics: Research and Applications*, vol. 13, pp. 691–695, 2005.

[87] S. Faÿ, J. Steinhauser, N. Oliveira, E. Vallat-Sauvain, and C. Ballif, "Opto-electronic properties of rough LP-CVD ZnO:B for use as TCO in thin-film silicon solar cells," *Thin Solid Films*, vol. 515, pp. 8558–8561, 2007.

[88] O. Isabella, F. Moll, J. Kr*c*, and M. Zeman, "Modulated surface textures using zinc-oxide films for solar cells applications," *physica status solidi a*, vol. 207, pp. 642–646, 2010.

[89] V. E. Ferry, M. A. Verschuuren, M. C. van Lare, R. E. I. Schropp, H. A. Atwater, and A. Polman, "Optimized spatial correlations for broadband light trapping nanopatterns in high efficiency ultrathin film a-Si:H solar cells," *Nano Letters*, vol. 11, pp. 4239–4245, 2011.

[90] K. Bittkau, A. Hoffmann, U. W. Paetzold, and R. Carius, "Broadening of light coupling to waveguide modes in solar cells by disordered grating textures," *Applied Sciences*, vol. 207, pp. 642–646, 2017.

[91] F. J. Haug, T. Söderström, O. Cubero, V. Terrazzoni-Daudrix, and C. Ballif, "Influence of the ZnO buffer on the guided mode

structure in Si/ZnO/Ag multilayers," *Journal of Applied Physics*, vol. 106, p. 044 502, 2009.

[92] S. Mokkapati and K. R. Catchpole, "Nanophotonic light trapping in solar cells," *Journal of Applied Physics*, vol. 112, p. 101 101, 2012.

[93] O. Isabella, S. Solntsev, D. Caratelli, and M. Zeman, "3-D optical modeling of thin-film silicon solar cells on diffraction gratings," *Progress in Photovoltaics: Research and Applications*, vol. 21, pp. 94–108, 2012.

[94] V. E. Ferry, L. A. Sweatlock, D. Pacifici, and H. A. Atwater, "Plasmonic nanostructure design for efficient light coupling into solar cells," *Nano Letters*, vol. 8, pp. 4391–4397, 2008.

[95] U. W. Paetzold, E. Moulin, D. Michaelis, W. Böttler, C. Wächter, V. Hagemann, M. Meier, R. Carius, and U. Rau, "Plasmonic reflection grating back contacts for microcrystalline silicon solar cells," *Applied Physics Letters*, vol. 93, p. 181 105, 2011.

[96] E. R. Martins, J. Li, Y. Liu, J. Zhou, and T. F. Krauss, "Engineering gratings for light trapping in photovoltaics: The supercell concept," *Physical Review B*, vol. 86, p. 041 404, 2012.

[97] K. Okamoto, I. Niki, A. Shvartser, Y. Narukawa, T. Mukai, and A. Scherer, "Surface-plasmon-enhanced light emitters based on InGaN quantum wells," *Nature Materials*, vol. 3, pp. 601–605, 2004.

[98] B. Riedel, Y. Shen, J. Hauss, M. Aichholz, X. Tang, U. Lemmer, and M. Gerken, "Tailored highly transparent composite hole-injection layer consisting of PEDOT:PSS and SiO_2 nanoparticles for efficient polymer light-emitting diodes," *Advanced Materials*, vol. 23, pp. 740–745, 2011.

[99] C. Fröhlich and J. Lean, "Solar radiative output and its variability: Evidence and mechanisms," *The Astronomy and Astrophysics Review*, vol. 12, pp. 273–320, 2004.

[100] National Renewable Energy Laboratory, *Best Research-Cell Efficiency Chart*. [Online]. Available: `https://www.nrel.gov/pv/cell-efficiency.html`.

[101] J. Ramanujam and U. P. Singh, "Copper indium gallium selenide based solar cells – a review," *Energy & Environmental Science*, vol. 10, pp. 1306–1319, 2017.

[102] A. Fakharuddin, R. Jose, T. M. Brown, F. Fabregat-Santiago, and J. Bisquert, "A perspective on the production of dye-sensitized solar modules," *Energy & Environmental Science*, vol. 7, pp. 3952–3981, 2014.

[103] A. Kojima, K. Teshima, Y. Shirai, and T. Miyasaka, "Organometal halide perovskites as visible-light sensitizers for photovoltaic cells," *Journal of the American Chemical Society*, vol. 131, pp. 6050–6051, 2009.

[104] H. Kim, C. Lee, J. Im, K. Lee, T. Moehl, A. Marchioro, S. Moon, R. Humphry-Baker, J. Yum, J. E. Moser, M. Grätzel, and N. Park, "Lead iodide perovskite sensitized all-solid-state submicron thin film mesoscopic solar cell with efficiency exceeding 9%," *Scientific Reports*, vol. 2, p. 591, 2012.

[105] R. Tagliaferro, D. Colonna, T. M. Brown, A. Reale, and A. di Carlo, "Interplay between transparency and efficiency in dye sensitized solar cells," *Optics Express*, vol. 21, pp. 3235–3242, 2013.

[106] T. M. Brown, F. d. Rossi, F. d. Giacomo, G. Mincuzzi, V. Zardetto, A. Reale, and A. d. Carlo, "Progress in flexible dye solar cell materials, processes and devices," *Journal of Materials Chemistry A*, vol. 2, pp. 10 788–10 817, 2014.

[107] M. Freitag, J. Teuscher, Y. Saygili, X. Zhang, F. Giordano, P. Liska, J. Hua, S. M. Zakeeruddin, J. Moser, M. Grätzel, and A. Hagfeldt, "Dye-sensitized solar cells for efficient power generation under ambient lighting," *Nature Photonics*, vol. 11, pp. 372–379, 2017.

[108] H. Otaka, M. Kira, K. Yano, S. Ito, H. Mitekura, T. Kawata, and F. Matsui, "Multi-colored dye-sensitized solar cells," *Journal of Photochemistry and Photobiology and A: Chemistry*, vol. 164, pp. 67–73, 2004.

[109] R. Kern, N. v. Burg, G. Chmiel, J. Ferber, G. Hasenhindl, A. Hinsch, R. Kinderman, J. Kroon, A. Meyer, T. Meyer, R. Niepmann, J. van Roosmalen, C. Schill, P. Sommeling, M. Späth, and I. Uhlendorf, "Long term stability of dye-sensitized solar cells for large area power applications," *Opto-electronics Review*, vol.
8, pp. 284–288, 2000.

[110] A. Hinsch, J. M. Kroon, R. Kern, I. Uhlendorf, J. Holzbock, A. Meyer, and J. Ferber, "Long-term stability of dye-sensitised solar cells," *Progress in Photovoltaics: Research and Applications*, vol. 9, pp. 425–438, 2001.

[111] G. Xue, Y. Guo, T. Yu, J. Guan, X. Yu, J. Zhang, J. Liu, and Z. Zou, "Degradation mechanisms investigation for long-term thermal stability of dye-sensitized solar cells," *International Journal of Electrochemical Science*, vol. 7, pp. 1496–1511, 2012.

[112] S. Ito, S. M. Zakeeruddin, P. Comte, P. Liska, D. Kuang, and M. Grätzel, "Bifacial dye-sensitized solar cells based on an ionic liquid electrolyte," *Nature Photonics*, vol. 2, pp. 693–698, 2008.

[113] A. Kay and M. Grätzel, "Low cost photovoltaic modules based on dye sensitized nanocrystalline titanium dioxide and carbon powder," *Solar Energy Materials and Solar Cells*, vol. 44, pp. 99–117, 1996.

[114] B. O'Regan and M. Grätzel, "A low-cost, high-efficiency solar cell based on dye-sensitized colloidal TiO_2 films," *Nature*, vol. 353, pp. 737–740, 1991.

[115] M. Grätzel, "Photoelectrochemical cells," *Nature*, vol. 414, 338 –344, 2001.

[116] A. Yella, H. Lee, H. N. Tsao, C. Yi, A. K. Chandiran, Md. K. Nazeeruddin, E. W. Diau, C. Yeh, S. M.Zakeeruddin, and M. Grätzel, "Porphyrin-sensitized solar cells with cobalt (II/III)-based redox electrolyte exceed 12 percent efficiency," *Science*, vol. 334, pp. 629–634, 2011.

[117] A. Hagfeldt, G. Boschloo, L. Sun, L. Kloo, and H. Pettersson, "Dye-sensitized solar cells," *Chemical Reviews*, vol. 110, pp. 6595–6663, 2010.

[118] H. J. Snaith, "Estimating the maximum attainable efficiency in dye-sensitized solar cells," *Adv. Funct. Mater.*, vol. 20, pp. 13–19, 2010.

[119] A. Usami, "Theoretical study of application of multiple scattering of light to a dye-sensitized nanocrystalline photoelectrochemical cell," *Chemical Physics Letters*, vol. 277, pp. 105–108, 1997.

[120] Z. Wang, H. Kawauchi, T. Kashima, and H. Arakawa, "Significant influence of TiO_2 photoelectrode morphology on the en-

ergy conversion efficiency of N719 dye-sensitized solar cell," *Coordination Chemistry Reviews*, vol. 248, pp. 1381–1389, 2004.

[121] S. Hore, C. Vetter, R. Kern, H. Smit, and A. Hinsch, "Influence of scattering layers on efficiency of dye-sensitized solar cells," *Solar Energy Materials & Solar Cells*, vol. 90, pp. 1176–1188, 2006.

[122] H. Koo, J. Park, B. Yoo, K. Yoo, K. Kim, and N. Park, "Size-dependent scattering efficiency in dye-sensitized solar cell," *Inorganica Chimica Acta*, vol. 361, pp. 677–683, 2008.

[123] M. Son, H. Seo, S. Kim, N. Hong, B. Kim, S. Park, K. Prabakar, and H. Kim, "Analysis on the light-scattering effect in dye-sensi-tized solar cell according to the TiO_2 structural differences," *International Journal of Photoenergy*, vol. 2012, 2012.

[124] J. Xi, Q. Zhang, K. Park, Y. Sun, and G. Cao, "Enhanced power conversion efficiency in dye-sensitized solar cells with TiO_2 aggregates/nanocrystallites mixed photoelectrodes," *Electrochimica Acta*, vol. 56, pp. 1960–1966, 2011.

[125] S. Hore, P. Nitz, C. Vetter, C. Prahl, M. Niggemann, and R. Kern, "Scattering spherical voids in nanocrystalline TiO_2 – enhancement of efficiency in dye-sensitized solar cells," *Chemical Communications*, pp. 2011–2013, 2005.

[126] Z. Tian, H. Tian, X. Wang, S. Yuan, J. Zhang, X. Zhang, T. Yu, and Z. Zou, "Multilayer structure with gradual increasing porosity for dye-sensitized solar cells," *Applied Physics Letters*, vol. 94, p. 031 905, 2009.

[127] U.S. Department of Energy, *2015 U.S. Lighting Market Characterization*, 2017. [Online]. Available: `https://www.energy.gov/sites/prod/files/2017/12/f46/lmc2015_nov17.pdf`.

[128] M. Born and T. Jüstel, "Elektrische Lichtquellen," *Chem. Unserer Zeit*, vol. 40, pp. 294–305, 2006.

[129] H. Amano, N. Sawaki, I. Akasaki, and Y. Toyoda, "Metalorganic vapor phase epitaxial growth of a high quality GaN film using an AlN buffer layer," *Applied Physics Letters*, vol. 48, pp. 353–355, 1986.

[130] H. Amano, M. Kito, K. Hiramatsu, and I. Akasaki, "P-type conduction in Mg-doped GaN treated with low-energy electron beam irradiation (LEEBI)," *Japanese Journal of Applied Physics*, vol. 28, pp. L2112–L2114, 1989.

[131] S. Nakamura, T. Mukai, and M. Senoh, "Candela-class high-brightness InGaN/AlGaN double-heterostructure blue-light-emitting diodes," *Applied Physics Letters*, vol. 64, pp. 1687–1689, 1994.

[132] S. Nakamura, M. Senoh, N. Iwasa, and S. Nagahama, "High-brightness InGaN blue, green and yellow light-emitting diodes with quantum well structures," *Japanese Journal of Applied Physics*, vol. 34, pp. L797–L799, 1995.

[133] T. Y. Shimizu, A. K. Sakano, T. Y. Noguchi, and A. T. Moriguchi, "Light emitting device with blue light led and phosphor components," US Patent US7531960B2, 2009.

[134] C. Yang, C. Lin, Y. Chen, Y. Wu, S. Chuang, R. Liu, and S. Hu, "Highly stable three-band white light from an InGaN-based blue light-emitting diode chip precoated with (oxy)nitride green/red phosphors," *Applied Physics Letters*, vol. 90, p. 123 503, 2007.

[135] K. Uheda, H. Takizawa, T. Endo, H. Yamane, M. Shimada, C. M. Wang, and M. Mitomo, "Synthesis and luminescent property of Eu^{3+}-doped $LaSi_3N_5$ phosphor," *Journal of Luminescence*, vol. 87, pp. 967–969, 2000.

[136] H. Kamioka, T. Yamaguchi, M. Hirano, T. Kamiya, and H. Hosono, "Structural and photo-induced properties of Eu^{2+}-doped
$Ca_2ZnSi_2O_7$: A red phosphor for white light generation by blue ray excitation," *Journal of Luminescence*, vol. 122, pp. 339–341, 2007.

[137] H. A. Höppe, M. Daub, and M. C. Bröhmer, "Coactivation of α-$Sr(PO_3)_4$ and $SrM(P_2O_7)$ (M = Zn, Sr) with Eu^{2+} and Mn^{2+}," *Chemistry of Materials*, vol. 19, pp. 6358–6362, 2007.

[138] A. B. Greytak, P. M. Allen, W. Liu, J. Zhao, E. R. Young, Z. Popovi, B. J. Walker, D. G. Nocera, and M. G. Bawendi, "Alternating layer addition approach to CdSe/CdS core/shell quantum dotswith near-unity quantum yield and high on-time fractions," *Chemical Science*, vol. 3, pp. 2028–2034, 2012.

[139] B. O. Dabbousi, J. Rodriguez-Viejo, F. V. Mikulec, J. R. Heine, M. Mattousi, R. Ober, K. F. Jensen, and M. G. Bawendi, "(CdSe) ZnS core-shell quantum dots: Synthesis and characterization

of a size series of highly luminescent nanocrystallites," *Journal of Physical Chemistry B*, vol. 101, pp. 9463–9475, 1997.

[140] H. S. Jang, H. Yang, S. W. Kim, J. Y. Han, S. Lee, and D. Y. Jeon, "White light-emitting diodes with excellent color rendering based on organically capped CdSe quantum dots and Sr_3SiO_5:Ce^{3+},Li^+ phosphors," *Advanced Materials*, vol. 20, pp. 2696–2702, 2008.

[141] P. Schlotter, R. Schmidt, and J. Schneider, "Luminescence conversion of blue light emitting diodes," *Applied Physics A*, vol. 64, pp. 417–418, 1997.

[142] G. Lozano, D. J. Louwers, S. R. K. Rodríguez, S. Murai, O. T. A. Jansen, M. A. Verschuuren, and J. G. Rivas, "Plasmonics for solid-state lighting: Enhanced excitation and directional emission of highly efficient light sources," *Light: Science & Applications*, vol. 2, e66, 2013.

[143] X. Xu, R. Ray, Y. Gu, H. J. Ploehn, L. Gearheart, K. Raker, and W. A. Scrivens, "Electrophoretic analysis and purification of fluorescent single-walled carbon nanotubes fragments," *Journal of the American Chemical Society*, vol. 126, pp. 12 736–12 737, 2004.

[144] S. N. Baker and G. A. Baker, "Luminescent carbon nanodots: Emergent nanolights," *Angewandte Chemie International Edition*, vol. 49, pp. 6726–6744, 2010.

[145] M. D. Weber, L. Niklaus, M. Pröschel, P. B. Coto, U. Sonnewald, and R. D. Costa, "Bioinspired hybrid white light-emitting diodes," *Advanced Materials*, vol. 27, pp. 5493–5498, 2015.

[146] L. Niklaus, S. Tansaz, H. Dakhil, K. T. Weber, M. Pröschel, M. Lang, M. Kostrzewa, P. B. Coto, R. Detsch, U. Sonnewald, A. Wierschem, A. R. Boccaccini, and R. D. Costa, "Micropatterned down-converting coating for white bio-hybrid light-emitting diodes," *Advanced Functional Materials*, vol. 27, p. 1601792, 2017.

[147] G. Glickman, B. Byrne, C. Pineda, W. W. Hauck, and G. C. Brain- ard, "Light therapy for seasonal affective disorder with blue narrow-band light-emitting diodes (LEDs)," *Biological Psychiatry*, vol. 59, pp. 502–507, 2006.

[148] M. Münch, S. Kobialka, R. Steiner, P. Oelhafen, A. Wirz-Justice, and C. Cajochen, "Wavelength-dependent effects of evening light exposure on sleep architecture and sleep EEG power density in men," *American Journal of Physiology-Regulatory, Integrative and Comparative Physiology*, vol. 290, R1421–R1428, 2006.

[149] T. Narimatsu, Y. Ozawa, S. Miyake, S. Kubota, K. Yuki, N. Nagai, and K. Tsubota, "Biological effects of blocking blue and other visible light on the mouse retina," *Clinical and Experimental Ophthalmology*, vol. 42, pp. 555–563, 2014.

[150] D. M. Dominoni, "The effects of light pollution on biological rhythms of birds: an integrated, mechanistic perspective," *Journal of Ornithology*, vol. 156, S409–S418, 2015.

[151] T. Raap, R. Pinxten, and M. Eens, "Light pollution disrupts sleep in free-living animals," *Scientific Reports*, vol. 5, 2015.

[152] A. Rodríguez, N. D. Holmes, P. G. Ryan, K. Wilson, L. Faulquier, Y. Murillo, A. F. Raine, J. F. Penniman, V. Neves, B. Rodríguez, J. J. Negro, A. Chiaradia, P. Dann, T. Anderson, B. Metzger, M. Shirai, L. Deppe, J. Wheeler, P. Hodum, C. Gouveia, V. Carmo, G. P. Carreira, L. Delgado-Alburqueque, C. Guerra-Correa, F. Couzi, M. Travers, and M. Corre, "Seabird mortality induced by land-based artificial lights," *Conservation Biology*, vol. 31, pp. 986–1001, 2017.

[153] D. Sanders, R. Kehoe, K. Tiley, J. Bennie, D. Cruse, T. W. Davies, F. J. F. Veen, and K. J. Gaston, "Artificial nighttime light changes aphid-parasitoid population dynamics," *Scientific Reports*, vol. 5, 2015.

[154] R. H. ffrench-Constant, R. Somers-Yeates, J. Bennie, T. Economou, D. Hodgson, A. Spalding, and P. K. McGregor, "Light pollution is associated with earlier tree budburst across the United Kingdom," *Proceedings of the Royal Society B*, vol. 283, 2016.

[155] T. Fujii, Y. Gao, R. Sharma, E. L. Hu, S. P. DenBaars, and S. Nakamura, "Increase in the extraction efficiency of GaN-based light-emitting diodes via surface roughening," *Applied Physics Letters*, vol. 84, pp. 855–857, 2004.

[156] H. Kim, Y. Cho, H. Lee, S. I. Kim, S. R. Ryu, D. Y. Kim, T. W. Kang, and K. S. Chung, "High-brightness light emitting diodes using dislocation-free Indium Gallium Nitride/Gallium Nitride

multiquantum-well nanorod arrays," *Nano Letters*, vol. 4, 1059 –1062, 2004.

2 Methods

This chapter focuses on depicting the diverse tools employed for the development of the work presented in this thesis. The exhaustive studies performed leading to the results herein described cover a wide range of aspects, for which different experimental and calculation techniques were required. The first section is devoted to methods related to the fabrication of the materials, covering aspects ranging from the synthesis of nanoparticles to the fabrication of full optoelectronic devices. After that, the different characterisation techniques that allowed determination of the optical response of the fabricated materials are described. Eventually, the last section depicts the analytical and numerical tools employed for the modelling and design of the studied systems, providing the theoretical insight required for a thorough understanding of their properties.

2.1 Processing methods

The highly experimental character of this thesis involves the use of a vast number of synthesis and fabrication methods. This section addresses experimental methods oriented toward the fabrication of random media for integration into either DSSCs or light-emission applications, giving details on the techniques and the implicated processes.

2.1.1 Nanoparticle synthesis

This section provides references to the synthetic routes of nanoparticles employed in this research. Specifically, a procedure for the synthesis of spherical crystalline TiO_2 nanoparticles and the synthesis method of nano-sized phosphors are mentioned.

2.1.1.1 Crystalline TiO_2 spheres

Spherical anatase particles in the sub-micrometre scale were used as scattering elements in order to endow transparent matrices with optical disorder. TiO_2 spheres were synthesised according to a modified

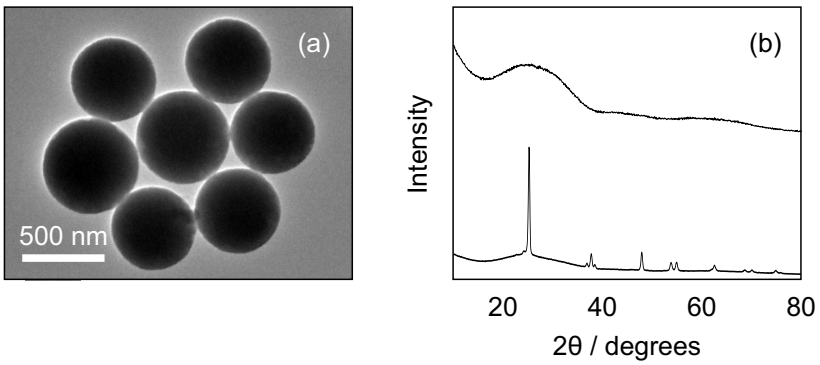

Figure 2.1: (a) TEM image of the spherical structures resulting from the synthesis process before sintering. (b) X-ray diffraction diagram of the synthesised spheres before (upper half) and after (lower half) sintering.

version of a procedure reported elsewhere[1]. This procedure consists in a sol-gel method combining a step of controlled hydrolysis and nucleation with a subsequent step of hydrothermal reaction. The spherical structures employed in this work correspond to those resulting from the former process, therefore omitting the step of hydrothermal reaction. The Transmission Electron Microscopy (TEM) image in Fig. 2.1(a) illustrates the spherical shape of the resulting particles after the synthesis process, which were in the amorphous phase, as evidenced by the upper X-ray diffraction (XRD) diagram in Fig. 2.1(b). A crystalline phase was displayed after the sintering process performed to achieve mechanical stability of the materials, as the lower XRD diagram in Fig. 2.1(b) demonstrates. The method allowed control over the size of the spherical structures through the hydrolisis conditions, more specifically, through the volume of H_2O added to the initial solution.

2.1.1.2 $GdVO_4$-based nanophosphors

Due to the interest in the preparation of mesoporous luminescent matrices, near-UV excitable, Europium (Eu)- and Bismuth (Bi)-doped phosphors of nanometric size based on rare-earth (RE) vanadates, namely, $GdVO_4$, were synthesised according a procedure already reported[2]. The synthesis is based on a precipitation process and it pro-

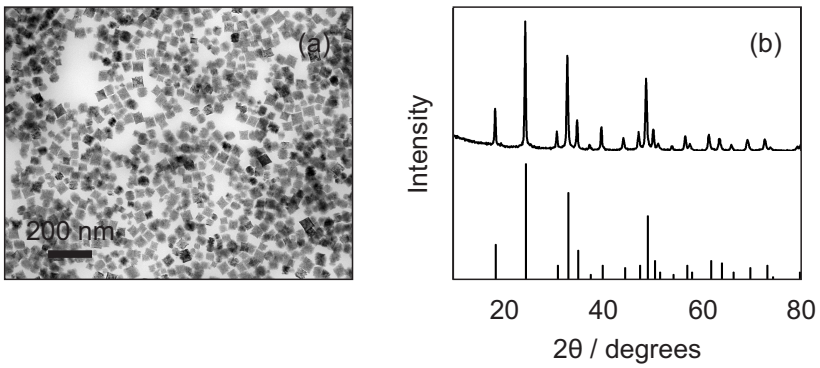

Figure 2.2: (a) TEM image of the synthesised $GdVO_4$:Bi^{3+},Eu^{3+} nanophosphors. (b) XRD diagram yielded by dry $GdVO_4$:Bi^{3+},Eu^{3+} powder (upper half), along with the standard PDF 86-0996, ICDD 2014 reference (lower half) included for comparison.

duced phosphors of an average size of (36 ± 7) nm, as visible in the TEM image shown in Fig. 2.2(a). Such small size prevented visible light from being significantly scattered, thus yielding high transparency when used for film preparation. Co-doping with Bi^{3+} endowed the phosphor crystals with a cubic shape, as concluded after comparing with phosphors devoid of Bi^{3+} centres. The particles resulting from the synthesis presented an amorphous phase, which converted into crystalline after a thermal treatment, as confirmed by the XRD pattern shown in Fig. 2.2(b). Comparison with the standard PDF 86-0996, ICDD 2014 reference demonstrated crystallisation into the tetragonal $GdVO_4$ structure. A crystallite size of 39.5 nm was estimated from the Scherrer formula, in good agreement with that determined from the TEM image in Fig. 2.2(a). Alternatively, the Eu^{3+} cations could be replaced by Dy^{3+} cations so a to achieve a different emission spectrum by substituting the Eu-salt by the corresponding Dy-salt during the synthesis.

2.1.2 Paste preparation

Most of the materials designed and analysed in this thesis were fabricated from precursors in the form of a viscous paste. These pastes generally consisted of a mixture of the nanoparticles and organic binders

in a viscous solvent. Using pastes as precursors is revealed advantageous when aiming at large film thicknesses not feasible through other solution-processing methods. Besides, the deposition methods compatible with paste precursors can offer acceptable control over the thickness of the film.

2.1.2.1 TiO_2 nanoparticle paste

Mesoporous anatase matrices were prepared from a commercial paste (18-NRT, GreatCell Solar©) containing irregular TiO_2 particles with an average size of 20 nm. Films prepared employing this precursor displayed high optical transparency in the visible region.

2.1.2.2 $GdVO_4$-based nanophosphor paste

Transparent luminescent films comprising $GdVO_4$-based nanophosphors doped with Bi^{3+} and a RE cation were fabricated from a viscous paste. For the paste preparation, the total weight of the nanophosphors, m_{nph}, in a methanol suspension resulting from the synthesis was determined in the first place. Further methanol was added to produce a 120-ml diluted suspension. Subsequent sonication was performed by means of tip sonication so as to minimise aggregation of the phosphors for the sake of optical quality of the resulting films. As organic binder, $0.3 \cdot m_{nph}$ grams of ethyl cellulose (Sigma Aldrich, powder) were added to the suspension, followed by tip sonication. $4 \cdot m_{nph}$ grams of α-terpineol (SAFC, ≥96%) were added as a solvent

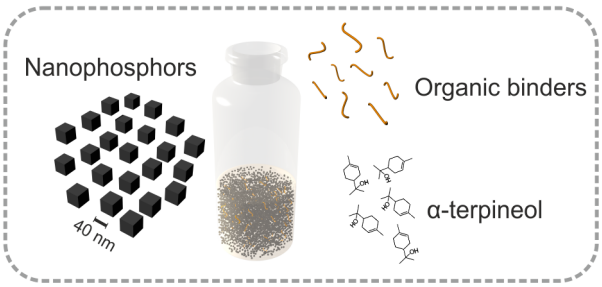

Figure 2.3: Description of the preparation process of a viscous paste of $GdVO_4$:Bi^{3+},Eu^{3+} nanophosphors

and sonicated. This preparation process is illustrated in Fig. 2.3. Eventually, the methanol in the dispersion was evaporated at reduced pressure, yielding a viscous paste.

2.1.2.3 Integration of optical disorder

The process of integration of optical disorder in the transparent matrices entails the random inclusion of scattering spheres previously synthesised. This was achieved by dispersing a specific amount of scattering centres in the precursor pastes for a desired volume filling fraction of the inclusions in the eventual film, see Fig. 2.4. For experimental realisation, it was necessary to convert the inclusion filling fraction value into weight ratio:

$$wr = \frac{\rho_{matrix}}{\rho_{inclusions}} \frac{f}{k(1-p)(1-f)}, \tag{2.1}$$

where wr refers to the (scattering centre)/(embedding material) weight ratio, ρ_{matrix} and $\rho_{\text{inclusions}}$ to the density of the material constituting the matrix and the scattering centres, respectively, f refers to the volume filling fraction, k is an adimensional term accounting for the presence of an air shell surrounding the inclusions due to contraction effects during thermal treatment, being $k = 1$ for the absence of shell, and p corresponds to the porosity of the mesoporous matrix, typically $p \approx 0.5$ in this work. Experimental observations from SEM pictures allowed an estimation of $k \approx 5$ for those materials based on a high refractive index matrix fabricated during this thesis, for which

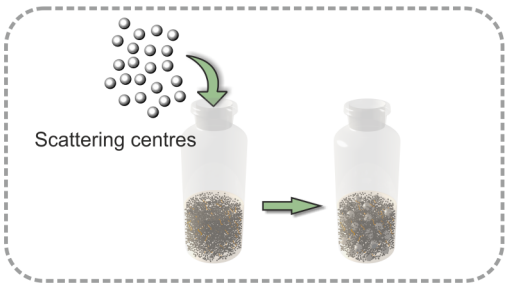

Figure 2.4: Inclusion of scattering centres in a nanoparticle-based paste

an air shell surrounding the scattering inclusions was generated. The desired amount of material in the eventual paste, m_{total}, defines the required quantities of matrix paste, m_{paste}, and scattering centre dispersion, $m_{inclusions}$, given by:

$$m_{paste} = \frac{(1 - wr) \cdot m_{total}}{c_{paste}}; m_{inclusions} = \frac{wr \cdot m_{total}}{c_{inclusions}}, \tag{2.2}$$

being c_{paste} and $c_{inclusions}$ the weight concentration of material in the paste and the weight concentration of inlusions in the scattering centre dispersion, respectively. This amount of m_{paste} was roughly dissolved in 5 ml of absolute ethanol. After a brief sonication process, the dispersion was vigorously mixed using a vortex mixer, followed by a 10-minute process of magnetic stirring. An amount $m_{inclusions}$ of the scattering centre dispersion was added to the mixture, as well as a certain amount of α-terpineol, performing 5-minute magnetic-stirring processes in between additions. The amount of α-terpineol was key for the viscosity of the paste and hence, the minimum attainable film thickness. Particularly, 0.8257 g were added when preparing photoanodes for DSSCs and 1.6514 g for the paste devoted to the fabrication of *Mie glasses* for colour conversion and the nanophosphor-based paste. Eventually, the ethanol in the mixture was removed through evaporation at reduced pressure.

2.1.3 Film preparation

This part of the chapter includes detailed information on the different procedures and techniques employed for the preparation of films of the studied materials. The procedures are classified according to the high or low refractive index of the porous matrix of the material.

2.1.3.1 High refractive index materials

This section includes the description of the fabrication of films of matrices based on high refractive index materials, namely, TiO_2 and $GdVO_4$, for either colour conversion applications or integration into DSSCs and the fabrication of flexible emitting films based on nanosized phosphors, respectively.

TiO_2 matrix: *Mie glasses* consisting of anatase spheres embedded in a mesoporous TiO_2 matrix were fabricated in order to study fundamental aspects of the propagation of the light in a disordered medium, see Ch. 3, and later on for the integration as photoanodes into DSSCs, Ch. 4, and to demonstrate their potential for the improvement of light emission when infiltrated with luminescent molecules, as depicted in Ch. 5. The samples were prepared from either the commercial 18-NRT GreatCell Solar© paste or a mixture of this with scattering spheres. 1-mm thick glass slides were cleaned through a 15-minute sonication process in absolute ethanol and used as substrates. Either 1-cm^2 (for the disorder characterisation and application as efficient colour converter) or 0.25-cm^2 (for integration into DSSCs) area layers were deposited *via* screen printing. Screen printing is a versatile and inexpensive deposition technique allowing the preparation of thick films, while offering control over their thickness. A mesh attached to a frame is used to transfer the paste onto a substrate placed underneath, as illustrated in Fig. 2.5. The mesh is delimited by a blocking stencil, impermeable to the paste, so that the transferred pattern is defined by the unblocked mesh area, step (1). After spreading some paste near the pattern, step (2), the mesh is infiltrated with it by sweeping with a squeegee while gently applying pressure, step (3) and (4). A sec-

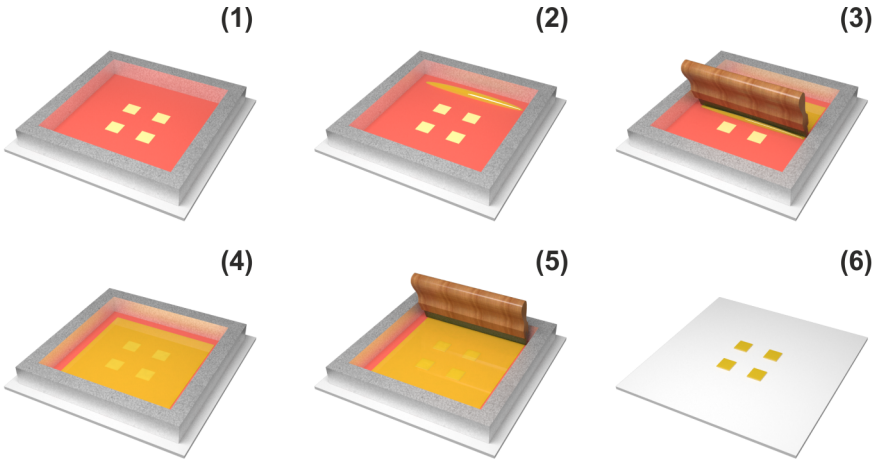

Figure 2.5: Procedure of screen printing for the deposition of layers from a viscous paste.

ond sweeping, applied with enough pressure to bring the screen and the substrate into contact, transfers the paste onto the substrate, step (5), thus resulting in a fresh layer reproducing the pattern imposed by the frame on the substrate, step (6). The properties of the resulting layer depend not only on factors related to the composition of the paste, but also to the deposition technique itself, such as the mesh density, which highly affects the eventual thickness of the film and is thus considered as a thickness-control parameter, the applied pressure or the speed of the sweeping. In particular, the thickness of the films was controlled through the mesh density and the number of successive depositions, for which processes of solvent evaporation at 150^{o}C during 5 minutes in between depositions were required for film stabilisation. The area of the eventual film was defined by the screen features. In the case of TiO_2 matrices intended for integration as photoanode into DSSCs, due to the need for charge collection in DSSCs, the films were deposited on conductive substrates. In particular, FTO glass substrates (XOP Glass, FTO TEC-11X) were employed, which combine the possibility of charge transport with high optical transparency. The substrates were cleaned following a 15-minute sonication process in a 2% vol. Hellmanex solution in deionised (DI) water, followed by DI water rinsing and sonication in absolute ethanol for 15 minutes. 0.25-cm^2 area layers were prepared *via* screen printing. Two deposition processes were performed, including the corresponding solvent evaporation process in between. A sintering process was required after the deposition of the films in all the cases for mechanical stabilisation by removing the organic components of the paste. Specifically, this thermal treatment consists of a heating ramp from room temperature to 180^{o}C for 10 minutes, where it plateus for 10 minutes, a subsequent heating process from 180^{o}C to 450^{o}C during 30 minutes followed by a 15-minute plateau, and a last heating ramp from 450^{o}C to 500^{o}C, where it stays for 15 minutes. The procedure offers an estimated precision around $\pm$ 500 nm in the thickness of the films. Figures 2.6 and 2.7 demonstrate the reliability of the deposition technique, which ensures thickness-controlled and structurally homogeneous films. Specifically, the profile of a *ca.* 15-μm thick mesoporous anatase film prepared with the 18-NRT GreatCell Solar© paste through a few deposition steps and acquired with a profilometer is presented in Fig. 2.6. Figure 2.7(a) displays an SEM image of the cross

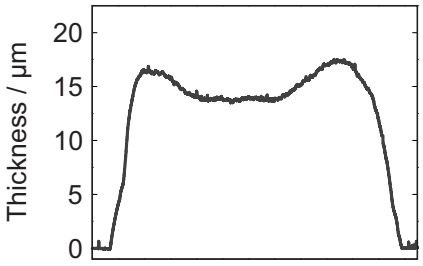

Figure 2.6: Profile of a mesoporous crystalline TiO_2 film of thickness around 15 μm prepared through a few depositions with the screen-printing technique and employing the 18-NRT GreatCell Solar© paste.

section of a bare TiO_2 film (reference) and Fig. 2.7(b) shows the structure of the film resulting from the inclusion of scattering TiO_2 spheres in the initial paste. The SEM cross section image in Fig. 2.7(b) reveals the presence of an air layer surrounding the TiO_2 spheres, which was attributed to shrinking effects during the thermal process required for stabilisation of the films. For the study of light propagation in this random medium as a funcion of the conditions of the included optical disorder, films with thicknesses ranging between 2 μm and 12 μm were prepared by means of this procedure.

For the preparation of photoanodes including a backscattering layer, a film was screen-printed on top of a sintered bare electrode from a commercial paste containing irregular particles of average size between *ca.* 150 nm and *ca.* 250 nm (WER2-O, GreatCell Solar©). After

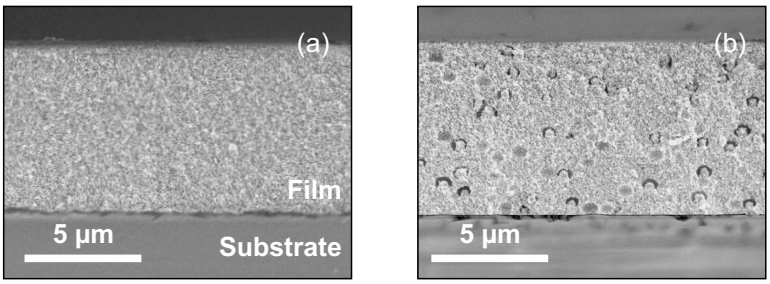

Figure 2.7: SEM cross section image of (a) a sintered TiO_2-nanoparticle film and (b) a TiO_2-nanoparticle film integrating spherical TiO_2 scattering centres, both deposited *via* screen printing

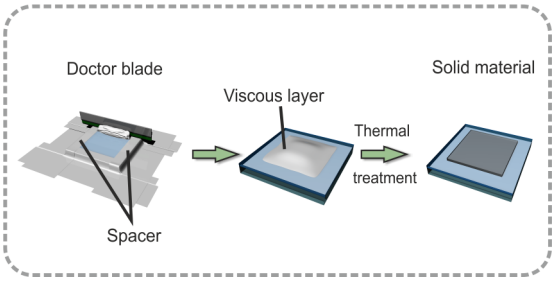

Figure 2.8: Preparation of a nanophosphor film through deposition *via* doctor blade.

a thermal treatment consisting of a heating process up to 450^{o}C during 30 minutes and sintering for 30 minutes, a solid layer of thickness around 4 μm on top of the photoanode resulted.

$GdVO_4$ matrix: Pastes based on nanophosphors were employed for the fabrication of luminescent films. On top of a glass or quartz substrate, a nanophosphor-based film was deposited *via* doctor blade from the paste previously prepared. Doctor blade is a technique for the deposition of thick films, analogous to screen printing, based on the removal of the excess of a liquid solution or viscous paste from a delimited area employing a blade, as illustrated in Fig. 2.8. The thickness of the as-prepared film was controlled through the number of spacers attached to the substrate defining the deposition area. Identical sintering process based on three heating stages previously described yielded a solid porous luminescent film.

2.1.3.2 Low refractive index materials

This section provides details on the fabrication of ultralow refractive index films based on a highly porous SiO_2 film, in which spherical TiO_2 scattering centres can be included. The procedure covers the preparation of films of polystyrene (PS) spheres from a liquid suspension, infiltration through chemical vapour deposition (CVD) and removal of the PS scaffold.

Highly porous SiO_2 matrix: In a quest for highly diffusive optically random media, low refractive index materials appeared as an indis-

putable requirement towards this goal. Through combination with scattering centres of high refractive index, intense scattering is expected, since the scattering cross section of an inclusion, and thus the scattering strength, is highly dependent on the refractive index contrast between the inclusion itself and its surrounding medium.

With this purpose, films consisting of a highly porous SiO_2 framework with a porosity close to 90% were fabricated from PS-sphere films *via* infiltration through CVD. The fabrication procedure consists of three steps: preparation of a scaffold consisting in a film of spherical PS particles randomly distributed, sequential infiltration of this scaffold through CVD for the formation of SiO_2 in the pores between the PS spheres and removal of the PS scaffold by means of a thermal treatment.

In order to fabricate films consisting of disordered stacks of spherical PS particles, a suspension of PS spheres in a mixture of water and absolute ethanol as solvent was prepared. In particular, 20 ml of a 10 vol% dispersion of PS spheres of diameter d = (168 $\pm$ 1) nm in water (IKERLAT Polymers S.L.©) were centrifuged at 24000 rpm for 40 minutes and the solvent removed. 9 ml Milli-Q water and 9 ml absolute ethanol were added to the solid part in order to prepare a 10:45:45 (v/v/v) dispersion. Eventually, the dispersion was sonicated for redispersion of the PS spheres. For the preparation of a film integrating TiO_2 spheres, the scattering centres were added from a dispersion in absolute ethanol to the PS-sphere dispersion. The added amount was dictated by the desired volume filling fraction, which can be calculated through Eq. 2.1 and 2.2, for which k = 1 has to be considered in this material.

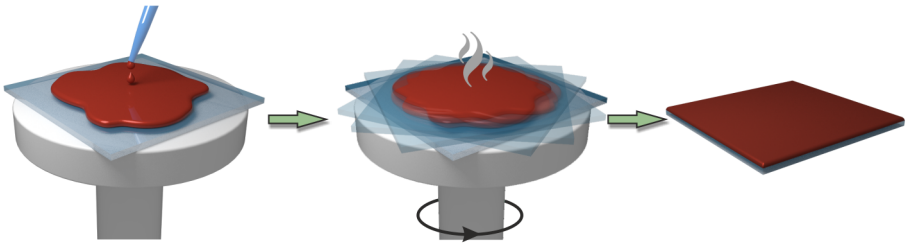

Figure 2.9: Deposition of a film from a liquid solution through spin coating.

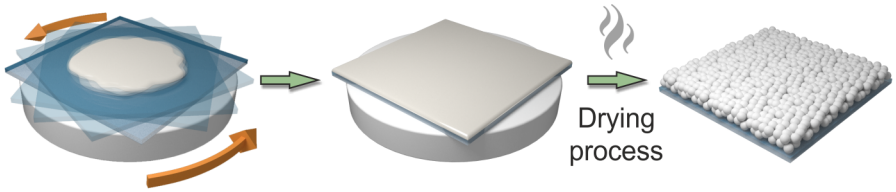

Figure 2.10: Process of deposition of a PS-sphere film *via* spin coating from a dispersion of PS spheres.

The films were deposited *via* spin coating using this dispersion of spherical PS particles. Spin coating is one of the most common techniques for the deposition of thin films on a substrate. It relies on the centrifugal force originated by the high-speed rotation of a substrate for its coating from a small amount of a solution or a dispersion, usually in a volatile solvent. Spinning of the substrate causes spreading of the solution, while accelerating solvent evaporation, as illustrated in Fig. 2.9. After complete evaporation, often promoted through thermal annealing, a conformal layer results. Thickness of the eventual film depends exclusively on the rotation speed and the viscosity of the solution, offering an estimated precision around $\pm$ 10 nm. 200 μL of the suspension were casted on a 2.5 x 2.5 cm^2 glass substrate, spun at 2000 rpm for 40 s and left to dry for 10 minutes at 60^{o}C, see Fig. 2.10. A second deposition with the same conditions was performed. Eventually, the layers were dried overnight at 60^{o}C, yielding films constituted by spherical PS stacks of thickness between 1-2 μm, as visible in Fig. 2.11.

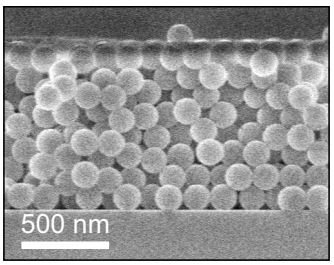

Figure 2.11: SEM cross section image of a film constituted by PS spheres prepared by spin coating.

For the fabrication of the material of interest, the PS scaffold was infiltrated through CVD. This deposition technique consists in the infiltration through the porous structure of a material serving as a scaffold with one or more volatile precursors in vapour phase. Reaction of silicon tetrachloride, $SiCl_4$, and water in vapour phase was promoted inside the pores of the PS-sphere film through sequential infiltration. In a first stage, the film was infiltrated with $SiCl_4$ in vapour phase, followed by infiltration with water vapour, triggering the formation of a continuous SiO_2 layer in the pores of the PS structure, as well as some by-products. Specifically, reaction between $SiCl_4$ and H_2O triggers the formation of silicic acid, $Si(OH)_4$, and chloridric acid, HCl. This HCl catalyses in turn the formation of H_2O and siloxane bonds from ≡Si-OH bonds[3].

For the deposition procedure, a homemade set-up was built. The setup consists of two lines like the one displayed in Fig. 2.12, for the circulation of the two precursors, which are stored in individual glass tubes. The gas flow is controlled by means of valves, which are manually opened and closed. Each line includes a $N_2(g)$ inlet, which is

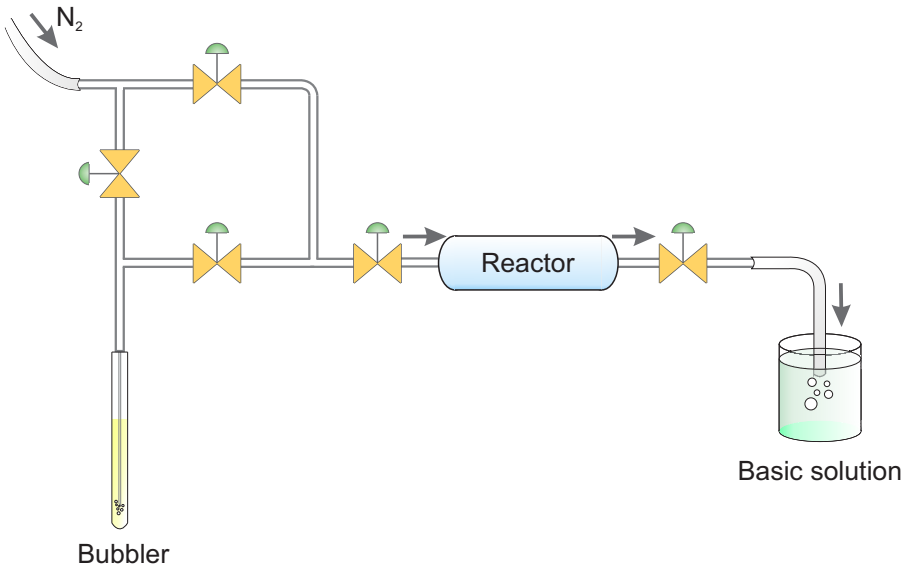

Figure 2.12: Schematic of a gas line of a homemade setup in order to perform infiltration through Chemical Vapour Deposition (CVD) of a material in vapour phase.

used to generate a gas flow throughout the line, bubble the precursors and enable their transport. The film is placed inside a tubular quartz reactor, carefully sealed in order to allow maintaining an inert atmosphere during the infiltration process. A first step of purging of the reactor by successive N_2 filling and emptying is required in order to remove any possible reactant inside the chamber. The line presents a gas outlet leading to a basic solution for neutralisation of the acidic by-products of the reaction. The first precursor, $SiCl_4(g)$, is bubbled by N_2 flow and transported throughout the line to the reactor, where infiltration of the film occurs. In order to trigger the reaction and subsequent formation of SiO_2, a process of $H_2O(g)$ infiltration by N_2 bubbling is subsequently performed. Posterior N_2 flow is advisable before sample removal in order to fully extract any acidic reactant left in the reactor chamber. For the formation of SiO_2 throughout the PS scaffold, 1-minute infiltration processes with each reactant were perfomed.

Eventually, a thermal treatment consisting in a heating process up to 400^{o}C for two hours, where it plateaus for one hour, was performed in order to remove the PS scaffold, yielding an around 2 x 2-cm^2 film consisting in a SiO_2 network with porosities up to 90%.

2.1.4 Preparation of multifunctional films

The porosity imposed upon the films enables infiltration with different fluorophores, chromophores or polymers in order to endow them with further functionality. According to such added functionality, the system can result suitable for specific applications. This part of the chapter briefly depicts the procedures of sensitisation of the materials with diverse molecules for particular purposes, as well as a procedure to transfer them into a flexible support.

2.1.4.1 Sensitisation of films

With the purpose of endowing the material comprising a mesoporous TiO_2 matrix with functionality and analyse its suitability in particular applications, it was infiltrated with two types of dyes.

Photoanode for DSSCs: Charge generation in DSSCs is enabled by an absorbing dye anchored to the internal surface of their anatase photoanode. For sensitisation of the material for DSSC integration, the films were immersed overnight in a 0.5 mM solution of N719 (GreatCell Solar©), commonly employed in the field of DSSCs. After that, the infiltrated films were rinsed with absolute ethanol and dried with pressurised nitrogen.

Colour conversion: In order to demonstrate the potential of the TiO_2-based *Mie glass* as an efficient colour converter for solid-state lighting applications, it was infiltrated with fluorophores. Specifically, films of thicknesses around 7.5 μm were sensitised through overnight immersion in a 0.075 wt% solution of a perylene dye, namely, Lumogen® F Red 305, BASF, in ethanol.

2.1.4.2 Flexible films

The porous nature of the prepared films enabled infiltration with a polymer, which allowed endowing the material with flexibility[4]. The result was a self-standing and flexible version of the depicted materials. In this section, the procedure is depicted for the particular case of nanophosphor films, although application to the TiO_2-based matrix is completely analogous.

In order to prepare a flexible version of a nanophosphor film, a sacrificial layer underneath the emitting material was required. Specifically, a dense SiO_2 layer was coated on the substrate from a SiO_2 solution, which was prepared by diluting 18 ml tetraethyl orthosilicate (TEOS, Sigma Aldrich, 98%) in 136 ml absolute ethanol. 6.88 ml of Milli-Q water were added after vigorous stirring for some minutes. Subsequently, 0.32 ml of a 0.05 N hydrochloric acid (HCl, VWR, 37%) solution were added. After stirring for 24 hours, the solution was ready for use. The SiO_2 was coated on a glass slide by means of dip coating. Dip coating is a solution-processing technique for the deposition of thin films of precisely controlled thickness with an estimated precision around $\pm$ 10 nm, Fig. 2.13. A dip coating process generally consists in the immersion of a substrate at a constant speed in a solution or particle suspension. After a dwell time for full wetting of the substrate, it is withdrawn at a controlled speed. The withdrawal

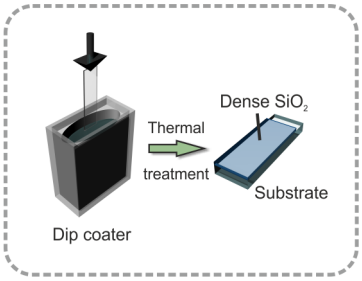

Figure 2.13: Deposition of the sacrificial SiO_2 layer.

speed is a key parameter allowing control over the thickness of the resulting layer, along with the concentration of the solution. Eventually, evaporation of the solvent leads to a thin film. In this work, the SiO_2 sacrificial layer was prepared by immersing a glass slide in the solution previously depicted and withdrawn at a speed of 150 mm min^{-1}. The wet substrate was heated up to 500^{o}C for 30 minutes so as to remove any organic residue and achieve conformation of the film, yielding a transparent SiO_2 film.

Poly(methyl methacrylate) (PMMA) was employed as support material and thus used for infiltration. The polymer was infiltrated through the pores of the nanophosphor film from a 15 wt% solution of PMMA (Alfa Aesar, powder) in anisole *via* spin coating at 2000 rpm for 40 seconds, followed by drying at 60^{o}C for at least one hour, Fig. 2.14(a). For etching of the SiO_2 sacrificial layer and release of the flexible film, the infiltrated layer was immersed in a 1% hydrofluoric acid (HF, Fluka, 48%) solution for 40-60 minutes, Fig. 2.14(b). After

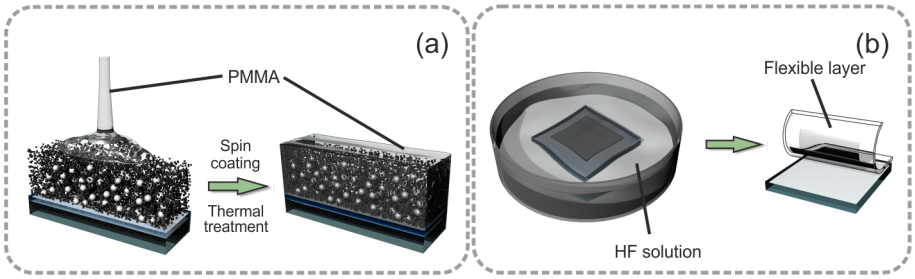

Figure 2.14: (a) Polymer infiltration of the nanophosphor film. (b) Immersion in HF solution and flexible film detachment.

detachment, the flexible film was rinsed abundantly in water in order to wash away any HF trace.

2.1.5 Solar cell fabrication process

The experimental procedure for the fabrication of the solar cells is depicted in this section. The preparation process of solar cells comprising a *Mie glass*-based photoanode encompasses the synthesis of a viscous paste for the subsequent deposition of the photoanode, the sensitization of the photoanode with an absorbing dye, the preparation of the counterelectrodes, cell assembly, electrolyte infiltration and sealing.

2.1.5.1 Electrode preparation

Photoanode: The photoanodes were prepared and sensitised with N719 according to the procedure already described in Sec. 2.1.3.1 and 2.1.4.1.

Counterelectrode: Clean FTO-coated glass substrates were drilled for posterior electrolyte injection and spin coated with a 6 mM chloroplatinic acid hexahydrate (H_2PtCl_6, Sigma-Aldrich, $\geq$37.50%) solution in 2-propanol. 10 μl of the solution were deposited on the substrate and spin coated at 2000 rpm for 20 seconds after a first stage at 500 rpm for 5 seconds. Three depositions were performed with drying processes at 80^{o}C for 5 minutes in between. After that, the samples were heated up to 400^{o}C for 20 minutes so as to trigger thermal decomposition.

2.1.5.2 Cell assembly

The cell was assembled by means of a thermoplastic polymer gasket (Surlyn-Low Temperature Thermoplastic Sealant, GreatCell Solar©), which melts at 110-130^{o}C. In that way, the photoanodes were attached to the drilled counterelectrodes by applying heat and pressure, so that the polymer acted as a sealant after melting. The assembled system was afterwards infiltrated with an electrolyte consisting of an iodide/triiodide (I^-/I_3^-) redox couple in a mixture of acetonitrile and

valeronitrile and some additives. Specifically, the electrolyte solution contained 0.7 M 1-butyl-3-methylimidazolium iodide (BMII, Sigma-Aldrich, 99%), I_2 (Sigma Aldrich, 99.999%), 0.1 M guanidinium-isothiocyanate (GdnSCN, Sigma-Aldrich, ≥97%), 0.5 M 4-*tert*-butylpyridine (Sigma-Aldrich, 99%) in acetonitrile (Sigma-Aldrich, ≥99.9%) and valeronitrile (Sigma-Aldrich, 99.5%) in a proportion 85:15 (v/v). The holes were eventually sealed with a cover glass small enough not to cover the active area in order to avoid additional reflections at operation under rear illumination using the thermoplastic polymer.

2.2 Characterisation methods

Apart from the synthesis and fabrication, the materials were subjected to diverse types of characterisation techniques in order to gain full understanding of the relation between their structural features and optical response, as well as to assess the operation of the devices into which they had been integrated. This section is devoted to the main techniques employed for the characterisation of different aspects of the fabricated materials, for which either commercial equipments or specific experimental setups were employed.

2.2.1 Structural characterisation

The exploration of the structural properties of the fabricated materials was essential for an appropriate description of their configuration. It allowed, for instance, the verification of an adequate integration of the scattering centres into the transparent matrices or the determination of the size and shape of the different synthesised nanoparticles. For that purpose, the materials were subjected to examination by different techniques. This part of the section presents a brief description of each of the techniques employed for that purpose.

Scanning Electron Microscopy (SEM): An SEM microscope relies on the interaction of an accelerated electron beam with a specimen to retrieve information on its structural properties. Most commonly, the properties of the secondary electrons generated from the interaction between the electron beam and the sample are analysed and used to

produce an image. This technique mainly provides information on the topography and morphology of the specimen. In this work, an SEM microscope (S-4800, Hitachi®) allowed, for instance, the determination of film thickness through examination of cross section images or the observation of the stratified configuration of the scattering spheres when integrated into specific matrices. In some cases, a Focused Ion Beam combined with an SEM (FIB-SEM) was used for the preparation and exploration of the structures. In an FIB equipment, an accelerated beam of ions, usually gallium, is employed to produce controlled etching of a sample. When coupled to an SEM microscope, the equipment offers the possibility of sample examination. This technique appears as especially convenient for the exploration of fragile structures or when aiming at the observation of specific features susceptible to be easily ruined by mechanical action during the process of specimen preparation for microscope exploration. Cross section images obtained in this work through this technique were generated employing a dual-beam Auriga FIB-SEM (ZEISS®).

Transmission Electron Microscopy (TEM): While similar to an SEM microscope inasmuch as the interaction between an accelerated electron beam and the specimen is the principle of image formation, the TEM technique collects the electrons transmitted through the sample. As an example, images produced by a TEM microscope (CM200, Philips®) allowed determination of the size and shape of the synthesised nanophosphors.

X-Ray Diffraction (XRD): XRD is a non-destructive technique providing information on the crystalline structure of any material. The technique is based on the analysis of the constructive interference of X-rays diffracted at specific lattices in a crystalline structure. The sample, which can rotate an angle θ, defined by the incidence direction and the direction perpendicular to the surface of the sample, is irradiated with X-rays and the diffracted beam is collected by a detector at an angle 2θ. Whenever the geometry of the incident beam in relation to the structure of the sample verifies the Bragg equation for the diffraction, constructive interference occurs and a maximum in intensity is detected.

2.2.2 Optical characterisation

A full study of the optical response of the fabricated random media is crucial in order to understand how the conditions of the included disorder affects the propagation of light. This characterisation is mostly based on spectroscopic techniques, such as reflectance and transmittance or photoluminescence (PL) in the case of emitting materials.

2.2.2.1 Reflectance and Transmittance

In a large number of cases, spectroscopic reflectance and transmittance measurements were performed on the materials in order to characterise their optical response. This type of characterisation was crucial for the determination of essential magnitudes studied in this thesis, such as ℓ_{sc} and ℓ_t.

Specular and ballistic: The measurements of specular reflectance, R_s, and ballistic transmittance, T_b, were performed by means of a UV-Vis-NIR spectrophotometer (Cary 5000, Agilent Technologies©), which operates by collecting the light either transmitted or reflected by the sample and referring it to the intensity of the incoming beam,

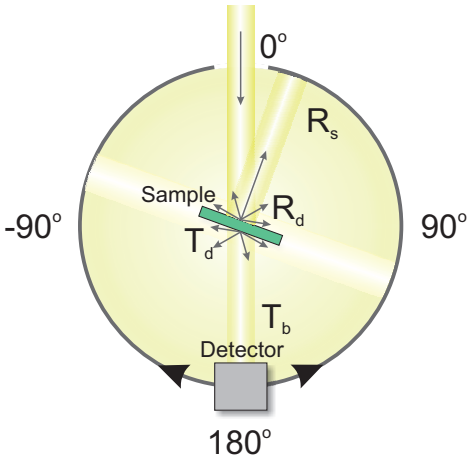

Figure 2.15: Operation of the Universal Measurement Accessory, UMA (Agilent Technologies©), and different measurable magnitudes.

thus spectrally determining the relative intensity of the collected light. When coupled to the Universal Measurement Accessory, UMA, the equipment enables angular collection of the light either reflected or transmitted by a film in an absolute way, see Fig. 2.15. A rotary clamp-like sample mount is placed at the centre of the measurement chamber. The detector consists of a combination of Si and InGaAs detectors, providing coverage in the 190-2800 nm wavelength range. The automated detector allows collection of light at any angle in the incidence plane around the sample, thus allowing the determination of the angular distribution pattern of the light emerging from the sample in a plane perpendicular to the film. In this work, for the measurement of R_s and T_b, the sample mount was rotated 6^o with respect to the incident beam and the detector placed at 12^o and 180^o, respectively, as indicated in Fig. 2.15. The samples were illuminated with light generated by either a Deuterium UV or a Visible QI lamp, depending on the wavelength range.

Total and diffuse. Angle-resolved measurements: For the determination of the total reflectance, R, total transmittance, T, as well as their respective diffuses, R_d and T_d, the Internal Diffuse Reflectance accessory was coupled to the equipment, consisting in an integrating sphere coated with a highly diffusive material. The accessory allows spectral measurement of the light inside the sphere and determination of the relative intensity after comparing with a reference beam. The position of the sample dictates whether the collected intensity corresponds to either a reflectance or a transmittance measurement, see Fig. 2.16. The absorptance of the films, A, can be determined from R and T according to

$$A(\lambda) = 1 - R(\lambda) - T(\lambda). \tag{2.3}$$

When indicated, R and T measurements were performed on a set-up mounted on an optical table, consisting of an integrating sphere (10 inches, Labsphere©) coupled to an optical fiber in order to guide the light into a spectrophotometer (USB 2000+, Ocean Optics©). Using a white light lamp (HL-2000, Ocean Optics©) for illumination of the films, the set-up enables determination of R and T, and therefore, A, by means of a standard procedure.

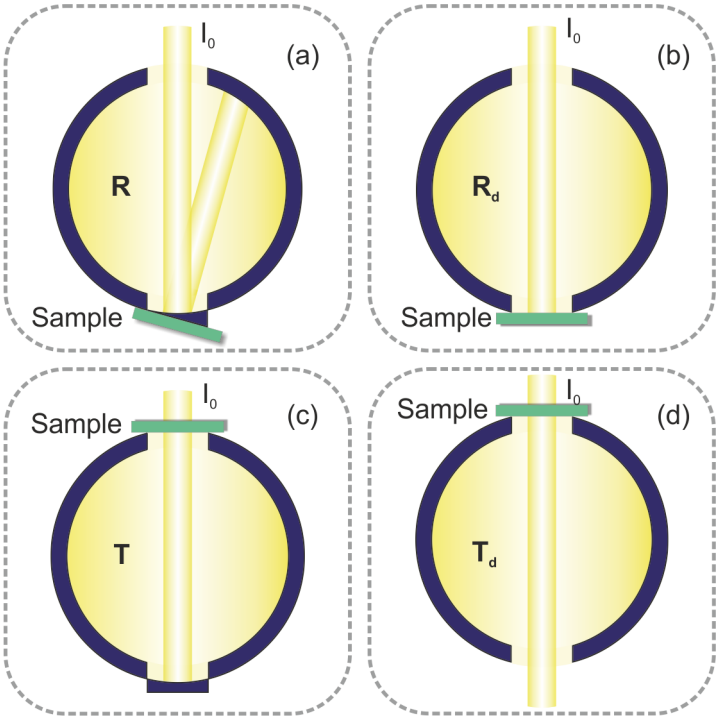

Figure 2.16: Position of the sample for the determination of (a) R, (b) R_d, (c) T and (d) T_d by means of the Internal Diffuse Reflectance accessory.

Determination of angular-resolved diffuse magnitudes was possible by means of the UMA set-up described above.

2.2.2.2 Photoluminescence

Some of the fabricated materials displayed photoluminescence, since they either comprised a luminescent matrix or had been infiltrated with emitting molecules. The characterisation of their PL properties was therefore required in order to understand the influence of the inclusion of optical disorder on their emission features, as well as to quantify any variation of these.

Static and angular dependent measurements: The static PL of the light-emitting films was determined by means of a spectrofluorom-

eter (Fluorolog®-3, Horiba Jobin Yvon). White light generated by a Xenon lamp is directed towards a monochromator at the entrance of the measurement chamber so as to select the pumping wavelength, λ_{pump}. The beam at λ_{pump} impinges on the sample for excitation and the emitted light is sent to a second monochromator allowing its decomposition for spectral analysis. The intensity of the light at each wavelength is determined through collection with a photodetector. Besides, the measured intensity is steadily corrected during data acquisition by the signal collected by a photodetector of the incoming beam at the entrance of the measurement chamber, in order to avoid contributions from instabilities in the emission of the lamp. The equipment allows coupling of an integrating sphere, which enables collection of the light emitted in all directions.

For the characterisation of the angular-dependent PL of the films, an experimental set-up was designed and built. This set-up consists in a back focal plane microscope based on Fourier analysis. Operation of this set-up relies on the fact that the complex amplitude of any monochromatic wave in the frontal focal plane of a lense is related to that in the back focal plane through the Fourier transform. All the rays emerging from the object plane at a given angle converge into the same point in the back focal plane, which can be associated to a specific k vector. Therefore, this set-up enables the determination of the intensity distribution of the light emitted by a luminescent film over all the wave vectors included in the numerical aperture (NA) of the objective. The film was excited by a laser diode and its emission intensity collected by a 100x objective with 0.75 NA, consequently forming an image at the back focal plane. The image is scanned through a mobile optical fiber controlled by a motor system and coupled into a spectrophotometer (USB 2000+, Ocean Optics©), which provides spectral information for each scanned point. The angular resolution is defined by the fiber section. In this way, the PL spectrum of the film was attained as a function of the angle of emission.

Time-resolved measurements: For the decay dynamic emission of the luminescent films, the spectrofluorometer equipment described above coupled to a Multichannel Scaler (MCS) was employed.

2.2.3 Optoelectrical characterisation of solar cells

In order to assess the effect of integrating optical disorder into the photoanode of DSSCs, an optoelectrical characterisation of the devices was required. During the measurements, a black opaque mask limiting the active area to 0.25 cm^2 was placed on the cell, so that only the active area of the device was illuminated, thus ensuring that no light derived from parasitic reflections or refraction would contribute to the generation of the photocurrent and therefore result in an overestimation of the measurements.

2.2.3.1 Spectral Incident Photon-to-Current Efficiency

For the determination of the spectral η_{IPCE}, a specific set-up was built. White light generated by a 300-W xenon arc lamp was sent to a monochromator consisting in a large 1140 lines-per-milimeter grating (model 272, McPherson®), controlled by a digital scan drive system (Model 789A-3, McPherson®), therefore allowing selection of the wavelength of the light impinging on the solar cell. In order to avoid the presence of second-order harmonics, a longpass UV filter with a cut-off wavelength $\lambda = 400$ nm was placed after the monochromator. The solar cell was fixed to a holder and the generated photocurrent was measured at each wavelength in the range 400-800 nm by a picoammeter (Model 6485, Keithley®) connected to the contacts. Data of the wavelength-dependent current were acquired with a computer. The photon flux of the incident light was measured using a calibrated silicon diode (D8-Si-100 TO-8 Detector, SphereOptics©) for correction of the device response.

2.2.3.2 J-V characteristics

The most widespread method for the assessment of the operation of a solar cell consists in the determination of its J-V curve. The parameters yielded by this curve enables the calculation of the PCE. To this end, the device was illuminated with 100-mW cm^{-2} light generated by a solar simulator (Sun 2000, Abet Technologies©) by a 150-W xenon arc lamp combined with an AM1.5G filter. The power of the incident light was regularly verified by means of a calibrated silicon

solar cell. Under illumination, the photocurrent generated by the cell is measured using a source meter (Model 2400, Keithley®) while applying an external variable bias voltage. The data were processed by a software for the extraction of the J-V curves.

2.3 Theoretical methods

The systems studied throughout this thesis present the advantage of enabling tailoring of their optical properties in order to meet specific requirements for particular applications. Besides, the availability of a theoretical model capable of supporting the experimental results reinforces the method and highlights its potential, while also serving as a design tool. In this section, the theoretical background, as well as the numerical approaches employed either as design tools for the materials or complete devices or as a means to analyse the experimental results are detailed.

In the first place, an analytical (Mie formalism) and a numerical (Finite-Difference Time-Domain) method for the description of the optical response of light scattering by an individual particle are described. After that, the modelling is extended to a material integrating scattering centres. Here, the mathematical expressions required for the determination of ℓ_{sc} and ℓ_t from experiments and a numerical tool based on a Monte Carlo approach for the description of light propagation throughout multilayer systems, which allows to consider the effect of scattering particles, are provided. Eventually, details on the modelling of DSSCs are provided.

2.3.1 Response of an individual scattering particle

This section focuses on the modelling of the behaviour of light after interaction with an individual particle. The Mie formalism for the analytical determination of light scattering by a sphere is provided, followed by a description of the details of the numerical simulations of the optical response of an individual particle of any shape through Finite-Difference Time-Domain (FDTD).

2.3.1.1 Mie formalism

The main route for the generation of optical disorder employed during this thesis consists in the random inclusion of spherical scattering centres in transparent matrices. The scattering of light by this disordered distribution triggers a diffuse propagation of the incoming light, see Fig. 2.17(a), endowing the material with properties typical of turbid media. Light is therefore removed from the incidence direction and scattered at larger angles, describing an angular pattern in reflection and transmittance dependent on the scattering strength of the material, Fig. 2.17(b).

In all cases, low volume concentration values of the inclusions were considered, thereby minimising correlations among particles when aiming at describing the scattering of light. In this limit of high dilution, single-particle scattering can be expected to account reasonably well for the total scattering of light in the system, thus allowing a description of light propagation based on the scattering of light caused by an individual particle. The problem of the scattering of an electromagnetic plane wave by a small sphere of arbitrary radius and refractive index is exactly soluble and it was resolved a long time ago, as described by the formalism formulated by Gustav Mie in 1908, the

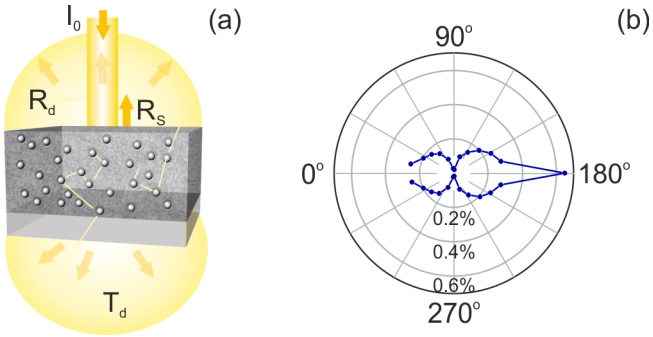

Figure 2.17: (a) Illustration of the diffuse propagation of light throughout an optically random medium. (b) Experimental angular distribution of the light scattered by a mesoporous anatase film integrating TiO_2 spherical scattering centres of size r = (225 ± 20) nm in a 10% concentration at λ = 600 nm. Measurements were performed every 14^o.

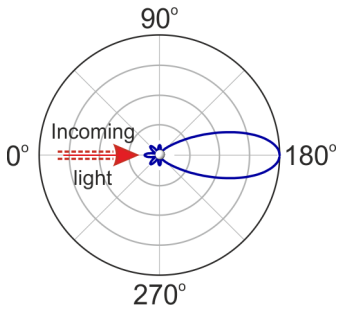

Figure 2.18: Angular distribution of the light scattered by a 300-nm radius anatase sphere at $\lambda = 600$ nm.

Mie theory[5,6]. An interesting peculiarity of the Mie scattering for a sphere of a size comparable to the wavelength of the incident light is a largely forward-oriented distribution of the scattered light, see Fig. 2.18. Throughout this thesis, the propagation of light in random media was assessed through Mie theory considering spherical scattering particles embedded in an absorbing medium[7], based on the standard parameters employed for the characterisation of turbid media, namely, ℓ_{sc}, and ℓ_t.

As mentioned in the previous chapter for Eq. 1.1, in the limit of independent scattering, ℓ_{sc} is a function of the number particle density and the scattering cross section of an individual scattering centre. Taking into account the definition of particle number density and volume filling fraction, that is,

$$\rho = \frac{N}{V}; f = \frac{V_{incl}}{V}, \tag{2.4}$$

where N refers to the number of inclusions, V to the considered volume and V_{incl} to the total volume occupied by the scattering inclusions, which in this case correspond to spheres of radius r, Eq. 1.1 results

$$\ell_{sc} = \frac{\frac{4}{3}\pi r^3}{f \cdot \sigma_{sc}}. \tag{2.5}$$

According to Mie theory, σ_{sc} for a spherical particle is a function of the radius of the sphere, the complex refractive index of both the particle, N_p, and the surrounding medium, N_m, and the wavelength of the

impinging light, λ, and it is given by

$$\sigma_{sc} = \frac{2\pi}{k^2} \sum_{n=1}^{\infty} (2n+1) \left({a_n}^2 + {b_n}^2 \right), \tag{2.6}$$

where $k = \frac{2\pi}{\lambda n_m}$ refers to the modulus of the wave vector, in which $\mathrm{n_m}$ corresponds to the real part of $\mathrm{N_m}$. In this thesis, the model considered the possibility of a stratified sphere as scattering structure. This was necessary in order to account for the air shell surrounding the scattering particle present in some of the modelled materials, as well as for any possible coating of the particle. In that scenario, the Mie formalism provides the expression for the coefficients a_n and b_n as a function of the Riccati-Bessel functions. These coefficients were calculated by means of a script[8,9] based on the formalism formulated by Arthur L. Aden and Milton Kerker[10]. In particular,

$$a_n = \frac{\psi_n(y)[\psi_n'(m_2 y) - A_n \xi_n'(m_2 y)] - m_2 \psi_n'(y)[\psi_n(m_2 y) - A_n \xi_n(m_2 y)]}{K_n(y)[\psi_n'(m_2 y) - A_n \xi_n'(m_2 y)] - m_2 K_n'(y)[\psi_n(m_2 y) - A_n \xi_n(m_2 y)]}, \tag{2.7}$$

$$b_n = \frac{m_2 \psi_n(y)[\psi_n'(m_2 y) - B_n \xi_n'(m_2 y)] - \psi_n'(y)[\psi_n(m_2 y) - B_n \xi_n(m_2 y)]}{m_2 K_n(y)[\psi_n'(m_2 y) - B_n \xi_n'(m_2 y)] - K_n'(y)[\psi_n(m_2 y) - B_n \xi_n(m_2 y)]}, \tag{2.8}$$

being

$$A_n = \frac{m_2 \psi_n(m_2 x) \psi_n'(m_1 x) - m_1 \psi_n'(m_2 x) \psi_n(m_1 x)}{m_2 \xi_n(m_2 x) \psi_n'(m_1 x) - m_1 \xi_n'(m_2 x) \psi_n(m_1 x)}, \tag{2.9}$$

$$B_n = \frac{m_2 \psi_n(m_1 x) \psi_n'(m_2 x) - m_1 \psi_n'(m_1 x) \psi_n(m_2 x)}{m_2 \xi_n'(m_2 x) \psi_n(m_1 x) - m_1 \xi_n(m_2 x) \psi_n'(m_1 x)}. \tag{2.10}$$

$\psi_n(z)$, $\xi_n(z)$ and $K_n(z)$ refer to Riccati-Bessel functions of the form

$$\psi_n(z) = \left(\frac{\pi z}{2} \right)^{1/2} J^{(1)}_{n+\frac{1}{2}}(z), \tag{2.11}$$

$$\xi_n(z) = \psi_n(z) + i X_n(z), \tag{2.12}$$

where

$$X_n(z) = -\left(\frac{\pi z}{2} \right)^{1/2} Y^{(2)}_{n+\frac{1}{2}}(z), \tag{2.13}$$

and

$$K_n(z) = \left(\frac{\pi z}{2}\right)^{1/2} H^{(1)}_{n+\frac{1}{2}}(z), \tag{2.14}$$

where $J^{(1)}_{n+\frac{1}{2}}(z)$ corresponds to the semi-integer Bessel function of first kind, $Y^{(2)}_{n+\frac{1}{2}}(z)$ to the semi-integer Bessel function of second kind and $H^{(1)}_{n+\frac{1}{2}}(z)$ is the semi-integer Hankel function of first kind. The optical characteristics of the different considered media play an essential role on the expressions above. Indeed, being N_p and N_c the complex refractive indices of the scattering particle and the coating material, respectively, the expressions for coefficients a_n and b_n depend on the refractive indices of the scattering sphere and its coating relative to the embedding medium, namely, $m_1 = \frac{N_p}{n_m}$ and $m_2 = \frac{N_c}{n_m}$. Two size parameters are defined, $x = kr_p$ for the scattering sphere and $y = kr_c$ for the coating, where r_p and r_c correspond to the radius of the particle and the coating thickness, respectively.

Knowing ℓ_{sc} allows the determination of ℓ_t through the angular distribution of the light scattered by the particle predicted by Mie formalism, according to Eq. 1.2.

2.3.1.2 Finite-Difference Time-Domain (FDTD) simulations

The calculations of the angular distribution of the scattered light and scattering efficiency of non-spherical particles were performed by means of 3-dimensional Finite-Difference-Time-Domain (FDTD) simulations with the software 'FDTD Solutions' from Lumerical Solutions[11]. In order to account for shrinkage effects experimentally observed for the scattering particles, a hollow with the same shape as the considered particle between the inclusion and the embedding medium was included in the simulations. Besides, since the calculations were aimed at justifying the specific shape chosen for the scattering centres for the particular case of the integration into photoanodes of DSSCs, this hollow was considered to be filled with electrolyte. With these assumptions, the simulated system consisted of a scattering structure comprising a TiO_2 particle surrounded by an electrolyte-filled shell

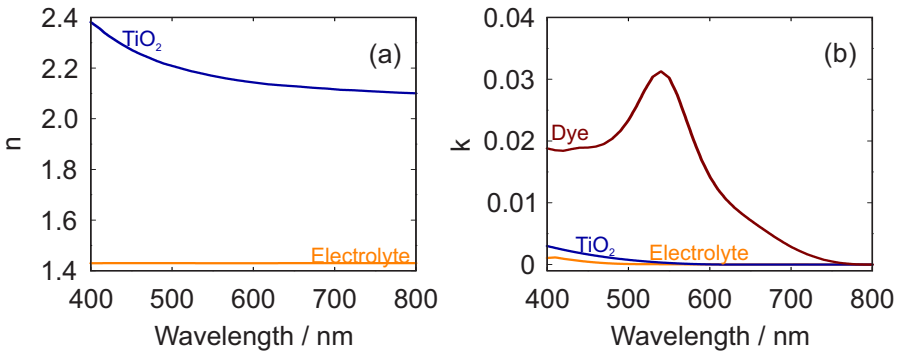

Figure 2.19: Optical constants of the materials used in the FDTD simulations of the light scattered by individual TiO_2 particles of diverse shapes: (a) Real part of the complex refractive index. (b) Imaginary part of the complex refractive index.

of the same shape embedded in an external absorbing medium constituted by a sensitised mesoporous TiO_2 matrix infiltrated with electrolyte. The spectral complex refractive index of the materials considered in the simulations are displayed in Fig. 2.19.

In order to numerically evaluate the absorption, scattering efficiency and angular distribution of the light scattered by individual particles, FDTD calculations considering a simulation box size of $1.0 \times 1.0 \times 1.0\ \mu m^3$ and perfectly matching layer conditions on every boundary were performed. Four particle shapes were simulated, namely, spheres, cubes, truncated pyramids and distorted cubes. The volume of the simulated particles corresponds to that of a sphere of radius r = 150 nm, except for slight volume variations for irregular shapes. As excitation source, a plane wave of wavelength $\lambda = 650$ nm was considered. As for the particles presenting irregular shapes, namely, truncated pyramids and distorted cubes, the resulting distributions and spectra derived from averaging over several angles and illumination sides. The mesh grid was established to 150 nm over the complete simulation volume, considering a refinement of 4 nm over a $0.72 \times 0.72 \times 0.72\ \mu m^3$ volume spanning over and around the volume occupied by the scattering structure. These parameters provided convergent results for all the considered shapes. The scattered power was determined through the total-field scattered-field method by placing

frequency-domain transmission monitors in the region of the scattered field.

2.3.2 Response of a material integrating scattering centres

With the information of the scattering of light triggered by a single particle, the next step consisted in the simulation of light propagation in a disordered material including a random distribution of the previously modelled scattering centres. The first part of the section describes the mathematical formalism required for the determination of ℓ_{sc} and ℓ_t from experimental magnitudes. The second part provides the details of a model based on a Monte Carlo approach combined with Mie theory for the simulation of the photon trajectory throughout any multilayer system, thus enabling the modelling of light propagation.

2.3.2.1 Scattering and transport mean free path

The spectral ℓ_{sc} of each material is determined by fitting measurements of T_b and R_s of the material to Lambert-Beer's law for the diffuse propagation of light in random media in a valid wavelength range. If the material is described as a homogeneous slab of thickness L, the intensity attenuation of a beam of light impinging on its surface due to the scattering of light, see Fig. 2.20, is given by

$$I_b(z) = I_0 e^{-z/\ell_{sc}}, \tag{2.15}$$

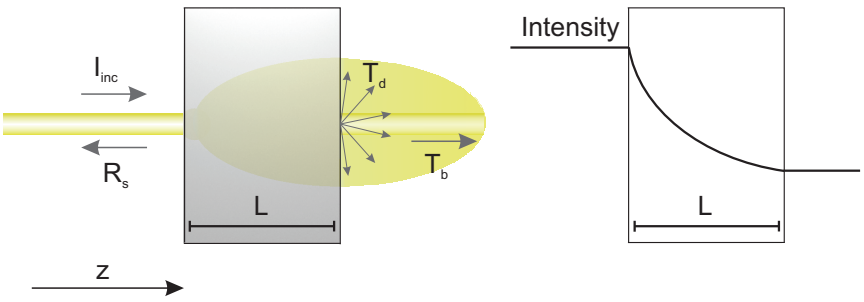

Figure 2.20: Illustration of the intensity attenuation of a beam through a slab of thickness L in a turbid medium according to Lamber-Beer's law.

being $I_b(z)$ the intensity of the beam at any point inside the slab along the direction of incidence, z, and I_0 the value of the intensity of the incoming beam at the entrance plane inside the slab. The presence of interfaces causes reflection losses at the entrance and end of the slab, which are accounted for through a decrease in the intensity measured at z = 0 inside the slab and at z = L outside of it, that is, $I_0 = I_{inc} - I_R$, where I_{inc} corresponds to the intensity of the beam impinging on the slab and I_R the value of the total intensity lost due to reflections at the interfaces. The intensity measured outside of the slab along the propagation direction of the incident beam is therefore determined by the expression

$$I_b(L) = (I_{inc} - I_R)e^{-L/\ell_{sc}}, \tag{2.16}$$

and dividing by I_{inc} results

$$T_b = (1 - R_s)e^{-L/\ell_{sc}}, \tag{2.17}$$

Finally:

$$\frac{T_b}{1 - R_s} = e^{-L/\ell_{sc}}, \tag{2.18}$$

where T_b is obtained from the measurement of the emerging intensity at any point after the slab along the direction of the incident beam and R_s includes interference effects due to reflections at the entrance and exit of the slab. Eq. 2.18 is used in this work for the extraction of the spectral ℓ_{sc} of the different proposed systems from experimental data.

Light transport throughout a turbid media is considered diffusive if verifying the condition $\lambda \ll \ell_t \ll L$. In the weak-scattering limit, where the density of scattering centres is low and/or σ_{sc} is small enough to yield $k\ell_{sc} \gg 1$, while having enough thickness to achieve randomisation of the propagated light, its transport can be described by the diffuse equation,

$$S(\vec{r}, t) = \left(\frac{\partial}{\partial t} - D \cdot \nabla^2 + \frac{v_e}{\ell_i} \right) I(\vec{r}, t), \tag{2.19}$$

where $S(\vec{r},t)$ represents a light source, D is the diffusion coefficient, v_e the energy velocity and ℓ_i corresponds to the inelastic absorption length, *i.e* the average distance into the slab at which the intensity of the light, $I(\vec{r},t)$, has been attenuated by a factor *e*. This approximation is not valid in conditions of localisation, that is, $k\ell_{sc} \simeq 1$, where

the scattering is excessively strong and light propagation is seriously hampered. The stationary solution of the monodimensional diffusion equation relates the total transmittance through the slab, T(L,λ), to $\ell_t(\lambda)$ and the slab thickness:

$$T(L,\lambda) = \frac{1}{\alpha z_e} \frac{sinh[\alpha(z_e + z_p)]sinh[\alpha z_e]}{sinh[\alpha(L + 2z_e)]} \tag{2.20}$$

Here, α corresponds to the reciprocal absorption length and z_e and z_p are extrapolation and penetration lengths, respectively, which can be calculated according to[12]

$$z_p = z_e = \frac{1}{2\alpha} ln\left(\frac{1 + \alpha z_0}{1 - \alpha z_0}\right), \tag{2.21}$$

and

$$z_0 = \frac{2}{3}\ell_t\left(\frac{1 + R}{1 - R}\right), \tag{2.22}$$

being R the polarisation-averaged Fresnel internal reflectivity at an imaginary boundary between the disordered medium and the embedding material[13]. In line with the derivation of Eq. 2.18, Eq. 2.20 can be modified in order to account for reflections at the interfaces of the material:

$$\frac{T(L,\lambda)}{1 - R_s(\lambda)} = \frac{1}{\alpha z_e} \frac{sinh[\alpha(z_e + z_p)]sinh[\alpha z_e]}{sinh[\alpha(L + 2z_e)]} \tag{2.23}$$

Equation 2.23 is often referred to as the photonic Ohm's law. The total transmittance through the slab is directly proportional to ℓ_t and inversely proportional to L, $\frac{T(L,\lambda)}{(1-R_s(L))} \sim \ell_t(\lambda)/L$. The expression in Eq. 2.23 is employed in this thesis for the extraction of the spectral ℓ_t values of the material comprising a random distribution of TiO_2 spheres in a mesoporous TiO_2 matrix from experiments. Another way to determine ℓ_t from experimental magnitudes entails measurements of the enhanced backscattering cone[14,15]. Whereas a sample presenting a large thickness is required for determination of ℓ_t through the latter, the former relies on the measurement of total transmission of several samples of different thicknesses. In this work, estimation of ℓ_t is performed through fitting Eq. 2.23 to experimental data of T(L,λ) for slabs of diverse thicknesses.

2.3.2.2 Determination of photon trajectory in layered media

An optical model able to predict light propagation is a key tool in order to perform a full description of the interaction of light with the optically random materials studied in this thesis, since it enables designing the optical response of the system, as well as provides a theoretical support for the empirical observations. For this purpose, a Monte Carlo approach combined with Mie theory was employed in order to simulate the trajectory of individual photons propagating throughout a multilayer system[16–19]. The model consists in a ray-tracing method capable of fully accounting for the trajectory of each photon through any multilayer structure. It provides full information on light interaction with the system, specifically, specular and total reflectance, ballistic and total transmittance, their corresponding diffuse magnitudes, the absorption profile at each of the layers, the angular distribution of light emerging from the system and photon scattering event statistics, allowing an angular representation of the photons undergoing a specific number of scattering events. The system is represented as a 3-dimensional multilayer structure comprising any number of layers, each characterised by their thickness, L_i, and the optical constants of the material constituting it, n_i^j, Fig. 2.21(a). Additionally, each layer can include any number of components, such as a homogenous distribution of a different phase or scattering centres, for which further input parameters are required.

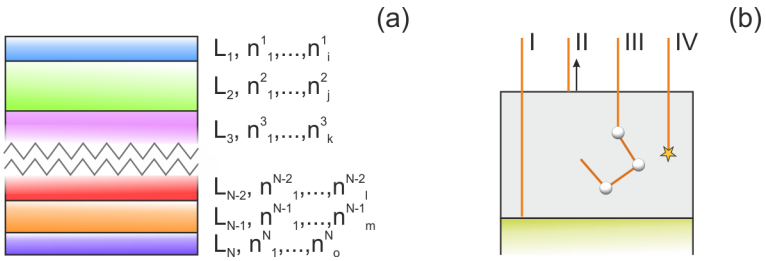

Figure 2.21: (a) Illustration of a general multilayer structure considered in the model. (b) Different possible fates for a photon contemplated in the model: I. Transmitted photon, II. Reflected photon, III. Transmitted and scattered photon, IV. Transmitted and absorbed photon.

In this description, the incident beam is depicted as a collection of individual photons. A photon is randomly generated outside the structure and impinges on the first interface of the system at a given angle. The distance travelled by the photon before undergoing an scattering or absorption event, ℓ, is given by

$$\ell = -ln[r]/\alpha_{ext}, \tag{2.24}$$

being r a randomly generated number in the range $0 < r \leq 1$ and α_{ext} an extinction coefficient accounting for different phenomena depending on the components included in that layer. Extinction is herein regarded as any phenomenon substracting photons from the incident beam, such as absorption or scattering, thus resulting

$$\alpha_{ext} = \alpha_A + \alpha_{sc}, \tag{2.25}$$

where α_A and α_{sc} refer to the absorption and scattering coefficient, respectively. The scattering coefficient is given by $\alpha_{sc} = \rho\sigma_{sc}$, being ρ the number density of the scattering inclusions and σ_{sc} their scattering cross section, according to the Mie formalism. If $\ell > L_i$, the photon reaches the following interface without deviation from the trajectory of the incident beam. At this point, there is a certain likelihood that the photon results either transmitted or back reflected, Fig. 2.21(b) I and II, respectively, as defined by the Fresnel coefficients. If the photon is transmitted, the process is repeated at the next layer. In the case the photon undergoes an absorption or scattering event, then $\ell < L_i$. Here, a new random number r' is generated and a casuistry for the fate of the photon depending on its value unfolds. Specifically, if $r' \leq \alpha_{sc}/\alpha_{ext}$, the photon is scattered, Fig. 2.21(b) III, while $r' \geq \alpha_{sc}/\alpha_{ext}$ results in a photon absorbed at the layer, Fig. 2.21(b) IV. This latter condition can be expanded for a layer comprising more than one single component in order to account for the relative contribution of each of the components to the absorption at the layer. In the case of scattering of the photon, the new propagation direction, (ϕ, θ), is determined by the angular distribution of the light scattered by a particle yielded by Mie theory. The absorption by the external medium is included when evaluating this. The process is extrapolated to a larger number of photons and their trajectories are traced. Collection of the photons emerging from the structure at the incoming and outgoing media enables re-

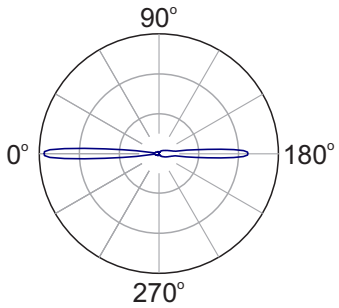

Figure 2.22: Angular distribution of the light scattered by a disordered system simulated according to the depicted model. The conditions of the material correspond to a 7-μm thick mesoporous anatase slab integrating nanocrystalline TiO_2 spheres of size r = 225 nm in a 12% concentration at $\lambda = 600$ nm.

trieving information on the reflectance and transmittance, while distinguishing between diffuse light and T_b or R_s through the photon exit angle. In a similar way, the model provides information on the spatial absorption of photons at each layer, therefore enabling the generation of spatial absorption profiles by each component comprising the layers. Besides, information regarding the direction of each emerging photon in both the incoming and outgoing medium enables the determination of the pattern of angular distribution of the scattered light, which illustrates the number of photons exiting the system at every angle. An example is presented in Fig.2.22, where 0^o and 180^o refer, respectively, to T_b and R_s.

2.3.3 DSSC modelling

The numerical simulation method depicted above in Sec. 2.3.2.2 was applied to a DSSC. Considering the cell as a multilayer system, the model enabled extraction of magnitudes relevant for the characterisation of the operation of the device, as well as allowing comparison with the empirical values. At this point, it is convenient to define the principal magnitudes involved in the optoelectrical characterisation of a photovoltaic device.

2.3.3.1 Key performance parameters of DSSCs

The optoelectrical characterisation of a solar cell is an essential step in order to assess the operation of a device, since it enables determination of its performance and other magnitudes directly affected by the implementation of any approach oriented towards a more efficient operation. Generally, the electrical characterisation of solar cells consists in the determination of the spectral Incident Photon-to-Current Efficiency, $\eta_{IPCE}(\lambda)$, and the extraction of the photocurrent-voltage curve.

Incident Photon-to-Current Efficiency: The Photon-to-Current Efficiency ($\eta_{IPCE}(\lambda)$) quantifies the number of photons responsible for the generation of electrons eventually contributing to the photocurrent in relation to the amount of incident photons at each wavelength, also designated as External Quantum Efficiency, EQE. An $\eta_{IPCE}(\lambda)$ spectrum yielded by a DSSC is displayed in Fig. 2.23(a). $\eta_{IPCE}(\lambda)$ is a function of the wavelength and it can be expressed as a product of efficiencies related to different processes occurring in the cell:

$$\eta_{IPCE}(\lambda) = \eta_{LH}(\lambda)\eta_{COL}(\lambda)\eta_{INJ}(\lambda)\eta_{REG}(\lambda), \tag{2.26}$$

where $\eta_{LH}(\lambda)$ refers to the light-harvesting efficiency, which quantifies the absorptance at the active layer by the dye, $\eta_{COL}(\lambda)$ is the efficiency of the collection of chargers by the contacts of the device, $\eta_{INJ}(\lambda)$ corresponds to the efficiency of the process of electron injection from the excited dye molecules to the TiO_2 matrix and $\eta_{REG}(\lambda)$ is the regeneration rate of the dye molecules by the electrolyte soaking the system. As evidenced by Eq. 2.26, the value of $\eta_{IPCE}(\lambda)$ depends on optical and electrical processes of the device and it is directly related to the device output performance.

J-V characteristics: The usual method for the characterisation of the performance of a PV device consists in the determination of the photocurrent-voltage, I-V, characteristics, or current density-voltage, J-V, characteristics, when evaluated per unit area. A current-voltage curve relates the photocurrent generated by a solar cell under illumination to the potential difference across its terminals. The importance of this

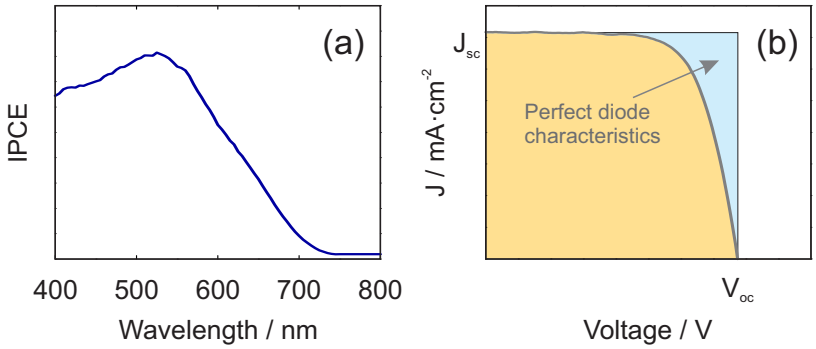

Figure 2.23: (a) Spectral η_{IPCE} curve of a DSSC. (b) Typical J-V characteristics of a DSSC along with the photovoltaic parameters extracted from it.

method resides in the fact that it provides electrical parameters enabling the determination of the efficiency of the device. Figure 2.23(b) displays a typical J-V characteristics. In effect, the power conversion efficiency, PCE, of a solar cell, *i.e.* the fraction of incident power effectively converted into usable electricity, is defined according to

$$PCE = \frac{P_{max}}{P_{in}} = \frac{J_{sc} \cdot V_{oc} \cdot FF}{P_{in}}, \tag{2.27}$$

where P_{max} refers to the maximum power extracted from the device and P_{in} to the incident sunlight power. The short-circuit current density, J_{sc}, defines the value of the current density under short circuit conditions, *i.e.* at zero voltage and it is related to optical and electrical processes in the cell. The open-circuit voltage, V_{oc}, refers to the voltage value measured between the contacts of the cell when not connected to any load and it is ideally defined by the difference between the Quasi-Fermi level of TiO_2 under illumination and the potential energy of the redox-couple. Eventually, the fill factor, FF, measures the degree of similarity of the cell characteristics to that of a perfect diode and it is affected by resistances in the device. The fill factor is related to J_{sc} and V_{oc} through

$$FF = \frac{P_{max}}{J_{sc} \cdot V_{oc}}. \tag{2.28}$$

J_{sc} is in fact related to $\eta_{IPCE}(\lambda)$ through the expression

$$J_{sc} = q \int_{\lambda_1}^{\lambda_2} \eta_{IPCE}(\lambda) \Phi(\lambda) d\lambda, \tag{2.29}$$

being q the electron charge and $\Phi(\lambda)$ the spectral incident photon flux, evaluated from the AM1.5G solar spectral irradiance.

2.3.3.2 Modelling of an ideal DSSC. Schockley-Queisser limit and determination of maximum short-circuit current density

The maximum attainable efficiency of a solar cell is limited by different loss processes occurring in the cell. In that regard, the Shockley-Queisser limit[20] provides the maximum theoretically achievable efficiency for a single-junction solar cell. Shockley and Queisser established this maximum efficiency as a function of the energy bandgap (E_g) of the active material and found a maximum efficiency of about 30% for silicon, $E_g = 1.1$ eV, under standard AM1.5G solar irradiation conditions. In the particular case of a DSSC, losses causing a decrease of the cell performance can originate from different processes:

- Spontaneous emission, which is governed by blackbody radiation.
- Unabsorbed photons. Photons with energies below E_g are not absorbed by the active material. In a DSSC, for which the common dyes absorb up to 750-800 nm, *i.e* $E_g \approx 1.5$ eV, only UV and visible light can contribute to the generation of photocarriers.
- Thermal relaxation to the conduction band edge of electrons injected from the dye into the semiconductor.
- Recombination of electrons in the TiO_2 matrix with holes in the electrolyte and dye.

Among these processes, blackbody radiation cannot be avoided. Assuming zero losses originating from the remaining processes, the current density generated by the device can be expressed as

$$J(E_g, V, T) = J_{ph}(E_g) - J_r(E_g, V, T), \tag{2.30}$$

where V refers to the photo-generated voltage across the device, T is the temperature, $J_{ph}(E_g)$ is the photocurrent density, given by

$$J_{ph}(E_g) = q \int_{E_g}^{\infty} \Phi(E) dE, \tag{2.31}$$

being q the electron charge, E the energy, $\Phi(E)$ the spectral incident photon flux and $J_r(E_g, V, T)$ corresponds to the current density due to radiative recombination

$$J_r(E_g, V, T) = qa \int_{E_g}^{\infty} \frac{E^2}{e^{\frac{E-V}{kT}} - 1} dE, \tag{2.32}$$

where k is Boltzmann's constant and $a = \frac{2\pi q^3}{c^2 h^3}$, being c the speed of light and h Planck's constant. Figure 2.24 displays the curve of maximum attainable PCE by a solar cell depending on the bandgap of the absorber according to Shockley-Queisser equation.

In any single-junction device, there is an inevitable net loss causing deviation of the PCE of the cell from the maximum theoretical value predicted by Shockley-Queisser theory. This loss is represented as a potential defined by $\frac{E_g}{q} - V_{oc}$. Whereas a 28.1%-efficient GaAs cell presents a loss potential around 300 mV[21], the relatively large potentials required for the processes of electron injection and dye regeneration in DSSCs are expected to result in a loss potential above 700

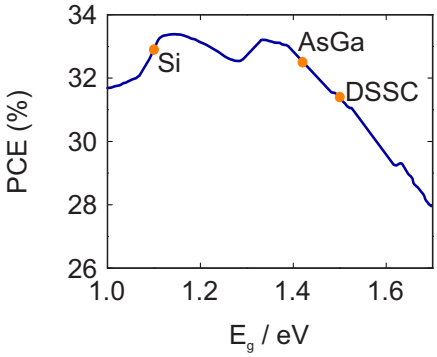

Figure 2.24: Maximum attainable PCE by a single-junction solar device in relation to the bandgap of the absorber according to Shockley-Queisser equation. The PCE values corresponding to absorbers employed in different PV technologies have been indicated with orange dots.

mV for Ru-complex-based devices[22], for which a maximum $V_{oc}^{SQ} \approx$ 1 V is predicted considering a bandgap of $E_g = 1.5$ eV, according to Shockley-Queisser calculations[23]. As a consequence, the efficiency of a DSSC with these features is limited to a maximum PCE of 13.4%[24], far from the PCE ≈ 32% expected by Shockley-Queisser theory. While other PV technologies, such as thin-film GaAs- or monocrystalline Si-based devices, for which PCE values as high as 28% and 25%, respectively, have been attained as compared to the maximum ≈ 32% derived from Shockley-Queisser calculations[23], DSSCs still have enough room for improvement. This is the reason why the DSSC is regarded as an emerging technology and further advances are expected to cause a rise in their efficiency around 20%[24]. With that purpose, the strategies employed should focus on extending light-harvesting into the NIR and increasing V_{oc} through reduction of the redox-potential of the electrolyte.

The determination of the electrical parameters of a cell rendering optimal performance through simulation of a lossless device is interesting in order to assess the degree of influence of the processes limiting its real PCE. In that regard, the model allows the estimation of the maximum possible J_{sc} values yielded by the device when illuminated from either the front or the rear side. These resulted from assuming no losses for the processes involved in the generation of the photocurrent, that is, $\eta_{IPCE}(\lambda) = \eta_{LH}(\lambda)$, according to Eq. 2.26. The collection, injection and regeneration efficiencies are considered to be 100% and the calculation of J_{sc}, see Eq. 2.29, solely depends on the productive absorption at the electrode. In this ideal picture, each photon absorbed by the dye contributes to the photocurrent, thus rendering the maximum possible values for J_{sc}.

2.3.3.3 Electron-generation function and light-harvesting efficiency

Herein, details on the modelling of the principal magnitudes defining the performance of a DSSC are provided.

Electron-generation function ($g(z,\lambda)$): In the electrode of a DSSC, a photon is absorbed by a dye molecule, creating a hole-electron pair, which is required for the subsequent generation of a photocurrent.

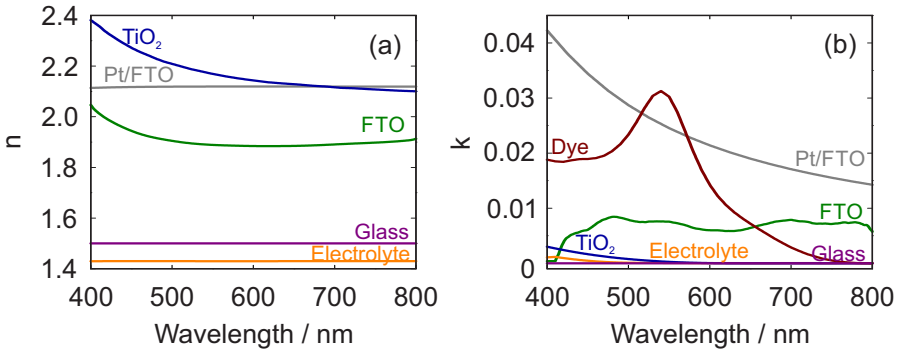

Figure 2.25: Optical constants of the materials provided as input data for the simulation of DSSC devices: (a) Real part of the complex refractive index. (b) Imaginary part of the complex refractive index.

Information regarding the spatial absorption of light along the electrode is given by the electron generation function, g(z,λ), being z the position inside the electrode, defined along the direction of propagation of the incident light, which can present values along the whole electrode thickness. For a non-scattering film,

$$g(z,\lambda) = \alpha_A e^{-\alpha_A z}, \tag{2.33}$$

where α_A is the absorption coefficient, which corresponds to the Lambert-Beer law for an absorbing film (as defined in Sec. 2.3.2.1). However, light scattering affects the absorption of photons along the sensitised film and, consequently, g(z,λ). The electron-generation function is calculated by means of the model presented in Sec. 2.3.2.2, which can account for the photons absorbed throughout the system and thus provide the absorption profile along each of its layers. The cell was modelled as a 3-dimensional multilayer structure comprising a semi-infinite glass substrate coated with a 575-nm thick FTO layer, an 8-μm thick photoanode, a 30-μm thick electrolyte layer, and a 575-nm Pt/FTO film coated on a semi-infinite glass substrate. The spectral complex refractive indices of these materials, displayed in Fig. 2.25, were provided as input data for the calculations. In the simulations, the trajectory of 10^7 photons per wavelength was determined.

Light-harvesting efficiency calculation ($\eta_{LH}(\lambda)$): Integration of g(z,λ) along the thickness of the electrode provides $\eta_{LH}(\lambda)$. Since the

numerical approach depicted in Sec. 2.3.2.2 allows the calculation of the absorption profile by each material at any layer of the structure, it is therefore possible to distinguish between productive and parasitic absorptance, that is, between light absorbed, respectively, by the dye molecules and light absorbed by any other material in the cell, such as the FTO film, the catalytic Pt or the electrolyte, thus allowing an estimation of $\eta_{LH}(\lambda)$.

Incident-Current-to-Photon Efficiency ($\eta_{IPCE}(\lambda)$): Eq. 2.26 indicates that $\eta_{IPCE}(\lambda)$ can be expressed as a product of efficiencies of different processes involved in the generation of the photocurrent from the absorption of photons. For the calculation of $\eta_{IPCE}(\lambda)$, $\eta_{INJ}(\lambda) = \eta_{REG}(\lambda) = 1$ was assumed, that is, lossless electron injection and dye regeneration processes, thus $\eta_{IPCE}(\lambda) = \eta_{LH}(\lambda) \cdot \eta_{COL}(\lambda)$. The integration of optical disorder mainly modifies the absorption of light along the electrode and thus $\eta_{LH})(\lambda)$. However, due to the dependence of $\eta_{COL}(\lambda)$ on g(z,λ), the former is expected to be affected as well. For the calculation of $\eta_{IPCE}(\lambda)$, $\eta_{COL}(\lambda)$ was computed according to

$$\eta_{COL}(\lambda) = \frac{\int_0^L g(z,\lambda) \cdot \frac{cosh(\frac{L-z}{L_e})}{cosh(\frac{L}{L_e})} dz}{\int_0^L g(z,\lambda) dz}, \tag{2.34}$$

where L refers to the thickness of the photoanode and L_e corresponds to an 'effective' electron diffusion length, which accounts for the average distance covered by an electron before undergoing recombination.

Bibliography

[1] Y. J. Kim, M. H. Lee, H. J. Kim, G. Lim, Y. S. Choi, N. Park, K. Kim, and W. I. Lee, "Formation of highly efficient dye-sensitized solar cells by hierarchical pore generation with nanoporous TiO_2 spheres," *Advanced Materials*, vol. 21, pp. 1–6, 2009.

[2] A. Escudero, C. Carrillo-Carrión, M. V. Zyuzin, S. Ashraf, R. Hartmann, N. O. Núñez, M. Ocaña, and W. J. Parak, "Synthesis and functionalization of monodisperse near-ultraviolet and visible excitable multifunctional Eu^{3+},Bi^{3+}:$REVO_4$ nanophosphors for bioimaging and biosensing applications," *Nanoscale*, vol. 8, pp. 12 221–12 236, 2016.

[3] H. Míguez, N. Tétreault, B. Hatton, S. M. Yang, D. Perovic, and G. A. Ozin, "Mechanical stability enhancement by pore size and connectivity control in colloidal crystals by layer-by-layer growth of oxide," *Chemical Communications*, vol. 0, pp. 2736–2737, 2002.

[4] M. E. Calvo, O. S. Sobrado, G. Lozano, and H. Míguez, "Molding with nanoparticle-based one-dimensional photonic crystals: A route to flexible and transferable Bragg mirrors of high dielectric contrast," *Journal of Materials Chemistry*, vol. 19, pp. 3144–3148, 2009.

[5] G. Mie, "Beiträge zur Optik trüber Medien, speziell kolloidaler Metallösungen," *Annalen der Physik*, vol. 330, pp. 377–445, 1908.

[6] C. F. Bohren and D. R. Huffman, *Absorption and scattering of light by small particles*. Wiley, 1983, ISBN: 0-471-05772-X.

[7] I. W. Sudiarta and P. Chylek, "Mie-scattering formalism for spher- ical particles embedded in an absorbing medium," *Journal of the Optical Society of America A*, vol. 18, pp. 1275–1278, 2001.

[8] J. Schäfer, "Implementierung und Anwendung analytischer und numerischer Verfahren zur Lösung der Maxwellgleichungen für die Untersuchung der Lichtausbreitung in biologischem Ge- webe," PhD thesis, Fakultät für Naturwissenschaften, Ulm Universität, Ulm, 2011. [Online]. Available: `https://oparu.uni-ulm.de/xmlui/handle/123456789/1941`.

[9] J. Schäfer, S.-C. Lee, and A. Kienle, "Calculation of the near fields for the scattering of electromagnetic waves by multiple infinite cylinders at perpendicular incidence," *Journal of Quantitative Spectroscopy & Radiative Transfer*, vol. 113, pp. 2113–2123, 2012.

[10] A. L. Aden and M. Kerker, "Scattering of electromagnetic waves from two concentric spheres," *Journal of Applied Physics*, vol. 22, pp. 1242–1246, 1951.

[11] Lumerical Inc., *FDTD Solutions*. [Online]. Available: `https://www.lumerical.com/products/fdtd-solutions/`.

[12] N. Garcia, A. Z. Genack, and A. A. Lisyansky, "Measurement of the transport mean free path of diffusing photons," *Physical Review B*, vol. 46, pp. 475–479, 1992.

[13] J. X. Zhu, D. J. Pine, and D. A. Weitz, "Internal reflection of diffusive light in random media," *Physical Review A*, vol. 44, pp. 3948–3959, 1991.

[14] M. P. van Albada and A. Lagendijk, "Observation of weak localization of light in a random medium," *Physical Review Letters*, vol. 55, pp. 2692–2695, 1985.

[15] P. Wolf and G. Maret, "Weak localization and coherent backscattering of photons in disordered media," *Physical Review Letters*, vol. 55, pp. 2696–2699, 1985.

[16] J. Ferber and J. Luther, "Computer simulations of light scattering and absorption in dye-sensitized solar cells," *Solar Energy Materials & Solar Cells*, vol. 54, pp. 265–275, 1998.

[17] G. Rothenberger, P. Comte, and M. Grätzel, "A contribution to the optical design of dye sensitized nanocrystalline solar cells," *Solar Energy Materials & Solar Cells*, vol. 58, pp. 321–336, 1999.

[18] A. Usami, "Theoretical simulations of optical confinement in dye-sensitized nanocrystalline solar cells," *Solar Energy Materials & Solar Cells*, vol. 64, pp. 73–83, 2000.

[19] F. E. Gálvez, P. R. F. Barnes, J. Halme, and H. Míguez, "Dye sensitized solar cells as optically random photovoltaic media," *Energy & Environmental Science*, vol. 7, pp. 689–697, 2014.

[20] W. Shockley and H. J. Queisser, "Detailed balance limit of efficiency of *p-n* junction solar cells," *Journal of Applied Physics*, vol. 32, pp. 510–519, 1961.

[21] M. A. Green, K. Emery, Y. Hishikawa, W. Warta, and E. D. Dunlop, "Solar cell efficiency tables (Version 38)," *Progress In Photovoltaics: Research and Applications*, vol. 19, pp. 565–572, 2011.

[22] B. E. Hardin, H. J. Snaith, and M. D. McGehee, "The renaissance of dye-sensitized solar cells," *Nature Photonics*, vol. 6, pp. 162–169, 2012.

[23] S. Rühle, "Tabulated values of the Shockley–Queisser limit for single junction solar cells," *Advanced Functional Materials*, vol. 130, pp. 139–147, 2016.

[24] H. J. Snaith, "Estimating the maximum attainable efficiency in dye-sensitized solar cells," *Advanced Functional Materials*, vol. 20, pp. 13–19, 2010.

3 *Mie glasses*: fabrication and characterisation

3.1 Introduction

Liquid media comprising a suspension of spherical particles have drawn special attention due to their interesting optical properties. As long as the concentration of the scattering centres is kept low enough so as to allow neglecting correlation effects, the scattering phenomena and optical properties of these suspensions are well described by Mie theory, that is, taking into account single-particle considerations[1,2]. Such liquid suspensions are especially advantageous for several reasons. In the first place, their generally low refractive index promotes a high dielectric constant contrast between the dispersed phase and the liquid medium, ensuring considerable scattering strength. Furthermore, they accept chromophores, so that light scattering triggered by the presence of particles can result in an enhancement of their absorption, thus also emission, intensity. These features were exploited in the decade of 1990, which led to the development of random lasers[3].

In the case of solids, however, pre-designing the optical response of the disordered medium by means of analytical models has exclusively met with success for photonic glasses, which consist in disordered packings of identical unit blocks[4–6]. As for the remainder, the spectral properties of solid random media generally remain unknown prior to fabrication. Attempts to design the scattering properties of diffusive media for subsequent fabrication have been recently made, such as the case of V. Y. F. Leung *et al.*[7], who analysed light transport in YAG:Ce plates, the most commonly employed material for colour conversion in LEDs, which are known to present significant light scattering.

This chapter introduces a procedure for the fabrication in an uncomplicated and cost-effective manner of films of materials of an optically random medium in a novel configuration, which can be regarded as a solid version of a liquid dilute suspension of spheres. Such configuration features the advantage of enabling a design of its scattering response prior to fabrication according to Mie formalism and was accordingly coined *Mie glass*. In the first place, different combinations of materials in a *Mie glass* configuration are tested in

order to assess their performance as highly scattering media. The results of these calculations enable choosing the most suitable combinations for intense scattering strength, thus defining the materials to be developed and analysed throughout this thesis. After that, the fabrication procedure of each material is depicted, along with a integral characterisation of their optical response, including that of the base transparent matrix when required.

3.2 Analytical study for different material combinations

The presence of disorder in a non-absorbing medium typically causes successive elastic scattering of the light, therefore producing diffuse propagation of the waves. In this thesis, maximisation of the diffusion strength in a controlled manner was sought for, due to its potential regarding the fabrication of optoelectronic devices with enhanced properties.

ℓ_{sc} and ℓ_t serve as a measure of the diffusion ability of a slab of a random material in relation to its thickness. As previously mentioned, in the approximation of independent scattering, Sec. 1.1 in Ch. 1, ℓ_{sc} exclusively depends on σ_{sc} of an individual inclusion embedded in a support material (a porous transparent matrix in this case) and the volume concentration of particles, ρ, embedded in it:

$$\ell_{sc} = \frac{1}{\rho \cdot \sigma_{sc}}. \tag{3.1}$$

At the same time, and as described by Eq. 2.6, σ_{sc} is a function of the size of the inclusions, their refractive index, that of the surrounding medium and, more specifically, their constrast, as well as of the wavelength of the incident light.

The work presented in this thesis proposes the fabrication of solid films of controlled thickness integrating optical disorder in a controlled manner named *Mie glasses*. Specifically, the proposed configuration consists in porous films displaying transparency in the visible range of the spectrum, such as TiO_2 or SiO_2, including a random distribution of monodisperse TiO_2 spheres of size around a few hundred nanometres, that is, of the order of the wavelength of visible light, as

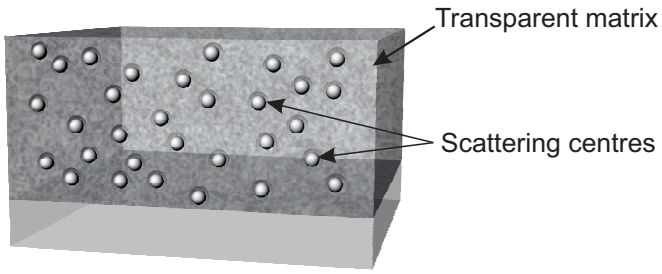

Figure 3.1: Illustration of the structure proposed for the optically random media studied in this thesis.

illustrated in Fig. 3.1. In the first place, identical scattering by each inclusion is ensured due to the monodispersity in size of the inclusions, as well as their well-defined shape. Indeed, the disorder can be easily tuned through the size and volume filling fraction of particles dispersed in the matrix, which enables control over the photonic strength of the resulting film. A spherical shape was preferred for the inclusions, since Mie formalism provides an analytical expression for σ_{sc}, which is essential for the calculation of the optical response of the material. Moreover, a spherical shape can be easily synthesised through standard experimental procedures. However, it is important to highlight that any other shape would have been equally valid for the intended study, as long as the shape would remain identical for all inclusions. In this case, the determination of σ_{sc} would require numerical computational methods, such as Finite-difference time-domain (FDTD) calculations. In the limit of high dillution, correlation terms among inclusions regarding scattering can be neglected and the scattering of light in the material can be described taking into account exclusively single-particle considerations. In fact, for high inclusion density values Eq. 3.1 is not valid, and dependent scattering causes an increase of ℓ_{sc}[8], that is, a reduction of the diffusion strength. A size of the inclusions comparable to the wavelength of the incident light ensures scattering in the Mie scattering range, where σ_{sc} is maximal. This in combination with sufficient refractive index contrast between them and the surrounding medium allows minimisation of ℓ_{sc} for high scattering strength. Furthermore, porosity is imposed in the transparent matrices, which not only helps reducing their refrac-

tive index to increase the contrast with the scattering centres, but also provides them with versatility, since they would accept infiltration with fluorophores, chromophores or polymers that could endow them with further funcionality. A noteworthy advantage of the disordered materials herein proposed is that their fabrication process depends to a great extent on solution-processing methods, which are known to be cost-effective and easily implemented.

Based on the premise that light propagation in the media herein studied could be properly described by Mie formalism, it was employed in order to explore the scattering properties of different combination of materials in the configuration of interest. With this purpose, a series of different available materials susceptible to be synthesised as a colloid in the shape of spherical particles, such as titanium dioxide (TiO_2), silicon dioxide (SiO_2) or void scatterers resulting from the etching of organic spheres embedded in an inorganic matrix, were considered. As for the matrices, only low density media for which a wide number of synthetic routes had been developed, such as mesostructured TiO_2 and SiO_2, were taken into account. The value of σ_{sc} of the scattering inclusions, necessary for the calculation of ℓ_{sc}, were semianalitically obtained through Mie theory. A 50% porosity was assumed for the matrices in the calculations. Figure 3.2 displays the spectral optical constants of the different materials employed in these simulations. Figure 3.3(a) and (b) compare σ_{sc} and ℓ_{sc} values in

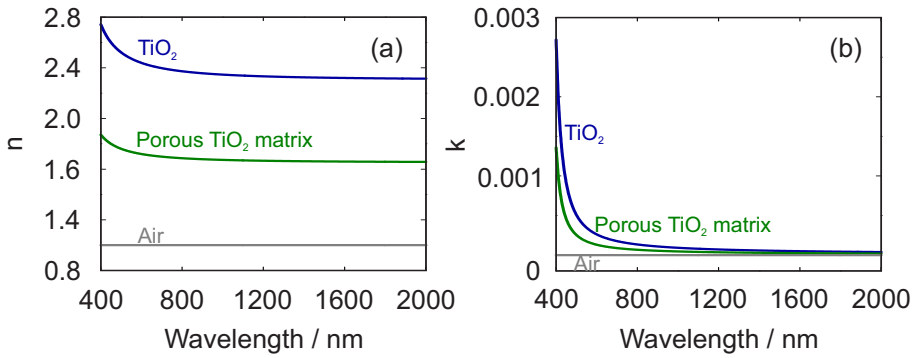

Figure 3.2: Optical constants of the materials considered in the simulations. (a) Real part of the complex refractive index. (b) Imaginary part of the complex refractive index.

relation to the size of the spherical inclusions for a transparent porous TiO_2 matrix integrating crystalline TiO_2 spheres. In these calculations, an air void of thickness th = 0.43r, where r is the radius of the spherical inclusions, surrounding the TiO_2 spheres was considered due to experimental observations, as previously addressed in Sec. 2.1.3.1 of Ch. 2. While bigger scattering structures are responsible for a higher scattering strength for a fixed wavelength, as expected, a similar effect originates from increasing the filling fraction value, which yields a gradual decrease of ℓ_{sc}, according to Mie formalism. The same calculations were performed when considering a SiO_2 matrix, Fig. 3.3 (c) and (d). Although this system did not wholly represent the material depicted below in Sec. 3.4.2 due to a 50% porosity considered herein against the nearly 90% obtained from CVD fabrication, a higher scattering strength, thus, shorter ℓ_{sc} values, could be expected for a higher amount of porosity of the SiO_2 matrix when integrating TiO_2 inclusions due to a reduction of its refractive index. A standard 50% porosity was established in this study for the sake of comparison. Figure 3.3(e) and (f) display the results of the calculations when exchanging the materials of the matrix and that of the scattering centres, which revealed a weakly scattering material. Eventually, Fig. 3.3(g) and (h) display the diffusive behaviour of a mesoporous TiO_2 matrix including spherical air voids. All things considered, within the experimental possibilities and bearing in mind the goal of maximising the scattering strength, *i.e.* minimising ℓ_{sc}, the most interesting media to analyse corresponded to a mesoporous TiO_2 matrix integrating TiO_2 scattering centres and a SiO_2 matrix including TiO_2 spheres. This election was also convenient in terms of subsequent applications and integration into optoelectronic devices. For instance, the matrix of the former case is used as photoanode in DSSCs and, when sensitised with an emitting molecule, it can perform well as a colour-converting material. Along the lines of light emission, the TiO_2 matrix can also be replaced by a luminescent material of similar refractive index and thus be used as a conversion layer presenting the feature of enhanced light extraction due to the presence of scattering centres, which would result beneficial for integration into LEDs. Finally, using a matrix of low refractive index, such as porous SiO_2, would be advantageous in order to boost the diffusive properties of the material when integrat-

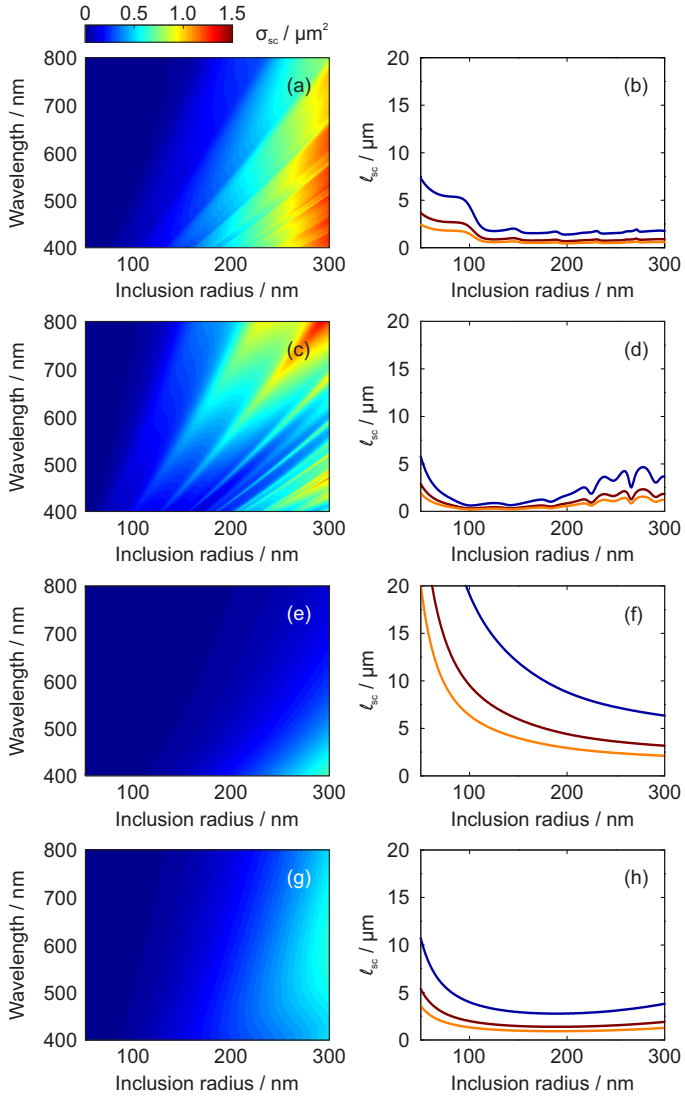

Figure 3.3: (a), (c), (e) and (g) Wavelength-dependent scattering cross section and (b), (d), (f) and (h) spectral ℓ_{sc} values at $\lambda = 530\,\text{nm}$ in relation to the scattering centre size for a system comprising a mesoporous TiO_2 matrix including crystalline TiO_2 spheres surrounded by an air shell as scattering centres, a system comprising a mesoporous SiO_2 matrix including TiO_2 spheres as scattering centres, a system comprising a mesoporous TiO_2 matrix including SiO_2 spheres as scattering centres and a system comprising a mesoporous TiO_2 matrix including spherical air voids as scattering centres, respectively, in a f = 5% (blue), f = 10% (dark red) and f = 15% (orange) concentration.

ing high refractive index particles, thus ensuring intense scattering strength, as desired.

3.3 TiO_2 scattering centres in a TiO_2 matrix

A mesoporous TiO_2 matrix embedding TiO_2 scattering spheres was the first studied case of a *Mie glass*. This section presents an integral optical characterisation of this material. In the first place, the optical response of the material is analysed as a function of the conditions of the disorder included and the possibility of describing light propagation according to Mie formalism is assessed in light of the experimental results. After that, a study of the effects of the finite size of a slab of this material on the eventual optical response based on a combination of experiments and calculations is performed. As a part of this study, photon statistics are analysed in terms of the number of scattering events undergone by the photons. Eventually, the material is sensitised with an absorbing dye and the effect of the inclusion of optical disorder on light absorption by this dye is assessed.

3.3.1 Material fabrication for the experimental study

In light of the results of the calculations, *Mie glasses* presenting different diffusion strength values were prepared. Specifically, two sizes, $r = (95 \pm 20)$ nm and $r = (225 \pm 20)$ nm, and three filling fraction values, $f = 5\%$, $f = 10\%$ and $f = 15\%$, were considered for the inclusions. The materials were fabricated from a viscous paste containing the TiO_2 nanoparticles for the mesoporous matrix, mixed with larger TiO_2 spheres as scattering centres. Films were deposited *via* screen printing, followed by a process of thermal annealing in order to achieve mechanical stability of the film. The different preparation procedures were thoroughly described in Ch. 2. The structure of the resulting material is shown in Fig. 3.4. For this analysis, films of thickness ranging from 2 μm to 12 μm were prepared. Values of film thickness were determined from averaging over those obtained from several SEM images in different areas along the same film.

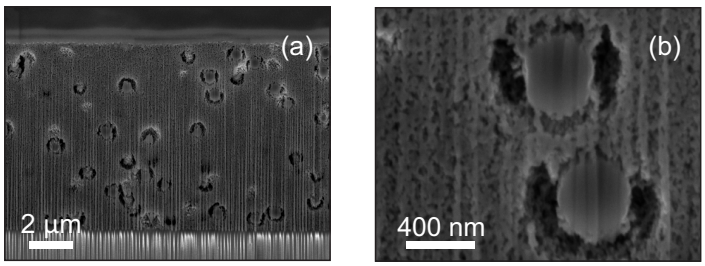

Figure 3.4: (a) FIB-SEM image of a cross section of the system comprising a mesoporous anatase matrix integrating scattering centres consisting in crystalline TiO_2 spheres surrounded by an air shell. (b) Detail of the scattering centre structure.

3.3.2 Analysis of the optical response

This section focuses on performing an integral optical response of the prepared materials and the analysis of the corresponding results.

3.3.2.1 Characterisation of optical disorder

By employing the formalism depicted in Sec. 2.3 of the *Methods* chapter, assessment of the performance of this optically disordered medium as a light diffuser from experimental measurementsit was possible. A spectroscopic analysis of the reflected and transmitted light by a *Mie glass*, Fig. 3.5(a), enabled determination of ℓ_{sc} and ℓ_t. Figure 3.5(b) reveals the variations in the diffusive character of the material for different conditions of the inclusions, illustrated by their transparency, defined by

$$\Sigma = \int_{\lambda_1}^{\lambda_2} T_b(\lambda) d\lambda. \tag{3.2}$$

Here, λ_1 and λ_2 define the integration range, which, in this study corresponds to 400 - 2000nm. Notice that $\Sigma = 1$ corresponds to a situation where no film is present, only air. The following conclusions can be extracted from the data displayed in Fig. 3.5(b):

- Thicker films yield lower transparency, *i.e.* higher opacity.
- Considering the same volume filling fraction, the material becomes more diffusive for an increase of the size of the inclu-

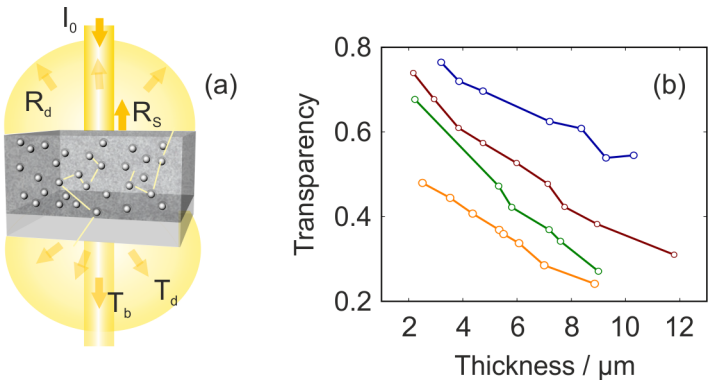

Figure 3.5: (a) Illustration of light propagation throughout the depicted *Mie glass*. (b) Transparency yielded by films of the different studied materials in relation to their thickness. The considered conditions are r = (95 ± 20) nm - f = 5% (blue), r = (225 ± 20) nm - f = 5% (dark red), r = (225 ± 20) nm - f = 10% (green) and r = (225 ± 20) nm - f = 15% (orange). The diameter of the data circles indicates the averaged thickness uncertainty for each condition of the scattering inclusions.

sions, since bigger spheres yield larger σ_{sc} values, as previously observed. This results in shorter ℓ_{sc}.

- For a fixed size of the inclusions, increasing the filling fraction also results in a more diffusive medium.

For the determination of ℓ_{sc} and ℓ_t from experimental measurements, films of various thicknesses were required. According to the formalism depicted in the *Methods* chapter, Sec. 2.3.2.1, an estimation of ℓ_{sc} was possible by analysing the relationship between the measured T_b emerging from the film and its thickness. Data corresponding to T_b and R_s of the films for different conditions of the inclusions are provided in Fig. 3.6. Figure 3.7 shows the thickness dependence of $ln(\frac{T_b}{1-R_s})$ resulting from the measurements in Fig. 3.6 at $\lambda = 800$ nm and $\lambda = 500$ nm. A linear depencence was revealed for the set of data displayed in Fig. 3.7(a). Let us point out that Eq. 2.18 failed to describe light propagation in certain wavelength ranges due to the predominance of other scattering processes blurring the expected behaviour. In that case, Eq. 2.18 does not hold and dependence between $ln(\frac{T_b}{1-R_s})$

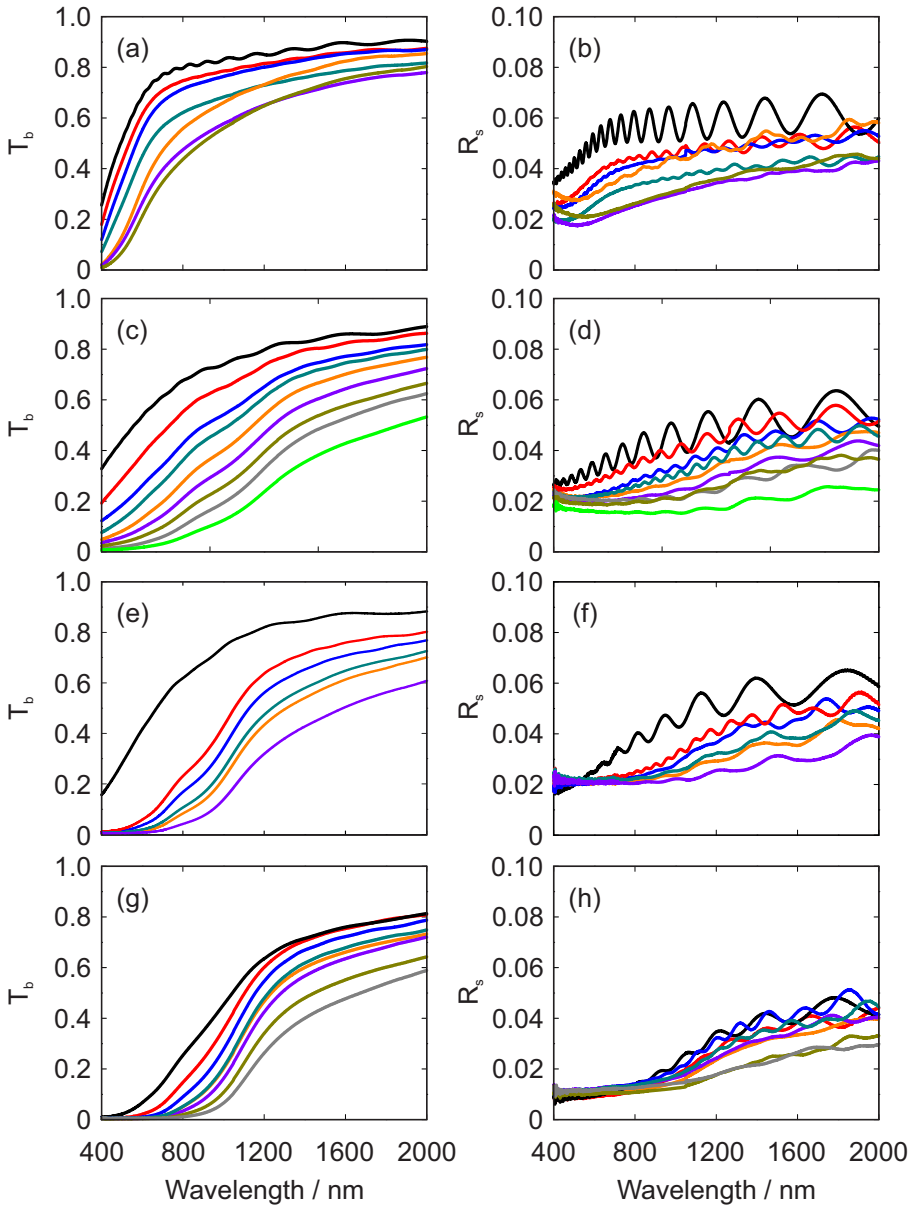

Figure 3.6: Spectral T_b and R_s measurements for films of diverse thicknesses integrating scattering centres in different conditions. (a) T_b and (b) R_s curves for r = (95 $\pm$ 20) nm - f = 5% films, (c) T_b and (d) R_s curves for r = (225 $\pm$ 20) nm - f = 5% films, (e) T_b and (f) R_s curves for r = (225 $\pm$ 20) nm - f = 10% films and (g) T_b and (h) R_s curves for r = (225 $\pm$ 20) nm - f = 15% films.

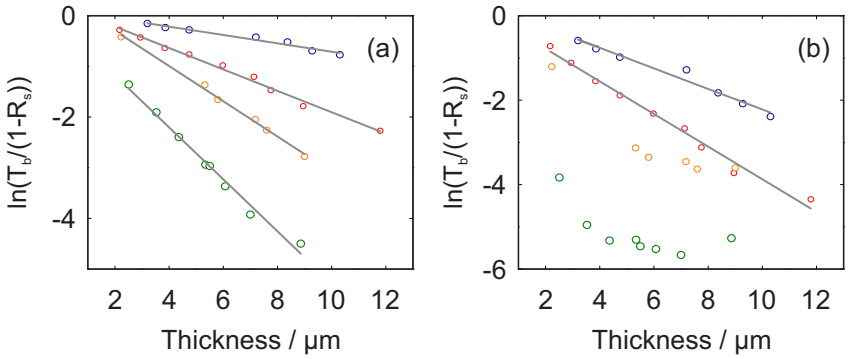

Figure 3.7: Values of $\ln(\frac{T_b}{1-R_s})$ in relation to slab thickness and their corresponding lineal fittings, when possible, for the *Mie glass* under consideration including scattering centres with the conditions r = (95 $\pm$ 20) nm - f = 5% (blue dots), r = (225 $\pm$ 20) nm - f = 5% (red dots), r = (225 $\pm$ 20) nm - f = 10% (orange dots) and r = (225 $\pm$ 20) nm - f = 15% (green dots) at (a) λ = 800 nm and (b) λ = 500 nm.

and slab thickness is not linear for every wavelength, as illustrated in Fig. 3.7(b). Here, whereas a linear behaviour was revealed for the cases r = (95 $\pm$ 20) nm - f = 5% and r = (225 $\pm$ 20) nm - f = 5%, it was no longer possible to obtain a reasonable fitting assuming a linear dependence for the rest of conditions. In order to standardise the procedure, only linear fits yielding a correlation coefficient verifying $r^2 > 0.95$ were considered. Else, extraction of a faithful value of ℓ_{sc} from the experimental data was not possible. The slope of the linear fit allowed extraction of ℓ_{sc} at the considered wavelength, Fig. 3.8(a). As the size or the concentration of the inclusions increased, so did the slope of the resulting linear fit, which was translated into shorter ℓ_{sc} values, in accordance with the theoretical predictions, Fig. 3.8(b). The fair agreement between the curves obtained from the experiments and those resulting from the calculations provided evidence so as to assert that the behaviour of light in this material can be described to a good extent by means of Mie theory, *i.e.* assuming single-particle considerations for the scattering of the light, hence corroborating its behaviour as a *Mie glass*. The possible reasons for the deviation from a linear dependence depicted in Fig. 3.7(b) hindering the determina-

tion of a reliable value of ℓ_{sc} can be classified according to the wavelength range of the deviation:

- Range of long wavelength values: The expected ℓ_{sc} values significantly exceeded the maximum thickness of the films.
- Range of short wavelength values: Due to the wavelength of the light in comparison with the size of the inclusions and their mean separation distance, scattering correlations between them can become relevant enough, so that the single-particle approximation would no longer be accurate at describing the diffusive behaviour of the material.

The angular distribution of the scattered light plays a crucial role on the randomisation of light propagation. In order to gain a better insight into this feature, ℓ_t was studied. Measurements of T, and R_s allowed the determination of ℓ_t, according to the photonic Ohm's law, Eq. 2.23. In this expression, z_p and z_e depend on the polarisation-averaged Fresnel reflectivity, R, see Eq. 2.21 and 2.22, calculated at an imaginary boundary between the disordered medium and the embedding material, which for a mesoporous TiO_2 matrix integrating spherical TiO_2 scattering centres yielded R = 0.07 for f = 5%, R = 0.16

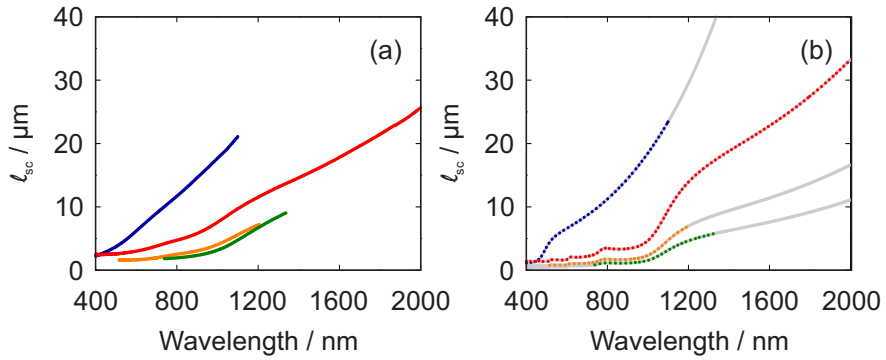

Figure 3.8: Spectral ℓ_{sc} curves obtained for the *Mie glass* under consideration from (a) experimental data and (b) according to Mie formalism. The considered conditions correspond to r = (95 ± 20) nm - f = 5% (blue), r = (225 ± 20) nm - f = 5% (red), r = (225 ± 20) nm - f = 10% (orange) and r = (225 ± 20) nm - f = 15% (green).

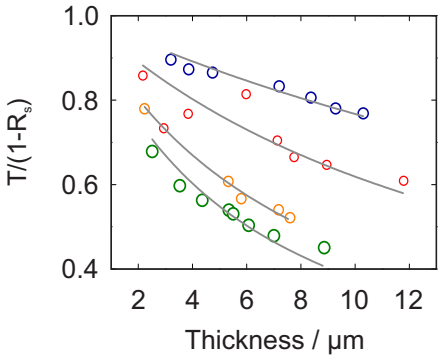

Figure 3.9: Values of $\frac{T}{1-R_s}$ in relation to the slab thickness and their corresponding fittings employing Eq. 2.23 for the *Mie glass* under consideration including scattering centres with the conditions r = (95 ± 20) nm - f = 5% (blue dots), r = (225 ± 20) nm - f = 5% (red dots), r = (225 ± 20) nm - f = 10% (orange dots) and r = (225 ± 20) nm - f = 15% (green dots) at λ = 800 nm.

for f = 10% and R = 0.27 for f = 15%. Along the same lines of the ℓ_{sc} analysis, Fig. 3.9 displays the fittings of the experimental data to Eq. 2.23 at λ = 800 nm. In this case, R_s and T were measured em-

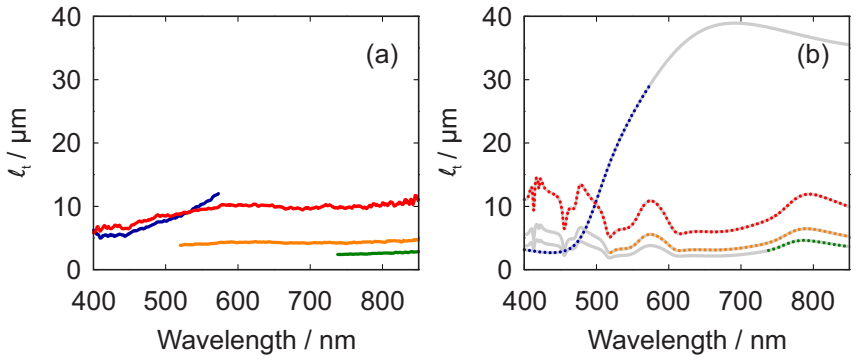

Figure 3.10: Spectral ℓ_t curves obtained for the *Mie glass* under consideration integrating inclusions with different conditions from (a) experimental data and (b) Mie formalism. The considered conditions correspond to r = (95 ± 20) nm - f = 5% (blue), r = (225 ± 20) nm - f = 5% (red), r = (225 ± 20) nm - f = 10% (orange) and r = (225 ± 20) nm - f = 15% (green).

ploying an integrating sphere coupled to a spectrophotometer capable of detecting intensity up to $\lambda = 850$ nm. Figure 3.10(a) displays the ℓ_t curves resulting from these fittings. For the case r = (95 ± 20) nm - f = 5%, ℓ_t yielded larger values than the largest thickness of the fabricated films, L $\sim$ 12 μm, for $\lambda > 575$ nm, therefore not fulfilling the condition L $\gg \ell_t$. In this situation, Eq. 2.23 is unable to describe the propagation of light for $\lambda > 575$ nm and these values have been accordingly not included in the graph. Shorter values of ℓ_t were observed for larger inclusions or concentrations, holding $\ell_t > \ell_{sc}$, as expected for particles yielding non-isotropic light scattering, see Eq. 1.2. Fair agreement was observed when comparing to the spectra derived from Mie formalism, Fig. 3.10(b), in spite of the discrepancies for the case of the material yielding the weakest scattering strength and the unability to reproduce resonant features. The latter was justified by the experimental polydispersity in size of the TiO_2 inclusions. Mie formalism predicts resonances sustained by scattering particles of a well-defined size at specific wavelength values. Nevertheless, when polydispersity is introduced, the size distribution is not sharp enough and the resonant features easily smooth out. Additionally, while each scattering centre was considered to share its geometrical centre with its corresponding surrounding air shell in the model, this was not a faithful reproduction of the real system. As a consequence, discrepancies in the shape of the angular distribution of the scattered light arose, hindering an accurate reproduction of the expected ℓ_t values. Discrepancies were more pronounced in the determination of ℓ_t, as it is a function of ℓ_{sc}, which depends on both, σ_{sc} and the angular distribution of the scattered light, which is apparently highly sensitive to shape deviations of the inclusions. Notwithstanding, the reasonable agreement of the results proves that the optically random medium herein proposed behaves as a solid version of a dilute dispersion of spherical particles, as well as demonstrating the validity of the Mie formalism for the description its angular scattering properties.

3.3.2.2 Finite size effects and photon statistics of light transport in diffusive random media

This section presents a general study based on a combination of experiments with calculations on how the thickness of a finite slab of the

optically random medium under consideration affects the degree of randomisation of light transport, from a regime where ballistic transmittance prevails to the limit where full randomisation is achieved. An analysis on photon statistics in terms of the number of scattering events these photons underwent is also performed.

Analysis of the spectral and angular optical response: In order to study finite size effects on light propagation through this *Mie glass*, the spectral and angular response of three slabs of thickness L = 9 μm characterised by different ℓ_{sc} values were determined. The value of ℓ_{sc} was controlled through the size and concentration of scattering centres. Specifically, the scattering centre conditions of the materials under consideration were r = (95 $\pm$ 20) nm - f = 5%, r = (225 $\pm$ 20) nm - f = 5% and r = (225 $\pm$ 20) nm - f = 10%, which according to Mie formalism yielded ℓ_{sc} of 6.6 μm, 1.7 μm and 1.1 μm, respectively, at λ = 600 nm. Negligible contributions due to absorption by the material were expected at this wavelength. The T_b spectra, as displayed in Fig. 3.11(a), revealed that shorter ℓ_{sc} values caused a decrease of the fraction of light ballistically transmitted, as expected. In particular, a decrease of T_b from 29% to 6% was observed at λ = 600 nm for a change of ℓ_{sc} from 6.6 μm to 1.7 μm, and a 3% T_b was yielded

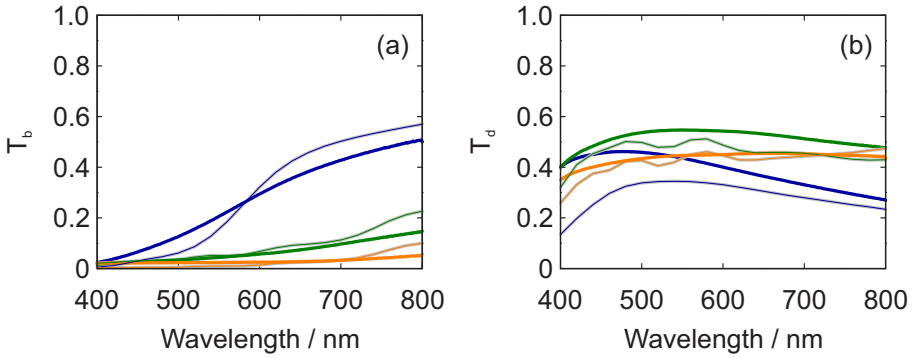

Figure 3.11: (a) Ballistic and (b) diffuse transmittance spectra of 9-μm thick films of the *Mie glass* under consideration for the conditions r = (95 $\pm$ 20) nm - f = 5% (blue), r = (225 $\pm$ 20) nm - f = 10% (green) and r = (225 $\pm$ 20) nm - f = 15% (orange). The spectra corresponding to the simulated systems have been included as thin lines.

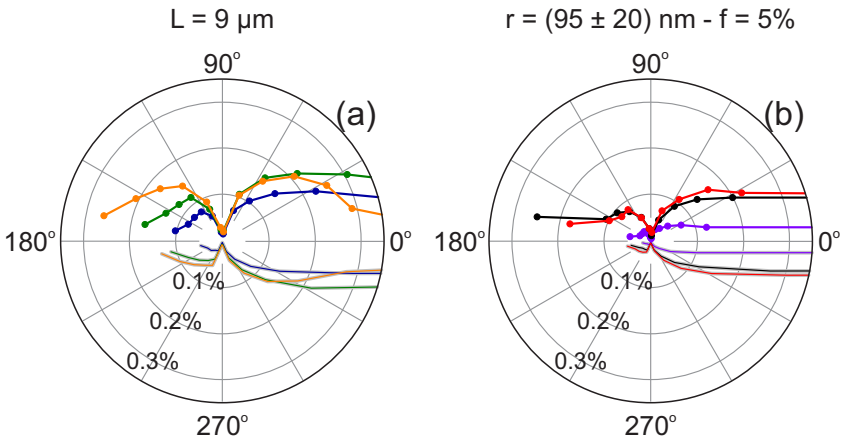

Figure 3.12: Evolution of the angular distribution of the light scattered by films of different characteristics. (a) Variable ℓ_{sc}, namely, 6.6 μm (blue), 1.7 μm (green) and 1.1 μm (orange), respectively corresponding to the conditions r = (95 $\pm$ 20) nm - f = 5%, r = (225 $\pm$ 20) nm - f = 5% and r = (225 $\pm$ 20) nm - f = 10%, for a fixed thickness of L = 9 μm at λ = 600 nm. (b) Fixed ℓ_{sc} = 6.6 μm, corresponding to the condition r = (95 $\pm$ 20) nm - f = 5%, and variable slab thickness, namely, (1.84 $\pm$ 0.07) μm (violet), (6.59 $\pm$ 0.18) μm (black) and (9.3 $\pm$ 0.3) μm (red), at λ = 600 nm. The angular distributions corresponding to the simulated systems were included as thin lines. Calculations consider the conditions r = 115 nm - f = 8%, r = 225 nm - f = 7.5% and r = 225 nm - f = 12%.

for a further reduction of ℓ_{sc} to 1.1 μm. Shorter ℓ_{sc} implies an increase of the scattering strength of the material, resulting in an increase of T_d, Fig. 3.11(b). The size dispersion of the spheres (around 20 nm) was considered in the calculations by averaging the spectra yielded by spheres of sizes within the experimental dispersion range. The angular distribution of the scattered light at λ = 600 nm was measured, Fig. 3.12(a). A shortening of ℓ_{sc} modifies the pattern of the angular distributions by causing an angular broadening of both, the transmitted and reflected intensity. A larger number of scattering events led to a higher fraction of light diffusively propagated and, as a consequence, the angular pattern approached the distribution of a Lambertian emitter as the diffusive strength of the material gradually increased. The effect of a variation of L was inspected for the material with scattering

centre conditions of r = (95 ± 20) - f = 5%, corresponding to $\ell_{sc} = 6.6$ μm, an intermediate value in relation to the available thickness range. The angular distributions in Fig. 3.12(b) displayed a similar trend in terms of the evolution of the angular patterns, evidencing that an increase of the scattering strength was equivalent to an increase of the slab thickness, as the average number of scattering events escalated in both cases. The corresponding theoretical spectra and angular distributions, calculated according to the approach detailed in Sec. 2.3.2.2 of Ch. 2, were included in Fig. 3.11 and 3.12 for the sake of comparison. Size and filling fraction values of the simulated systems were chosen within the experimental uncertainty regarding the nominal experimental values. The simulated systems included a 100-nm thick film of intermediate refractive index between that of the air and the porous TiO_2, that is, n = 1.35, on top of the *Mie glass* in order to account for the slightly inhomogeneous nature of the interface, which would result in an increased in-coupling of the light into the system. The spectra and angular distributions calculated employing the model confirmed the trends experimentally observed, thus demonstrating its reliability and proving its ability to predict light propagation in the considered material without accounting for phase correlation effects, that is, the total scattering was described as a series of successive individual scattering events as dictated by Mie theory. Based on this agreement, the model was hereinafter applied in order to inspect the origin of the angular distribution of light yielded by slabs of the *Mie glass* depending of their thickness in relation to their scattering strength.

Scattered photon statistics: This section presents an analysis of the shape of the angular distribution of the light after interacting with slabs of different thicknesses of the *Mie glass* under study in terms of the distribution of scattering events that light undergoes. The structural parameters considered in the simulated film correspond to r = 225 nm - f = 12%, for which $\ell_{sc} = 0.7$ μm and $\ell_t = 3.0$ μm at $\lambda = 600$ nm according to Mie formalism. The value of ℓ_t was also extracted from applying Eq. 2.23 to the results of T and R_s for different slab thicknesses yielded by theoretical experiments employing the model. This procedure provided a value of $\ell_t = 3.7$ μm, which roughly agreed with the $\ell_t = 3.0$ μm derived from Mie theory. Light is expected to reach

full diffusive propagation for $L \gg \ell_t$. For that reason, the values of L for the simulated films ranged from $L = \ell_t$ up to $L = 7\ell_t$ (corresponding to $30\ell_{sc}$), which covered thickness values from a point where the optical response should be strongly determined by the finite size of the slab to displaying the typical features of a fully developed random 'bulk' material. If thickness was short, *e.g.* $L = \ell_t$, light only underwent a few scattering events during propagation and a small fraction of light deviated from the incidence direction, thus resulting in an angular distribution displaying a strong ballistic component. In effect, in this case, around 24% of the incident light was transmitted ballistically, as shown in Fig. 3.13(a). As Fig. 3.13(b) revealed, in a

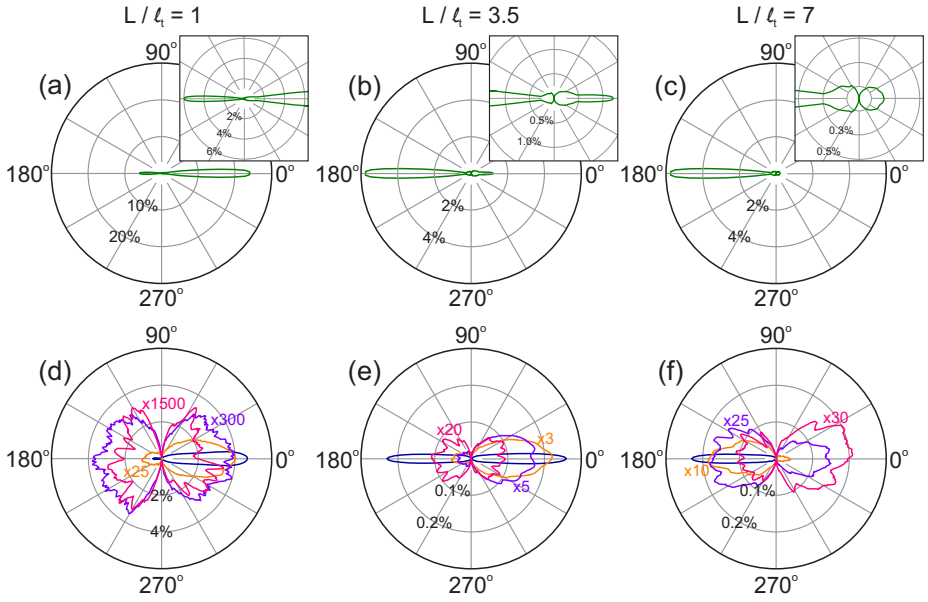

Figure 3.13: Evolution with thickness of the angular distribution of the light scattered by a simulated slab with the conditions r = 225 nm - f = 12%. (a)-(c) Total angular distribution for slabs of thickness $L = \ell_t$, $L = 3.5\ell_t$ and $L = 7\ell_t$, respectively. The insets show a zoom-in of the respective angular distributions for a better visualisation of the shape. (d)-(f) Angular distribution of photons undergoing s = 1 (blue), s = 3 (orange), s = 5 (violet) and s = 10 (pink) scattering events in slabs of thickness $L = \ell_t$, $L = 3.5\ell_t$ and $L = 7\ell_t$, respectively. The calculations were performed at $\lambda = 600$ nm.

thicker slab, L = 3.5ℓ_t (equivalent to L = 15ℓ_{sc}), light was given the possibility to be scattered a larger number of times, thus resulting in a higher fraction of diffuse light at the expense of T_b, which was reduced to an exiguous 1.2%. As a consequence of the pronunciated decrease of total transmittance, the film should display a whitish opacity typical of an optically random material. Moreover, in contrast to the slab of thickness L = ℓ_t, the angular pattern of the light yielded by a film of thickness L = 3.5ℓ_t presented a fairly isotropic shape, resembling that of a Lambertian diffuser, due to the important fraction of light propagating diffusively. Eventually, for film thicknesses significantly larger than ℓ_t, for instance L = 7ℓ_t (corresponding to 30ℓ_{sc}), light underwent numberless scattering events, which hampered transmittance and, as a consequence, most of the incident light was diffusively reflected, resulting in high opacity of the film, as illustrated in Fig. 3.13(c). Furthermore, the perfectly Lambertian profile of the transmitted intensity indicates full randomisation of the light. While T_b is largely affected by the irregular variations of the refractive index throughout the material, under the assumptions considered herein and in good agreement with the measurements, the value of R_s is dictated to a great extent by the refractive index contrast between that of the *Mie glass* and the surrounding medium, air in this case. This became evident when inspecting the evolution of R_s for increasing thickness of the slab, namely, 5.5%, 5.3% and 5.3% for L = ℓ_t, L = 3.5ℓ_t and L = 7ℓ_t, respectively, as shown in Fig. 3.14. For short enough

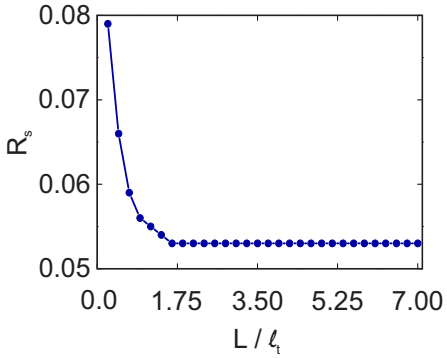

Figure 3.14: Evolution of R_s for simulated slabs of the system under consideration for increasing value of L/ℓ_t.

values of L, where the probability of photons undergoing a scattering event is low, a fraction of the incident photons can be reflected at the second interface of the slab, travel back throughout the material and escape in the backward direction without undergoing any further scattering, thus contributing to R_s. As thickness is increased, the probability of a photon crossing the material slab twice avoiding scattering by an inclusion is reduced, therefore causing a decrease of R_s up to a critical thickness, above which no contribution from unscattered photons reflected at the back interface is possible. At this point, the value of R_s stabilised at 5.3%, which was independent on L. This point is discussed again below when inspecting the angular distributions described by the fraction of light undergoing a specific number of scattering events. The angular distributions in Fig. 3.13(a)-(c) can be understood as a sum of the individual angular patterns described by each fraction of light undergoing a specific number of scattering events. Indeed, Fig. 3.13(d)-(f) illustrate particular cases for the three slab thicknesses under consideration. Even though by definition any phenomenon removing photons from the incident beam would be regarded as a scattering event, photons specularly reflected at any of the slab interfaces were considered as non-scattered light. Indeed, in the model only modifications of the trajectory of the photons originated from interaction with the spherical inclusions were considered scattering events. Comparison between Fig. 3.13(d) and (a) evinced that the total angular distribution for a slab of $L = \ell_t$ was mainly defined by those photons scattered once. Photons scattered once preserved to a great extent the forward-oriented angular distribution typical of Mie scattering. In contrast, owing to the low probability of undergoing a higher number of scattering events across such thickness, the contribution of higher order distributions played a small part in the total intensity. This was evidenced by the high magnifications required in Fig. 3.13(d) for the visualisation of distributions of photons scattered above once. For a thicker slab, *e.g.* $L = 3.5\ell_t$ the contribution of light undergoing more than one scattering event to the intensity of the total angular distribution started becoming relevant, as pointed out by the lower magnifications required in Fig. 3.13(e) in comparison to those previously observed for the case $L = \ell_t$. For such thickness, not only was there substantial probability that photons were scattered 3 and 5 times, but the slab was still thin enough for these photons to reach

the opposite interface and exit the system as transmitted light, thus resulting in an important strong forward component of these higher-order distributions. Figure 3.13(e) reveals a virtually equal probability of photons scattered once to exit the slab either in the forward or backward direction. Whereas photons undergoing one scattering events can easily reach the opposite interface without further scattering in thin slabs, as thickness of the slab increases, the probability of photons scattered once exiting the slab as transmitted light without being scattered again significantly drops, thus becoming comparable to the fraction of light scattered in the backward direction after one scattering event (given by Mie theory), justifying the observation in Fig. 3.13(e). Eventually, if thickness becomes large enough, as in the case of $L = 7\ell_t$, photons undergoing one scattering event could exclusively be collected in the backward direction, since the large thickness prevented light scattered in the forward direction from reaching the opposite interface and exit the slab in transmission before undergoing further scattering events, as evidenced by Fig. 3.13(f). Here, the angular distribution described by photons scattered 3 times still displays a pattern mostly determined by reflected light, thus revealing the prevalence of photons scattered in the backward direction. The relative contribution of photons scattered a larger number of times to the total angular distribution decreased slowly with respect to the cases of shorter thicknesses previously inspected, which was evidenced by the similar magnification required for the visualisation of the angular patterns corresponding to light scattered 5 and 10 times. For this reason, the small fraction of transmitted intensity was expected to be fully randomised.

The histograms in Fig. 3.15, which illustrate the fraction of light collected after being scattered by the slab as a function of the number of undergone scattering events, provided a further analysis of the trends for the three thicknesses previously inspected. For each slab, a most likely scattering event number was expected, which increased as L became larger, as the histograms show. Whereas for short thicknesses the probability of light being scattered more than once was reasonably low and most of the photons exited the material either specularly reflected or ballistically transmitted or after undergoing one scattering event, Fig. 3.15(a), a dramatic rise in the number of photons scattered above once at the expense of T_b was observed if L

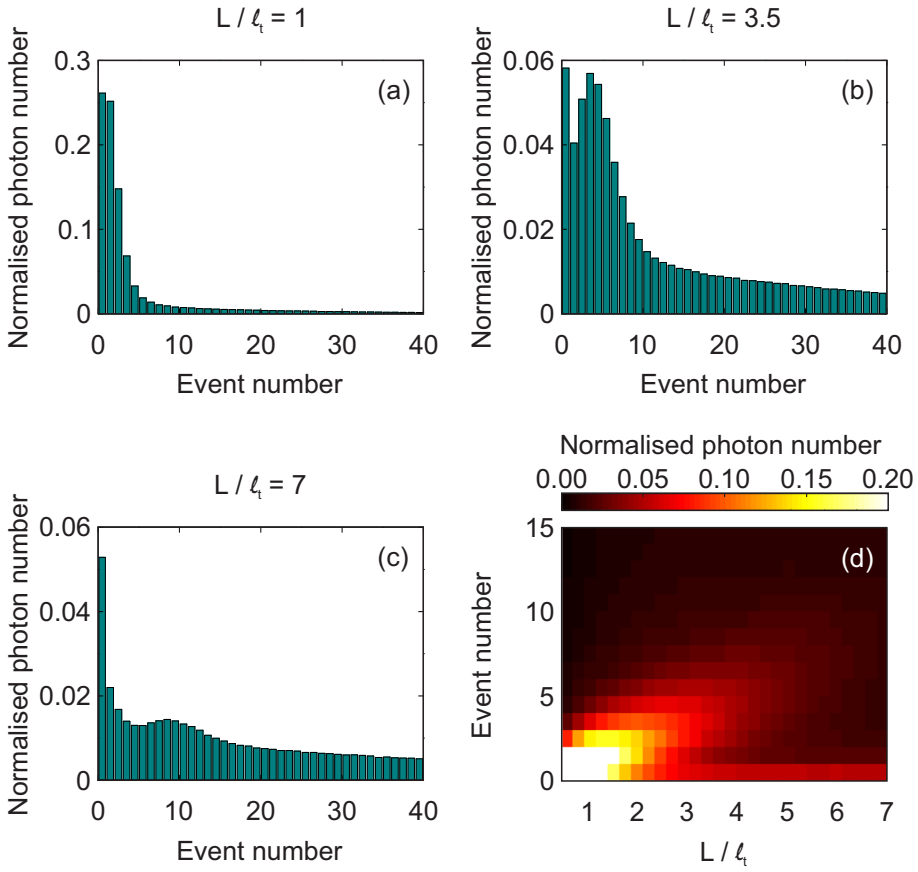

Figure 3.15: (a)-(c) Histograms of the fraction of scattered photons in relation to the number of scattering events they underwent at λ = 600 nm for slabs of thickness L = ℓ_t, L = 3.5ℓ_t and L = 7ℓ_t of the considered system. (d) Fraction of the scattered photons in relation to the number of scattering events they underwent at $\lambda = 600$ nm as a function of the thickness of the slab of the system under consideration in units of ℓ_t.

increased, as displayed in Fig. 3.15(b) for L = 3.5ℓ_t. For large enough thickness, such as L = 7ℓ_t, Fig. 3.15(c), when the slab was expected to behave as a perfect diffuser, the amount of photons undergoing the most likely number of scattering events significantly dropped, consequence of a distribution of the light among photons scattered a higher number of times. T_d could be therefore expected to become progres-

sively larger as the value of L/ℓ_t increased. The probability curve defined by the histogram flattened as the thickness of the slab increased, as visible in Fig. 3.15(d), where the evolution of the most likely scattering event number is perceptible.

3.3.2.3 Effects of optical disorder on the absorption of light

In order to evaluate the effects of randomly distributing scattering particles in a mesoporous anatase matrix on the absorption of light by a chromophore adsorbed to the film, several slabs were fabricated with different scattering centre conditions and sensitised with N719, a dye widely employed for the sensitisation of DSSCs, for absorption variation assessment. Particularly, with the purpose of evaluating the influence of both parameters, inclusion size and filling fraction, two sets of samples were considered: one with a fixed inclusion size of r = (100 $\pm$ 15) nm and volume filling fraction values ranging from 5% to 15%, and one with a fixed filling fraction f = 10% and inclusion size in the range 100 - 200 nm. With the idea of integrating this *Mie glass* as electrode into DSSCs, the films were deposited on top of an FTO-coated glass. In this way, evaluation of the optical response of this system allowed consideration of the possible contribution of the conductive FTO layer to the absorption of the photoanode. The SEM cross section images in Fig. 3.16(a) and (b) show the resulting structure of these photoanodes integrating scattering centres with different sizes. Figure 3.17(a) and (c) show the absorptance spectra measured for

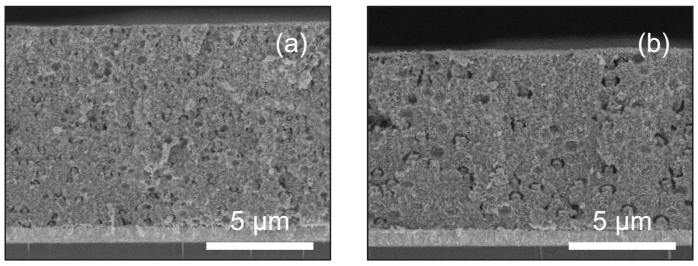

Figure 3.16: SEM cross section images of *Mie glass*-based electrodes for integration into DSSCs including spherical TiO_2 scattering centres of size (a) r = (100 $\pm$ 15) nm and (b) r = (200 $\pm$ 25) nm in a 10% volume filling fraction.

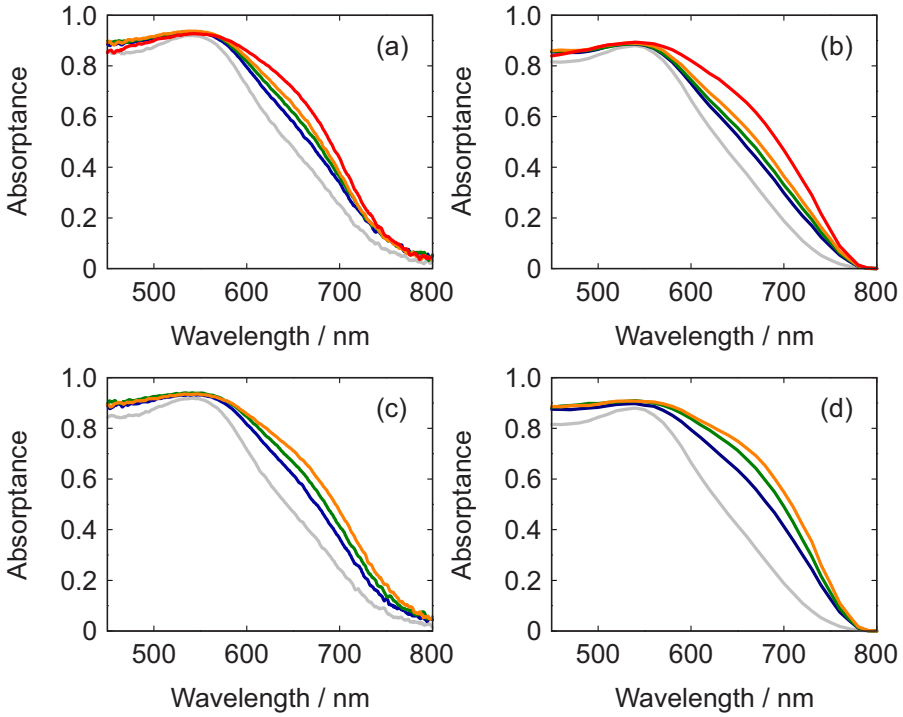

Figure 3.17: Absorptance enhancement of the system glass/FTO/*Mie glass* sensitised with dye owing to the inclusion of scattering centres. (a) Experimental and (b) theoretical absorptance spectra for films integrating scattering centres of size r = (100 ± 15) nm and filling fraction values f = 5% (blue line), f = 10% (green line), f = 15% (orange line) and f = 20% (red line). For the calculations in (b), r = 80 nm has been considered as scattering centre size for the sake of the best agreement. (c) Experimental and (d) theoretical absorptance spectra for films including scattering centres of size r = (100 ± 15) nm (blue line), r = (135 ± 15) nm (green line) and r = (200 ± 15) nm (orange line) in a filling fraction f = 10%. Spectral absorptance curve for a reference film has been included for comparison (gray line). 8-μm thick electrodes have been considered in all the cases.

both sets of samples when illuminating from the rear side, *i.e.* light impinges directly on the *Mie glass*. A broadband enhancement of the absorptance was evident for both cases in the wavelength range from 600 nm up to *ca.* 750 nm and it was revealed more intense with higher

values of any of both tested parameters. The absorptance spectrum of a reference film devoid of scattering centres has been included for the sake of comparison. This proved that, not only resulted the sole integration of this type of scattering centres beneficial for light absorption in this transparent matrix, but also such enhancement could be controlled by means of their size and concentration. The corresponding calculated absorptance spectra are displayed in Fig. 3.17(b) and (d), which show an excellent agreement with the measured spectra. The results were consistent with the relation between the scattering centre conditions and the ℓ_{sc} spectra previously analysed in Fig. 3.8. According to the ℓ_{sc} spectra, the increase of any of both parameters defining the conditions of the scattering centres yield shorter ℓ_{sc} values. As a consequence, the path length of the light inside the material is significantly enlarged and, when sensitised with an absorbing dye, it leads to a higher probability of photons being absorbed, equivalent to an increase of the absorption cross section of the dye molecules.

This analysis demonstrated therefore the efficacy of optical disorder as a tool to controllably boost the absorptance of dye molecules infiltrated in the pores of a mesoporous TiO_2 matrix. This result entails important implications when aiming at solar cell implementation, as later on inspected in Ch. 4.

3.4 TiO_2 scattering centres in a low refractive index matrix

In this section, the procedure for the fabrication, design and analysis of the optical response of a *Mie glass* of high photonic strength are described. The reason for such highly diffusive character resides in the transparent matrix supporting the scattering centres, consisting in a highly porous SiO_2 film of ultralow refractive index, which, in contrast to the spherical TiO_2 inclusions, yields a high refractive index contrast. The term ultralow is hereinafter applied to describe the low value of the refractive index of the fabricated transparent film within the terminology of the field, where refractive indices below 1.2 are usually designated as 'ultralow'[9–13]. The realisation of this *Mie glass* required the development of a procedure for the fabrication of ultralow refractive index SiO_2 films. The first part of this section is

devoted to the preparation, characterisation and study of the optical properties of these highly porous SiO_2 films, for which the possibility of tuning the resulting refractive index through the experimental parameters is demonstrated. After that, the controlled inclusion of optical disorder for the fabrication of a *Mie glass* is addressed, along with a characterisation of their optical response and inspection of their optical properties in relation to the conditions of the disorder included.

3.4.1 Ultralow refractive index films

A combination of solution-processing methods with a step of CVD enabled the fabrication of wide-area, highly transparent films of ultralow refractive index consisting in a SiO_2 with a high degree of porosity.

The material was fabricated from films of PS spheres, as depicted in the *Methods* chapter, which were subjected to a process of CVD consisting in sequential infiltration with $SiCl_4$ and H_2O in vapour phase, as described in Sec. 2.1.3.2 in Ch. 2, completing in that way one infiltration cycle. As a result of the reaction of $SiCl_4$ with H_2O throughout the PS scaffold, a SiO_2 network was formed from partial filling of the voids among the PS spherical particles, see Fig. 3.18(a). Additional infiltration cycles enabled further filling of the pores. Eventually, the PS scaffold was removed through a thermal procedure consisting in heating of the samples up to 500^oC for 2 hours, while mantaining the SiO_2 structure, resulting in a around 2 x 2-cm^2 highly porous SiO_2 network forming a film, as represented in the drawing in Fig. 3.18(b). The eventual structure is shown in the SEM images in Fig. 3.19(a) and (b), which display the high porosity of the material. Films of this material presented a high degree of transparency in the visible range of the spectrum, as shown in Fig. 3.19(c), evidenced by the low fraction of light diffusively propagated.

As previously mentioned, the value of R_s of a film is generally dictated by the refractive index constrast between that of the film and the surrounding medium, air in this case. As a consequence, the R_s spectra of the films were used to monitor variations of the refractive index of the films depending on the experimental conditions. Specifically, the study focused on inspecting the influence of different degrees of void filling with SiO_2 of the PS-based films, as a consequence of an

increase of the number of infiltration cycles, on the average refractive index of the eventual structure. The main aim of this analysis was not only the determination of the spectral refractive index of the fabricated films, but also inspect the possibility of experimentally tuning their value during the preparation process. The results corresponding to this study are shown in Fig. 3.20. Figure 3.20(a) displays the measured R_s for the prepared films, along with that for a glass substrate for the sake of comparison. The spectra revealed a reduction of R_s for increasing number of infiltration cycles. Such decrease was attributed to a higher amount of SiO_2 constituting the film, a consequence of increasing the number of infiltration cycles, which would reasonably result in higher refractive index values. At first glance, Fig. 3.20(a) clearly revealed an anti-reflective character of the fabricated films when comparing to the reference R_s spectrum of a glass, being more pronounced for increasing number of infiltration cycles within the range under consideration. As a matter of fact, calculations

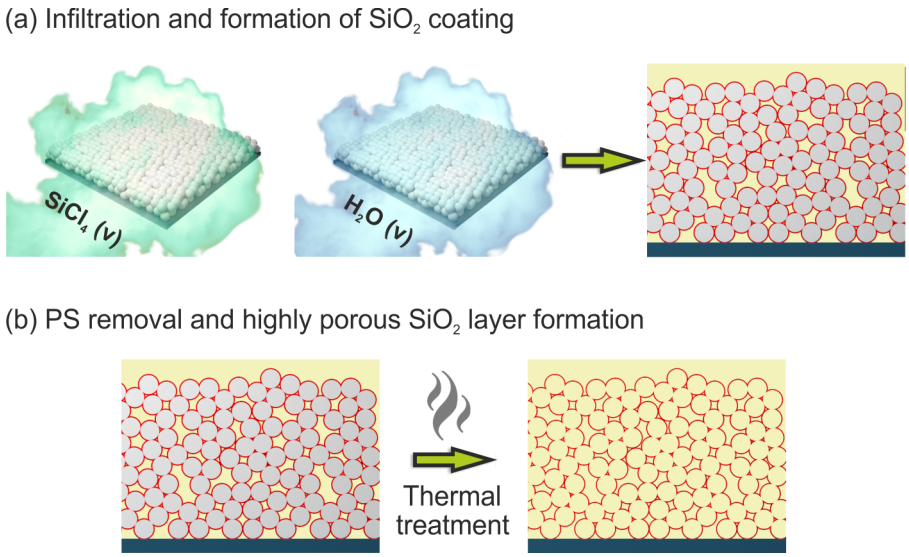

Figure 3.18: Fabrication process of a ultralow refractive index film. (a) Sequential infiltration of the PS scaffold through CVD and partial filling of the voids with SiO_2. (b) Removal of the PS scaffold and formation of a film consisting in a porous SiO_2 network. The coating in red represents the SiO_2.

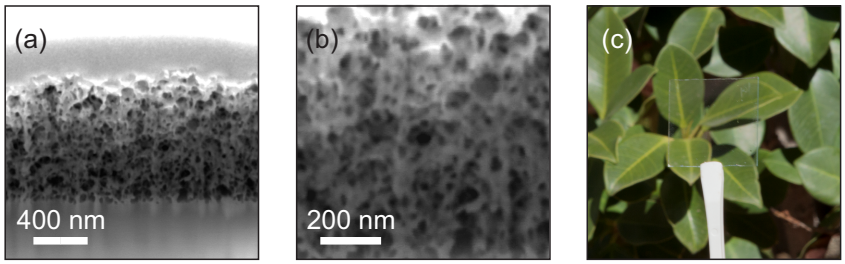

Figure 3.19: (a) SEM cross section image of the film prepared as described, consisting in a highly porous SiO_2 network. (b) Zoom-in of the film, displaying the highly porous nature of the material. (c) Picture of the prepared film on a glass substrate displaying high transparency.

demonstrated a reduction of the average R_s of the film before reaching a minimum value as its average refractive index grew, as displayed in Fig. 3.21. Specifically, the calculations considered in a first approximation a wavelength-independent refractive index for the materials and the values of R_s correspond to spectra averaged within the wavelength range 400 - 800 nm. The considered films were simulated and their spectral R_s determined, Fig. 3.20(b), employing for that purpose the refractive index spectra extracted from experimental measurements, Fig. 3.20(c). For the extraction of the refractive index, measurements of R_s and T_b for three different incidence angles and both polarisation states, *s* and *p*, were fitted to those calculated by means of the transfer-matrix method employing a genetic algorithm, designed to find the required complex refractive index providing the best fitting according to a designated model. Here, the Cauchy Absorbent model was considered. The trend experimentally observed for the R_s spectra was faithfully reproduced by the calculations, thus displaying good agreement between measurements and theory. As anticipated, Fig. 3.20(c) demonstrated that the refractive index of the resulting films was directly affected by the number of infiltration cycles performed *via* CVD. Indeed, the value of the refractive index increased for a higher number of infiltration cycles, as expected. Specifically, a nominal refractive index as low as $n = 1.03$ at $\lambda = 600$ nm was achieved for the film subjected to one infiltration cycle. This analysis demonstrated that, not only the proposed experimental procedure enabled

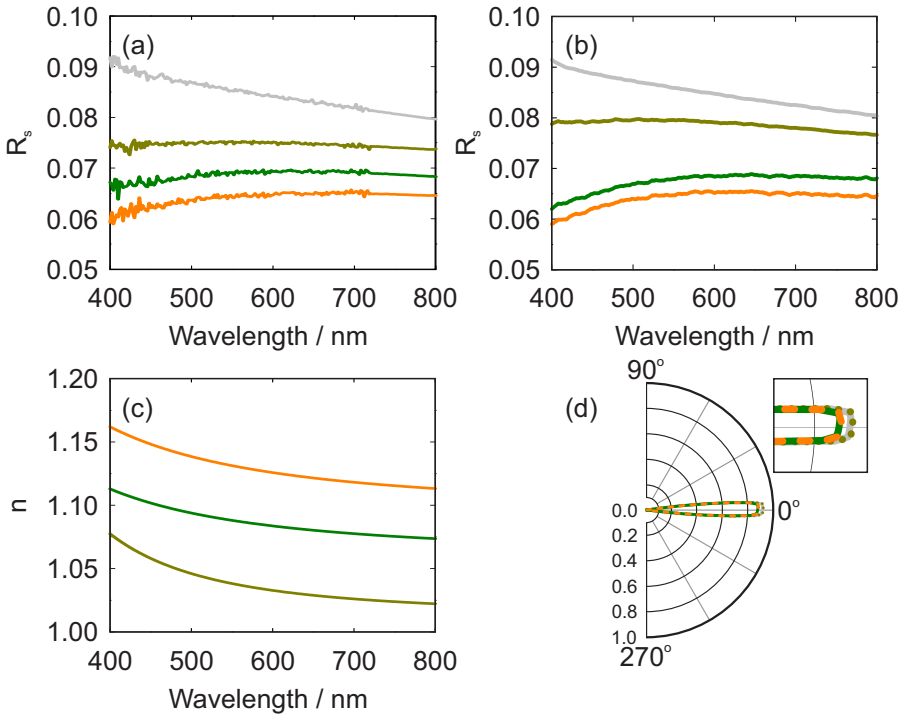

Figure 3.20: Optical characterisation of the fabricated films. (a) Experimental and (b) calculated R_s spectra for a glass substrate (gray line) and a glass substrated coated with a highly porous SiO_2 film fabricated through one (dark-yellow line), two (green line) and three (orange line) CVD infiltration cycles. (c) Spectral refractive indices extracted from R_s and T_b measurements for the films fabricated with one (dark-yellow line), two (green line) and three (orange line) CVD infiltration cycles. (d) Angular distribution of the light transmitted through a glass substrate (gray line) and a glass substrate coated with a highly porous SiO_2 film prepared through one (dark-yellow line), two (green line) and three (orange line) CVD infiltration cycles at λ = 575 nm.

the preparation of wide-area and highly transparent films of ultralow refractive index, but it also allowed control over its optical properties. A porosity of p = 0.9 could be estimated for the film subjected to one infiltration cycle according to the Lorentz-Lorenz expression considering an average refractive index of n_1 = 1.05 for the SiO_2-network

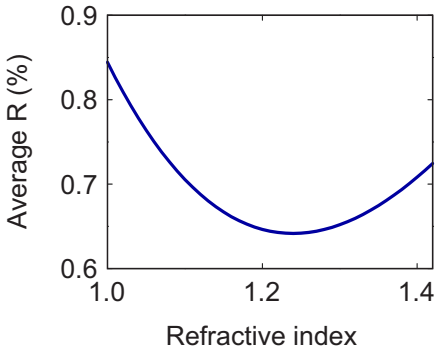

Figure 3.21: Calculated average R_s as a function of the refractive index of the SiO_2 film.

film and taking $n_2 = 1.425$ for SiO_2:

$$p = 1 - \frac{n_1^2 - 1}{n_2^2 - 1}. \tag{3.3}$$

From the high transparency observed in Fig. 3.19(b), the scattering strength of the films was expected to be negligible, which was confirmed by measurement of the angular patterns of the light scattered by the films, Fig. 3.20(d). The largely forward-oriented profiles of the angular distributions indicated that most of the transmitted light propagated ballistically, revealing a virtually inexistent diffuse propagation as a consequence of a lack of significant scattering. Indeed, the angular distributions of the films were highly similar to that for a bare glass substrate, which demonstrated a high degree of transparency.

3.4.2 Scattering properties of an optically random material based on a low refractive index film

After the development of ultralow refractive index films, the next step in the fabrication of an optically random medium of high diffusive strength consisted in the inclusion of high refractive index scattering particles, namely, monodisperse nanocrystalline TiO_2 spheres. The fabrication procedure allowed the inclusion of scattering particles in the eventual film by dispersing them in the initial suspension of PS spheres, calculated according to Eq. 2.1. The amount of TiO_2 in relation to the volume of PS spheres approximately defined the volume

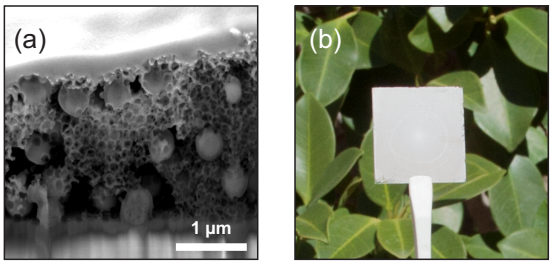

Figure 3.22: (a) SEM cross section image of the fabricated optically disordered medium consisting of a highly porous SiO_2 film integrating a random distribution of crystalline TiO_2 spheres of size r = (225 $\pm$ 20) nm in a 5% concentration. (b) Picture of the material exhibiting high opacity.

filling fraction of scattering centres in the eventual film. Due to experimental limitations, a volume filling fraction f = 5% was considered in the study herein performed. Suspensions prepared for f > 5% were not suitable for the fabrication of films with good optical quality due to inhomogeneities arising during the deposition process. The image shown in Fig. 3.22(a) reveals the desired structural properties of the resulting material, namely, a random distribution of monodisperse spherical TiO_2 particles in a SiO_2 matrix of high porosity forming a film. Due to the presence of TiO_2 particles, intense light scattering was triggered in the film, therefore adopting a white appearance and high opacity typical of turbid media, as visible in Fig. 3.22(b).

The opacity of the resulting material was evidenced by the determination of the T_b spectra, Fig. 3.23, which revealed a considerable reduction when compared to the T_b spectrum of the initial low refractive index SiO_2 film. Following the same procedure previously employed in Sec. 3.3.2.1 for the characterisation of the disorder, the spectral ℓ_{sc} were determined from R_s and T_b measurements of films integrating optical disorder with different conditions, namely, different sizes of the scattering centres in a 5% concentration, as visible in Fig. 3.24(a), and the corresponding spectra calculated through Mie theory, Fig. 3.24(b). A porosity p = 0.9 was considered for the SiO_2 matrix of the simulated films according to Eq. 3.3. Smaller inclusions yielded shorter values of ℓ_{sc}, as opposed to the trend exhibited by the *Mie glass* based on a mesoporous TiO_2 matrix previously discussed in

Sec. 3.3.2.1, for which bigger scattering centres were required to minimise ℓ_{sc}. In order to understand this, it was necessary to analyse ℓ_{sc}

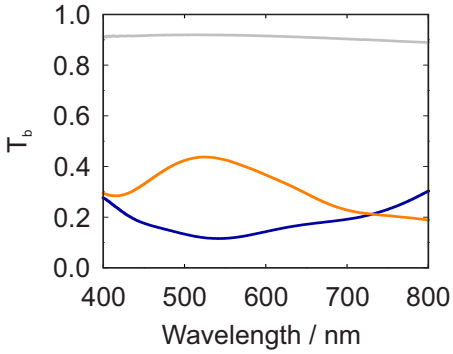

Figure 3.23: T_b spectra for a *Mie glass* consisting of a highly porous SiO_2 film integrating nanocrystalline spherical TiO_2 particles of size r = (146 ± 15) nm (blue line) and r = (250 ± 30) nm (orange line) in a 5% concentration. The spectrum corresponding to a ultralow refractive index SiO_2-based film before the inclusion of scattering centres have been included (gray line) for comparison.

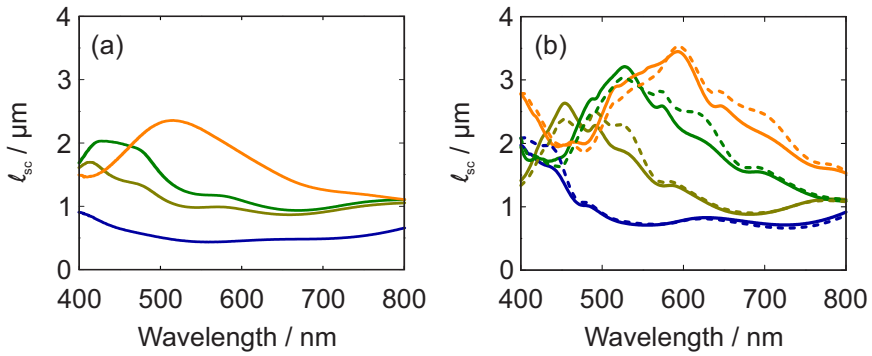

Figure 3.24: ℓ_{sc} spectra extracted from (a) measurements and (b) calculations for a *Mie glass* comprising a low refractive index SiO_2 film including a random distribution of nanocrystalline TiO_2 spheres of size r = (146 ± 15) nm (blue line), r = (188 ± 15) nm (dark yellow line), r = (225 ± 20) nm (green line) and r = (250 ± 30) nm (orange line) in a f = 5% concentration. The dashed lines in (b) correspond to a hypothetical system consisting in spherical scattering centres of the same size suspended in air in a 5% concentration.

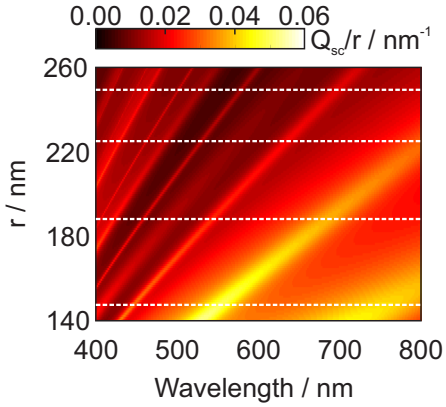

Figure 3.25: Calculation of the ratio Q_{sc}/r for an optically random medium consisting of a low refractive index SiO_2 film integrating nanocrystalline TiO_2 spheres in a 5% concentration. The dashed lines highlight the corresponding sizes considered in the analysis.

in terms of the ratio of the scattering efficiency, Q_{sc}, to the size of the particle, *i.e* Q_{sc}/r. Considering a spherical shape, ℓ_{sc} (Eq. 2.5), can be expressed in terms of the volume filling fraction, the scattering efficiency and the size of the particles:

$$\ell_{sc} = \frac{4}{3f\frac{Q_{sc}}{r}}, \tag{3.4}$$

where $Q_{sc} = {}^{\sigma_{sc}}/_{\pi r^2}$, was taken into account. In light of Eq. 3.4, ℓ_{sc} was expected to vary inversely with Q_{sc}/r. With that purpose, the modification of Q_{sc}/r as a function of the size of the inclusions was determined, Fig. 3.25, which justified the trends observed for ℓ_{sc} in Fig. 3.24. ℓ_{sc} values as short as 436 nm at $\lambda = 565$ nm were attained for a particle size $r = (146 \pm 15)$ nm due to the high refractive index contrast between the TiO_2 inclusions and the porous SiO_2 matrix, thus justifying the quest for a ultralow refractive index support matrix for the scattering inclusions. The spectra calculated through Mie formalism, Fig. 3.24(b), reproduced the trends of the spectra extracted from experiments. Such agreement demonstrated the validity of Mie formalism for the description of light transport in this material, proving it to behave as a *Mie glass*. The observation that the spectra extracted from experiments were generally shorter than those yielded

by the calculations was attributed to a likely somewhat larger filling fraction of scattering centres in the materials fabricated, since this parameter does not experimentally offer a fine control over its value, as previously noticed for the *Mie glass* based on a porous anatase matrix, Sec. 3.3.2.2. The ℓ_{sc} spectra corresponding to a hypothetical situation where the TiO_2 scattering centres are randomly suspended in air were also included in Fig. 3.24(b). The great similarities between these spectra and those corresponding to the *Mie glass* evinced an air-like character of the porous SiO_2 matrix in terms of optical properties. This confirmed the ultralow refractive index of the porous SiO_2 matrix, demonstrating its behaviour as a film of air to a great extent, yet capable of supporting particles serving as scattering centres. In this regard, if a SiO_2 film exhibiting this property were to be infiltrated with any photoluminescent molecule, an efficient out-coupling of the light could be expected. Owing to the small refractive index contrast between the film and the surrounding air, the escape cone would result wide enough to ensure small losses due to light trapped by total internal reflection, guided along the film and lost through the edges.

3.4.3 *Mie glasses* as efficient light diffusers: comparison

In order to assess the relevance of the photonic strength of this optically random material within the framework of strongly diffusive *Mie glasses*, a comparison of its ℓ_{sc} spectrum with that for the TiO_2-based *Mie glass* previously analysed in Sec. 3.3 with the same conditions of disorder was established. In particular, the conditions of the integrated disorder consisted in scattering centres of size $r = (225 \pm 20)$ nm and concentration 5%. The comparison is illustrated in Fig. 3.26(a). In both cases, ℓ_{sc} displayed considerably short values, between 1 μm and 3 μm. The relative scattering strength between both materials was, however, revealed to be importantly dependent on the considered wavelength range. Specifically, ℓ_{sc} showed shorter values in the wavelength range 400 - 635 nm for the TiO_2-based *Mie glass*, becoming the trend reversed thenceforth, where the strongest diffusion strength was expected for the *Mie glass* based on a low refractive index material. This trend verified the relationship between Q_{sc}/r and ℓ_{sc} previously inspected in Fig. 3.24 and 3.25 according to Eq. 3.4, as evidenced through the determination of Q_{sc}/r for both materials, Fig.

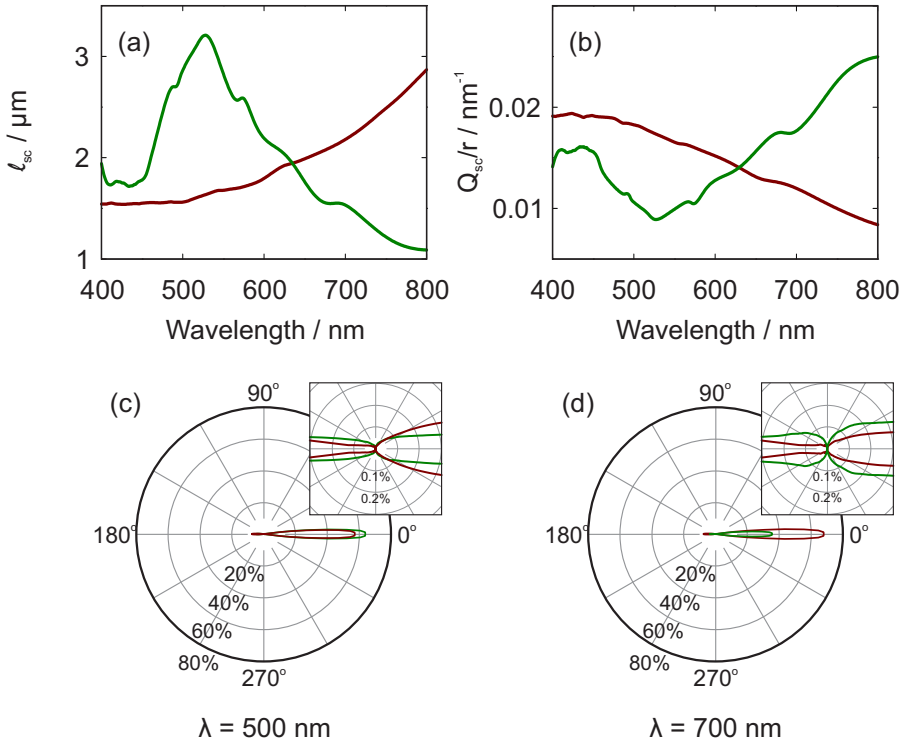

Figure 3.26: (a) Calculated ℓ_{sc} spectra for a *Mie glass* comprising a mesoporous TiO_2 (dark red line) or a highly porous SiO_2 (green line) matrix integrating nanocrystalline TiO_2 spheres of size $r = (225 \pm 20)$ nm in a 5% concentration. (b) Spectral values of the ratio Q_{sc}/r for the TiO_2-based (dark red line) and the SiO_2-based (green line) *Mie glasses* under consideration. (c) Calculated angular distributions of the light emerging from a 2-μm slab of the *Mie glasses* based either on a TiO_2 (dark red line) or a highly porous SiO_2 (green line) matrix under consideration at $\lambda = 500$ nm and (d) $\lambda = 700$ nm. The insets in (c) and (d) display a zoom-in of the corresponding angular distributions.

3.26(b). The choice of the material for its use as an efficient diffuser would therefore depend on the targeted wavelength, which dictates the predominance of the intensity of the scattering strength of one material over the other. Indeed, at $\lambda = 500$ nm, where the TiO_2-based *Mie glass* was expected to yield a stronger photonic strength than its SiO_2 counterpart, the angular distribution of the scattered light displayed

a weaker ballistic component as a consequence of an increased scattering intensity, Fig. 3.26(c). Higher diffusion strength removes photons from the ballistic direction, forcing them to emerge from the film at greater angles, thus justifying the broadening of its angular distribution shown in the inset. The opposite behaviour was observed at $\lambda = 700$ nm, Fig. 3.26(d), where a more diffusive character was expected for the SiO_2-based *Mie glass*.

3.5 Conclusions

This chapter focuses on the design and fabrication of new optically random media in the configuration of a *Mie glass*. The *Mie glass* was defined as an optically disordered material consisting of a transparent matrix integrating a random distribution of spherical scattering centres in a controlled manner with concentration values within the range of high dillution for a description of light propagation according to Mie formalism for the scattering of individual particles.

First of all, different combinations of materials in this configuration were theoretically tested with the purpose of finding specific combinations maximising the photonic strength. From this study, two particular materials demonstrated the desired properties: a mesoporous TiO_2 matrix and a ultralow refractive index porous SiO_2 matrix, both integrating nanocrystalline spherical TiO_2 scattering centres.

In the case of the TiO_2-based material, films integrating disorder with different conditions of the scattering centres were fabricated and a characterisation of the optical disorder through the determination of ℓ_{sc} and ℓ_t from experiments was performed. Comparison with the results of the corresponding calculations performed by means of Mie theory proved that in specific wavelength ranges, light propagation could be predicted in terms of Mie scattering from the scattering of light by an individual particle. Furthermore, the effects of finite size regarding light propagation were studied for this material. Specifically, the effect of shortening ℓ_{sc} through the conditions of the optical disorder included for a fixed size of a slab of this material was demonstrated to affect light transport in a similar way to increasing the thickness of the slab for a particular ℓ_{sc} value. A theoretical model was employed for the analysis of the modification of the angular distribu-

tion of the light scattered by slabs of different thickness from a regime in which ballistic propagation prevails to a regime in which light exclusively propagates in a diffuse manner and light transport is randomised. The model allowed an unprecedented analysis of light propagation in terms of the number of scattering events photons undergo, enabling a statistical study of the evolution of the angular distribution of photons undergoing a specific number of scattering events as a function of slab thickness.

In the case of the SiO_2-based random material, a procedure based on a CVD technique for the fabrication of ultralow refractive index SiO_2 films of an area around 2 x 2 cm^2 and thickness below 2 μm was presented. The optical response of the films was characterised and their refractive index estimated. The procedure demonstrated control over the refractive index of the eventual film, for which values as low as n = 1.03 at $\lambda = 600$ nm were obtained. Further inclusion of scattering spherical TiO_2 particles produced a new optically random medium which, after a characterisation of its optical disorder, was proved to behave as a *Mie glass*. Owing to the high refractive index contrast between the highly porous SiO_2 matrix and the TiO_2 scattering centres, ℓ_{sc} values as short as 436 nm were obtained at $\lambda = 565$ nm for a 5% concentration of r = (146 ± 15)-nm scattering centres, demonstrating its potential as a highly scattering diffuser.

Bibliography

[1] G. Mie, "Beiträge zur Optik trüber Medien, speziell kolloidaler Metallösungen," *Annalen der Physik*, vol. 330, pp. 377–445, 1908.

[2] C. F. Bohren and D. R. Huffman, *Absorption and scattering of light by small particles*. Wiley, 1983, ISBN: 0-471-05772-X.

[3] N. M. Lawandy, R. M. Balachandran, A. S. L. Gomes, and E. Sauvain, "Laser action in strongly scattering media," *Nature*, vol. 368, pp. 436–438, 1994.

[4] R. Sapienza, P. D. García, J. Bertolotti, M. D. Martín, Á. Blanco, L. Viña, C. López, and D. S. Wiersma, "Observation of resonant behaviour in the energy velocity of diffused light," *Physical Review Letters*, vol. 99, p. 233 902, 2007.

[5] P. D. García, R. Sapienza, J. Bertolotti, M. D. Martín, Á. Blanco, A. Altube, L. Viña, D. S. Wiersma, and C. López, "Resonant light transport through Mie modes in photonic glasses," *Physical Review A*, vol. 78, p. 023 823, 2008.

[6] P. D. García, R. Sapienza, and C. López, "Photonic glasses: A step beyond white paint," *Advanced Materials*, vol. 22, pp. 12–19, 2010.

[7] V. Y. F. Leung, A. Lagendijk, T. W. Tukker, A. P. Mosk, W. L. IJzerman, and W. L. Vos, "Interplay between multiple scattering, emission, and absorption of light in the phosphor of a white light-emitting diode," *Optics Express*, vol. 22, pp. 8190–8204, 2014.

[8] B. A. van Tiggelen, A. Lagendijk, A. Tip, and G. F. Reiter, "Effect of resonant scattering on localization of waves," *Europhysics Letters*, vol. 15, pp. 535–540, 1991.

[9] M. Schmidt, G. Boettger, M. Eich, W. Morgenroth, U. Huebner, R. Boucher, H. G. Meyer, D. Konjhodzic, H. Bretinger, and F. Marlow, "Ultralow refractive index substrates – a base for photonic crystal slab waveguides," *Applied Physics Letters*, vol. 85, pp. 16–18, 2004.

[10] D. Grosso, C. Boissiére, and C. Sanchez, "Ultralow-dielectric-constant optical thin films built from magnesium oxyfluoride vesicle-like hollow nanoparticles," *Nature Materials*, vol. 6, pp. 572–575, 2007.

[11] J. D. Bass, C. Boissiére, L. Nicole, D. Grosso, and C. Sanchez, "Thermally induced porosity in CSD MgF_2-based optical coatings: An easy method to tune the refractive index," *Chemistry of Materials*, vol. 20, pp. 5550–5556, 2008.

[12] M. Yamaguchi, H. Nakayama, K. Yamada, and H. Imai, "Ultralow refractive index coatings consisting of mesoporous silica nanoparticles," *Optics Letters*, vol. 34, pp. 2260–2262, 2009.

[13] F. Chi, L. Yan, H. Yan, B. Jiang, H. Lv, and X. Yuan, "Ultralow-refractive-index optical thin films through nanoscale etching of ordered mesoporous silica films," *Optics Letters*, vol. 37, pp. 1406–1408, 2012.

4 *Mie glasses* for bifacial DSSCs with enhanced performance

4.1 Introduction

The characteristic features of DSSCs make them especially attractive in comparison to other PV technologies when inexpensive solar cells presenting transparency or aesthetical attractiveness are required. PV devices based on a bifacial architecture have been proposed as a means to reduce costs. On the one hand, these devices are designed to present operation under front and rear illumination, either simultaneously or sequentially, which results in higher light harvesting by a cell of the same area[1]. On the other hand, such architecture could be of interest for operation in locations of unpredictable and variable illumination, such as indoor places[2]. After the first realisation of a bifacial DSSC[3], some effort was devoted toward enhancing their light-harvesting efficiency and charge transport so as to achieve better performances[4,5]. In particular, a plethora of approaches focused on maximising the transparency of the counterelectrode for optimised performance under rear illumination has been reported[4–15]. The integration of optical structures either inside[16–18] or outside[19–24] the active region of a DSSC has demonstrated acceptable effectiveness at improving light harvesting under front illumination in a wavelength range where the absorption cross section of the dye drops. Approaches based on the integration of periodical structures have been proven effective at boosting the efficiency of DSSCs[19,23,24], and so has the implementation of strategies based on disordered architectures. In fact, the integration of a backscattering layer of large TiO_2 particles[25–30] or the direct inclusion of high refractive index particles of submicron size inside the sensitised TiO_2 film[26,31–35] have produced high-performance DSSCs. Both disordered approaches take advantage of the diffuse propagation of light triggered by light scattered at large high refractive index particles. Whereas the former profits from the diffuse reflection of light at a scattering layer in order to counteract the effect of insufficient thickness, which hinders full light absorption, the latter uses the scattering caused by the particles inside the film in order to enlarge the optical

path of light and thus increase the probability of light absorption by the dye molecules. Proposals based on this idea very often employ irregular and polyhedral particles as scattering centres, which yield a mostly isotropic scattering when averaged over the different possible orientations of the particles. Furthermore, isotropic scattering produces losses at the entrance of the solar cell due to light scattered in the backward direction[26,36–38]. The majority of these photonic architectures has been oriented toward operation of the cells under front illumination, therefore lacking an appropriate optical design in order to optimise absorption for maximised performance under rear illumination.

The work described in this chapter stems from previous studies performed at the Multifunctional Optical Materials group, where the research activity for this thesis was developed. The group possesses a remarkable tradition in the integration of photonic structures, mostly periodic, into DSSCs for performance enhancement. In particular, DSSCs either based or including opals were realised and their operation studied[39–41]. The integration of one-dimensional photonic crystals comprising periodic stacks of different refractive index materials into such devices gave rise to numberless analyses of these combined systems, ranging from the controlled inclusion of structural colour to the study of the angular reponse of their operation[19,42–44]. Especially remarkable was the inclusion of white-light back reflectors capable of increasing the PCE of DSSCs while preserving transparency[23]. Other strategies were proposed and demonstrated effective at tailoring and improving the performance of these solar cells[24,45]. Eventually, progress was also made regarding the fabrication of flexible photonic crystal-based DSSCs[46].

This chapter is devoted to the integration of a *Mie glass* in the structure of a bifacial DSSC as a means of boosting light harvesting for the fabrication of high-performance solar cells. Specifically, the TiO_2-based *Mie glass* previously characterised in Sec. 3.3 of Ch. 3 sensitised with N719 is integrated as photoanode in a DSSC and the effect of absorption enhancement on the performance of the device already demonstrated in Ch. 3 is analysed in relation to the structural parameters of such *Mie glass*. The starting point of this analysis lies in the results of the works by F. E. Gálvez *et al.*[35,47], who theoretically analysed

the effects of diffuse light propagation in cells including submicron spherical particles in their photoanode.

In the study presented herein, the proposed system is modelled and the performance of the device is analysed in relation to the conditions of the scattering particles. The validity of the approach for absorption enhancement regardless of the incidence side of the light is demonstrated and, since bifacial operation of the devices was sought for, a process of optimisation of the transmittance of the counterelectrode is described. Also, an electrical characterisation of the fabricated cells is presented, through which the relationship between the conditions of the introduced disorder and the performance of the cell previously inspected during the modelling is confirmed.

4.2 Theoretical study of the system

According to the approach proposed in this thesis for the fabrication of optically disordered media, the features of the scattering centres employed to introduce optical disorder the material are deliberately selected among the different possible options in such a manner that light propagation can be reasonably well predicted by means of calculations, as previously illustrated in Ch. 3. A meaningful consequence derived from this particularity is the possibility of tailoring the disorder and designing the material properties in order to meet a specific application. Based on this concept, this section describes a theoretical analysis justifying the shape of the particles employed as scattering centres, as well as the results from calculations related to the maximum achievable J_{sc} values depending on the conditions of the considered inclusions.

The way light is scattered when impinging on a particle of a size comparable to its wavelength is not generally intuitive and it is highly dependent on its structural, as well as its material properties. The shape of the particle inevitably defines the pattern described by the electromagnetic field posterior to the scattering event, provided that its size is comparable to the wavelength of the incoming radiation. Calculations of the angular distribution of the light scattered by TiO_2 particles of diverse shapes were performed according to the methods described in Sec. 2.3.1.2 in Ch. 2. Due to the the presence of an air shell

surrounding the TiO_2 sphere, as addressed in Ch. 3, an electrolyte-filled layer surrounding the particle and with the same shape of this was included in the calculations, as detailed in Ch. 2. The patterns resulting from the calculations are displayed in Fig. 4.1(a) for the shapes indicated as schematics in the inset, specifically, spheres, cubes, truncated pyramids and distorted cubes. The angular distributions presenting the narrowest forward-oriented patterns corresponded to the spherical and the cubic shapes, for which they happened to be virtually identical. As a matter of fact, spherical and cubic TiO_2 par-

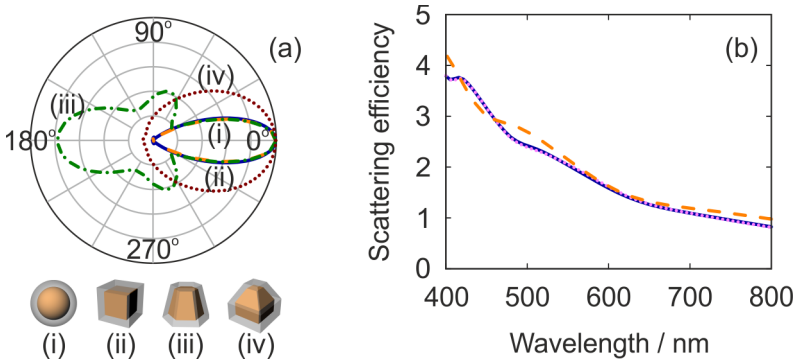

Figure 4.1: (a) FDTD calculated angular distribution of the light scattered by TiO_2 nanoparticles of diverse shapes and surrounded by an electrolyte shell of thickness 0.5r, where r is the radius of a spherical particle, and same shape as the particle, embedded in a mesoporous TiO_2 matrix, at $\lambda = 650$ nm. The same volume was considered for the four scattering structures. The distributions are the result of averaging several distributions yielded for different orientations of the particles with respect to the incident light. The angular patterns correspond to (i) a sphere of size r = 150 nm (blue solid line), (ii) a cube of side L = 242 nm (orange dashed line), (iii) a truncated pyramid of hexagonal base (green dash-dotted line) and (iv) a modified cube (dark red dotted line). (b) FDTD calculated scattering efficiency of a TiO_2 sphere of size r = 150 nm (blue solid line) and a cube of the same volume (orange dashed line). The scattering efficiency for a sphere of size r = 150 nm obtained through analytical calculations by means of Mie theory was included for the sake of comparison (pink dotted line).

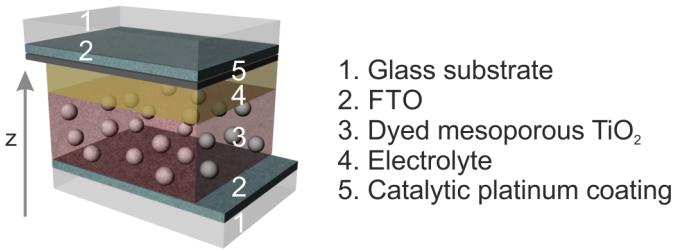

Figure 4.2: Illustration of the different components constituting the bifacial solar cell under consideration.

ticles displayed similar scattering efficiencies, as Fig.4.1(b) demonstrates. Thus, cubic- and spherical-shaped scattering centres direct light more efficiently towards deeper regions of the photoanode, effectively reducing reflection losses due to backward-scattered light at the entrance of the cell. In the same line of thought, the broader angular distributions of the light scattered by more irregular shapes, *e.g.* truncated pyramid and distorted cube, prove them as less preferable options for the aim pursued herein. Despite resulting both the cube and the sphere optimal for the integration into photoanodes, only the spherical shape was considered throughout the rest of the study due to the ease of experimental fabrication.

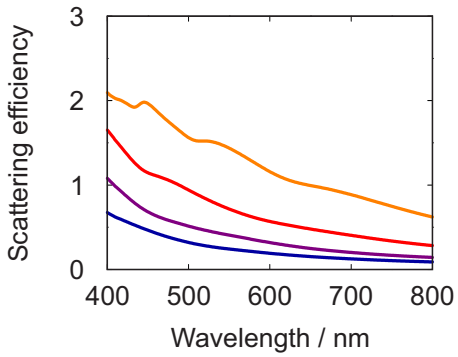

Figure 4.3: Scattering efficiency spectra of crystalline TiO_2 spheres of size r = 80 nm (blue line), r = 100 nm (purple line), r = 112 nm (red line) and r = 135 nm (orange line) surrounded by an electrolyte-filled shell of thickness sh = 0.5r embedded in a mesoporous TiO_2 matrix. The spectra were obtained from Mie formalism.

The photovoltaic system considered in this study comprised a photoanode based on a dye-sensitised TiO_2 *Mie glass* incorporating spherical TiO_2 scattering centres and sandwiched between front and rear contacts consisting in an FTO-coated glass substrate, being the latter coated with platinum for catalytic action, Fig. 4.2. Not only the concentration of the scattering centres increases the diffusive propagation of light throughout the photoanode, as pointed out by Eq. 1.1, but also their size, as evidenced by the calculated scattering efficiency spectra shown in Fig. 4.3. In order to theoretically assess the effect of the variation of these two parameters on the absorptance and further performance of the PV system herein proposed, calculations of the maximum expected J_{sc} values with respect to both the volume filling fraction, f, and the size of scattering centres, r, were carried out for a cell under front, Fig. 4.4(a), and rear, Fig. 4.4(b), illumination. As Eq. 2.27 reveals, the value of J_{sc} is directly related to the efficiency of the cell. The optimum configuration is met within scattering centre filling fraction up to 20% and size up to r = 300 nm. In effect, $J_{sc} = 15.62$ mA cm^{-2} and $J_{sc} = 10.90$ mA cm^{-2} are yielded by the calculations

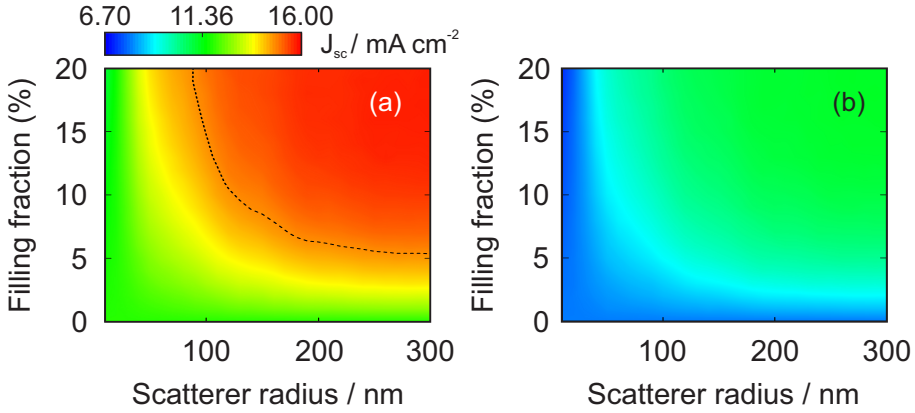

Figure 4.4: Simulated upper limit of J_{sc} for a cell under (a) front and (b) rear illumination in relation to the volume filling fraction value and the size of the scattering inclusions. The black dashed line in (a) corresponds to the value $J_{sc} = 14.20$ mA cm^{-2} yielded by a device including a backscattering layer. The value $J_{sc} = 3.87$ mA cm^{-2} corresponding to the same configuration under rear illumination has not been included in (b), since it is shorter than that for a reference cell.

as the highest attainable J_{sc} values for r = 180 nm and f = 19% under front and rear illumination, respectively. Such values correspond to a 35% efficiency enhancement under front illumination and a 40% efficiency enhancement under rear illumination when compared to a bare cell, that is, f = 0%. Even though the colour maps displayed a trend of increasing J_{sc} for bigger inclusions and larger concentrations, the parameter map was restricted to a 20% concentration and size r = 300 nm due to limitations of the model. This Monte Carlo approach fails at predicting light transport in the considered materials outside of the high-dillution regime, since it describes light scattering according to single-particle considerations and does not account for correlation terms between inclusions. For high enough particle concentration or size, the event of light scattering by an inclusion is not anymore independent on the light scattered by the surrounding centres. As previously indicated, the most common approach for the increase of optical absorption in the photoanode of DSSCs consists in the inclusion of a scattering layer made out of larger TiO_2 particles than those of the electrode between the photoanode and the Pt-coated back contact. Considering this scattering layer in a reference cell, the calculations yielded a maximum $J_{sc} = 14.20$ mA cm^{-2} (front illumination), included in Fig. 4.4(a), and a $J_{sc} = 3.87$ mA cm^{-2} (rear illumination). This shows that the integration of a scattering layer, although resulting beneficial for operation under front illumination, hinders the performance of the device when illuminated from the rear side. It is noteworthy that the addition of these two values is close to that considering those corresponding to a reference cell, specifically, $J_{sc} = 11.69$ mA cm^{-2} and $J_{sc} = 7.83$ mA cm^{-2} under front and rear illumination, respectively.

The implications of the shape of the scattering particles and its relationship with the anisotropy of the yielded scattered light pattern, earlier explored in Fig. 4.1(a), on the attainable efficiency enhancement in the device was evidenced when analysing a hypothetical situation, in which an isotropic angular distribution of the light scattered by the inclusions was assumed. Figure 4.5 presents the results of the maximum attainable J_{sc} values for front and rear illumination, in analogy to Fig. 4.4, when considering equal probability at all angles of the scattered light and identical scattering intensity than a spherical inclusion surrounded by an electrolyte-filled shell. In this nonfac-

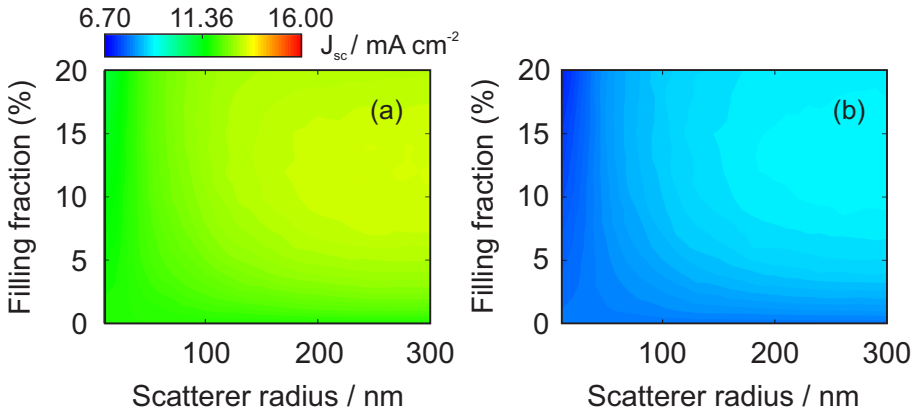

Figure 4.5: Simulated upper limit of J_{sc} for a cell under (a) front and (b) rear illumination integrating imaginary scattering inclusions yielding perfectly isotropic angular distributions of the scattered light.

tual situation, only a maximum $J_{sc} = 13.2$ mA cm^{-2} and $J_{sc} = 8.97$ mA cm^{-2} can be at best achieved under front and rear illumination, respectively, which means a scant 13% and 14% enhancement, in comparison to the 35% and 40% improvement demonstrated in Fig. 4.4 for spherical scattering centres. Such contrast revealed the relevance of employing inclusions yielding a highly narrow forward-oriented light scattering on the final performance of the device, resulting otherwise in optical losses due to backscattered light. This observation justifies the seek for particle shapes triggering highly anisotropic scattering initially contemplated at the beginning of the section.

4.3 Counterelectrode optimisation and preparation

The back part of the cell, or counterelectrode, comprises a conductive substrate coated with Pt. This coating is in fact essential for proper operation of the device, since it acts as a catalyst for the reaction of regeneration of the dye molecules through the electrolyte in which the entire system is immersed. In a bifacial configuration of the cell, the high absorption by the Pt coating results detrimental for the performance of the device when operating under rear illumination, as it would entail a lower light intensity reaching the photoanode for ex-

citation of the dye molecules. For this reason, trade-off between high transparency and maintaining enough catalytic action must be met. A study of the performance of cells depending on the amount of Pt coating the counterelectrode was performed. Two concentrations of the H_2PtCl_6 solution, namely, 6 mM and 7 mM, and up to three depositions were tested. Coating of the substrates by casting a drop of the solution was also tested for the sake of comparison. The transmittance of the different counterelectrodes was measured, Fig. 4.6(a)

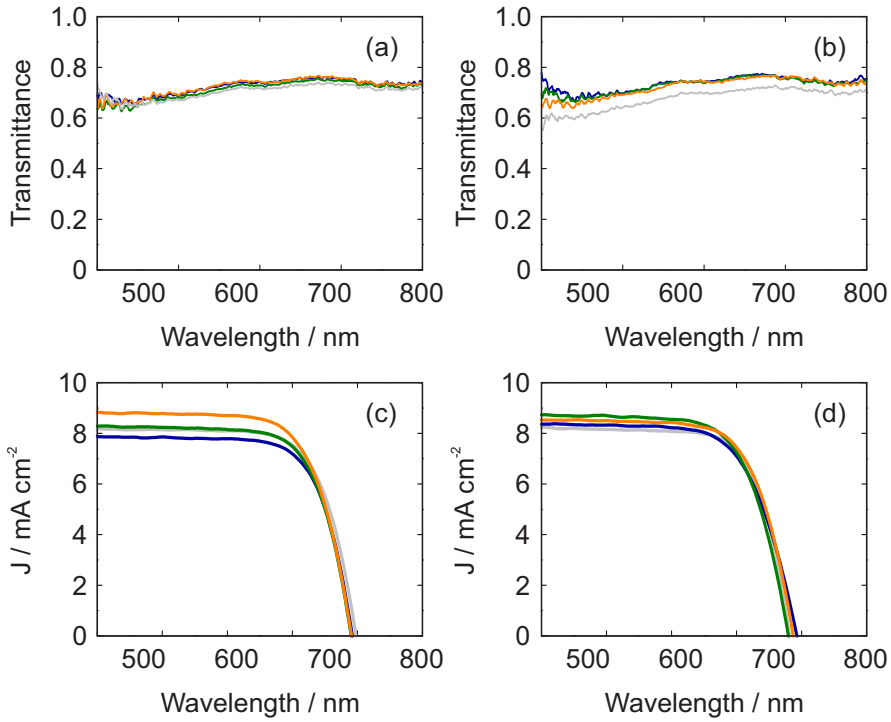

Figure 4.6: Transmittance of glass/FTO/Pt-coated substrates prepared with different deposition number through spin coating of a (a) 6-mM and (b) 7-mM concentration H_2PtCl_6 solution. (c) J-V curves determined for solar cells fabricated employing the as-prepared counterelectrodes employing a 6-mM and a (d) 7-mM concentration H_2PtCl_6 solution. The spectra correspond to counterelectrodes coated with one (blue line), two (green line) and three (orange line) depositions of a H_2PtCl_6 solution. Data for a system prepared through drop casting were also included (gray line).

Table 4.1: Electrical parameters measured for devices integrating a counterelectrode prepared with a H_2PtCl_6 solution of different concentration.

6-mM H_2PtCl_6 solution concentration				
Cell	J_{sc} exp. / mA cm^{-2}	$\mathbf{V_{oc}}$ / mV	FF (%)	PCE (%)
Drop casting	7.91	799	69.6	4.4
1 deposition	7.87	784	70.0	4.3
2 depositions	8.29	781	69.4	4.5
3 depositions	8.83	782	68.2	4.7
7-mM H_2PtCl_6 solution concentration				
Drop casting	8.22	762	70.0	4.4
1 deposition	8.37	785	65.2	4.3
2 depositions	8.73	759	66.6	4.4
3 depositions	8.54	774	67.8	4.5

and (b). From these spectra, it was straightforward to conclude that the method of drop casting yielded lower transmittance values than spin coating. As a consequence, it was preferable to rely on the latter for the coating process. After that, these counterelectrodes were employed for the fabrication of standard cells comprising an 8-μm thick photoanode. An electrical characterisation of the devices allowed the determination of the J-V curves for the evaluation of the influence of the amount of Pt coating the counterelectrode on the performance of the cell. Although no significant influence of the solution concentration on the transmittance spectra on was revealed, the J-V curves, Fig. 4.6(c) and (d), displayed a clear dependence. Whereas the efficiency of the devices including counterelectrodes prepared by using a 7-mM Pt solution remained virtually unvariable, see Table 4.1, the efficiency yielded by those devices including a counterelectrode prepared with a 6-mM solution displayed a clear increasing trend with the number of depositions, showing a maximum 4.7% PCE for 3 depositions. Such value corresponded to the maximum observed for all of the considered cases. In light of these results, a 6-mM concentration solution

and 3 depositions by spin coating were established as the most suitable conditions for the preparation of the counterelectrodes.

4.4 Integration of scattering centres in photoanodes: absorptance enhancement

The entire fabrication process of photoanodes integrating optical disorder, from the synthesis of the spherical inclusions to the final solid film, is based on solution-processing methods, which are known to be inexpensive. Plus, the lack of order in the included structures reduces the need for sophisticated integration methods, therefore demanding lower complexity during the fabrication process. Altogether, these characteristics demonstrate the suitability of the proposed approach when aiming at an efficient and low-cost solar technology, typical features of third-generation photovoltaics.

The integration of optical disorder in the sensitised mesoporous TiO_2 films typically employed as photoanode in DSSCs was previously proved in Ch. 3 to induce an effective increase of the optical absorption of light by the dye molecules. Hence the potential of this material for the fabrication of solar cells with improved performance. Essential for the fabrication of bifacial solar cells is the ability of the device to efficiently operate regardless of the incidence side and angle of the incoming light, which is ensured by the random nature of the approach herein proposed[20–22,24]. For the demonstration of this point, measurements of the absorptance were performed under front and rear illumination for two conditions of the inclusions, Fig. 4.7, revealing spectra that remained virtually unaffected by the illumination side. Such effect was also promoted by the fully symmetric shape of the scattering particles, which ensured identical scattering regardless of the incidence angle. Although the absorption enhancement yielded by a system integrating a backscattering layer was revealed significant under front illumination, the absorptance dramatically decreased under illumination from the rear side due to light lost through efficient diffuse reflection that could not be coupled into the system. Were this electrode configuration to be part of a device, one should take into account its unsuitability for bifacial operation. Let us remember that the integration of a backscattering layer is a widely

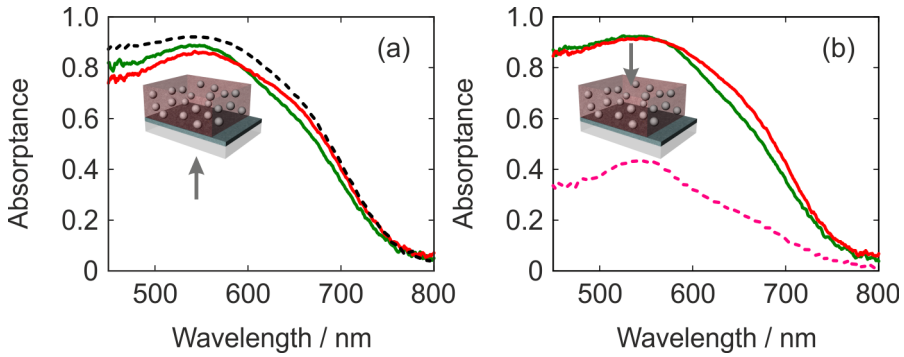

Figure 4.7: Demonstration of the invariability of the absorptance spectra of a system glass/FTO/sensitised electrode including scattering centres of size r = (100 ± 15) nm and concentration f = 10% (green line) and f = 20% (red line) under (a) front and (b) rear illumination. The absorptance spectra for a system glass/FTO/sensitised bare electrode/backscattering layer have been included as a black dashed line in (a) for front illumination and as a pink dashed line in (b) for rear illumination in order to illustrate the strong dependence of the light-harvesting capability of this system on the illumination side.

extended strategy for the fabrication of high-performance DSSCs. In fact, the certified record PCE of 11.9% for a DSSC up to date was yielded by a device including a 5-μm backscattering layer[29]. On the whole, such analysis proved one of the major points of this approach, that is, its appropriateness for the fabrication of photoanodes for DSSCs to operate under bifacial conditions.

Determination of the diffuse properties of the base material would allow an assessment of its diffusive strength, generally regarded as a way to evaluate its scattering and light-trapping ability. The *haze* is in fact a straightforward manner to easily assess the diffusive character of a material and it accounts for the fraction of light scattered by a material and it is defined as the ratio of T_d to T of the light emerging from the material at the exit interface. High haze values have been reported to yield high η_{IPCE}[34]. However, it should not be regarded as a unequivocal magnitude providing the light-trapping ability of a material, since it lacks information about essential factors of the diffuse propagation of light. The haze only considers the fraction of light being transmitted. Besides, it cannot account for the

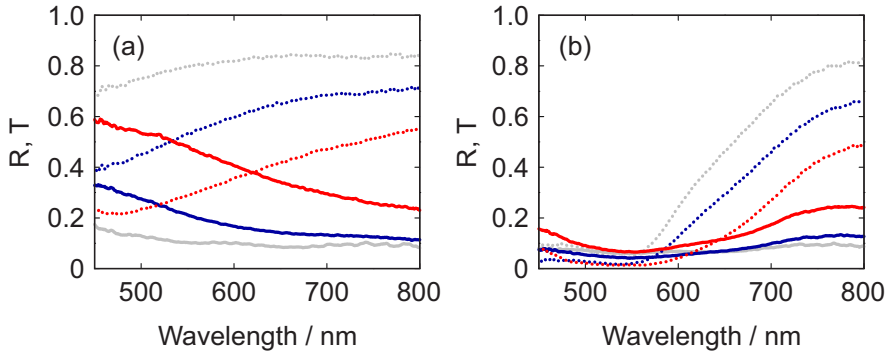

Figure 4.8: Total reflectance (solid lines) and transmittance (dotted lines) for a system glass/FTO/electrode integrating scattering centres of size r = (100 ± 15) nm and filling fraction f = 5% (blue lines) and f = 20% (red lines) (a) before and (b) after dye soaking. The reflectance and transmittance spectra corresponding to a reference system devoid of scattering centres have been included as gray lines.

manner the diffuse light is generated and how it contributes to an improvement of the absorptance by a homogeneous distribution of dye molecules. Therefore, determination of the R and T spectra are required for the electrodes prepared herein in order to evaluate their level of light trapping. Measurement of the diffuse magnitudes of the electrodes demonstrated that higher R_d was responsible for the increase of the reflectance displayed in Fig. 4.8(a). After sensitisation with dye molecules, these electrodes demonstrated a significant increase of the optical absorptance, Sec. 3.3.2.3 of Ch. 3, as a consequence of multiple scattering, which generated an effect of efficient light trapping, while displaying negligible reflectance losses at the entrance interface in the wavelength region where the dye absorbs most efficiently, Fig. 4.8(b). In contrast, if a material presenting a high concentration of scattering centres is considered, an inefficient in-coupling of the light would be expected owing to important reflection losses, whereas the small fraction of transmitted light would mostly propagate diffusively, thus still yielding large haze values. Consequentially, efficient light trapping cannot be expected from such a system.

4.5 Electrical characterization of the cells

Bifacial solar cells including optical disorder with diverse conditions in their photoanodes were built and duly characterised. The electrical characterisation herein performed includes the determination of the η_{IPCE} curves and J-V characteristics so as to assess the effect of integrating optical disorder into the electrode on the performance of the device as a bifacial solar cell.

As defined in Sec. 2.3.3.3 of Ch. 2, the electron-generation function, $g(z,\lambda)$, provides the absorption per unit length along the electrode of

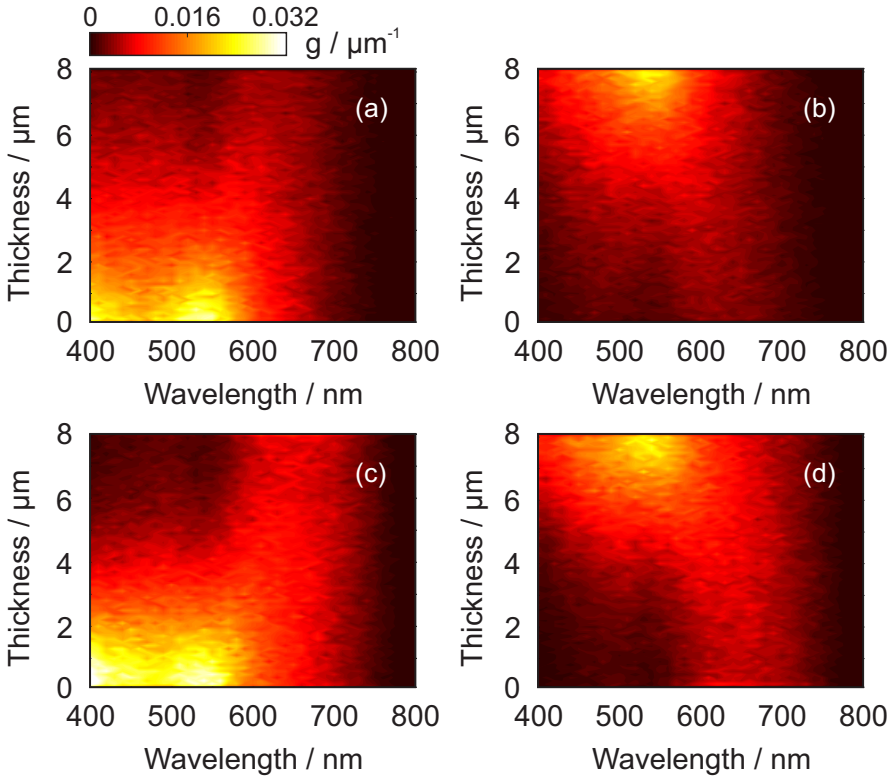

Figure 4.9: Calculation of $g(z,\lambda)$ per unit length for the electrode of a reference cell under (a) front and (b) rear illumination and for the electrode of a cell including spherical TiO_2 particles of size r = 160 nm and concentration f = 15% under (c) front and (d) rear illumination. A thickness of 8 μm was considered for both electrodes.

the DSSC. The integration of scattering centres triggers a modification of $g(z,\lambda)$, thus modifying the absorption profiles in the photoanode. An example of this is illustrated in Fig. 4.9, where $g(z,\lambda)$ in two types of electrodes under front and rear illumination is displayed. In particular, calculations were performed for the electrode of a reference cell and an electrode integrating $r = 160$ nm scattering particles in a $f = 15\%$ concentration. Comparison between Fig. 4.9(c) and (a) and Fig. 4.9(d) and (b), respectively, revealed an absorption boost deeper in the film in both cases, especially in the range between *ca.* 600 nm to *ca.* 750 nm. Furthermore, light harvesting was improved in regions close to the photoanode under front illumination, which may result beneficial for devices presenting a low electron collection efficiency, due to the lower recombination probability associated to electrons generated at distances closer to the contacts.

The generated photocurrent is strongly dependent on η_{IPCE} and, in fact, according to Eq. 2.29, J_{sc} is directly related to it. Figures 4.10 and 4.11 reveal how the absorptance enhancement triggered by the inclusion of scattering centres resulted in a more efficient performance of the device. As expected from the absorptance curves analysed in Sec. 3.3.2.3 of Ch. 3, a broadband enhancement in the η_{IPCE} curves was mainly observed in the spectral range between *ca.* 600 nm and *ca.* 750 nm when comparing to a reference cell. The η_{IPCE} curves corresponding to the simulated systems reproduced the spectra experimentally determined. In accordance with the absorptance spectra, the increase of either of both parameters positively affected the values of the η_{IPCE} curves. The noteworthy observation of a similar enhancement trend under front and rear illumination pointed out the suitability of this electrode configuration for operation as a bifacial device, as already indicated by the spectra in Fig. 4.7. The calculated η_{IPCE} spectra were determined as detailed in Sec. 2.3.3.3 of Ch. 2, where only η_{LH} and η_{COL} are assumed to contribute. In the calculation of η_{COL}, the value of L_e was adjusted for best agreement of the maximum of the generated η_{IPCE} spectra to the corresponding experimental curves, yielding a value of $L_e = 18$ μm.

The J-V curves of the devices integrating scattering centres with different conditions were determined in order to assess their perfomance. For each condition, around 5 cells were measured and the results averaged. These are displayed in Table 4.2, and the curves shown

in Fig. 4.12 correspond to a representative curve for each case. In order to assess the PCE enhancement as a function of the scattering centre conditions, the value of ℓ_{sc} weighted by the extinction coefficient of the dye and integrated along the whole wavelength range, $\ell_{sc}^{\dagger}$, was included in Table 4.2, calculated according to

$$\ell_{sc}^{\dagger} = \frac{\int_{\lambda_1}^{\lambda_2} \ell_{sc}(\lambda) k_{dye}(\lambda) d\lambda}{\int_{\lambda_1}^{\lambda_2} k_{dye}(\lambda) d\lambda}, \tag{4.1}$$

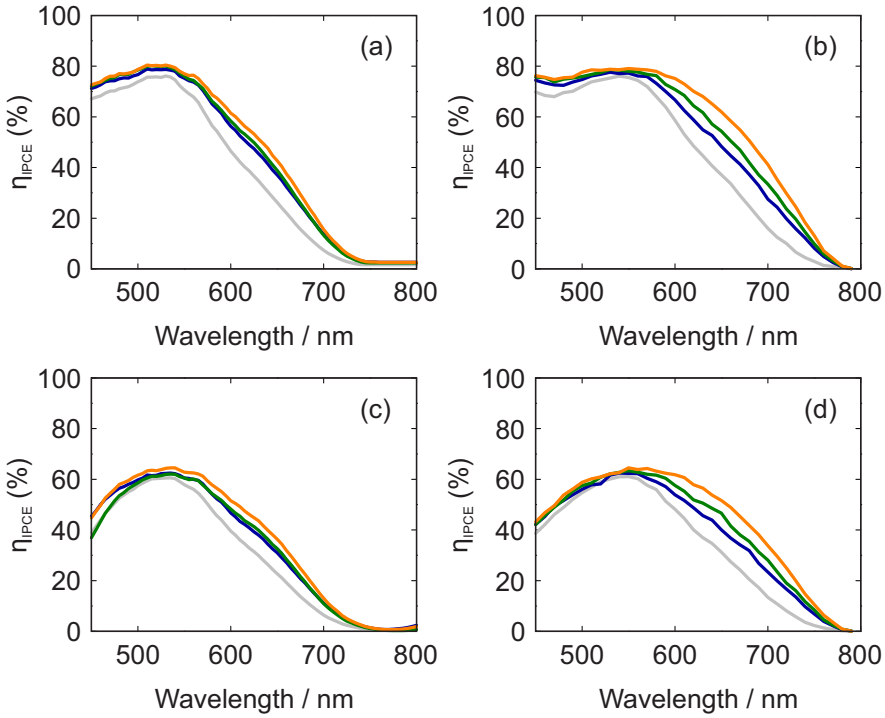

Figure 4.10: Influence of inclusion filling fraction on the η_{IPCE} values. (a) Experimental and (b) calculated η_{IPCE} spectra obtained for solar cells under front illumination. (c) Experimental and (d) calculated η_{IPCE} spectra obtained for solar cells under rear illumination. The spectra correspond to a reference cell devoid of scattering centres (gray line) and devices integrating inclusions of size r = (160 ± 50) nm and concentration f = 5% (blue line), f = 10% (green line) and f = 15% (orange line). The thickness of the electrodes was L = 8 μm.

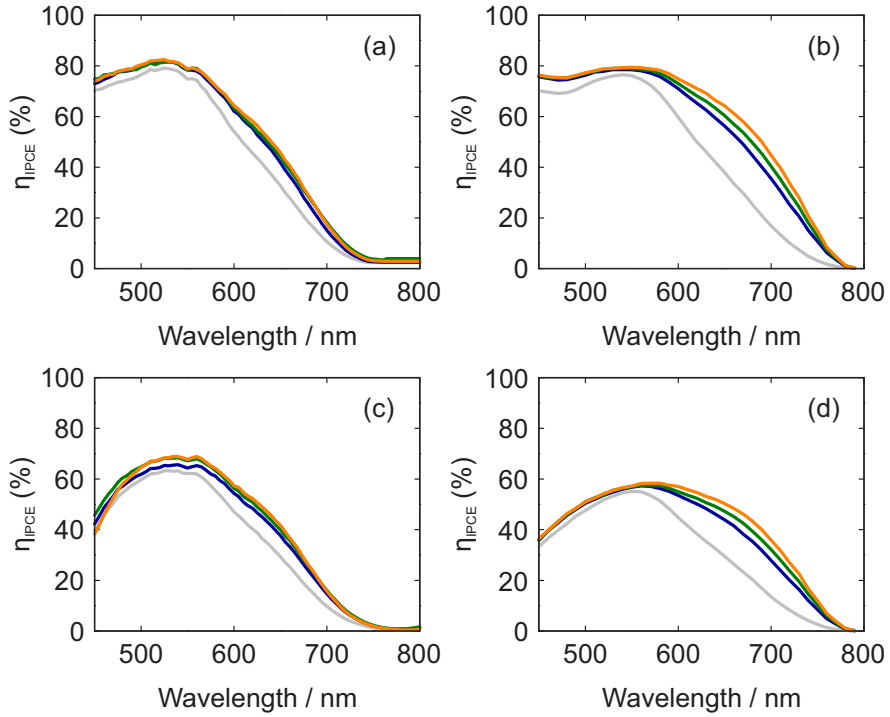

Figure 4.11: Influence of inclusion size on the η_{IPCE} values. (a) Experimental and (b) calulated η_{IPCE} spectra obtained for solar cells under front illumination. (c) Experimental and (d) calculated η_{IPCE} spectra obtained for solar cells under rear illumination. The spectra correspond to a reference cell devoid of scattering centres (gray line) and devices integrating inclusions of size r = (100 $\pm$ 15) nm (blue line), r = (135 $\pm$ 15) nm (green line) and r = (200 $\pm$ 25) nm (orange line) with a filling fraction f = 10% . The thickness of the electrodes was L = 8 μm.

where, $k_{dye}(\lambda)$ refers to the spectral extinction coefficient of the N719 dye and λ_1 and λ_2 define the integration range, corresponding to 400 - 800 nm in this case. Following the trend observed in the η_{IPCE} spectra, the inclusion of scattering particles improved the performance of the cells as a consequence of boosting light absorption in the photoanode and such improvement escalated with shorter values of $\ell_{sc}^{\dagger}$, achieved by either an increase in the size or the concentration of the inclusions. Besides, the enhancement trend was preserved regardless

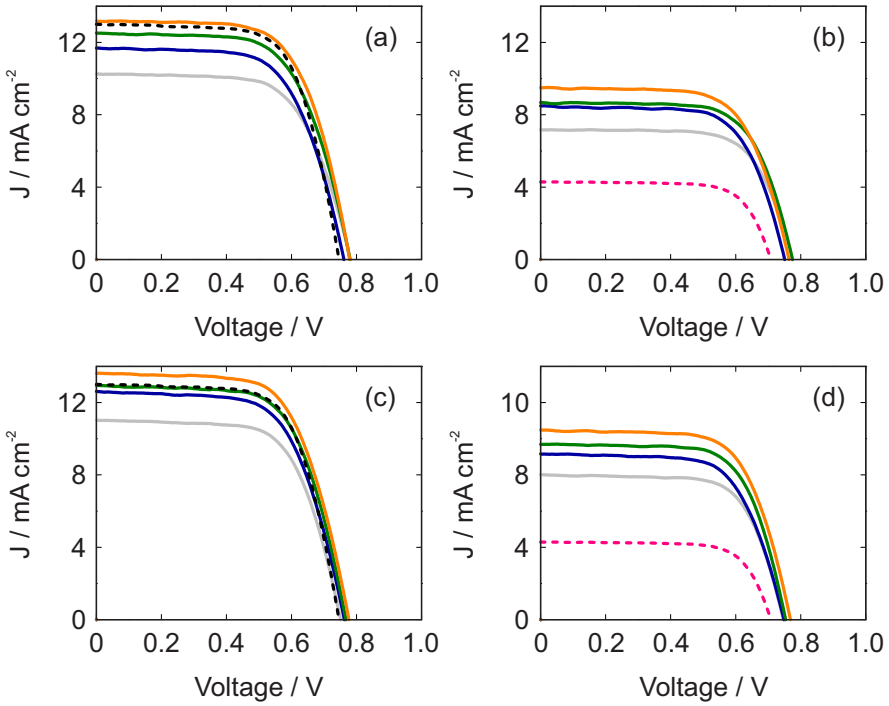

Figure 4.12: Averaged J-V characteristics for the fabricated solar cells. (a) J-V curves for cells including scattering centres of size r = (160 ± 50) nm and volume filling fraction f = 5% (blue line), f = 10% (green line) and f = 15% (orange line) under front and (b) rear illumination. (c) J-V curves for cells including scattering centres of size r = (100 ± 15) nm (blue line), r = (135 ± 15) nm (green line) and r = (200 ± 25) nm and volume filling fraction f = 10% under front and (d) rear illumination. The J-V characteristic of a reference solar cell (gray line) and that yielded by a bare device integrating a backscattering layer under front (black dashed line) and rear (pink dashed line) illumination have been included for comparison. The electrode thickness was around 8 μm in all the cases.

of the illumination side, as expected. PCE values obtained for the cells integrating scattering centres were above the *ca.* 5.4% PCE of a reference cell under front illumination for all the cases. The highest PCEs obtained during the analysis of both parameters, specifically, f = 15% - r = (160 ± 50) nm, and f = 10% - r = (200 ± 25) nm, accordingly

Table 4.2: Averaged experimental electrical parameters yielded by DSSCs integrating optical disorder with different conditions into their photoanode. The values were extracted from the J-V curves and averaged over different cells with the same parameters of the scattering centres. Data regarding reference cells and devices integrating a backscattering layer were included for the sake of comparison.

r = (160 ± 50) nm						
Cell	Illumination	J_{sc} exp. / mA cm^{-2}	V_{oc} / mV	FF (%)	PCE (%)	η_{rear}/η_{front}
Reference	Front	10.30 ± 0.06	780 ± 2	65.6 ± 0.8	5.3 ± 0.0	0.72 ± 0.0
	Rear	7.19 ± 0.02	773 ± 4	69.3 ± 0.2	3.8 ± 0.0	
f = 5%	Front	11.50 ± 0.30	764 ± 4	63.8 ± 0.8	5.6 ± 0.1	0.74 ± 0.11
$l_{sc}^{\dagger}$ = 3.3 μm	Rear	8.20 ± 0.30	752 ± 1	67.1 ± 0.3	4.2 ± 0.2	
f = 10%	Front	12.40 ± 0.30	784 ± 6	64.4 ± 0.4	6.2 ± 0.1	0.74 ± 0.09
$l_{sc}^{\dagger}$ = 1.6 μm	Rear	8.68 ± 0.16	779 ± 5	68.1 ± 0.6	4.6 ± 0.1	
f = 15%	Front	12.90 ± 0.30	782 ± 5	65.3 ± 1.1	6.6 ± 0.1	0.74 ± 0.08
$l_{sc}^{\dagger}$ = 1.1 μm	Rear	9.30 ± 0.40	768 ± 4	68.1 ± 0.8	4.9 ± 0.2	
f = 10%						
Reference	Front	11.02 ± 0.21	750 ± 5	65.1 ± 1.0	5.4 ± 0.4	0.75 ± 0.07
	Rear	8.00 ± 0.40	744 ± 6	68.4 ± 0.9	4.1 ± 0.2	
r = (100 ± 15) nm	Front	12.70 ± 0.60	761 ± 1	63.2 ± 1.1	6.1 ± 0.1	0.77 ± 0.06
$l_{sc}^{\dagger}$ = 2.5 μm	Rear	9.20 ± 0.05	750 ± 2	67.0 ± 0.6	4.7 ± 0.1	
r = (135 ± 15) nm	Front	12.96 ± 0.14	762 ± 4	64.4 ± 1.4	6.4 ± 0.1	0.78 ± 0.09
$l_{sc}^{\dagger}$ = 1.3 μm	Rear	9.80 ± 0.30	753 ± 2	67.7 ± 1.1	5.0 ± 0.1	
r = (200 ± 25) nm	Front	13.54 ± 0.12	769 ± 7	64.3 ± 0.5	**6.7 ± 0.1**	0.80 ± 0.11
$l_{sc}^{\dagger}$ = 0.8 μm	Rear	10.40 ± 0.30	766 ± 6	67.5 ± 0.5	**5.4 ± 0.1**	
Back scattering layer	Front	12.70 ± 0.40	762 ± 8	64.6 ± 0.4	6.3 ± 0.1	0.34 ± 0.03
	Rear	4.02 ± 0.06	737 ± 8	71.8 ± 0.4	2.1 ± 0.0	

corresponding to the shortest $l_{sc}^{\dagger}$ in each case, surpassed the PCE of the cells integrating a backscattering layer under front illumination (6.3% PCE associated with an averaged J_{sc} = 12.70 mA cm^{-2}) and, evidently, under rear illumination. A maximum PCE of 6.7%, bold in Table 4.2, associated with an averaged J_{sc} = 13.54 mA cm^{-2}, was attained under front illumination for the shortest $l_{sc}^{\dagger}$ value, namely, $l_{sc}^{\dagger}$ = 0.8 μm, as expected, which corresponds to a 25% enhancement with respect to a reference cell. Along the same lines, these conditions also yielded the best performance under rear illumination, particularly a 5.4% PCE, also bold in Table 4.2, which highly differs from the 2.1% yielded by the cell including a backscattering layer under rear illumination. When comparing to a reference cell, this 5.4% PCE value corresponds to a 33% enhancement. The reason for the lower J_{sc} val-

ues under rear-side operation resides in a lower fraction of intensity reaching the photoanode owing to the corresponding absorption and reflection of light by the additional layers, *i.e.* the Pt coating and the electrolyte layer, presenting the latter an important absorption peak near $\lambda = 400$ nm. This comparison revealed the potential for competitiveness of the inclusion of optical disorder as a means to boost light harvesting when compared to other standard methods that are exclusively valid for one-side illumination. The value $\ell_{sc}^{\dagger} = 0.8$ μm for the conditions f = 10% - r = (200 ± 25) nm was 10 times shorter than the thickness of the photoanode. This indicated that light underwent several scattering events before reaching the opposite side of the sensitised electrode, significantly enlarging the path length of the light inside it and thus increasing the probability of absorption by any dye molecule. Such value of ℓ_{sc} was therefore consistent with the observation of an improvement of the absorptance. Typically, high efficiency bifacial DSSCs comprise photoanodes of thickness around 15 μm. If optical disorder was integrated in sensitised films of such thickness and employed for the fabrication of devices, the model predicts PCE rear and front side enhancements above 20%. Experimental observations indicated there was a limit to the volume of inclusions to be integrated in the film before suffering from mechanical instability and delamination.

Regardless of the conditions of the inclusions in the electrodes, the values of V_{oc} and FF of the devices scarcely fluctuated, yielding values around $V_{oc} = 760$ mV and FF = 65% under front illumination and $V_{oc} = 750$ mV and FF = 68% for rear-side illumination. Let us point out that these values of the electrical parameters were in line with those reported for state-of-the-art devices using Pt as catalytic material. Besides, the PCE values obtained for the most efficient cells were among the largest reported for bifacial devices employing Pt as catalytic material and standard electrode thickness, < 10 μm[4–6,8–14]. What is more important, the J_{sc} and PCE values yielded under rear illumination by the cells fabricated herein surpassed most of those reported for the standard cell configuration employed in this approach, even though the thickness of the active layer of the devices herein fabricated was at least around 25% thinner than the ones for which the largest efficiencies have been reported. For instance, S. Ito *et al.*[3] reported a 5.62% efficiency under rear illumination, only around 0.2% higher than the

corresponding best PCE in this study, for a cell comprising a 16-μm thick electrode, just twice the thickness of the electrodes considered herein. D. Song *et al.*[10] built a reference cell integrating a Pt-coated countereletrode, which yielded a 4.69% PCE under rear illumination for a 12-μm thick electrode, still one third larger than the 8-μm electrodes of the cells characterised in this study. Maximum values of PCE under rear illumination from 2.47% up to 3.56% have been reported for Pt-coated counterelectrodes in cells integrating a standard 10-μm thick TiO_2 electrode[9,11–13,15]. Hence, a proper optimisation of the optical design of the bifacial solar cell allows a signicant reduction of the electrode thickness.

In terms of cell performance, the random nature of this approach responsible for a rather independent behaviour of the devices on the illumination side became evident when inspecting the rear/front efficiency ratios displayed in the last column of Table 4.2, which remained virtually invariable. This implies that a decrease of $l_{sc}^{\dagger}$ caused a similar improvement of the performance of the cell under front and rear illumination, therefore demonstrating their operation as highly bifacial devices and proving the efficacy of this approach as an effective route toward high performance cells displaying a greatly bifacial character. In particular, a maximum $\eta_{rear}/\eta_{front} = 80\%$ was yielded by the most favourable case. Additionally, the majority of approaches reported in the literature for the improvement of the performance of DSSCs are compatible with the inclusion of optical disorder in the photoanode herein proposed.

The real value of $\eta_{COL}(\lambda)$ could be roughly estimated from experimental data. According to Eq. 2.29, J_{sc} is related to $\eta_{IPCE}(\lambda)$. $\eta_{INJ}(\lambda)$ and $\eta_{REG}(\lambda)$ can be generally assumed 1. In this picture, Eq. 2.29 can be then re-written as:

$$J_{sc} = q \int_{\lambda_1}^{\lambda_2} \eta_{LH}(\lambda)\eta_{COL}(\lambda)\Phi(\lambda)d\lambda. \tag{4.2}$$

After demonstrating an excellent agreement between the measured and the calculated absorptance spectra, one can expect that any deviation of the experimental values of J_{sc} from the calculations would originate from a non-unity $\eta_{COL}(\lambda)$. Therefore, comparison between the experimental J_{sc} and that yielded by simulations for the most favourable situation, displayed in Fig. 4.4, could provide an estimation of the

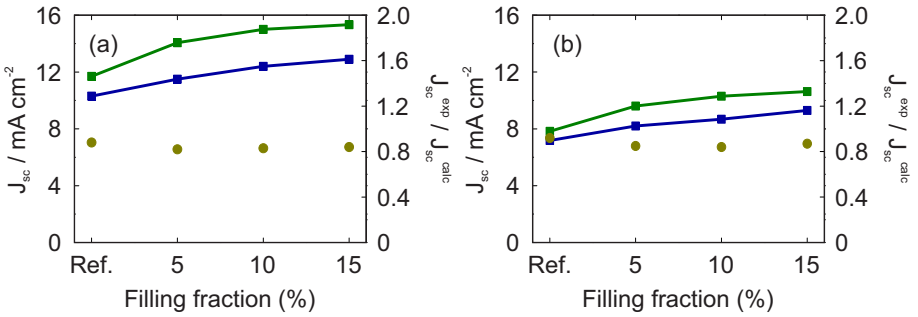

Figure 4.13: Estimation of the electron collection efficiency, η_{COL}, for devices integrating inclusions in different concentrations under (a) front and (b) rear illumination. η_{COL} values (dark yellow dots) were estimated through the expression $\eta_{COL} = J_{sc}^{exp}/J_{sc}^{calc}$ from the values of J_{sc} yielded by the devices, J_{sc}^{exp} (blue squares), and those extracted from the simulated systems, J_{sc}^{calc} (green squares).

real $\eta_{COL}(\lambda)$. As shown in Fig. 4.13, $\eta_{COL}(\lambda) \approx 0.9$ could be extracted from such comparison, which was consistent with the 18 μm electron diffusion length previously estimated. This value close to 1 indicated that the electrical properties of the cells were not significantly compromised by the integration of scattering centres in the electrodes, therefore not affecting charge transport, as it has been demonstrated by means of Electrical Impedance Spectroscopy for other systems integrating scattering elements[48,49].

4.6 Conclusions

In this chapter, a combined theoretical-experimental approach for the fabrication of high-performance bifacial DSSCs by means of randomly distributing submicron TiO_2 inclusions in their photoanodes has been developed and presented. An optical design based on calculations allowed sweeping the phase space of the scattering inclusion features, that is, size and volume filling fraction, so as to find the optimum design providing the highest PCE.

The random inclusion of scattering centres was proved in a previous chapter to induce a broadband enhancement of the absorptance of this *Mie glass*-based photoanode when sensitised with an absorbing

dye, specifically, N719. Measurements of the absorptance under front and rear illumination evinced the independence of such improvement on the illumination side as a consequence of the disordered nature of the approach.

An electrical characterisation of the solar cells revealed a gradual increment of the J_{sc} values in devices integrating scattering centres, thus resulting in higher PCEs, when increasing either the volume filling fraction or the size of the particles, which induced a decrease of $\ell_{sc}^{\dagger}$. Furthermore, this improvement resulted independent on the illumination direction, evidenced by the high front to rear efficiency ratios yielded by the devices, for which a maximum 80% was obtained. The possibility of optically designing the device enabled the fabrication of cells providing values of the relevant PV parameters comparable to those reported for state-of-the-art bifacial devices comprising standard cell components, which generally include electrodes at least 25% thicker than those modified herein considered. This proved the potential of this approach, demonstrating that a proper optical design can significantly reduce the thickness of the active layer for an efficient bifacial DSSC, thus requiring less amount of material for fabrication. Moreover, this modification of the working electrode can be complemented by any method for enhanced performance under rear illumination. An advantage of this approach is the possibility of extension to other systems in which a fine tuning of the disorder properties may be proved favourable, therefore offering potential benefits for the development of other optoelectronic devices in which an accurate control of light absorption and emission are sought for.

Bibliography

[1] A. Hübner, A. G. Aberle, and R. Hezel, "Novel cost-effective bifacial silicon solar cells with 19.4% front and 18.1% rear efficiency," *Applied Physics Letters*, vol. 70, pp. 1008–1010, 1997.

[2] A. Sacco, L. Rolle, L. Scaltrito, E. Tresso, and C. F. Pirri, "Characterization of photovoltaic modules for low-power indoor application," *Applied Energy*, vol. 120, pp. 1295–1302, 2013.

[3] S. Ito, S. M. Zakeeruddin, P. Comte, P. Liska, D. Kuang, and M. Grätzel, "Bifacial dye-sensitized solar cells based on an ionic liquid electrolyte," *Nature Photonics*, vol. 2, pp. 693–698, 2008.

[4] X. Li, Z. Ku, Y. Rong, G. Liu, L. Liu, T. Liu, M. Hu, Y. Yang, H. Wang, M. Xu, P. Xiang, and H. Han, "Design of an organic redox mediator and optimization of an organic counter electrode for efficient transparent bifacial dye-sensitized solar cells," *Physical Chemistry Chemical Physics*, vol. 14, pp. 14 383–14 390, 2012.

[5] Y. Rong, Z. Ku, X. Li, and H. Han, "Transparent bifacial dye-sensitized solar cells based on an electrochemically polymerized organic counter electrode and an iodine-free polymer gel electrolyte," *Journal of Materials Science*, vol. 50, pp. 3803–3811, 2015.

[6] Q. Tai, B. Chen, F. Guo, S. Xu, H. Hu, B. Sebo, and X. Zhao, "In situ prepared transparent polyaniline electrode and its application in bifacial dye-sensitized solar cells," *ACS Nano*, vol. 5, pp. 3795–3799, 2011.

[7] N. Fu, Y. Fang, Y. Duan, X. Zhou, X. Xiao, and Y. Lin, "High-performance plastic platinized counter electrode *via* photoplatinization technique for flexible dye-sensitized solar cells," *ACS Nano*, vol. 6, pp. 9596–9605, 2012.

[8] Y. Duan, Q. Tang, J. Liu, B. He, and L. Yu, "Transparent metal selenide alloy counter electrodes for high-efficiency bifacial dye-sensitized solar cells," *Angewandte Chemie International Edition*, vol. 53, pp. 14 569–14 574, 2014.

[9] Y. Duan, Q. Tang, B. He, R. Li, and L. Yu, "Transparent nickel selenide alloy counter electrodes for bifacial dye-sensitized so-

lar cells exceeding 10% efficiency," *Nanoscale*, vol. 6, pp. 12 601–12 608, 2014.

[10] D. Song, M. Li, Y. Li, X. Zhao, B. Jiang, and Y. Jiang, "Highly transparent and efficient counter electrode using SiO_2/PEDOT–PSS composite for bifacial dye-sensitized solar cells," *Applied Materials & Interfaces*, vol. 6, pp. 7126–7132, 2014.

[11] J. Wu, Y. Li, Q. Tang, G. Yue, J. Lin, M. Huang, and L. Meng, "Bifacial dye-sensitized solar cells: A strategy to enhance overall efficiency based on transparent polyaniline electrode," *Scientific Reports*, vol. 4, p. 4028, 2014.

[12] H. Cai, Q. Tang, B. He, R. Li, and L. Yu, "Bifacial dye-sensitized solar cells with enhanced rear efficiency and power output," *Nanoscale*, vol. 6, pp. 15 127–15 133, 2014.

[13] J. Liu, Q. Tang, B. He, and L. Yu, "Cost-effective bifacial dye-sensitized solar cells with transparent iron selenide counter electrodes. An avenue of enhancing rear-side electricity generation capability," *Journal of Power Sources*, vol. 275, pp. 288–293, 2015.

[14] S. Xu, Y. Luo, G. Liu, G. Qiao, W. Zhong, Z. Xiao, Y. Luo, and H. Ou, "Bifacial dye-sensitized solar cells using highly transparent PEDOT:PSS films as counter electrodes," *Electrochimica Acta*, vol. 156, pp. 20–28, 2015.

[15] H. Zhang, Q. Tang, and B. He, "Alloying of platinum and molybdenum for transparent counter electrodes. A strategy of enhancing power output for bifacial dye-sensitized solar cells," *RSC Advances*, vol. 5, pp. 51 600–51 607, 2015.

[16] N. C. Jeong, C. Prasittichai, and J. T. Hupp, "Photocurrent enhancement by surface plasmon resonance of silver nanoparticles in highly porous dye-sensitized solar cells," *Langmuir*, vol. 27, pp. 14 609–14 614, 2011.

[17] X. Dang, J. Qi, M. T. Klug, P. Chen, D. S. Yun, N. X. Fang, P. T. Hammond, and A. M. Belcher, "Tunable localized surfaces plas- mon-enabled broadband light-harvesting enhancement for high-efficiency panchromatic dye-sensitized solar cells," *Nano Letters*, vol. 13, pp. 637–642, 2013.

[18] K. Guo, M. Li, X. Fang, X. Liu, B. Sebo, Y. Zhu, Z. Hu, and X. Zhao, "Preparation and enhanced properties of dye-sensitized solar cells by surface plasmon resonance of Ag nanoparticles

in nanocomposite photoanode," *Journal of Power Sources*, vol. 230, pp. 155–160, 2013.

[19] S. Colodrero, A. Mihi, L. Häggman, M. Ocaña, G. Boschloo, A. Hagfeldt, and H. Míguez, "Porous one-dimensional photonic crystals improve the power-conversion efficiency of dye-sensitized solar cells," *Advanced Materials*, vol. 21, pp. 764–770, 2009.

[20] J. Kim, J. K. Koh, B. Kim, J. H. Kim, and E. Kim, "Nanopatterning of mesoporous inorganic oxide films for efficient light harvesting of dye-sensitized solar cells," *Angewandte Communications*, vol. 51, pp. 6864–6869, 2012.

[21] D. Barettin, A. d. Carlo, D. D. Angelis, M. Casalboni, and P. Prosposito, "Effect of dielectric Bragg grating nanostructuring on dye-sensitized solar cells," *Optics Express*, vol. 20, A888–A897, 2012.

[22] S. Wooh, H. Yoon, J. Jung, Y. Lee, J. H. Koh, B. Lee, Y. S. Kang, and K. Char, "Efficient light harvesting with micropatterned 3D pyramidal photoanodes in dye-sensitized solar cells," *Advanced Materials*, vol. 25, pp. 3111–3116, 2013.

[23] C. López-López, S. Colodrero, and H. Míguez, "Panchromatic porous specular back reflectors for efficient transparent dye solar cells," *Physical Chemistry Chemical Physics*, vol. 16, pp. 663–668, 2014.

[24] C. López-López, S. Colodrero, A. Jiménez-Solano, G. Lozano, R. Ortiz, M. E. Calvo, and H. Míguez, "Multidirectional light-harvesting enhancement in dye-sensitized solar cells by surface patterning," *Advanced Optical Materials*, vol. 2, pp. 879–884, 2014.

[25] A. Usami, "Theoretical study of application of multiple scattering of light to a dye-sensitized nanocrystalline photoelectrochemical cell," *Chemical Physics Letters*, vol. 277, pp. 105–108, 1997.

[26] Z. Wang, H. Kawauchi, T. Kashima, and H. Arakawa, "Significant influence of TiO_2 photoelectrode morphology on the energy conversion efficiency of N719 dye-sensitized solar cell," *Coordination Chemistry Reviews*, vol. 248, pp. 1381–1389, 2004.

[27] S. Hore, C. Vetter, R. Kern, H. Smit, and A. Hinsch, "Influence of scattering layers on efficiency of dye-sensitized solar

cells," *Solar Energy Materials & Solar Cells*, vol. 90, pp. 1176–1188, 2006.

[28] H. Koo, J. Park, B. Yoo, K. Yoo, K. Kim, and N. Park, "Size-dependent scattering efficiency in dye-sensitized solar cell," *Inorganica Chimica Acta*, vol. 361, pp. 677–683, 2008.

[29] A. Yella, H. Lee, H. N. Tsao, C. Yi, A. K. Chandiran, Md. K. Nazeeruddin, E. W. Diau, C. Yeh, S. M.Zakeeruddin, and M. Grätzel, "Porphyrin-sensitized solar cells with cobalt (II/III)-based redox electrolyte exceed 12 percent efficiency," *Science*, vol. 334, pp. 629–634, 2011.

[30] M. Son, H. Seo, S. Kim, N. Hong, B. Kim, S. Park, K. Prabakar, and H. Kim, "Analysis on the light-scattering effect in dye-sensi-tized solar cell according to the TiO_2 structural differences," *International Journal of Photoenergy*, vol. 2012, 2012.

[31] J. Ferber and J. Luther, "Computer simulations of light scattering and absorption in dye-sensitized solar cells," *Solar Energy Materials & Solar Cells*, vol. 54, pp. 265–275, 1998.

[32] A. Usami, "Theoretical simulations of optical confinement in dye-sensitized nanocrystalline solar cells," *Solar Energy Materials & Solar Cells*, vol. 64, pp. 73–83, 2000.

[33] Y. Tachibana, K. Hara, K. Sayama, and H. Arakawa, "Quantitative analysis of light-harvesting efficiency and electron-transfer yield in ruthenium-dye-sensitized nanocrystalline TiO_2 solar cells," *Chemistry of Materials*, vol. 14, pp. 2527–2535, 2002.

[34] Y. Chiba, A. Islam, Y. Watanabe, R. Komiya, N. Koide, and L. Han, "Dye-sensitized solar cells with conversion efficiency of 11.1%," *Japanese Journal of Applied Physics*, vol. 45, pp. L638–L640, 2006.

[35] F. E. Gálvez, E. Kemppainen, H. Míguez, and J. Halme, "Effects of diffuse light scattering designs on the efficiency of dye solar cells: An integral optical and electrical description," *The Journal of Physical Chemistry C*, vol. 116, pp. 11 426–11 433, 2012.

[36] C. J. Barbé, F. Arendse, P. Comte, M. Jirousek, F. Lenzmann, V. Shklover, and M. Grätzel, "Nanocrystalline titanium oxide electrodes for photovoltaic applications," *Journal of the American Ceramic Society*, vol. 80, pp. 3157–3171, 1997.

[37] S. H. Kang, J. Kim, H. S. Kim, H. Koh, J. Lee, and Y. Sung, "Influence of light scattering particles in the TiO_2 photoelectrode for solid-state dye-sensitized solar cell," *Journal of Photochemistry and Photobiology A: Chemistry*, vol. 200, pp. 294–300, 2008.

[38] H. Arakawa, T. Yamaguchi, T. Sutou, Y. Koishi, N. Tobe, D. Matsumoto, and T. Nagai, "Efficient dye-sensitized solar cell sub-modules," *Current Applied Physics*, vol. 10, S157–S160, 2010.

[39] A. Mihi and H. Míguez, "Origin of light-harvesting enhancement in colloidal-photonic-crystal-based dye-sensitized solar cells," *Journal of Physical Chemistry B*, vol. 109, pp. 15 968–15 976, 2005.

[40] A. Mihi, F. J. López-Alcaraz, and H. Míguez, "Full spectrum enhancement of the light harvesting efficiency of dye-sensitized solar cells by including colloidal photonic crystal multilayers," *Applied Physics Letters*, vol. 88, p. 193 110, 2006.

[41] A. Mihi, M. E. Calvo, J. A. Anta, and H. Míguez, "Spectral reponse of opal-based dye-sensitized solar cells," *Journal of Physical Chemistry C*, vol. 112, pp. 13–17, 2008.

[42] G. Lozano, S. Colodrero, O. Caulier, M. E. Calvo, and H. Míguez, "Theoretical analysis of the performance of one-dimensional photonic crystal-based dye-sensitized solar cells," *Journal of Physical Chemistry C*, vol. 114, pp. 3681–3687, 2010.

[43] D. Colonna, S. Colodrero, H. Lindström, A. d. Carlo, and H. Míguez, "Introducing structural colour in DSCs by using photonic crystals: interplay between conversion efficiency and optical properties," *Energy & Environmental Science*, vol. 5, pp. 8238–8243, 2012.

[44] C. López-López, S. Colodrero, M. E. Calvo, and H. Míguez, "Angular response of photonic crystal based dye sensitized solar cells," *Energy & Environmental Science*, vol. 6, pp. 1260–1266, 2013.

[45] M. Anaya, M. E. Calvo, J. M. Luque-Raigón, and H. Míguez, "Resonant photocurrent generation in dye-sensitized periodically nanostructured photoconductors by optical field confinement effects," *Journal of the American Chemical Society*, vol. 135, pp. 7803–7806, 2013.

[46] Y. Li, M. E. Calvo, and H. Míguez, "Integration of photonic crystals into flexible dye solar cells: A route toward bendable and adaptable optoelectronic devices displaying structural color and enhanced efficiency," *Advanced Optical Materials*, vol. 4, pp. 464–471, 2016.

[47] F. E. Gálvez, P. R. F. Barnes, J. Halme, and H. Míguez, "Dye sensitized solar cells as optically random photovoltaic media," *Energy & Environmental Science*, vol. 7, pp. 689–697, 2014.

[48] G. Lee, H. Lee, M. Um, and M. Kang, "Light scattering amplification on dye sensitized solar cells assembled by hollyhock-shaped CdS-TiO_2 composites," *Bulleting of the Korean Chemical Society*, vol. 33, pp. 3043–3047, 2012.

[49] J. Durantini, P. P. Boix, M. Gervaldo, G. M. Morales, L. Otero, J. Bisquert, and E. M. Barea, "Photocurrent enhancement in dye-sensitized photovoltaic devices with titania–graphene composite electrodes," *Journal of Electroanalytical Chemistry*, vol. 683, 43–46, 2012.

5 *Mie glasses* for light emission applications

5.1 Introduction

From lighting of households or workplaces to more specific applications, such as backlighting in screens or traffic lights, artificial illumination has become an essential requirement in the daily activities of the current civilisation. The targeted application defines the characteristics of the light, such as colour, intensity or even directionality. For that reason, the devising of routes allowing an efficient generation of light with tunable properties appears as a task of uttermost importance. In that regard, a revolution started with the entrance of LEDs into the market. These devices usually present a PC-LED structure, which rely on a conversion layer for the down-shifting of light emitted by an LED chip. Colour conversion is therefore a fundamental step in the process of light generation.

Conversion layers usually included in commercial lamps are constituted by phosphor crystals of a size around a few microns. As a consequence, these films present high opacity. The lack of transparency hinders a design of their optical response. Optical quality is required in a film as a starting point in order to controllably tune its optical properties by means of any approach entailing the integration of photonic structures. Besides, the lack of transparency hinders their suitability for use as transparent emissive screens and therefore their application in displays. Total internal reflection of light inside the high-refractive index of the different elements comprising LEDs leads to light guiding and subsequent escape through the edges, thus resulting in unusable light, which is known for being one of the principal causes of efficiency loss in LEDs[1,2]. The inclusion of scattering structures has been widely employed as a means to tackle this issue in different sorts of light-emitting devices[3–10]. In an attempt to enhance the luminescence of emitters through plasmonic approaches, the inclusion of metallic structures has also been tested[11–15]. Nevertheless, large absorption losses are expected in the excitation range of the phosphors when compared to dielectric inclusions[16]. The problem has been thoroughly studied for LEDs integrating a RE-based conversion layer[17]. Nonetheless, the limitations imposed by the nature

of the materials have hindered the development of new strategies for the tuning and enhancement of light extraction.

This chapter presents a discussion on the use of different types of *Mie glasses* as efficient colour converters. In the first section, the TiO_2-based *Mie glass* is infiltrated with an emitting dye and the changes in the PL in relation to the conditions of the introduced disorder are inspected. The emission of the material is characterised for different size and concentration conditions of the scattering centres and several aspects are analysed. The study demonstrates how optical disorder enables PL enhancement through a combination of resonant excitation and a more efficient extraction of the light, which is justified by the ℓ_{sc} values of the material at the wavelengths of interest. The second section investigates the effect of the presence of optical disorder in a *Mie glass* based on a luminescent matrix on its PL. Besides, the material is susceptible to be supported in a polymeric matrix for the development of a flexible version. In particular, a PL enhancement dependent on the disorder conditions is revealed, which is demonstrated to exclusively derive from a more efficient out-coupling of the generated light from the film. Static and dynamic PL measurements are demonstrated to enable an analysis of the range of the disorder parameters where the integration of scattering particles boosts the PL of the film.

5.2 TiO_2 inclusions in a TiO_2 matrix for efficient colour conversion

The *Mie glass* has been introduced as a low-cost material integrating optical disorder in a controlled manner that allows the study of fundamental aspects of the propagation of light in turbid media by means of an analytical formalism. Specifically, Sec. 3.3 in Ch. 3 includes a full study on the optical properties of a *Mie glass* consisting of TiO_2 inclusions in a mesoporous TiO_2 matrix, which has been proved to behave as a solid dilute suspension of spheres. Accordingly, its scattering properties have been demonstrated to be susceptible to be designed prior to fabrication. Nevertheless, the potential of *Mie glasses* does not reside entirely on the easy tuning of their scattering properties for a desired optical response. Their high specific surface area,

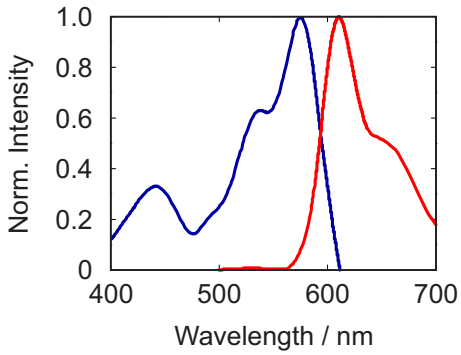

Figure 5.1: Normalised excitation (blue line) and emission (red line) spectra of the Lumogen® F Red 305 fluorophore.

$\approx$ 150 $m^2 \cdot cm^{-3}$, enables infiltration with an emitting dye, whose luminescence properties can be significantly altered by the presence of strongly scattering particles. This feature reveals the capability of the developed material for implementation in light emission applications. In this section, the *Mie glass* based on a mesoporous TiO_2 matrix is demonstrated to yield improved emission when sensitised with luminescent organic molecules in comparison to a bare sensitised porous anatase film, therefore proving its potential as an efficient colour converter.

Lumogen® F Red 305 dye was employed for sensitisation of the films through adsorption to the TiO_2-nanoparticle matrix. This is an appealing fluorophore in the field of solid-state lighting owing to its chemical stability and high quantum yield[15] as compared with other organic molecules. Figure 5.1 shows the excitation and emission spectra of this fluorophore, which reveals three main excitation peaks at $\lambda_{pump} = 440$ nm, $\lambda_{pump} = 530$ nm and $\lambda_{pump} = 575$ nm, and one main emission line at *ca.* $\lambda_{em} = 616$ nm. Details about the infiltration process are available in the *Methods* chapter. Fourier image spectroscopy, a technique detailed in Ch. 2, allowed the determination of the angular dependence of the PL of the sensitised films, Fig. 5.2, which consisted in a bare mesoporous TiO_2 film and *Mie glasses* integrating scattering centres with the size and concentration values r = (95 $\pm$ 20) nm - f = 5%, r = (225 $\pm$ 20) nm - f = 5% and r = (225 $\pm$ 20) nm - f = 10%. Figure 5.2(a) illustrates the angular-dependent PL of a reference film, *i.e.* a mesoporous TiO_2 matrix infiltrated with the red-emitting

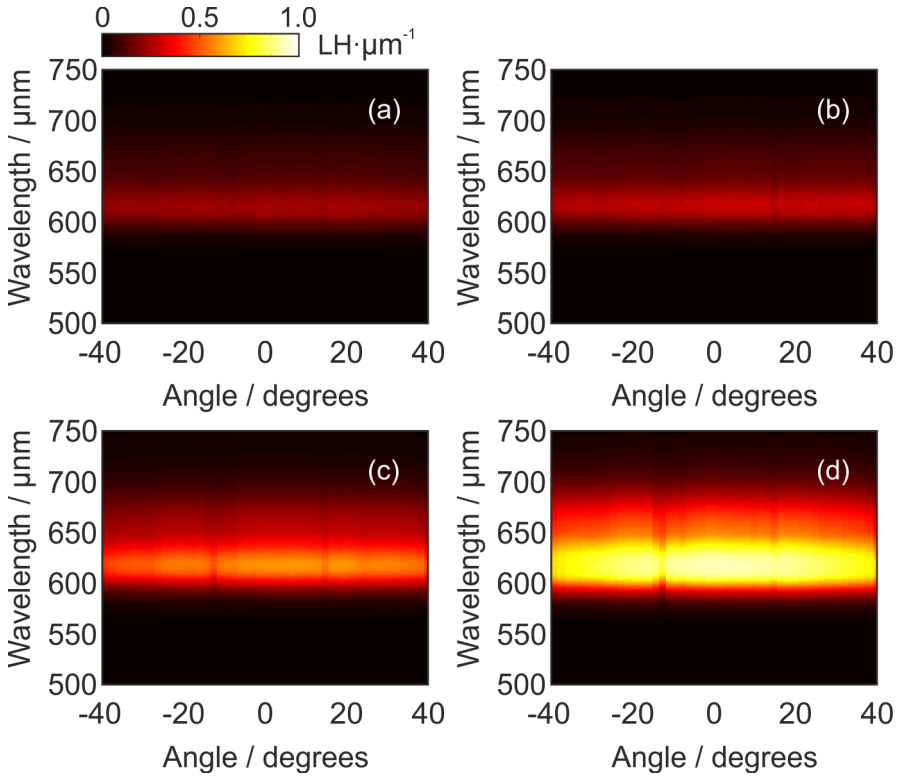

Figure 5.2: Normalised angular-dependent PL spectra for (a) a sensitised reference film and sensitised films integrating inclusions with the conditions (b) r = (95 $\pm$ 20) nm - f = 5%, (c) r = (225 $\pm$ 20) nm - f = 5% and (d) r = (225 $\pm$ 20) nm - f = 10%. The films were excited at λ_{pump} = 532 nm. Thickness of the film was 7.5 μm for all the cases. The spectra were normalised to the maximum value obtained for the measurement yielding the most intense PL.

dye, when excited at λ_{pump} = 532 nm by a laser diode. The emitted light revealed a Lambertian profile, typical of an optically flat luminescent film. The integration of scattering centres boosted the emission intensity while preserving the angular profile, Fig. 5.2(b)-(d), and an increase of size and/or concentration of the inclusions led to a more intense PL. The PL enhancement was quantified through the

enhancement factor, $\beta_{tot}(\lambda_{pump},\lambda_{em})$, defined as

$$\beta_{tot}(\lambda_{pump},\lambda_{em}) = \frac{\int_{\lambda_1}^{\lambda_2} PL(\lambda_{pump},\lambda_{em})d\lambda_{em}}{\int_{\lambda_1}^{\lambda_2} PL_{ref}(\lambda_{pump},\lambda_{em})d\lambda_{em}} = \beta_{pump}(\lambda_{pump})\cdot\beta_{em}(\lambda_{em}), \tag{5.1}$$

being $\mathrm{PL}(\lambda_{pump},\lambda_{em})$ the photoluminescence spectrum of the corresponding *Mie glass*, $\mathrm{PL_{ref}}(\lambda_{pump},\lambda_{em})$ that of a reference film of comparable thickness, while λ_1 and λ_2 establish the integration range. The total PL enhancement ($\beta_{tot}(\lambda_{pump},\lambda_{em})$) can be originated by phenomena occurring at the pumping wavelength, $\beta_{pump}(\lambda_{pump})$, or at the emission wavelength, $\beta_{em}(\lambda_{em})$, of the dye molecules. On the one hand, PL can be boosted owing to resonant excitation, inducing a more efficient absorption of the pumping light by the dye molecules. For shorter values of ℓ_{sc}, the probability of a photon undergoing an scattering event increases, therefore enlarging the average path length of the light inside the film, yielding longer matter-radiation interaction times and resulting in a higher effective absorption cross section of the luminescent molecules, as previously corroborated in Sec. 3.3.2.3 of Ch. 3 for the dye N719. Table 5.1 includes the calculated ℓ_{sc} values for the three materials under consideration at the different pumping wavelengths. On the other hand, a more intense PL can originate from an enhanced out-coupling of the emitted light in defined directions or from the spatial fluctuation of the local density of optical states, LDOS, typical of complex random media[18,19], which may involve an increase of the QY of the system. However, due to insufficient light scattering, only the former effect could be expected to play an important role on the luminescence enhancement in the *Mie glasses* herein studied. In fact, a modification of the LDOS as the

Table 5.1: Scattering mean free path values at the different pumping wavelengths for the considered films.

	ℓ_{sc} / μm		
	λ_{pump} = 440 nm	λ_{pump} = 530 nm	λ_{pump} = 575 nm
r = (95 $\pm$ 20) nm - f = 5%	1.3	5.0	6.1
r = (225 $\pm$ 20) nm - f = 5%	1.4	1.6	1.6
r = (225 $\pm$ 20) nm - f = 10%	0.7	0.8	0.8

phenomenon originating a PL enhancement is not likely. The PL intensity of the emitting molecules is dependent on the radiative decay rate of the electrons in an excited state, which is a function of the LDOS. However, no significant variation of the LDOS is expected as a consequence of including scattering centres in such a low concentration. Thus, it can be reasonably assumed that no quantum yield enhancement is expected through this effect. Besides, a convenient variation of the LDOS leading to an improvement of the photoemission requires the design of a very specific optical environment particularly conceived to that purpose[19,20], far from the case herein studied. The presence of inclusions is therefore expected to improve the outcoupling of light due to efficient light scattering, leading to a higher probability of light reaching the material-air interface at angles within the escape cone. This means that light emitted at an angle above the critical angle could certainly have a probability to be effectively extracted as usable light. Figure 5.3 displays the variation in the PL intensity with respect to the conditions of the scattering centres in the different studied films in relation to λ_{pump}. The PL of the films was characterised by means of an integrating sphere coupled to a spec-

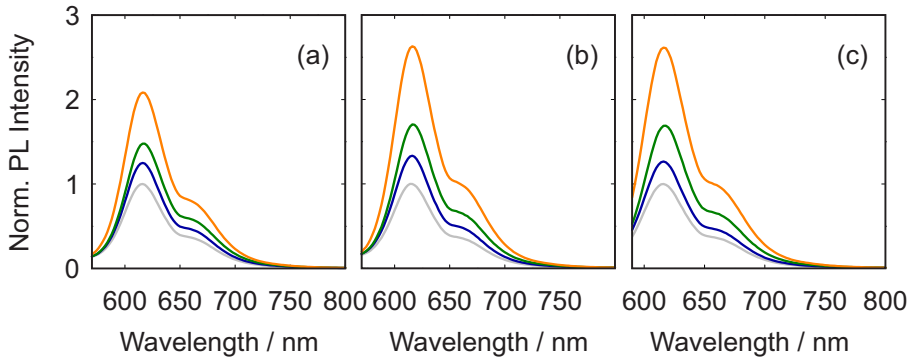

Figure 5.3: Normalised PL spectra for a sensitised reference film (gray line) and sensitised films integrating scattering centres with the conditions r = (95 $\pm$ 20) nm - f = 5% (blue line), r = (225 $\pm$ 20) nm - f = 5% (green line) and r = (225 $\pm$ 20) nm - f = 10% (orange line) under excitation at (a) λ_{pump} = 440 nm, (b) λ_{pump} = 530 nm and (c) λ_{pump} = 575 nm. The spectra were normalised to the highest value yielded by the reference film. Thickness of the film was 7.5 μm for all the cases.

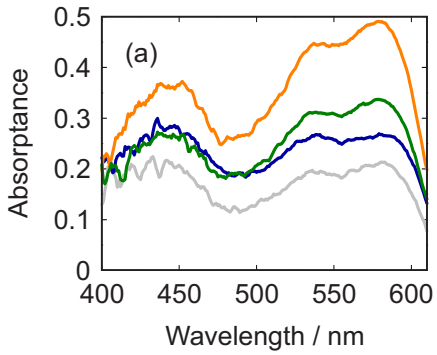

Figure 5.4: Absorptance spectra for a sensitised reference film (gray line) and films integrating scattering centres with the conditions r = (95 ± 20) nm - f = 5% (blue line), r = (225 ± 20) nm - f = 5% (green line) and r = (225 ± 20) nm - f = 10% (orange line).

trofluorometer, as detailed in Ch. 2, which allowed collection of the light emitted in all directions. The PL was enhanced for all the *Mie glasses* when comparing to a reference film, Fig. 5.3. β_{pump} at a specific wavelength was obtained for each film through determination of their absorptance and comparing to that for a reference film of comparable thickness devoid of scattering centres, so that $\beta_{pump} = \frac{A_{Mie}}{A_{ref}}$, where A_{Mie} refers to the absorptance of the sensitised *Mie glass* under consideration and A_{ref} to that of a reference film, which are shown in Fig. 5.4. The values obtained for β_{pump} at the three different pumping wavelengths considered for the studied films are displayed in Table 5.2. The total emission enhancement (β_{tot}) for each condition of scattering centres at the three different pumping wavelengths is illustrated in Fig. 5.5. Here, the length of the bar accounts for β_{tot}, while

Table 5.2: Absorptance enhancement factor (β_{pump}) at the different pumping wavelengths for the films under consideration.

	$\beta_{pump}(\lambda_{pump})$		
	λ_{pump} = 440 nm	λ_{pump} = 530 nm	λ_{pump} = 575 nm
r = (95 ± 20) nm - f = 5%	1.32	1.37	1.27
r = (225 ± 20) nm - f = 5%	1.28	1.62	1.62
r = (225 ± 20) nm - f = 10%	1.75	2.29	2.36

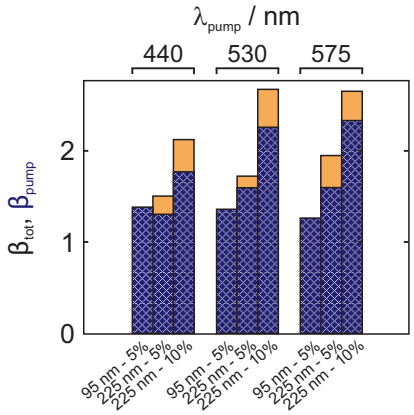

Figure 5.5: PL enhancement for each considered film excited at the three main excitation wavelengths. The length of each bar corresponds to the total PL enhancement, β_{tot}, the blue region accounts for the fraction of β_{tot} originating from an improvement at the wavelength of excitation, β_{pump}, and the dark yellow region indicates the fraction of β_{tot} deriving from a more efficient out-coupling of the generated light, β_{em}.

the blue region corresponds to the fraction of the emission enhancement caused by an increase of the absorptance, namely, β_{pump}. This representation indicates that most of the PL enhancement was a consequence of an increased absorption of light by the dye molecules at the pumping wavelength caused by the scattering of light, which could be therefore explained in terms of ℓ_{sc}. This means that a film integrating scattering centres is equivalent to a film devoid of inclusions of larger thickness. Besides, the fraction of β_{tot} owing to a more efficient extraction of light, quantified through β_{em} and indicated by a dark yellow area in Fig. 5.5, revealed a general increasing trend for a higher inclusion concentration or size due to shorter ℓ_{sc} values, according to Table 5.1. This demonstrated that a larger number of scattering events increased the probability that photons reached the film/air interface at an angle within the escape cone, therefore resulting in an average increase of the light extracted from the material. For this reason, for a small size and low volume filling fraction of inclusions, as it was for the case r = (95 ± 20) nm - f = 5%, β_{tot} roughly equaled β_{pump}, regardless of the pumping wavelength. A maximum β_{tot} of 2.68 was

attained for the conditions r = (225 ± 20) nm - f = 10%, for which $\beta_{pump} = 2.27$ at a pumping wavelength $\lambda_{pump} = 530$ nm.

All of the above confirmed that a tuning of light scattering in *Mie glasses* enables a fine control over the spontaneous emission intensity of luminescent molecules adsorbed to their porous matrix through modification of light absorption at the pumping wavelength and light out-coupling over a large area.

5.3 TiO_2 scattering centres in a luminescent matrix

The materials comprising the *Mie glass* addresses in the previous section are susceptible to be replaced by another material if resulting more suitable for specific applications. The optical response would be preserved as long as the refractive index of the material is similar to that of TiO_2. For instance, the TiO_2 matrix can be replaced by a mesoporous luminescent material. This would produce a new optically disordered medium presenting similar diffusive properties than its TiO_2 analogous plus the additional feature of light emission. This extra property endows the material with suitability for applications related to light emission.

As previously mentioned, a colour-converting material is generally required for light generation in commercial LEDs. Exhaustive studies on the suitability of RE-doped materials for this purpose have been performed[21–23]. In fact, a common route for the fabrication of adaptable and versatile colour conversion coatings for integration into LED devices consists in the dispersion of RE phosphors in a polymeric matrix[24–26]. The base material addressed in this section comprises an inorganic matrix doped with RE cations, endowing it with luminescent properties. In the first place, the fabrication and optical characterisation of mesoporous transparent films of this material, with a refractive index comparable to that of TiO_2, which is susceptible to be transferred into a flexible support, is depicted. From that starting point, spherical TiO_2 scattering centres are randomly distributed inside this luminescent matrix in the same fashion than the *Mie glass* depicted in the previous section, giving rise to a new random medium capable of yielding light emission. Eventually, the luminescent properties of this material are analysed in terms of the condi-

tions of the optical disorder included and the emission enhancement triggered by the presence of scattering particles is quantified. The potential of this material resides in the possibility of use as a colour-converting material for light-emitting applications.

5.3.1 Flexible and transparent luminescent mesoporous films

A sequential procedure based on solution-processing methods for the fabrication of a flexible and transparent film capable of displaying luminescence was developed. With that purpose, crystalline nanoparticles doped with RE cations were synthesised following a procedure already reported, as indicated in Sec. 2.1.3.1 in Ch. 2. These particles present luminescence when excited with light of the appropriate wavelength and are therefore suitable for operation as phosphors. Specifically, these phosphors consist of a crystalline gadolinium vanadate ($GdVO_4$) matrix co-doped with trivalent cations of bismuth and europium ($GdVO_4$:Bi^{3+},Eu^{3+}). As previously mentioned in the *Methods* chapter, nanoparticles of cubic shape and an average size of (36 $\pm$ 7) nm resulted from the synthesis. Due to the small size of the particles, they could be employed for the preparation of films yielding high transparency. Although the synthesis produced phosphors in an amorphous phase, the thermal treatment required to achieve mechanical stabilisation of the films modified their internal structure into a crystalline phase. Solid porous luminescent films were fabricated using crystalline nanophosphors as base material, SEM image in Fig. 5.6(a). The $GdVO_4$ matrices were co-doped with Bi^{3+}, since this caused a broadening of the excitation spectrum, thus enabling excitation at wavelengths closer to the visible region of the spectrum, as evidenced by the spectra displayed in Fig. 5.6(b). This would be profitable, considering the potential of such films as conversion layers in light-emitting applications dependent on UV radiation for excitation. The peak below 300 nm in the excitation spectrum derives from energy absorption by the VO_4^{3-} ions, which is later on efficiently transferred to the Eu^{3+} centres. In the spectrum, this absorption is followed by a broad decay up to 400 nm originated from energy absorption by the Bi^{3+} centres to be subsequently transferred into the Eu^{3+} cations. Eu^{3+} cations can also be directly excited at around λ = 393 nm. It is not however visible in the spectrum owing to its low ab-

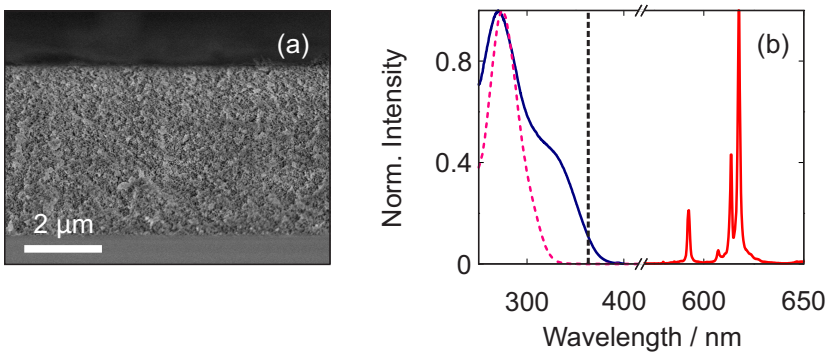

Figure 5.6: (a) SEM cross section image of a nanophosphor-based film deposited from a viscous paste by doctor blade. (b) Excitation (blue) and emission (red) spectrum of a mesoporous film comprising $GdVO_4$:Bi^{3+},Eu^{3+} nanophosphors. The excitation spectrum of an analogous film consisting of phosphors devoid of Bi^{3+} (dashed pink line) has been included for the sake of comparison. The excitation wavelength $\lambda = 365$ nm used in this study has been pointed out with a dashed black line.

sorption cross section in comparison to that for mediated $GdVO_4$:Bi^{3+} matrix excitation. As for the PL, an intense and narrow emission peak is visible around $\lambda = 617$ nm, in the red part of the spectrum, derived from the electric-dipole transition $^5D_0 \rightarrow {}^7F_2$ of Eu^{3+} cations. Aiming at UV-emitting LED integration, $\lambda = 365$ nm was purposely chosen as excitation wavelength.

The films should desirably present maximum extinction of the incident light at the excitation wavelength. In order to determine the minimum thickness required for maximum absorption, a study on the variation of the absorptance of a nanophosphor film with layer thickness was performed. Such study revealed that a film with thickness around 4 μm absorbed up to 76% of the incident light at $\lambda = 365$ nm, as Fig. 5.7(a) reveals. The corresponding R and T spectra are included in Fig. 5.7(b). Quartz was employed as a substrate so as to avoid any absorption component not originated at the nanophosphor film. Thicker layers would result inconvenient if maximum brightness is sought for, since no light would remain available to be absorbed beyond a depth around 4 μm at the wavelength of interest[23].

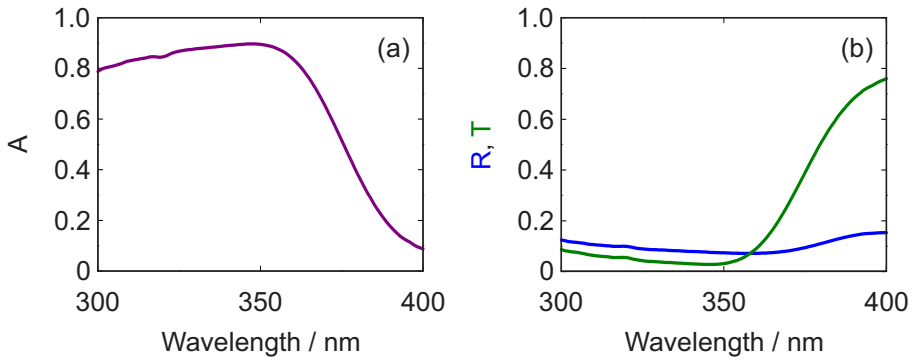

Figure 5.7: (a) Absorptance and (b) total reflectance and transmittance spectra of a nanophosphor-based film with thickness around 4 μm.

As previously pointed out, the nanometric size of the phosphors allowed the preparation of films displaying high transparency in the visible range of the spectrum, as evidenced in Fig. 5.8(a) for a 4-μm thick layer. Indeed, UV-light irradiation triggered intense red emission for both versions of the film, as demonstrated by the picture in Fig. 5.8(b). Besides, these luminescent films were expected to preserve the excellent thermal stability of the crystalline nanophosphors, a known feature of this sort of particles. The situation was however different for the flexible version. Here, the nanophosphors were encapsulated in a polymeric material endowing the film with flexibility.

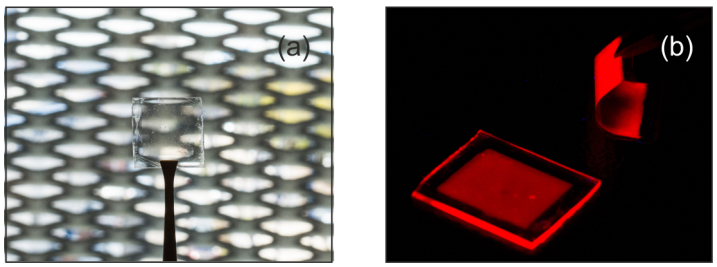

Figure 5.8: (a) Picture of a 4-μm nanophosphor film displaying high transparency in the visible range. (b) Picture of a rigid and a flexible nanophosphor-based film under UV irradiation. The films display intense red emission originated by the energy transfer from the $GdVO_4$:Bi^{3+} matrix into the Eu^{3+} centres.

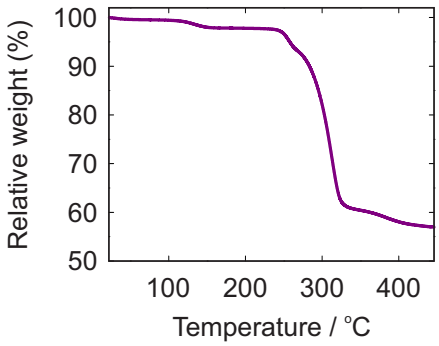

Figure 5.9: Thermogravimetric analysis of the flexible films comprising a nanophosphor layer embedded in PMMA.

In this case, the thermal stability of the film was predominantly restricted to that of the embedding material. In effect, the thermogravimetric analysis displayed in Fig.5.9 demonstrates that the thermal stability of the flexible film was dictated by that of the PMMA, which remains stable up to 250^{o}C, and therefore resulting compatible with high-power LED devices.

In short, all of the above proves the feasibility of highly transparent rigid and flexible luminescent films based on nano-sized phosphors, which display intense red PL under irradiation with light in the UVA region, that is, $\lambda_{pump} > 350$ nm. With that purpose, a procedure based on low-cost solution-processing methods was developed.

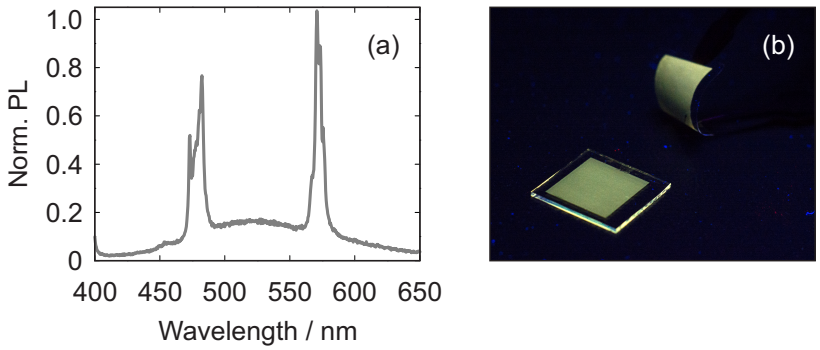

Figure 5.10: (a) PL spectrum of a light-emitting film comprising $GdVO_4$:Bi^{3+},Dy^{3+} nanophosphors. (b) Picture of a rigid and a flexible film fabricated with Dy^{3+}-based nanophosphors.

One of the main advantages of such procedure is its generality, which enables extension to other colour-emitting nanophosphors. For instance, the Eu^{3+} centres can be replaced by Dy^{3+}, yielding films based on $GdVO_4$:Bi^{3+},Dy^{3+} nanophosphors, which display a greenish luminescence due to the main emission lines at $\lambda = 482$ nm and $\lambda = 570$ nm. Both the emission spectrum and a picture of a rigid and a flexible film based on Dy^{3+}-doped nanophosphors under UV radiation are visible in Fig. 5.10(a) and (b), respectively. These luminescent films present the potential to be integrated into LEDs as a colour converter. Besides, a self-standing flexible colour converter is particularly attractive due to its ease of implementation and transport.

5.3.2 Optically random material based on a luminescent matrix

This section presents a study of the optical response of the material resulting from the integration of scattering centres into these transparent luminescent films, followed by an analysis of their luminescent properties in terms of the conditions of the scattering centres.

5.3.2.1 Scattering centre integration

Following the procedure established in this thesis for the inclusion of optical disorder in transparent matrices, a new optically disordered medium was fabricated by randomly distributing spherical TiO_2 scattering centres in a nanophosphor matrix. Specifically, nanocrystalline anatase spheres of radius $r = (225 \pm 20)$ nm were employed as scattering elements. Details on how to integrate these scattering centres in the nanophosphor matrix are available in Sec. 2.1.2.3 in Ch. 2. Figure 5.11(a), showing a film integrating scattering centres in a 10% volume concentration, proves that the *Mie glass* structure was maintained, thus allowing a similar discussion. It was therefore legitimate to assume that filling fraction values from 5% to 15% can be considered low enough to enable a description of light scattering exclusively dictated by single-particle considerations. In line of the disorder characterisation performed for the TiO_2-based *Mie glass*, Sec. 3.3.2.1 of Ch. 3, ℓ_{sc} was calculated for different concentration values in the range 5 - 15% in order to assess the effect of increasing the concentration of inclusions on the optical response of the material, Fig. 5.11(b). A 50%

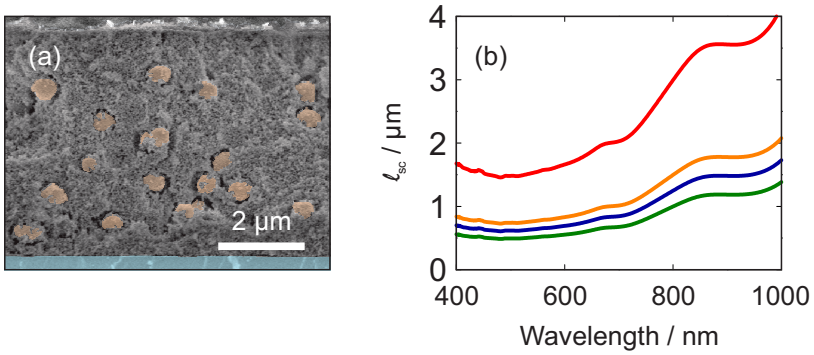

Figure 5.11: (a) SEM cross section image of a nanophosphor film integrating spherical TiO_2 scattering centres in a 10% volume concentration. The inclusions and the substrate were shaded with colour for the sake of clarity. (b) Spectral ℓ_{sc} curves calculated employing Mie formalism for systems comprising a nanophosphor film including TiO_2 spheres of size r = (225 $\pm$ 20) nm surrounded by an air shell of thickness 0.43r and concentration f = 5% (red), f = 10% (orange), f = 12% (blue) and f = 15% (green). The polydispersity in the size of the scattering centres was taken into account for the calculations.

porosity was assumed for the nanophosphor matrix and an air layer of thickness 0.43r, where r is the radius of the scattering inclusions, surrounding each scattering particle was taken into account. Polydispersity in the size of the scattering spheres was considered in the calculations. The optical constants employed for the ℓ_{sc} calculations according to the Mie formalism are presented in Fig. 5.12. Higher filling fraction values entail lower ℓ_{sc} values, namely, higher scattering strength. In effect, these ℓ_{sc} curves display a similar trend than those for the *Mie glass* comprising a TiO_2 matrix already displayed in Sec. 3.3.2.1 of Ch. 3. Such similarity had been anticipated due to the comparable optical refractive index of the nanophosphor matrix to that of a porous anatase matrix. Whereas the nanophosphor-based film displayed high transparency in the visible range of the spectrum, the inclusion of optical disorder triggered diffuse propagation of part of the traveling light, thus increasing its opacity. As a consequence, the film acquired a whitish appearance typical of turbid media, Fig. 5.13(a). The loss of transparency was evidenced by the reduction of the inten-

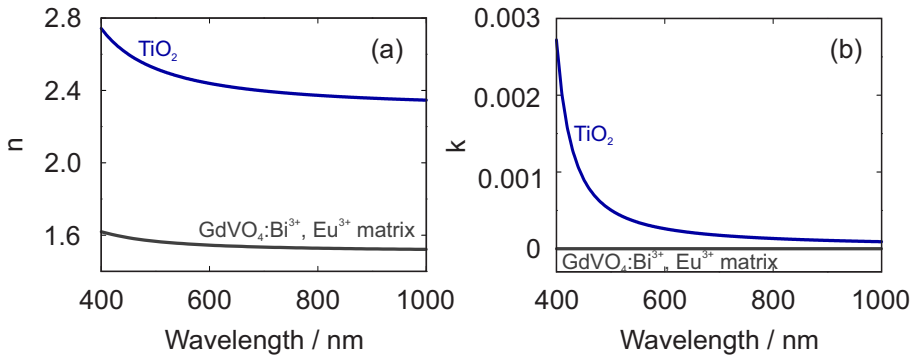

Figure 5.12: Optical constants of the materials considered in the simulations. (a) Real part of the complex refractive index. (b) Imaginary part of the complex refractive index.

sity of T_b, Fig. 5.13(b), further corroborating the trend revealed by the calculated ℓ_{sc} curves in Fig. 5.11(b).

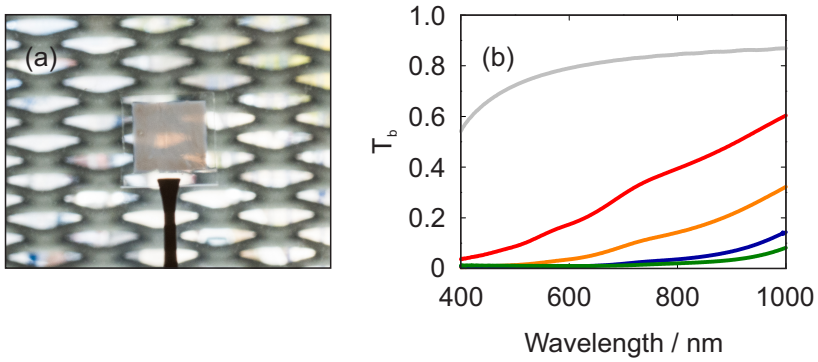

Figure 5.13: (a) Picture of a 4-μm nanophosphor film including crystalline TiO_2 spheres in a 5% volume concentration. The integration of scattering particles triggers diffuse propagation of the light. (b) Ballistic transmittance yielded by a reference nanophosphor film (gray) and nanophosphor films integrating scattering particles in a 5% (red), 10% (orange), 12% (blue) and 15% (green) concentration.

5.3.2.2 Optical disorder as a route towards efficient light out-coupling in luminescent films

Based on the results presented in Sec. 5.2, which demonstrated the enhancement of the extraction of light from a similar material due to the presence of scattering centres, the integration of identical inclusions in order to boost the emission efficiency of these films *via* increased out-coupling of the generated light was proposed. Owing to the possibility of tailoring the amount of disorder, the approach introduces the novelty of offering tuning of the out-coupling of the emitted light.

In order to explore the relationship between the PL enhancement, that is, β_{tot}, and the amount of optical disorder introduced in the film, TiO_2 spherical particles were randomly integrated with different conditions, namely, spheres of size r = (225 ± 20) nm in concentrations 5%, 10%, 12% and 15%. As Fig.5.14(a) illustrates, the PL of a nanophosphor film is preserved after transference into a flexible polymeric support. PMMA was employed as polymer due not only to the high optical quality of the resulting films, but also to the negligible absorption of the polymer in the visible range and especially at the excitation wavelength of the phosphors chosen for the study, namely, $\lambda = 365$ nm, as evidenced by Fig. 5.14(b). In light of this observation, the complete analysis was performed on rigid films for

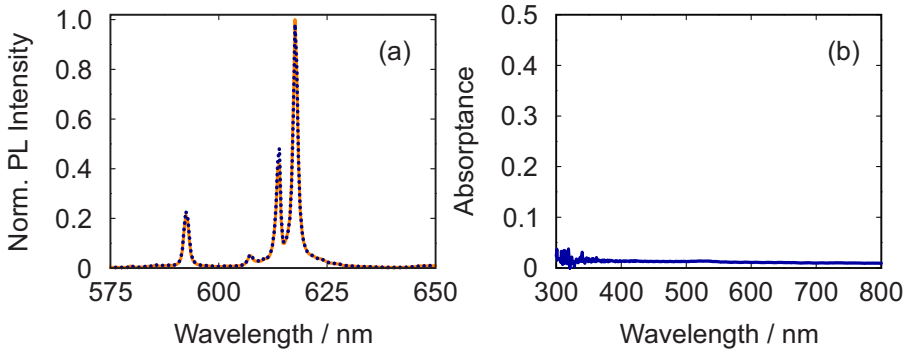

Figure 5.14: (a) Normalised PL spectra for a 4-μm $GdVO_4$:Bi^{3+},Eu^{3+} nanophosphor film infiltrated with PMMA under irradiation at $\lambda = 365$ nm before (dotted dark blue line) and after (orange line) layer release. (b) Absorptance spectrum of a PMMA layer of thickness larger than 4 μm.

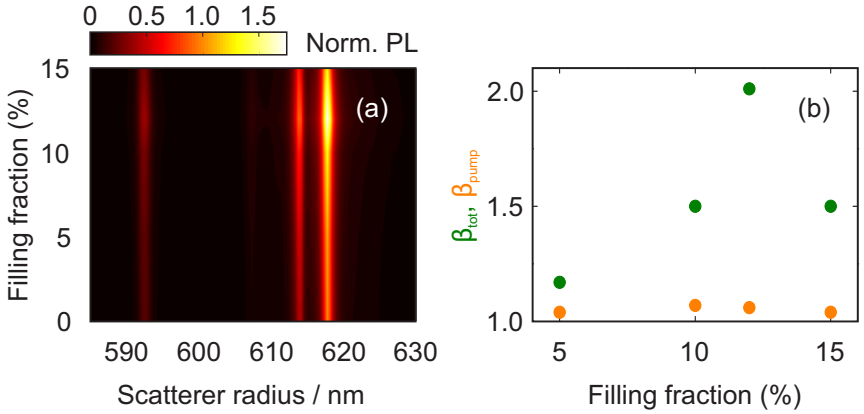

Figure 5.15: (a) Normalised PL spectra for the emitting *Mie glasses* under consideration resulting from integrating spherical TiO_2 particles into luminescent nanophosphor-based films with diverse concentrations. (b) Values of the PL enhancement, β_{tot} (green dots), and absorptance improvement at the pumping wavelength, β_{pump} (orange dots). All the films were infiltrated with PMMA.

the sake of experimental ease. Figure 5.15(a) displays the PL spectra for the different emitting *Mie glasses* in relation to the concentration of inclusions. Higher concentrations generally led to an average more intense emission, notably appreciable at the emission line at λ = 617 nm. Maximum PL was observed for a scattering centre volume filling fraction f = 12%. β_{tot} is illustrated in Fig. 5.15(b), calculated according to expression 5.1, along with the fraction of the emission enhancement deriving from an improvement of the absorptance at the pumping wavelength, β_{pump}, when compared to a reference film. The values of β_{pump} were calculated from the absorptance spectra determined through measurements, Fig. 5.16. β_{pump} remained virtually invariable with a value close to 1, regardless of the concentration of scattering particles, since the thickness of the film, 4 μm, had been carefully chosen in order to ensure absorption of most of the incident light at λ_{pump}. Therefore, any PL improvement had to necessarily be attributed to a more efficient out-coupling of the light from the film, $\beta_{tot} \approx \beta_{em}$, reducing the fraction of light remaining trapped inside. Measurements of decay dynamics usually help to gain understanding of underlying physical phenomena. As previously explained in

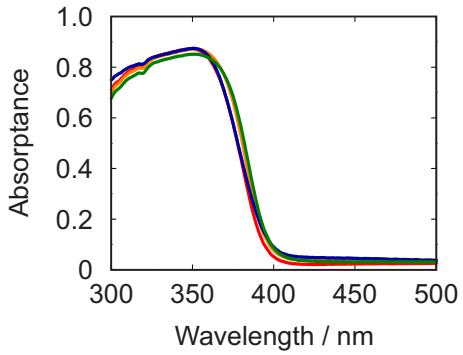

Figure 5.16: Absorptance spectra for nanophosphor-based films infiltrated with PMMA for a reference film (gray line) and films integrating spherical TiO_2 inclusions with concentration f = 5% (red line), f = 10% (orange line), f = 12% (blue line) and f = 15% (green line).

Sec. 5.2, the inclusion of crystalline TiO_2 spheres in the low concentration values herein considered was not expected to cause a modification of the available LDOS of the material. Consequently, the lifetime of the decay processes responsible for the PL of the nanophosphors should not be altered by the integration of scattering centres. The decay curves were obtained for the different films, Fig. 5.17(a), under excitation at $\lambda = 365$ nm and monitored at $\lambda = 617$ nm. A double exponential model was considered for the fitting of the time-resolved PL:

$$PL(t) = I_{01}e^{-\frac{t}{\Gamma_1}} + I_{02}e^{-\frac{t}{\Gamma_2}}. \tag{5.2}$$

Here, Γ_1 and Γ_2 refer to the short and long decay components, respectively, and I_{01} and I_{02} correspond to the amplitudes of each term of the fitting. The long decay component is commonly correlated with the transitions of the Eu^{3+} cations in the bulk of the nanoparticle, while the short component is associated with those of the cations closer to the surface. The parameters resulting from fitting the decays enabled the determination of the average lifetime of each decay, illustrated in Fig. 5.17(b), through the expression

$$\tau = \frac{\int tPL(t)dt}{\int PL(t)dt} = \frac{I_{01}\Gamma_1^2 + I_{02}\Gamma_2^2}{I_{01}\Gamma_1 + I_{02}\Gamma_2}. \tag{5.3}$$

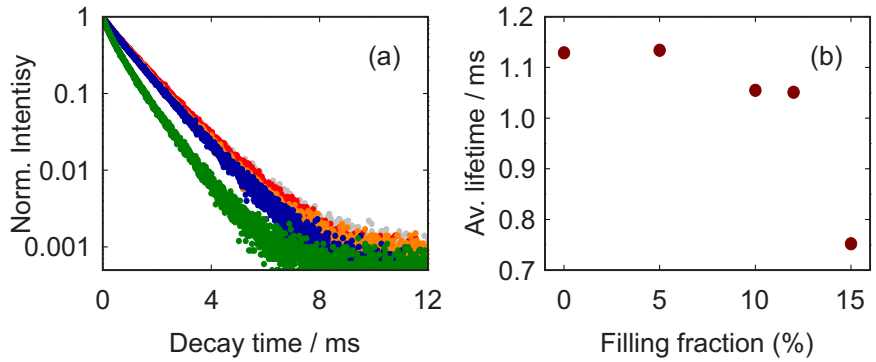

Figure 5.17: (a) Time-resolved PL decays for a reference nanophosphor film (gray decay) and nanophosphor films integrating scattering inclusions with a concentration of f = 5% (red decay), f = 10% (orange decay), f = 12% (blue decay) and f = 15% (green decay) under excitation at $\lambda = 365$ nm. (b) Average lifetime dependence on the filling fraction of the scattering centres in the films. All the films were infiltrated with PMMA.

The fitting curves of the time-resolved PL decay curves calculated employing Eq. 5.2 are displayed in Fig. 5.18, along with their corresponding residuals. The average lifetime hardly changed when scattering centres were integrated in a 5% concentration with respect to a bare nanophosphor film. This was a proof that, as expected, the inclusion of scattering particles would not significantly affect the processes responsible for the photoluminescence of the phosphors. While a slight decrease was visible for increasing concentrations, the average lifetime dramatically declined for f > 12%, in line with the previous observations regarding the PL spectra and the quantification of β_{tot}, Fig. 5.15. This behaviour was attributed to the high sensitivity of the PL performance of the nanophosphors to their environment and surface conditions. In fact, the medium surrounding the phosphor nanocrystals has been reported to seriously affect their emission properties[27–29], therefore altering their dynamic emission characteristics. The pictures in Fig. 5.19 present a visual proof of such emission enhancement, which was visible with the naked eye when comparing to a bare reference nanophosphor layer. In effect, the presence of scattering inclusions reduced the fraction of light trapped inside the film by total internal reflection and escaping at the edges, visible in Fig. 5.19(b) when com-

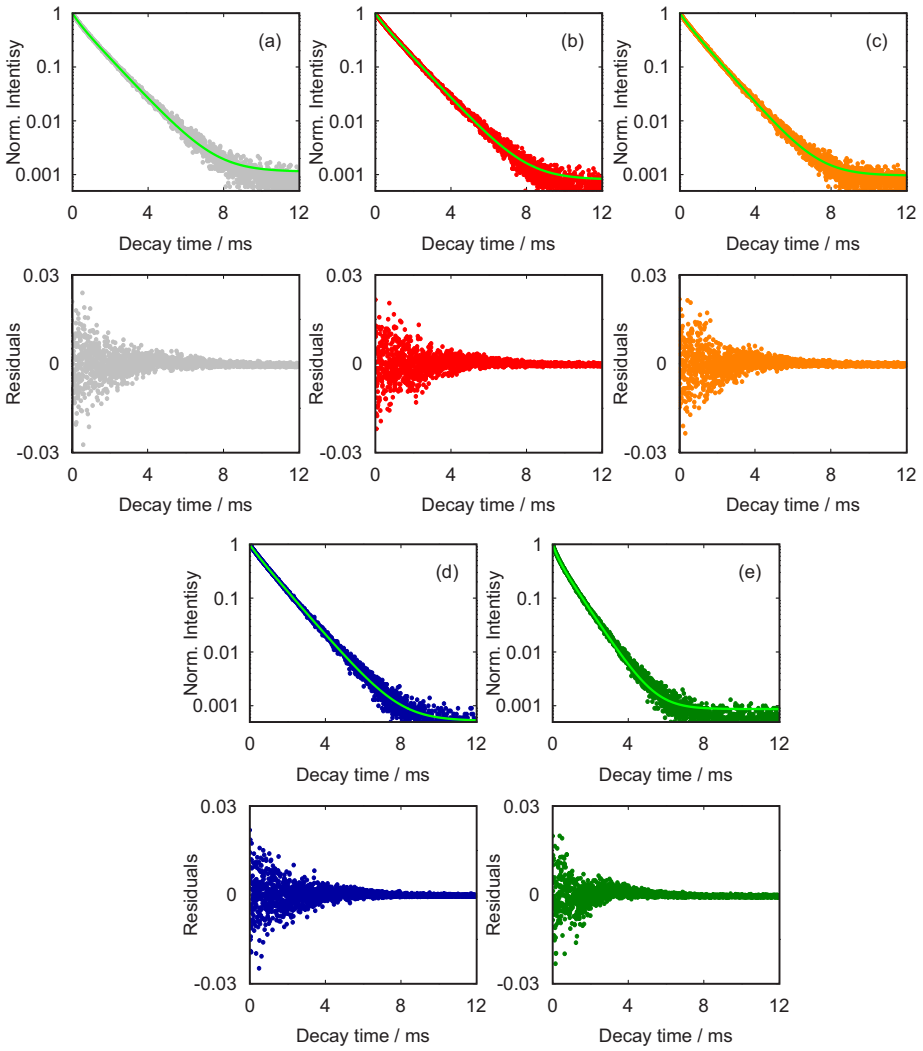

Figure 5.18: Time-resolved PL decays of the Eu^{3+} cations of the different nanophosphor films under excitation at $\lambda = 365$ nm and the corresponding curves (bright green line) resulting from fitting the decays to a bi-exponential model according to Eq. 5.2, along with their corresponding residuals. Data correspond to (a) a bare reference film devoid of inclusions and films integrating spherical scattering centres with concentration values of (b) f = 5%, (c) f = 10%, (d) f = 12% and (e) f = 15%.

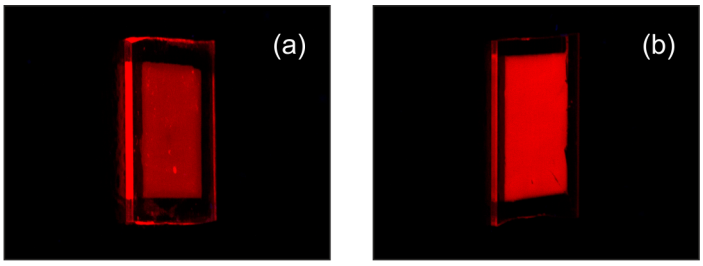

Figure 5.19: Intense red luminescence of (a) a reference film and (b) a film including scattering spheres in a 10% concentration under UV irradiation. Both films were based on $GdVO_4$:Bi^{3+},Eu^{3+} nanophosphors.

paring to the reference film shown in (a). As a consequence of a more efficient out-coupling, larger β_{tot} was observed. A similar behaviour was revealed when considering phosphors including Dy^{3+} as the RE centre. Films based on phosphors including this RE cation displayed a greenish emission, due to their emission lines at $\lambda = 482$ nm and $\lambda = 570$ nm, as illustrated in Fig.5.20(a). These spectra in combination with the picture in Fig.5.20(b) demonstrated analogous results for these films to those consisting in Eu-based phosphors. In order to test the suitability of the developed material for integration as a

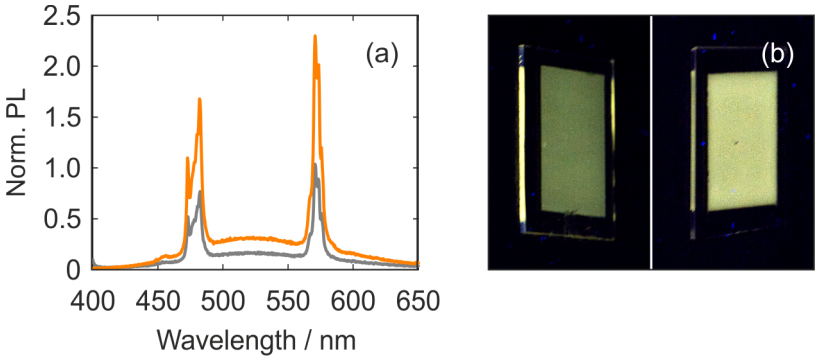

Figure 5.20: (a) PL spectra of $GdVO_4$:Bi^{3+},Dy^{3+} nanophosphors for a reference film (gray line) and a film integrating scattering spheres in a 10% concentration (orange line). (b) Intense greenish luminescence of a reference film (left) and a film including scattering spheres in a f = 10% concentration (right) under UV irradiation.

conversion layer in LEDs, it was irradiated with UVA-LED light, Fig. 5.21. Both, rigid and flexible versions of a reference film, exhibited red emission when shone with LED light at $\lambda = 380$ nm, thus demonstrating their potential to operate as a conversion layer when integrated into an emitting device.

The results herein presented proved the paradigmatic inclusion of spherical TiO_2 scattering centres in this work as a straightforward, inexpensive and easy-to-implement approach for the fabrication of efficient colour-converting films. The PL improvement has been demonstrated to originate from a more efficient extraction of the generated light from the film, owing to a lower fraction of light trapped, which is guided throughout the film by total internal reflection and escapes the system at the edges. Whereas the approach has been proved effective for low inclusion concentrations, the high sensitivity of the phosphor nanoparticles to the surrounding conditions demands special attention when increasing such concentration. The generality of the approach enables extension to phosphors including Dy^{3+} as the RE cation. The flexible films herein analysed present the advantage of being versatile enough to allow straightforward integration into LED devices, thus reducing costs by avoiding the need for other sophisticated integration routes. These results pave the way for the fabrication of versatile and more efficient solid-state illumination sources.

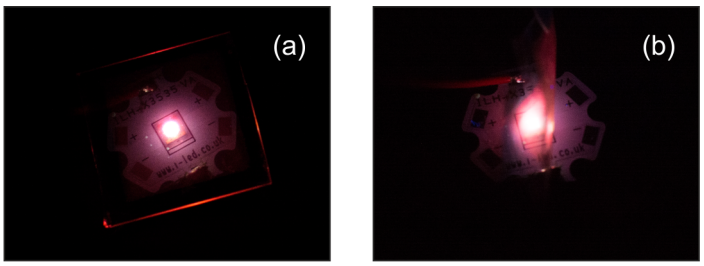

Figure 5.21: Red emission by a (a) rigid and (b) flexible $GdVO_4$:Bi^{3+},Eu^{3+}-based film under LED irradiation at $\lambda = 380$ nm.

5.4 Conclusions

The capability of optical disorder at enhancing the PL of emitting films has been demonstrated in this chapter. In the first section, the effect of integrating optical disorder into a mesoporous anatase film sensitised with emitting molecules of an organic dye has been studied. A PL enhancement dependent on the pumping wavelength after integrating spherical TiO_2 particles has been demonstrated. Such enhancement was proved to be a consequence of a combination of an increased absorption of light by the material at the pumping wavelength and a more efficient out-coupling of the light according to the ℓ_{sc} values. Control over such enhancement was offered through the size and concentration of the spherical inclusions, which define ℓ_{sc}.

The second section has been devoted to optically random media based on a transparent porous film consisting in $GdVO_4$:Bi^{3+},Eu^{3+} nanophosphors, which presented intense red emission under UV irradiation. In the first place, films of this material were fabricated and their optical response characterised, demonstrating that 4-μm thick films could absorb most of the incident light at the pumping wavelength, *i.e.* $\lambda = 365$ nm. Besides, they were successfully transferred into a polymeric support, endowing them with flexibility. Integration of scattering centres produced a new optically random medium with the added feature of light emission. An analysis of the PL enhancement of this emitting material was performed in terms of the conditions of the scattering centres included. An improvement of the PL for increasing concentration of scattering centres of $r = (225 \pm 20)$ nm was observed, displaying a PL maximum for $f = 12\%$. This PL enhancement was demonstrated to exclusively derive from a more efficient process of light extraction from the film. High inclusion concentrations, $f > 12\%$, were proved to have a detrimental effect on the PL enhancement, which was attributed to the high sensitivity of the phosphor surface to the environmental conditions, as dynamic emission measurements hinted. Visual proof of the beneficial effect of integrating scattering centres on the PL of the films was presented and the versatility of the approach proved by applying it to other colour-emitting phosphors, specifically, $GdVO_4$:Bi^{3+},Dy^{3+}, which displayed analogous results.

Bibliography

[1] C. Wiesmann, K. Bergenek, N. Linder, and U. T. Schwarz, "Photonic crystal LEDs – designing light extraction," *Laser & Photonics Reviews*, vol. 3, pp. 262–286, 2009.

[2] S. Reineke, "White organic light-emitting diodes: Status and perspective," *Reviews of Modern Physics*, vol. 85, pp. 1245–1293, 2013.

[3] T. Fuijii, Y. Gao, R. Sharma, E. L. Hu, S. P. DenBaars, and S. Nakamura, "Increase in the extraction efficiency of GaN-based light-emitting diodes via surface roughening," *Applied Physics Letters*, vol. 84, pp. 855–857, 2004.

[4] J. J. Wierer Jr, A. David, and M. M. Megens, "III-nitride photonic-crystal light-emitting diodes with high extraction efficiency," *Nature Photonics*, vol. 3, pp. 163–169, 2009.

[5] T. Bocksrocker, J. Hoffmann, C. Eschenbaum, A. Pargner, J. Preinfalk, F. Maier-Flaig, and U. Lemmer, "Micro-spherically textured organic light emitting diodes: A simple way towards high-ly increased light extraction," *Organic Electronics*, vol. 14, 396–
401, 2013.

[6] J. Lee, T. Koh, H. Cho, T. Schwab, J. Lee, S. Hofmann, J. Lee, S. Yoo, K. Leo, and M. C. Gather, "Transparent organic light-emitting diodes with different bi-directional emission colors using color-conversion capping layers," *Journal of Luminescence*, vol. 162, pp. 180–184, 2015.

[7] H. Xiang, Y. Li, L. Zhou, H. Xie, C. Li, Q. Ou, L. Chen, C. Lee, S. Lee, and J. Tang, "Outcoupling-enhanced flexible organic light-emitting diodes on ameliorated plastic substrate with built-in indium-tin-oxide free fransparent electrode," *ACS Nano*, vol. 9, pp. 7553–7562, 2015.

[8] T. Koh, J. A. Spechler, K. M. Lee, C. B. Arnold, and B. P. Rand, "Enhanced outcoupling in organic light-emitting diodes via a high-index contrast scattering layer," *ACS Photonics*, vol. 2, 1366–1372, 2015.

[9] J. B. Preinfalk, T. Eiselt, T. Wehlus, V. Rochnacher, T. Hanemann, G. Gomard, and U. Lemmer, "Large-area screen-printed

internal extraction layers for organic light-emitting diodes," *ACS Photonics*, vol. 4, pp. 928–933, 2017.

[10] Z. Chen, L. Liang, Y. Wang, N. Qiao, J. Gao, Z. Gan, and Y. Yang, "Tunable high reflective bands to improve quantum dot white light-emitting diodes," *Journal of Materials Chemistry C*, vol. 5, pp. 1149–1154, 2017.

[11] K. Okamoto, I. Niki, A. Shvartser, Y. Narukawa, T. Mukai, and A. Scherer, "Surface-plasmon-enhanced light emitters based on InGaN quantum wells," *Nature Materials*, vol. 3, pp. 601–605, 2004.

[12] S. Pillai, K. R. Catchpole, T. Trupke, G. Zhang, J. Zhao, and M. A. Green, "Enhanced emission from Si-based light-emitting diodes using surface plasmons," *Applied Physics Letters*, vol. 88, p. 161 102, 2006.

[13] O. L. Muskens, V. Giannini, J. A. Sánchez-Gil, and J. G. Rivas, "Strong enhancement of the radiative decay rate of emitters by single plasmonic nanoantennas," *Nano Letters*, vol. 7, pp. 2871–2875, 2007.

[14] J. DiMaria, E. Dimakis, T. D. Moustakas, and R. Paiella, "Plasmonic off-axis unidirectional beaming of quantum-well luminescence," *Applied Physics Letters*, vol. 103, p. 251 108, 2013.

[15] G. Lozano, D. J. Louwers, S. R. K. Rodríguez, S. Murai, O. T. A. Jansen, M. A. Verschuuren, and J. G. Rivas, "Plasmonics for solid-state lighting: Enhanced excitation and directional emission of highly efficient light sources," *Light: Science & Applications*, vol. 2, e66, 2013.

[16] P. Ding, M. Li, J. He, J. Wang, C. Fan, and F. Zeng, "Guided mode caused by silicon nanopillar array for light emission enhancement in color-converting LED," *Optics Express*, vol. 23, 21477–21 489, 2015.

[17] V. Y. F. Leung, A. Lagendijk, T. W. Tukker, A. P. Mosk, W. L. IJzerman, and W. L. Vos, "Interplay between multiple scattering, emission, and absorption of light in the phosphor of a white light-emitting diode," *Optics Express*, vol. 22, pp. 8190–8204, 2014.

[18] M. D. Birowosuto, S. E. Skipetrov, W. L. Vos, and A. P. Mosk, "Observation of spacial fluctuations of the Local Density of

States in random photonic media," *Physical Review Letters*, vol. 105, p. 013 904, 2010.

[19] R. Sapienza, P. Bondareff, R. Pierrat, B. Habert, R. Carminati, and N. F. van Hulst, "Long-tail statistics of the Purcell factor in disordered media driven by near-field interactions," *Physical Review Letters*, vol. 106, p. 163 902, 2011.

[20] A. Cazé, R. Pierrat, and R. Carminati, "Radiative and non-radiative local density of states on disordered plasmonic films," *Photonics and Nanostructures - Fundamentals and Applications*, vol.
10, pp. 339–344, 2012.

[21] C. Feldmann, T. Jüstel, C. R. Ronda, and P. J. Schmidt, "Inorganic luminescent materials: 100 years of research and application," *Advanced Functional Materials*, vol. 13, pp. 511–516, 2003.

[22] R. Mueller-Mach, G. Mueller, M. R. Krames, H. A. Höppe, F. Stadler, W. Schnick, T. Juestel, and P. Schmidt, "Highly efficient all-nitride phosphor-converted white light emitting diode," *phy- sica status solidi (a)*, vol. 202, pp. 1727–1732, 2005.

[23] C. C. Lin and R. Liu, "Advances in phosphors for light-emitting diodes," *Journal of Physical Chemistry Letters*, vol. 2, pp. 1268–1277, 2011.

[24] M. L. Saladino, A. Zanotto, D. C. Martino, A. Spinella, G. Nasillo, and E. Caponetti, "Ce:YAG nanoparticles embedded in a PMMA matrix: Preparation and characterization," *Langmuir*, vol.
26, pp. 13 442–13 449, 2010.

[25] A. M. Darwish, M. T. Sagapolutele, S. Sarkisov, D. Patel, D. Hui, and B. Koplitz, "Double beam pulsed laser deposition of composite films of poly(methyl methacrylate) and rare earth fluoride upconversion phosphors," *Composites: Part B*, vol. 55, 139–
146, 2013.

[26] J. Prakash, V. Kumar, L. J. B. Erasmus, M. M. Duvenhage, G. Sathiyan, S. Bellucci, S. Sun, and H. C. Swart, "Phosphor polymer nanocomposite: ZnO:Tb^{3+} embedded polystyrene nanocomposite thin films for solid-state lighting applications," *Applied Nano Materials*, vol. 1, pp. 977–988, 2018.

[27] R. S. Meltzer, S. P. Feofilov, B. Tissue, and H. B. Yuan, "Dependence of fluorescence lifetimes of Y_2O_3:Eu^{3+} nanoparticles on the surrounding medium," *Physical Review B*, vol. 60, R14012(R)–R14015(R), 1999.

[28] J. Zhao, Z. Lu, Y. Yin, C. McRae, J. A. Piper, J. M. Dawes, D. Jin, and E. M. Goldys, "Upconversion luminescence with tunable lifetime in $NaYF_4$:Yb,Er nanocrystals: Role of nanocrystal size," *Nanoscale*, vol. 5, pp. 944–952, 2013.

[29] T. Senden, F. T. Rabouw, and A. Meijerink, "Photonic effects on the radiative decay rate and luminescence quantum yield of doped nanocrystals," *ACS Nano*, vol. 9, pp. 1801–1808, 2015.

General conclusions

This thesis addresses the fabrication of optically random media with the appropriate features to observe an enhancement of the optical absorption and emission of the light by either dye molecules adsorbed to their structure or matrices comprising luminescent particles. An analysis of light propagation in them is presented and their integration into optoelectronic devices assessed.

- The fabrication of optically disordered materials based on transparent matrices of either high or ultralow refractive index in which the amount of disorder can be controlled was addressed. Solution-processing techniques, such as spin-coating, screen-printing or dip-coating, as well as a technique based on chemical vapour deposition, were proved effective at preparing transparent films of optical quality for the integration of optical disorder. The techniques enabled the transference of the materials based on a high refractive index matrix into a polymeric support for the development of a flexible version.

- An analysis of light propagation in the fabricated materials de-
  monstrated the possibility of describing light transport through Mie formalism, thus allowing a design of their scattering properties previous to fabrication.

- Sensitisation of the *Mie glass* based on a porous anatase matrix, the material photoanodes for DSSCs are based on, with an absorbing dye commonly employed in the field of DSSCs as photoactive material demonstrated a controlled enhancement of the absorption of light, directly related to the scattering strength of the material. As a consequence, the material was integrated as photoanode into bifacial DSSCs, resulting in devices with enhanced performance.

- Optical disorder was demonstrated to cause an improvement of light emission of a *Mie glass* based on a high refractive index matrix sensitised with luminescent molecules of an organic

dye as a consequence of a combination of improved light absorption at the pumping wavelength with enhanced light outcoupling at the emission wavelength. Along the same lines, a *Mie glass* based on a luminescent nanophosphor matrix exhibited a controlled increase of the emission, which was proved to exclusively originate from a more efficient extraction of the generated light. These observations indicated the potential of these random materials as efficient colour converters for light-conversion applications, such as light down-shifting in LEDs.

Publications

Part of the work presented in this thesis is included in the following publications:

"Efficient bifacial dye-sensitized solar cells through disorder by design" **J. M. Miranda-Muñoz**, S. Carretero-Palacios, A. Jiménez-Solano, Y. Li, G. Lozano, and H. Míguez. *Journal of Materials Chemistry A*, vol. 4, pp. 1953–1961, 2016. DOI: 10.1039/C5TA10091G

"Design and realization of a novel optically disordered material: A demonstration of a Mie Glass" **J. M. Miranda-Muñoz**, G. Lozano, and H. Míguez. *Advanced Optical Materials*, vol. 5, pp. 1700025, 2017. DOI: 10.1002/adom.201700025

"Flexible nanophosphor films doped with Mie resonators for enhanced out-coupling of the emission" **J. M. Miranda-Muñoz**, D. Geng, M. E. Calvo, G. Lozano, and H. Míguez. *Journal of Materials Chemistry C*, vol. 7, pp. 267–274, 2019. DOI: 10.1039/C8TC05032E

"Finite size effects on light propagation throughout random media: relation between optical properties and scattering event statistics" **J. M. Miranda-Muñoz**, V. Esteso, A. Jiménez-Solano, G. Lozano, and H. Míguez. *Advanced Optical Materials*, *under review*.

Multifunctional
Optical
Materials
Group